UNIVERSITA' DEGLI STUDI DELL' INSUBRIA
Dipartimento di Scienza ed Alta Technologia (DiSAT)
Philosophae Doctoral in Physics and Astrophysics

Toward the Extremely Large Telescopes era in Exoplanetary science: Simulation tools, instrumental optimization and design for high resolution spectroscopy. The cases of ESPRESSO and ELT-HIRES.

Doctoral Program Chair: Prof. Massimo Caccia
Supervisor: Dr. Marco Landoni
Tutors: Ing. Marco Riva - Dr. Filippo M. Zerbi

PhD Thesis of:
Matteo Genoni
Matr. 726033

PhD XXX Cycle
Academic years 2014 - 2017

Toward the Extremely Large Telescopes era in Exoplanetary science: simulation tools, instrumental optimization and design for high resolution spectroscopy. The cases of ESPRESSO and ELT-HIRES.

Matteo Genoni

A thesis submitted for the degree of
Doctor of Philosophy in Physics and Astrophysics,
28^{th} March 2018.

Doctoral Program Chair: Prof. Massimo L. M. Caccia
Supervisor: Dr. Marco Landoni, INAF-Osservatorio Astronomico di Brera
Tutors: Ing. Marco Riva, INAF-Osservatorio Astronomico di Brera
Dr. Filippo M. Zerbi, INAF-Scientific Director

Doctoral thesis reviewers:
Prof. Debra A. Fischer, Yale University
Prof. Stefano Cristiani, INAF-Osservatorio Astronomico di Trieste

Members of the Examination Committee:
Prof. Massimo L. M. Caccia, Università degli Studi dell' Insubria
Prof. Francesco Haardt, Università degli Studi dell' Insubria
Prof. Francesco A. Pepe, Observatoire Astronomique de l'Université de Genève

Front Cover: Exoplanet artistic impression - Very Large Telescope, UT3 (photo taken by the author) - Spectrograph ray-tracing model - Simulated fiber-fed spectrograph raw frame.
Rear Cover: Exoplanet artistic impression - side view of the Earth atmosphere.

Ai miei genitori, a Cecilia
e alla nostra futura famiglia.

Contents

List of Figures

List of Tables

Acronyms

APSU: Anamorphic Pupil Slicer Unit.
ADC: Atmospheric Dispersion Correction.
ADU: Analog-to-Digital Unit.
ASCII: American Standard Code for Information Interchange.
AU: Astronomical Unit.
AWS: Amazon Web Services.
BIC: Bayesian Information Criteria.
CCD: Charge Couple Device.
CCF: Cross-Correlation Function.
CCL: Combined Coudè Laboratory.
CMOS: Complementary Metal-Oxide Semiconductor.
CoRoT: Convection Rotation and planetary Transit.
CRIRES: CRyogenic high-resolution InfraRed Echelle Spectrograph.
CU: Calibration Unit.
CUDA: Compute Unified Device Architecture.
DCG: DiChromated Gelatin.
DRS: Data Reduction Software.
E2E: End-to-End.
EC2: Elastic Computing 2.
ELT: Extremely Large Telescope.
ELT-HIRES: ELT-HIgh REsolution Spectrograph.
EMM:ESO Meteo Monitoring.
ESO: European Southern Observatory.
ESPRESSO: Echelle SPectrograph for Rocky Exoplanets Super Stable Observations.
ETC: Exposure Time Calculator.
FEU:Front-End Unit.
FFT: Fast Fourier Transform.
FL: Fiber Link.
FITS: Flexible Image Transport System.
FWHM: Full Width Half Maximum.
GAIA (spacecraft): Global Astrometric Interferometer for Astrophysics.
GAIA (sw): Graphical Astronomy and Image Analysis.
GDAS: Global Data Assimilation System.
GMT: Giant Magellan Telescope.
GPI: Gemini Planet Imager.
GPU: Graphical Processing Unit.
HARMONI: High Angular Resolution Monolithic Optical and Near-infrared Integral

field spectrograph.
HARPS: High Accuracy Radial velocity Planet Searcher.
HARPS-N: HARPS north.
HAT: Hungarian Automated Telescope.
HET: Hobby-Eberly Telescope.
HR: High Resolution.
HST: Hubble Space Telescope.
HZ: Habitable zone.
IFU: Integral Field Unit.
IGM: Inter-Galactic Medium.
IP: Instrument Profile.
JWST: James Webb Space Telescope.
KOSI: Kaiser Optical System, Inc.
LBLRTM: Line-By-Line Radiative Transfer Model.
LBTI: Large Binocular Telescope Interferometer.
LSF: Line Spread Function.
METIS: Mid-infrared ELT Imager and Spectrograph.
MMP: Multi-Mini Prisms.
MICADO: Multi-adaptive optics Imaging CAmera for Deep Observations.
MIRI: Mid-Infrared Instrument (JWST).
MOA: Microlensing Observation in Astrophysics.
MR: Medium Resolution.
NACO: Nasmyth Adaptive Optics System (NAOS) – Near-Infrared Imager and Spectrograph (CONICA).
NASA: National Agency Space Administration.
NIR: Near Infra-Red.
NIRcam: Near Infrared Camera (JWST).
NIRISS: Near-InfraRed Imager and Slitless Spectrograph (JWST).
NIRSPEC: Near-Infrared Spectrometer (JWST).
NOAA: National Oceanic and Atmospheric Administration.
OGLE: Optical Gravitational Lensing Experiment.
OSIRIS: Optical System for Imaging and low-Intermediate-Resolution Integrated Spectroscopy.
ppm: part per million.
PSF: Point Spread Function.
PSR: pulsar.
PWV: Precipitable Water Vapor.
QE: Quantum Efficiency.
QSO: Quasi-Stellar Object.
RAM: Random Access Memory.
RCWA: Rigorous Coupled-Wave Analysis.
RON: Read Out Noise.
RV: Radial Velocity.
SCAO: Single Conjugate Adaptive Optics.
SG: Scrambling Gain.
SNR: Signal-to-Noise ratio.
SPHERE: Spectro-Polarimetric High-contrast Exoplanet Research.

SRE: Spectral Resolution Element.
TMT: Thirty Meter Telescope.
TNG: Telescopio Nazionale Galileo.
TrES: Trans-atlantic Exoplanet Survey (network).
TSS: Transmission spectra simulator
UHR: Ultra High Resolution.
UT: Unit Telescope.
UV: Ultra-Violet.
UVES: UV Echelle Spectrograph.
VLT: Very Large Telescope.
VPHG: Volume Phase Holographic Grating.
WASP: Wide Angle Search for Planets.
WFC3: Wide Field Camera 3.
WFEM: Wave-Front Error Matrices.
WP: Work Package.
WPM: Work Package Manager.

Abstract

Front line researches on extrasolar planets is entering a new era, where the detection capabilities will be pushed to unprecedented sensitivity. Exoplanetary atmospheres characterization through high resolution spectroscopy, with the ultimate goal of detecting the few ppm amplitude signal of an Exo-Earth orbiting Solar-like star, is one of the most fascinating example. In this context high dispersion transmission spectroscopy require high fidelity spectra produced by high resolution spectrograph coupled with large aperture telescopes (like ESO-VLT and the future ESO-ELT). In this thesis I will present my Ph.D. activities concerning the development of simulation tools both for high resolution spectrograph design and for scientific investigations.

In my Ph.D. path I have also been involved in two projects for ground-based high resolution spectrograph: ESPRESSO and ELT-HIRES. For what concern ESPRESSO (the Echelle SPectrograph for Rocky Exoplanets Super Stable Observations) the instrument modeling through ray-tracing software and ad-hoc developed sensitivity analysis tool have been fruitfully used for component optimization, instrument integration and alignment verification with the ultimate goal of achieving the best performance, like optical quality and throughput essential for the maximum scientific return. This was demonstrated with the successful installation and commissioning at the VLT complex in Paranal.

In the framework of the ELT-HIRES (the HIgh REsolution Spectrograph for the ELT) project, a parametric paraxial model of the spectrograph has been developed with the purpose to evaluate the impact that the different optical components parameters can have with respect to defined performance requirements and technical constraints. This tool has been detailed described, verified and then fruitfully exploited in the optical design analysis of the ELT-HIRES instrument, for the definition of the main parameters of the optical components of the infrared arm of the instrument, crucial for exoEarths characterization (where molecular band, H_20 and bio-signature are expected to lie).

The ELT-HIRES science case related to transmission spectroscopy for exoplanet atmospheres (especially for the study and characterization and Exo-Earths atmospheres in the Habitable zones of Sun-like stars) requires a careful analysis and design of the experiment in order to succeed. A key activity of my Ph.D. work has been the development of an End-to-End simulator to evaluate the different effects which can affect the final instrument performances, like resolving power, stability and throughput, since they directly influence the scientific data observational performances (e.g. in

terms of stability, instrumental profile, SNR). The design and continuous development of this End-to-End simulator directly during the different design phases of a complex instrument like ELT-HIRES, will allow Data Reduction, astronomers and engineers to perform science verification as well as to overcome possible problem related to the instrument well before the first light. The simulator design philosophy, physical modeling and computational architecture are described. The results concerning the synthetic echellogram (raw frame) produced and successfully processed by the beta recipes of the CRIRES+ instrument DRS have been presented, thus probing the full chain feasibility and consistency of the system.

For what concern the scientific part of my Thesis, I focused on development of a possible science module for the E2E simulator related to transmission spectroscopy. In details, large telescopes allowing very high contrast, could imply the possibility to detect the light emitted from background sources and/or from gravitationally bounded companion of exoplanetary system, which could act as signal contamination. The investigation of these scenarios has been one of main drivers for the development of a transmission spectra simulator, a tool aimed at generating synthetic spectra combining the star spectrum, exo-atmospheric absorption, earth telluric contribution and also contamination due to gravitationally bounded companions or background objects. This simulator was used to perform two kind of analyses. In the first one the pure astrophysical noise coming from a background (or foreground) source not gravitationally bounded is considered, without taking into account instrumental noise, SNR or telluric contribution (of Earth and exoplanet). The result is that the maximum contamination (in the order of 1000 ppm) occurs for background object which spectral type matches roughly the one of the host star (G or M type), while a much lower contamination (in the order of 10 ppm) is related to hot stars, like O and B type. In the second scenario (performed in collaboration with the Exoplanetary Science group of Geneva Observatory) the host star, the absorption features from the hot Jupiter atmosphere and the contaminant source are considered. A data-set of transmission spectra was generated to simulate the observations of HARPS spectra of the system HD189733, as a test-bed to reproduce what HARPS would be observed if an unbounded companion with apparent magnitude $m_V - 12$ and spectral type M were ingested by the spectrograph since confused in the seeing disk. After data reduction and processing, the absorption features coming from the exo-atmosphere has been recovered properly despite the presence of the contaminant star, although, tentatively, some line broadening could be observed. No obvious shift of the sodium line (like the one detected in the atmosphere of HD 189733b) are detected supporting the idea that the contamination from background source could not mimic this results (at least for the scenarios considered).

Chapter 1

Introduction

Only 22 years has passed when, for the first time, Mayor & Queloz in 1995 detected an orbiting planet around the 51 Peg nearby star. From that moment, hundreds of exoplanetes have been discovered with various method, from radial velocity (based on spectroscopic techniques) to transiting method and direct imaging. We are now entering a new era where we will not only detect the presence of these minor bodies around stars but we are approaching the possibility to characterise their atmosphere, composition and perhaps detect their life bio-signatures systematically.

However, the measurements of these properties is challenging both for the physics behind them and for the precise design, optimization and characterization of instrumentations needed to carry out this kind of research. I will focus on high resolution spectroscopy both from scientific and technological point of view aiming to design valuable tools that could be exploited for optimizing performances with the ultimate goal of maximizing the scientific return.

For what concern my contribution to instrumentation, I developed an End-to-End (E2E) simulator which has the objective to model the whole physical chain in astronomical observations: from the light source to synthetic raw frames and the reduced data. For the E2E simulator development we have focused on the High REsolution Spectrograph proposed for the future Extremely Large Telescope (which is called ELT-HIRES at the time of writing); the unprecedented photon collecting power of the ELT coupled with a high dispersion and high stability spectrograph will allow to do relevant discoveries in the field of exoplanetary atmospheres characterization (both in transmission and reflection). Moreover, also other physical research lines will benefit of its large aperture and stability. A non exhaustive example is the detection of fundamental constant variation or detecting the "breath" of the Universe (revealing the variation of the redshift with time).

With its modularity and flexibility the E2E simulator will be useful in all the different phases of such a complex and long-time project, enabling a very successful cooperation of a wide range of users: from project manager and engineers to instrument scientist and astronomers. In particular from a technical point of view E2E simulations are fundamentals to obtain the best possible scientific results since they are exploited both for the optimization of the instrumental performance, like sampling and efficiency (and thus Signal-to-Noise ratio, SNR), and requirements verification,

e.g. resolving power, in all design and integration phases for ELT-instrument projects. From scientific side this simulator gives the opportunity to perform in advance analyses and tests on the scientific drivers and it allows Data Reduction Software (DRS) development strategies and/or the evaluation of re-usability of existing pipelines.

It must be also underlined that the development of such a complex simulator requires the interface and interaction with the work-package managers and expertise of other work-packages in the whole framework of the ELT-HIRES project.

The End-to-End simulator design philosophy, global architecture and the development of the physical model of the different Modules (and Units), which compose the entire simulator, are described in Chapter 5. Furthermore in this Chapter the computational architecture of the simulator is detailed, highlighting its speed performance, and the results concerning the synthetic echellogram (raw frame) produced and successfully processed by the beta recipes of the CRIRES+ instrument DRS are presented.

In addition for what concern the ELT-HIRES instrument, a paraxial parametric model of the spectrometer is described in details in Chapter 4 (section 4.4). The flexibility and reliability of this optical model can be useful to quickly evaluate the impact that the different optical components parameters can have with respect to defined performance requirements and technical constraints. In this respect its application for the design analysis of the infra-red spectrograph module of ELT-HIRES is presented.

As said before concerning the science drivers of ELT-HIRES, high dispersion spectroscopy, applied both for transit and eclipse events, is one of the most powerful observation technique for exoplanets atmosphere characterization; for what concern transmission spectroscopy a tool aimed at generating synthetic spectra combining the star spectrum, exo-atmospheric absorption, earth telluric contribution and also contamination due to gravitationally bounded companions or background objects has been developed (and presented in Chapter 3). The analysis of the probabilities of transmission spectrum contamination is one of the possible application of this simulator. This kind of analysis and simulation is oriented to assess the impact of the spectral contamination in terms of ppm, which is particularly relevant for the characterization Exo-Earths atmospheres (which will be one of the most interesting and fascinating research fields in astronomy of the near future) whose spectral feature are in the order of few (in the order of 10) ppm. This tool is characterized by flexibility and can ingest both high resolution well-detailed templates and simplified models for each type of considered object. Therefore it can also be used to generate the input spectra for the End-to-End simulator (developed for the ELT-HIRES instrument).

Finally, during my PhD path I also had the great opportunity to work on the next (at time of this writing available to the community in few months) high resolution spectrograph that will address exoplanetary science cases: ESPRESSO. In this project, I focused on the component optimization, instrument integration and verification with the ultimate goal of achieving the best performance, like optical quality and throughput essential for the maximum scientific return. Results from the integration and alignment operations of ESPRESSO at VLT in Paranal are shown in section 4.2 of

Chapter 4.

In Chapter 2 an introduction on Exoplanetary science is given, with an overview of the different exoplanet detection methods and a brief review of the Exoplanetary atmospheres characterization, focusing on the transmission spectroscopy, which is the scientific field at which this work refers to.

Chapter 2

Exoplanetary Science

2.1 The exoplanet revolution (the solar system paradigm end)

Before the first exoplanets discoveries, clear observations about the solar system structure and characteristics of planets led to the formulation of the "Solar Nebula" theory. According to it, the Solar system was formed by the collapse of a quasi-spherical giant interstellar cloud of gas and dust, which eventually flattened in the plane perpendicular to its initial rotation axis; the denser material in the center collapsed further under self-gravity to form the Sun, while outside, the material had collapsed into a disk-shape nebula, in differential rotation, where planets are supposed to have formed. This theory well fits with some properties of all Solar system planets, like the fact that they have quasi-circular orbits, which are well aligned with the ecliptic plane (the plane perpendicular to the Sun rotation axis), and the direction of planets revolution around the Sun is the same of its rotation.

An additional relevant aspect about the Solar system is the arrangement of the planets around the Sun: the small, rocky planets (Mercury, Venus, Earth and Mars) are located at small orbital distances (less than 1.5 AU), while gas giant planets like Jupiter (318 Earth masses) and Saturn (95 Earth masses) are located further away (5 and 10 AU), and finally the icy giants Uranus and Neptune (14 and 17 Earth masses respectively) are located even further (20 and 30 AU). The relatively simple planet formation theory, based on the "Solar Nebula" paradigm and widely accepted by the scientific community, stated that:

- large gaseous planets require larger orbit, with respect to small planets, with enough amount of material available for the grow and accretion; in addition in large orbits the temperature is low enough to allow the condensation of ices, which increases the solid fraction of the material and ease the nucleation process. Jupiter and Saturn are in fact located beyond the snow line, which delimits the orbit at which most ices (water, methane, etc.) condense.

- planets located in orbits which are too wide, take more time to accomplish a given number of revolutions, and thus accrete less gas before it falls in the star or is dispersed away by the stellar wind; this explained why Saturn is less massive

than Jupiter, and why Uranus and Neptune are even lighter and contain a high fraction of ices.

- small planets are found in relatively close orbits, because they had little material to accrete.

All observed aspects of the Solar system planet structure and characteristics had a good explanation with this planet formation theory, which in addition proposed a strong paradigm: *Solar systems planets were formed in situ, at the orbital position they are seen today.*

The picture that emerged with this theory was believed to also apply to other exoplanetary systems and drove the design of the first campaigns of exoplanet searches: find a Jupiter-like planet located a few AU from another star than the Sun.

But the first exoplanet detected around a star similar to the Sun, 51 Peg b, was definitely different from what expected: although similar in nature to Jupiter (a gas giant), its orbit has a period of only 4 days against 12 years of Jupiter's orbit. The formation of this exoplanet in situ was ruled out because at its orbit it was too hot and it would not have had enough material to accrete. Thus the most widely accepted conclusion is that the planet formed at a larger orbital distance and eventually migrated inward toward the star through a specific mechanism and finally stopped at its current location.

This was only the first different aspect that the history of exoplanetary discoveries has shown with respect to the architecture of solar system; in fact exoplanets are characterized by a great diversity in term of many properties: chemical composition, masse, size, hosting star, type of orbits (orbit size, eccentricity and resonances).

Today planetary system formation theories have been expanded to include complex considerations and mechanisms, among which the migration of planets during their evolution is also relevant for the solar system. As described in [24] Jupiter is thought to have moved inward to 1.5 AU from an initial 5 AU formation orbit, and then migrated back outward due to disk torques before and after Saturn's formation. This scenario can account for another fundamental aspect: the delivery of water on Earth (and other terrestrial planets) in the form of water-rich planetesimals (today still present in the asteroid belt as water-rich asteroids) scattered inward during the gas giants' migration.

2.2 Detection methods

The detection of extrasolar planets is a big observational challenge because the angular separation between the planet and the host star is extremely small and because the brightness contrast is extremely high, in particular in the optical wavelength band. In addition, for ground-based observations the Earth's atmosphere perturbation plays a relevant role increasing the difficulties in capturing some features of extra solar planets. In the past 20 years engineers and scientist have witnessed a great improvement of the instruments, observation techniques and strategies, detection limits and data analyses in the search of Exoplanets, pushing towards the detection of

low-mass and small planets. In the following subsections the different exoplanets detection methods, which are summarized in the schematic tree of Fig.2.1, are briefly described.

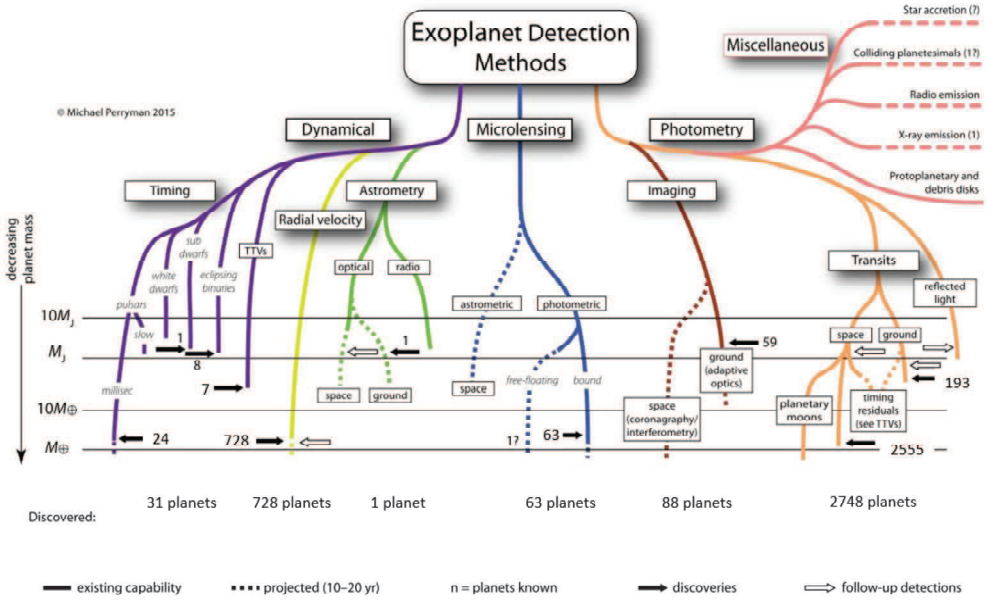

Figure 2.1: Schematic tree summary of the Exoplanets detection methods as of September 2017. The lower limits of the lines indicate the smallest masses that could be detectable with present measurements (solid lines), and those that might be expected within the next 10 – 20 years (dashed). The miscellaneous signatures at the upper right are less well quantified in mass terms. The figure is adapted from [90] taking numbers from *exoplanet.eu* and the NASA Exoplanet Archive [78].

2.2.1 Pulsar Timing

A pulsar is a magnetized neutron star which emits powerful radio waves in two cone-shaped beams which are inclined with respect to the spin axis; every time a cone points toward the Earth, a pulse is received. Their typical periods range from milliseconds to seconds, and are intrinsically extremely stable (millisecond pulsars did actually serve as time references). Because of the Doppler effect, the presence of a planet creates a time delay in these regular pulses. This method is so sensitive that it is able to detect very small planets, much lighter than any other method can currently do. This method was accidentally used in 1992 by A. Wolszczan to discover the very first two extra-solar planets around the millisecond pulsar PSR B1257+12, whose pulse arrival times were found to trace a smooth curve (upper panel of Fig.2.2). The presence of the two terrestrial planets (3 and 4 times the Earth mass) provided quasi-perfect fit the varying delay between the pulses (lower panel of Fig.2.2). This discovery in astrophysics history was very important not only because signaled the very first detection of an exoplanet but also because showed that exoplanets exist around star at all stages of their evolution, even in the final ones, and that formation of terrestrial planets can happen even in unfavorable environments.

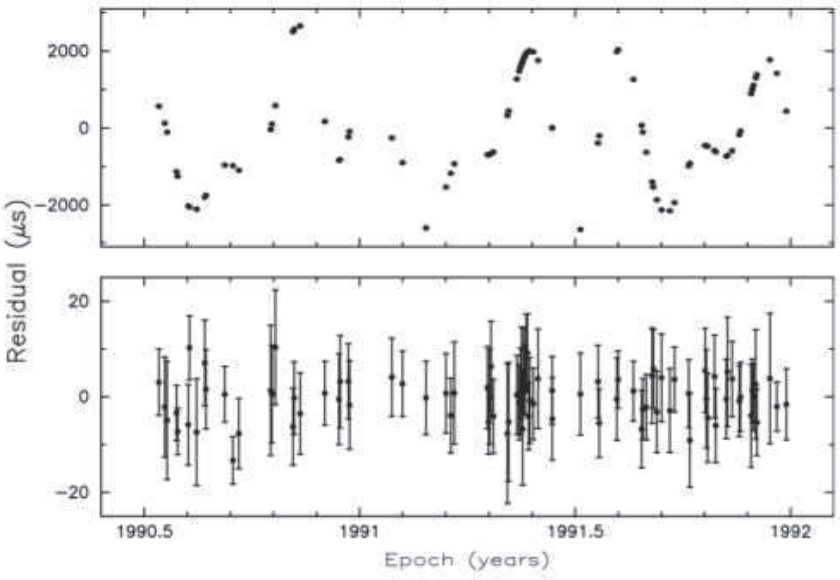

Figure 2.2: The upper panel shows the residuals (large residuals) of the pulse arrival times for the best pulsar timing model without companion; while the lower panel is the same but including two companion terrestrial planets (figure from [112]).

2.2.2 Astrometry

The basic idea of astrometry, probably the oldest branch of astronomy, consists in measuring the position and motion of objects in the plane of the sky; specifically if the position of the star is measured with precision and if the star has planets orbiting around, the difference in the position of star with respect to the center of mass of the system can be seen as an astrometric orbit caused by the (invisible) planetary companion. This method is most sensitive to wider orbits, because the center of mass displacement amplitude increases with orbital period; detectable orbital periods are typically several years. It is applicable to search for planets around active stars since it has a lower sensitivity to stellar activity with respect to other techniques like Doppler spectroscopy and photometric transits. As order of magnitude the astrometric amplitudes for a solar-mass star located at a distance of 10 pc caused by Earth-like planet is about 10^{-3} milli-arcsec (mas), while a Jupiter analog in a 10 year orbit requires much less precise astrometry in the order of 1 mas. In Fig.2.4 typical astrometric signal amplitudes are illustrated.

Astrometry has been used in combination with Doppler velocimetry, where only five of the seven orbital parameters are constrained. The advantage of astrometry in the determination of the real mass of a planet and the inclination of the orbit (which remain degenerated with the only use of radial velocity technique) has been exploited to confirm or refute the presence of a planet candidate. For example successful application of ground-based imaging astrometry allowed to infer a mass upper limit of about 3.6 M_J to the planet around GJ317 ([3]). In addition this combination permitted to distinguish between giant planets and brown dwarfs (as reported in [24]

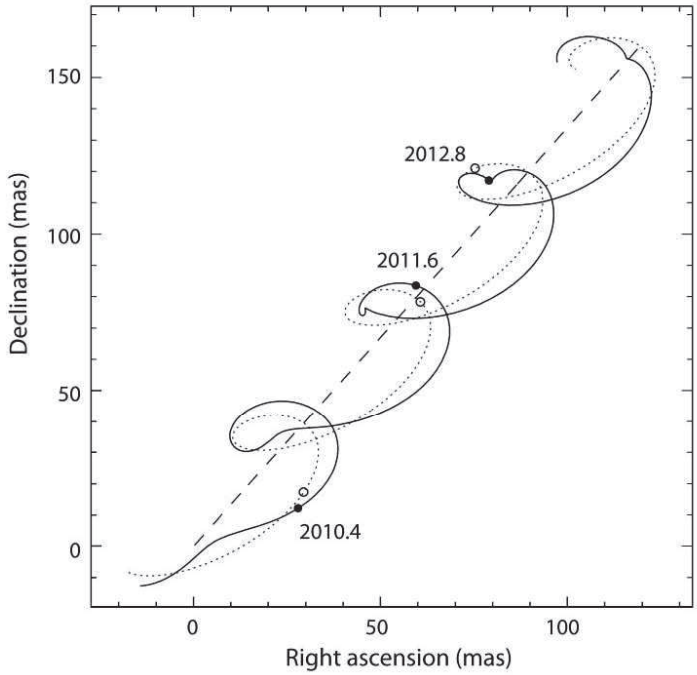

Figure 2.3: Schematic of the sky path of a star orbited by a planet. The straight dashed line shows the system barycenter motion viewed from the solar system barycentre frame. The dotted line shows the effect of parallax (the Earth orbital motion around the Sun). The solid line shows the motion of the star affected by the presence of the orbiting planet (the effect of the planet on the star is magnified by 30 for visibility. Taken from [90]

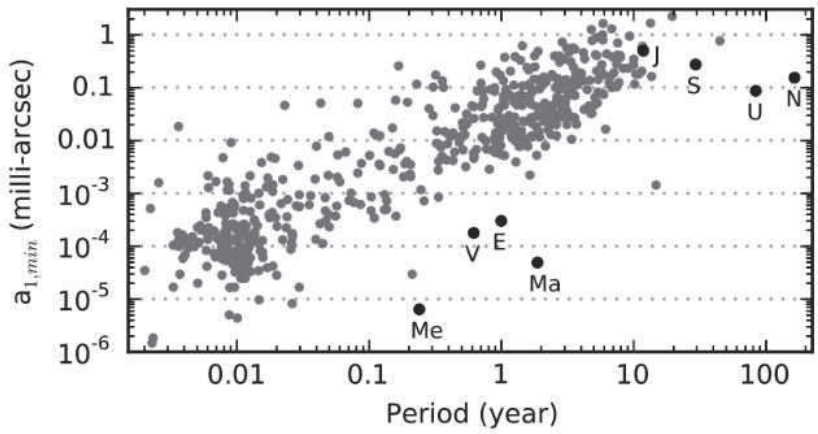

Figure 2.4: Minimum astrometric signature of the host star as a function of orbital period for 570 planets (grey circles). For comparison, the astrometric signatures of a solar-mass star located at distance of 10 pc would exibit due to the perturbation of Solar system planets are shown with black circles and labelled with the planet initials. Figure taken from [42].

the ESA satellite Hipparcos and HST were exploited for this purpose).

From space Gaia mission, launched on 2013, is performing an all-sky survey of about billion stellar objects with visible magnitude range of 6-20; as reported in [42] on average the astrometry of a star will be measured 70 times over the mission lifetime of five years with a single measurement precision of $\simeq 0.02 - 0.05$ mas. Thanks to this precision it is expected that thousands of new exoplanets will be discovered and it will also possible to build a wide census of giant planets in intermediate period orbits.

2.2.3 Microlensing

Microlensing is based on the same physics of the gravitational lensing effect described with the General Relativity; but since in this context the lensing effect, due to the presence of a star or a star-planet system, is much smaller than the one given by a galaxy or a cluster of galaxy it is called microlensing. The relevant aspect for

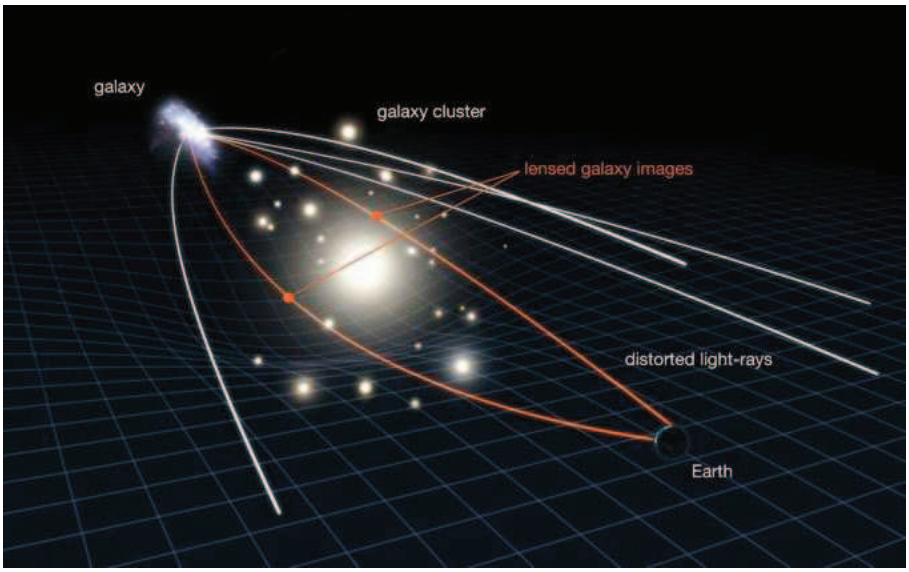

Figure 2.5: Example of a gravitational lensing effect caused by the presence of a cluster of galaxy which lies along the line of sight of the observer (Earth) and target (background galaxy).

the exoplanets detection is that it is the planet's star lensing effect of another, more distant bright object, which is searched for; not the planet lensing effect on its own hosting star. The more distant bright object could be another star, a quasar, or any other light-emitting object. The planet creates its own lensing effect as well, and it can be noticed the difference between lensing from the star, and lensing from a planet and star together. This method gives the measure of the mass of the candidate exoplanet and it works even if that planet is not very close to its star, which is an advantage over both the Doppler shift method and the transit method. Images of the source produced by the microlens are distorted and magnified so that the total flux appear amplified during a microlensing event [24]. An example of a light curve, with a typical bell shape magnification due to a planetary single-lens is shown in Fig.2.6. A

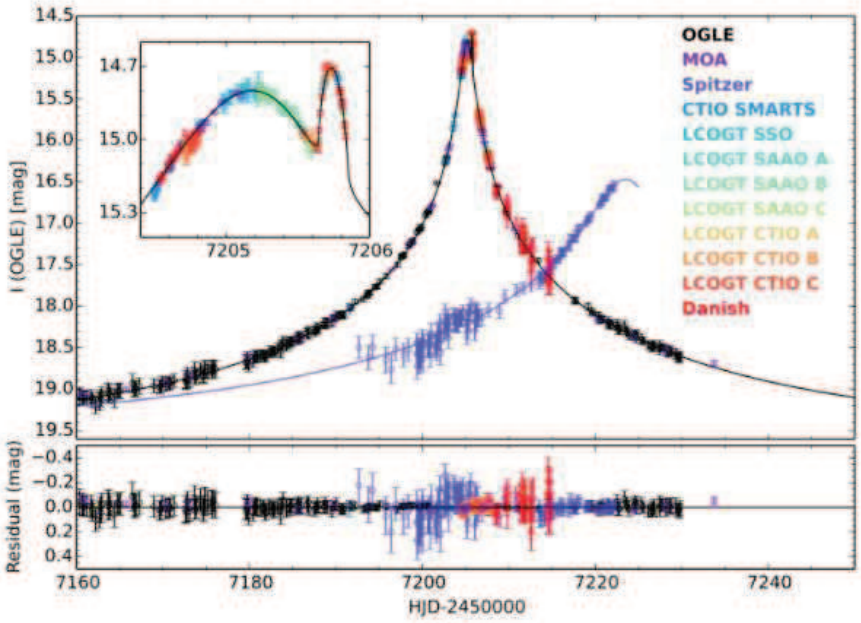

Figure 2.6: Bell shape light curve of OGLE-2015-BLG-0966, built combining and fitting data from 10 ground-based telescopes. The violet curve is a light curve obtained with the Spitzer satellite. Figure taken from [105].

disadvantage for this method is that it needs a large continuous photometric survey, because the probability of the alignment between the source, micro-lens system and observer is intrinsically low. Another issue is that the effect is observed only once, and so it cannot be verified [31].

The first microlensing exoplanet, a 2.6 M_J planet, was detected in event OGLE-2003-BLG-235/MOA-2003-BLG-53Lb (OGLE, Optical Gravitational Lensing Experiment; MOA, Microlensing Observation in Astrophysics). A milestone discovery was OGLE 2005-BLG-390, the very first cool super-Earth with a mass of 5.5 $M_\oplus$ and semi-major axis of 2.6 AU, and discovered in 2005 [14]. In 2006 a multi-planet system, with two planets very similar to Jupiter and Saturn, was discovered.

2.2.4 Direct Imaging

As the name says, this method consists in the direct observation of the light emitted by an exoplanet (in contrast with other methods which are based on indirect effects). The direct imaging challenge is to separate the light from the planet to the light from the star, which is diffracted by the telescope. The basic principle of classical direct imaging instruments, called coronographs, is the following: the light from the observed on axis star is blocked by a focal plane mask (called Lyot stop, who invented this technique in 1939), while in the pupil-plane located after, another mask blocks the star light diffracted off-axis, in order to remove it. Since the exoplanet is is located off-axis, making a small angle with respect to the on axis field, the light from it is not blocked by the Lyot stop and will consequently appear as a classical

image. An example of a typical direct imaged planetary system is shown in Fig.2.7. This method has its main target very different both from the planets which can be

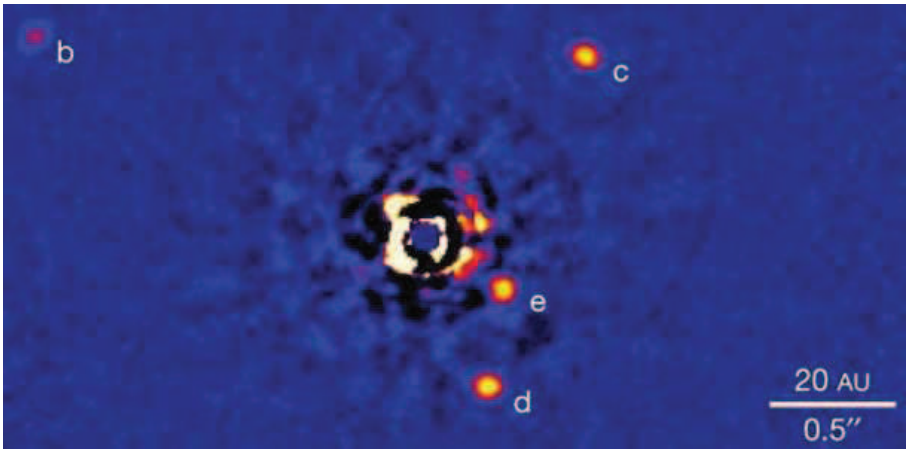

Figure 2.7: Example of direct imaged exoplanetary system. Image of the HR8799 system taken at Keck II telescope with with the Angular Differential Imaging technique (ADI); the residual speckle pattern is visible in the center, while four giant planets are visible in their near-infrared emission. Image taken from [71].

detected by other techniques, and from the planets present in our Solar system; in fact the main targets are young exoplanets at wide orbits, greater then 5 AU with typically orbital periods from tens to hundreds of years, from their hosting star. The reason is that young planets still emit light of their own. Part of this energy is the absorbed and re-radiated starlight, while some is the energy left over from the heat accumulated in the planet's formation, which is radiated away as the planet cools down. Thus bigger and younger exoplanets have a larger amount of energy to radiate away, especially in the near-infrared and infrared regions. This also explains why this technique exploits the infrared bands, where the planet-star contrast is higher (or equivalently the star-planet contrast is less demanding). Directly imaged planets are therefore our best opportunity to study young planets and young planetary systems, which offer a unique glimpse into the process of planet formation. The effective temperature of these young planets can reach up to 2000 K [24] (as a comparison Jupiter temperature today is about 150 K) and a luminosity up to 10^{-5} $L_{\odot}$. This method is also used to detect planets that are not in-line with their stars from our point of view, then non detectable with the two other most used methods (RV and transits). The observables are the planets luminosity and orbit, while the planetary mass, as reported in [42] and references therein, could only be estimated according to the knowledge of stellar age and initial planet formation conditions.

In 2004, the first discovery, with NACO instrument at VLT, was that of a giant planet of 5 times the Jupiter mass in orbit around a brown dwarf [28]. In 2008 the first direct images of an extra-solar planetary system around a star were obtained. This is the multi-planet system HR 8799 with four planets orbiting the intermediate mass host star in counterclockwise direction [71].

Advanced adaptive optics is required to correct for the blurring effect of the Earth's atmosphere on the point spread function (PSF), which otherwise overwhelms

the planet signal. Two recent instruments installed at 8-m class telescope are SPHERE (Spectro-Polarimetric High-contrast Exoplanet Research, see [15]) at VLT and GPI (the Gemini Planet Imager, see [64]) at Gemini-South. Both of them are designed with extreme adaptive optics with thousands of actuators controlling the shape of the deformable mirror, apodized-pupil-masks to reduce the diffraction pattern of the central field over the target location and also integral field capability. Thanks to these facilities the current performance of direct imaging allow to detect exoplanets at about $0.2 - 1$ arc-sec of separation and up to 10^6 times fainter than their host star.

It is also worth mentioning that the speckle patterns mitigation needed for high contrast imaging requires also clever post-processing methods; as said in [89] (and references and therein), improvements in data acquisition modes and analysis software (differential imaging via angular, polarimetric and spectral difference, see again Fig.2.7) have greatly enhanced planet detection capabilities.

Synergy between direct imaging and spectroscopy can be exploited when planets are clearly resolved from their parent star; in particular integral field spectrographs have given spectra of self-luminous planets with sufficiently high SNR, which allowed the detection of absorption features fundamental for the direct measurement and characterization of atmospheric composition [57].

The James Webb Space Telescope (JWST) will launch in 2018 and provide powerful capabilities for direct imaging. As reported in [24] all of its instruments (NIRcam, NIRISS, MIRI, NIRSPEC) will make relevant contributions to finding and characterizing extra-solar planets resolved from their host stars, including some of those already known today.

The next generation of extremely large telescopes (like LBTI, ELT, TMT, GMT) will have a suite of instruments designed with the goal to cross the 5 - 10 AU threshold in angular resolution of accessible targets, pushing the detectable separation down to 3 AU and enabling vast synergies between Doppler velocimetry and astrometry. For example ELT (called before E-ELT) with instruments having imaging and spectroscopic capabilities (HARMONI, MICADO and METIS) will enable to perform efficient imaging of exoplanets at separations below 0.1 arc-sec.

2.2.5 Transit photometry

A "transit" happens when an object passes between our viewpoint and a star. Giving the apparent magnitude of the host star, when one of its planet transits in front of its surface, the net flux received at the Earth is dimmed and its apparent magnitude raises. This effect repeats with the period of the exoplanets orbit. The light gathered from the star during a transit follows a characteristic curve known as a "light curve", shown in a schematic in Fig.2.8.

An example of real light curve data is shown in Fig.2.9. The light curve data analysis and fitting allow to infer the radius, the orbit inclination and the orbit semi-major axis of the detected planet. The radius is evaluated from the percentage of the blocked light, called transit depth, which is proportional to the ratio of the planet-to-star radius, assuming a model for the dimension of the host star; this assumption holds true when dealing with main sequence stars, where equilibrium model and star equations are well known. According to the hypothesis of circular or elliptical orbit it also possible to assess the ratio between the radius of the star and the semi-major

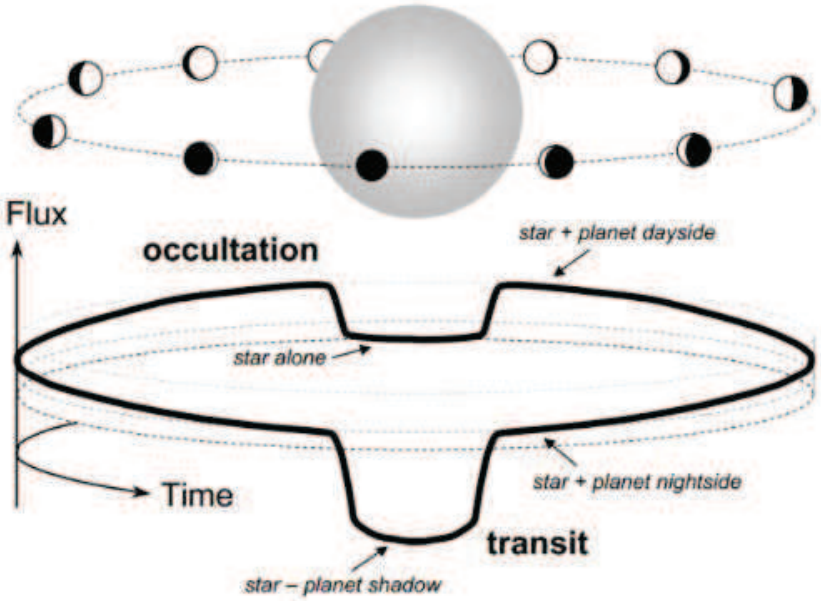

Figure 2.8: Schematic example of a light curve showing the flux variation due to the primary eclipse (transit), the secondary eclipse (occultation) and the different orbital phases of the exoplanet.

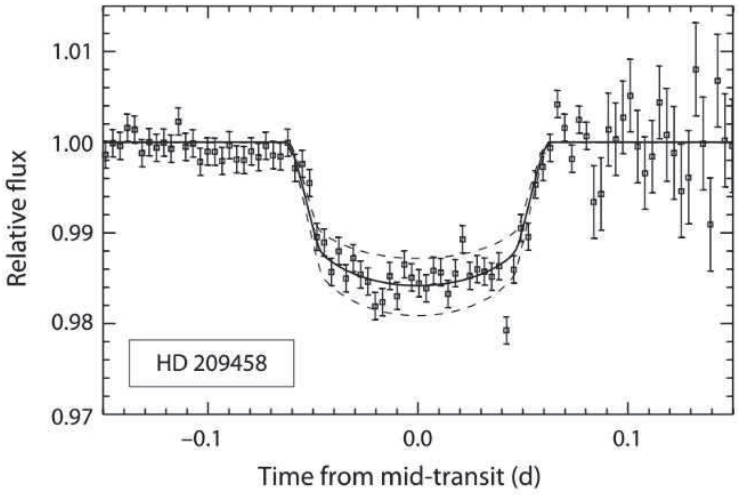

Figure 2.9: Light curve of the first detected transiting exoplanet, HD 209458, showing the measured flux versus time. The lower and upper dashed lines are the transit curves that would occur for a planet 10% larger and smaller in radius, respectively. Figure taken from [26].

axis, and the inclination of the orbit.

This method is more advantageous for large planets orbiting small quiet star since the transit depth is in this case higher and then the photometric precision requirement not so extreme. In addition it is effective in the detection of planets with short period because the transit probability is higher, and also because it is easier to

monitor photometrically shorter spans [31].

The probability that a given exoplanet transits its host star is primarily a function of the inclination of the planetary orbit and of the stellar radius. As order of magnitude a typical hot Jupiter of radius $\sim R_J$ and orbiting around a solar-type star with a period $\sim 3d$ has a transit probability $\sim 10\%$, a transit duration of $\sim 3hr$ and a photometric transit depth of $\sim 1\%$; while an Earth-like planet at 1 AU around a solar-type star has a transit probability $\sim 0.5\%$, transit depth of ~ 0.01 %, and a transit duration of $\sim 15hr$ (examples taken from [42] and [24]). These values make the detection very challenging.

The other issue which affects the detection performance of this method is the high rate of false positives, mainly due to grazing eclipsing binaries, the existence of triple systems, the occurrence of transit by a low mass star or a brown dwarf, which have similar size of giant planets, and the stellar activity according to the type of the hosting star itself.

This method can be effectively used in synergy with the Radial Velocity technique (see the following subsection 2.2.6) to have a complete characterization of the planet orbital parameters and also to infer a first guess consideration on the exoplanet density and then composition. The first exoplanet transit was detected in HD 209458, which was already known to harbor a planet thanks to Doppler spectroscopy, using the STARE project Schmidt camera telescope (Observatorio del Teide, Spain). The duration of the transit was about 2.5 hours and had a depth of about 1.5% [26]. This exoplanet was also the first transit detected from space, using the STIS instrument on board of the Hubble Space Telescope (HST).

In the past decade the number of transit candidates and detections has dramatically increased thanks both to ground-based long time surveys and especially to the space-based transit missions. For what concerns ground-based search programs, HATnet ([6], HAT-South and SuperWASP ([93]) have given important contribution in the stellar brightness regime $10 < V < 12$ with a photometric precision of order of milli-magnitude (mmag), leading to the detection of dozens of transiting planets. While the Wide Angle Search for Planets (WASP-SuperWASP) project is based on two wide field cameras with small aperture telescopes for the survey of a large fraction of sky, the Hungarian Automated Telescope Network (HATNet) exploits a network of small telescope located at different longitude to maximize the sky coverage and observing time. Another example of ground-based network for large sky coverage observation is TrES, the Trans-atlantic Exoplanet Survey network which employs three small aperture telescopes, of 0.1 m, and wide field (6°) cameras. As explained in [89] a complementary approach for transit detection is to observe crowded stellar fields; this strategy has been used for example by the 1.3 m telescope of the Optical Gravitational Lensing Experiment (OGLE) in the third phase of the project to perform photometric observations of three fields towards the Galactic center.

Space-based observations have speed up the transiting planets candidate discovery rate. The CoRoT (Convection Rotation and planetary Transit) satellite has a telescope with an effective diameter of 0.27 m and according to its polar orbit has two preferred viewing directions (towards to Galactic center and anti-center); the measured photometric precision is about 0.7 mmag at R−15 mag for 512 s of integration time (data taken from [90]). The photometric precision achieved with the Kepler satellite is about 30 ppm at V−12 mag; as reported in [24] the Kepler mission did

provide hundreds of planet detections with mass determinations, as well as hundreds of multiple transiting planets orbiting a single host star, many of which are coplanar and rather crowded systems. The impact of Kepler and K2 missions discoveries can be understood with the charts in Fig.2.10.

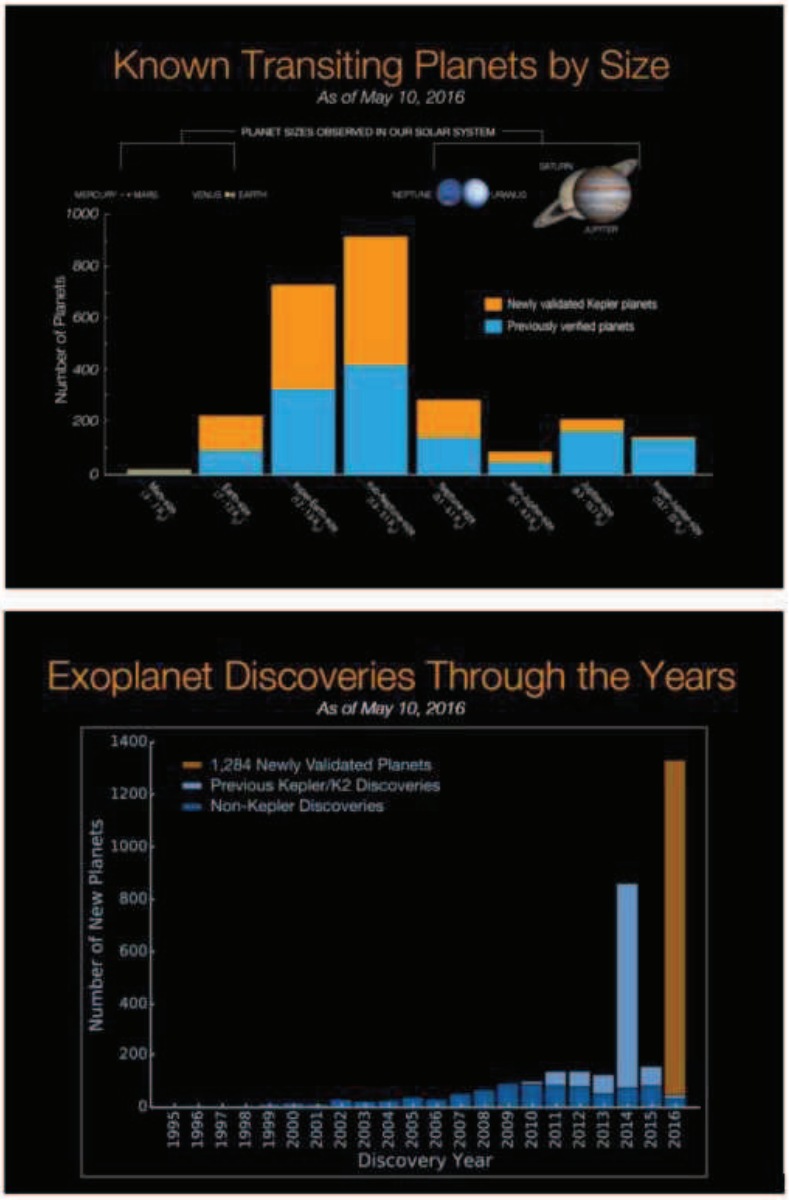

Figure 2.10: Kepler and K2 missions statistics: *Top*: Histogram of number of planets with respect to planet size as of May 2016; the orange part of the bars shows the contribution of Kepler missions on the amount of discoveries, while the blue part refers to previously verified planets. *Bottom*: Histogram of number of planets discovered by year as of May 2016; the contribution of Kepler missions with respect to non-Kepler discoveries is highlighted.

2.2.6 Radial Velocity / Doppler Spectroscopy

The radial velocity (RV) method derives the host star radial velocity, which is its velocity projected in the direction of the line of sight, by measuring the Doppler shift of the absorption lines in the star spectrum due to its motion around the center of mass of the star-planet system. Specifically, the wavelength of an identified spectral line is determined and compared with the theoretical value it would have when transferred into the solar system's rest frame; this wavelength shift measurement $\Delta\lambda$ can then be translated into the radial velocity v_r of the star according the Doppler equation $\Delta\lambda/\lambda - v_r/c$. In order to increase the precision, the average over several thousands of spectral lines is computed. When hosting one or more planets the star orbits around the system center of mass (as depicted in Fig.2.11) and this back-and-forth movement is traduced in periodic variations of the Doppler shift or the radial velocity; what is in practice evaluated is the semi-amplitude, $K_\star$, of this radial velocity periodic variation:

$$K_\star[cm/s] = \frac{8.95}{\sqrt{(1-e^2)}} \frac{msin(i))}{M_\oplus} (\frac{M_\star + m}{M_\odot})^{-2/3} (\frac{P}{yr})^{-1/3} \tag{2.1}$$

Where m is the planet mass, $M_\star$ is the star mass, $M_\odot$ and $M_\oplus$ are the Sun and Earth masses respectively, P is the orbital period expressed in years, e is the orbit eccentricity and i is the orbit inclination. The detailed modeling of the radial veloc-

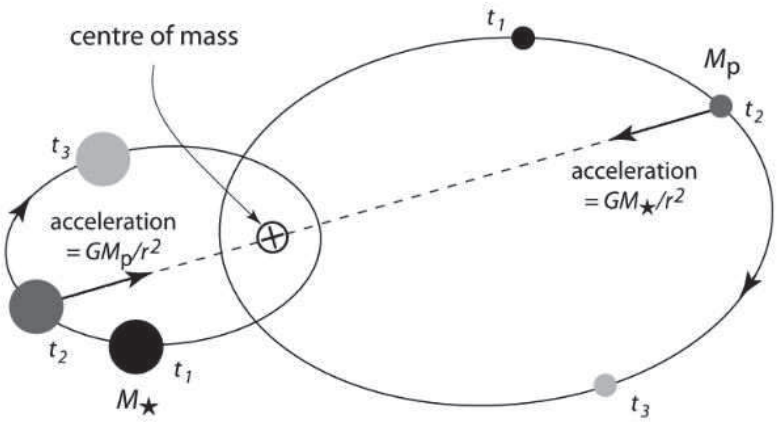

Figure 2.11: Schematic of two orbiting bodies moving about their common barycenter at times t1, t2 and t3. Figure taken from [90]

ity curve allows the evaluation of P, as well as the eccentricity, the longitude of the periastron and of $K_\star$. An example of a radial velocity curve is shown in Fig.2.12. The observed parameters are used in the expression of $K_\star$ to calculate the so called "planet minimum mass" $m \sin i$, if the mass of the star is known; then the true mass of the planet and the orbital inclination remain degenerated. In addition, the other orbital element which cannot be derived through radial velocity method is the longitude of the ascending node. The semi-amplitude formula shows that more massive planets are easier to detect as well as shorter period (i.e. close-in) planets, since in these conditions $K_\star$ is larger; planets are also easier to find around low-mass stars

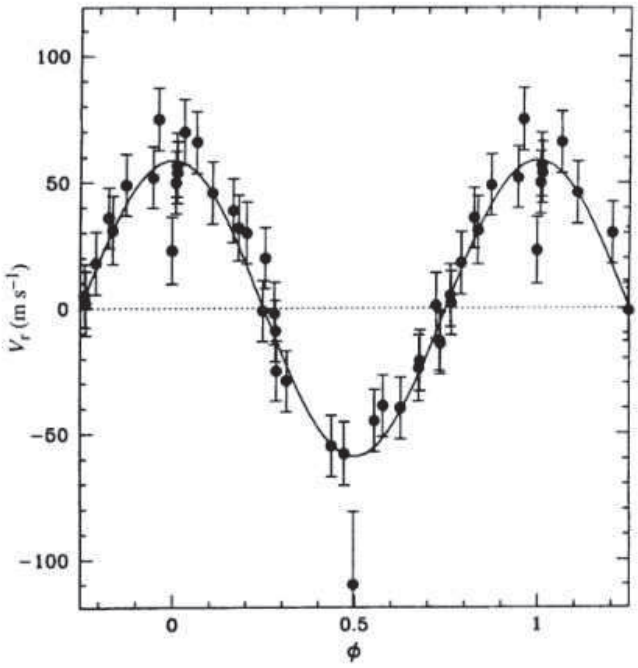

Figure 2.12: Radial velocity curve folded in phase of the 51 Peg b hot Jupiter. The data fitting model curve (solid line) accounts for a planet of half a Jupiter mass on a 4.2 days orbit. Figure taken from [68]

than heavier stars. Furthermore, radial velocity observations must cover at least one complete orbit in order to robustly measure the orbital period, although more orbits are usually needed to obtain good constraints on all parameters ([24]), and to rule out the presence of additional planets in the system. As an order of magnitude the radial velocity semi-amplitude experienced by the Sun because of the gravitational pulling of Jupiter and Earth are $K_{\star,J}$=12.5 m/s and $K_{\star,E}$=0.09 m/s; these values explain why, with the typical RV precision achieved by first spectrographs, the firsts exoplanet discovered, like 51 Peg b (whose RV curve is shown in Fig.2.12), were giant planets in close-in orbits.

The performance of spectrographs RV precision improved from around $10-15m/s$ of ELODIE (51 Peg b discovery) in 1995 to better than 1 m/s in 2003 with HARPS spectrograph, installed at the 3.6-m ESO telescope (La Silla, Chile), which led to the discovery of μ Ara c in 2004 [98], one of the first detected Neptune-Mass objects. The HARPS high precision coupled with many observation data points distributed in several years has been fundamental to detect the smallest velocity signals (see the example of HD85512 [87], and alpha Cen B, [35], described in [42]). The present, near-future and far future spectrographs are designed to achieve radial velocity precision at the level of $<$ 10 cm/s in order to try to discover Earth-like planets orbiting Sun-like star in the habitable zone (HZ).

These high precision RV detections and measurements have been possible also thanks to the use of the Cross-Correlation Function (CCF) technique in the spectral

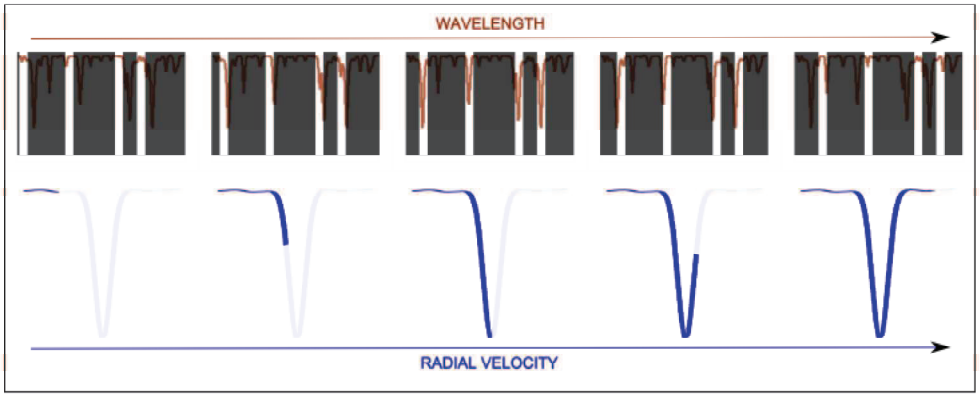

Figure 2.13: Example of construction of the CCF, taken from [31]. As the binary mask is shifted over the spectrum, the degree of similarity between the mask and the spectrum changes. It can be seen that the minimum of the CCF (corresponding to the largest degree of similarity) corresponds to the radial velocity where the mask holes are perfectly aligned with the spectral lines they correspond to.

data analysis. This technique, as described in [9], correlates the position and width of thousands absorption lines of the high resolution stellar spectrum with a box-shaped template. Specifically the mask is shifted as function of the radial velocity, as shown in Fig.2.13, in order to find the minimum of CCF:

$$CCF(v) = \sum_i S(\lambda(i)) \cdot M[\lambda(i)(1 + v/c)] \tag{2.2}$$

Where S is the spectrum intensity at wavelength $\lambda(i)$ and $M[\lambda(i)(1+v/c)]$ is the mask shifted by a Doppler effect with radial velocity of value v. In order to optimized the SNR and to reduce the perturbing effect of telluric lines, a weighted cross-correlation function CCF $w(v)$, which accounts for the relative absorption depth of each spectral line contained in the mask, was presented by Pepe and collaborators [85] and it is defined as:

$$CCF^w(v) = \sum_i S(\lambda(i)) \cdot M[\lambda(i)(1 + v/c)] \cdot w_i \tag{2.3}$$

As described in [89] the main potential error sources which affect the RV measurement and performance are: photon noise, instrumental drifts and spectrograph illumination effects which affect the stability of measurement by introducing perturbations in the recorded spectrum, spectral contamination and stellar 'noises', commonly referred to as stellar jitter. Stellar jitter, which comprises various stellar phenomena like activity in stellar atmospheres (spots, plages etc.), surface granulation and stellar oscillations, is one of the strongest limitations for Doppler velocimetry at sub-m/s precision and it should be robustly identified and modeled or de-correlated to achieve even higher accuracy ([42]).

While since the early days many discoveries and performance improvements have been made especially in the optical band, the near-infrared (NIR) wavelength region is becoming increasingly interesting because of the following aspects. M-dwarfs, which are estimated to harbor a high fraction of Earth-size planets in habitable zones, are

much brighter in the infrared than in the visible; in addition since these stars have low mass, potential habitable planets with short orbital periods are more easily detected by radial-velocity. The second advantage of the NIR compared to the visible is that the influence of stellar spots is strongly reduced ([89]).

2.3 Exoplanet characterization

Exoplanet search campaigns have shown a great variety of possible planets properties in terms of mass, size, orbital parameters (such as eccentricity and inclination), mean densities, composition and atmospheric structure. Since the beginning of exoplanet revolution, different studies have been conducted with goal of properties characterization, statistical interpretation and to link them with the possible argued planetary formation mechanisms. Today, the struggle of scientific community to put all the pieces of this fascinating puzzle is going on, and although much is still to be understood the future instrumentation and data analysis technique promise to allow big steps forward. In the following subsections a brief summary of the known properties of exoplanets is given.

2.3.1 Main Exoplanets constituents

The three principal types of compounds available in accretion disks, where planets form, are typically referred to as: gas, rock (generic term for non-volatile condensates), and ice (generic term for volatile condensates). Their proportions determine the planet bulk composition and mass, while the pressure-temperature conditions affect their phase and physical state, having impact also on the resulting planet radius.

- *Gas*: H and He gases comprise $\simeq 98.5\%$ of the mass in the solar nebula, leaving typically $\simeq 1.5\%$ of the total mass condensing in rocks and ices. These gases are also the quasi-total components of the envelope of gas giant planets.
- *Rocks*: all rocky compounds are relatively refractory and require high temperatures for condensation; being the first materials to condense they are expected to be present in large amount among other solids in accreting protoplanetary disks. Taking into consideration Solar system abundances as reference, the amount of rocky compound in protoplanetary accretion disks should be around 0.5% of the disk mass. Some of the most abundant minerals in planetary science, like olivine, oxides (magnetite), silicates (talk), sulphides (FeS) and metal alloy like FeNi are made of Si, Mg, Ca, Al, Fe and Ni; the percentage of these elements and their condensates depends also on the equilibrium or non-equilibrium conditions.
- *Ice*: in the exoplanetary context ice is a term which refers to the different forms and solid phases of water that can exists at sufficient high pressures. In addition in this context, ice encompasses various substances containing C, N, and O. Water ice is the most important, since O is the third most abundant element in the Solar system and also because it condenses at the highest temperature. Other possibly abundant ices are CH_4, CO, CO2, N2, NH3.

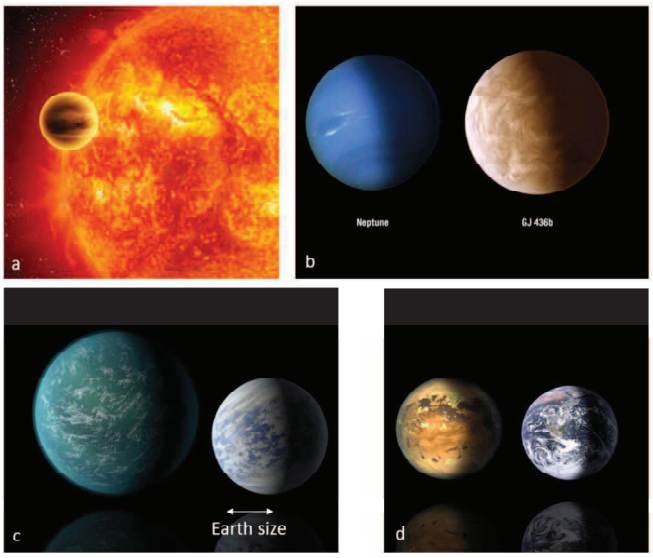

Figure 2.14: Artistic impressions of some types of exoplanets. In a) an hot Jupiter is depicted close to a Sun-like star; in b) an hot Neptune is compared in size with our Neptune; in c) two examples of Super-Earth with the Earth diameter shown as a reference size; in d) an Exo-Earth is compared to Earth.

The radius in the protoplanetary disk beyond which water ice can be present is referred to as the *snow line*, and it is believed to play an important role in the architecture of planetary systems. Within the Solar system, H2O-rich (C-class) asteroids are found predominantly in the outer asteroid belt ([75]), suggesting that the snow line in the solar nebula lay at around 2.7 AU. Different studies have tried to assess the snow line radius variation according to the properties of the star, in term of mass and age, and type of protoplanetary disk.

2.3.2 Main Exoplanets types

The main types in which the so far discovered exoplanets have been categorized are briefly described in the following. An artistic impression of some of them is shown ini Fig.2.14. It is important to underline that the exoplanet types discovered up to now are strictly depended on the detection methods described before, so that future technology developments and new detection methods could change the global picture and statistics about exoplanet types.

- *Hot Jupiters*: these are hot gas giant planets. They have masses within the range a half to 13 times that of Jupiter and their distances from the host star are typically a small fraction of AU; the proximity to the star results in very hot temperatures, which can be up to 2000 K or even more, of the top layers of their atmospheres. They are mainly made up from the lightest gases, hydrogen and helium, which even at their high temperatures cannot leave the atmosphere because the high gravitational fields of these massive planets. A possible extension to this class is the one of so called *Super-Jupiters* for which

core-accretion models predict planets having masses up to around 20 times[1] Jupiter mass, e.g. COROT-Exo-3b discovered in 2008.

- *Cold Jupiters*: about one third of the massive exoplanets discovered are at least twice as far from their stars as the Earth is from the Sun. Hence by analogy with hot Jupiters, this class of exoplanets is called the cold Jupiters or sometimes twin Jupiters. The first cold Jupiter, 55 Cnc d, detected in 2002 [69], has a 14-year orbital period around 55 Cnc A and is around 5.8 AU out from the star (as a comparison Jupiter has 11.9 years orbit at 5.2 AU).

- *Hot Neptunes*: this is a group of exoplanets that are similar to hot Jupiters, but with lower masses, typically about the Neptune mass.

- *Super-Earths*: they are defined exclusively by their mass, which is in the range from 1.5 to 10 Earth masses, independently from specific conditions of temperature, composition, orbital properties or habitability. Some of them have been found near the habitable zone (HZ, the region where liquid water can be sustained on the planetary surface) of their host star. Within this definition the first discovered Super-Earths were the two planets detected around the pulsar PSR B1257+12 with about 3 and 4 times the Earth mess (see subsection 2.2.1. The first Super-Earths discovered in proximity of habitable zone of their host star were Gliese 581 c and d in 2007 (see [108]).

- *Exo-Earths*: also called Twin Earths these have masses comprises between 0.5 and 1.5 Earth mass. Some of these planets have been found near the habitable zone (HZ, the region where liquid water can be sustained on the planetary surface) of their host star, while others are further out. In February 2017 a milestone was achieved with the discovery of a planetary system composed by at least seven planets with sizes and masses similar to the Earth, which orbit around the Jupiter-like size star TRAPPIST-1. As reported by the authors, the transiting configuration of this planetary system around this kind of star makes possible in-depth studies of the planets atmospheric properties with current and future astronomical facilities ([48]).

- *Free-Floating Planets*: Some exoplanets have been found that are not associated with host stars but which float as independent entities within the galaxy. Free-Floating Planet is a planetary- mass object that orbits the galaxy directly. They have either been ejected from the planetary system in which they formed or have never been gravitationally bound to any star or brown dwarf. A study conducted with the OGLE survey observations from 2010 to 2015 shows the existence of a large population of Earth-mass free-floating planets, while free-floating Jupiter-mass planets are rare ([77]).

[1]It must be recall that, according to the definition adopted by the International Astronomical Union's Working Group on Extrasolar Planets, objects more massive than 13 times Jupiter's mass are classified as brown dwarfs, since they are capable of fusing deuterium.

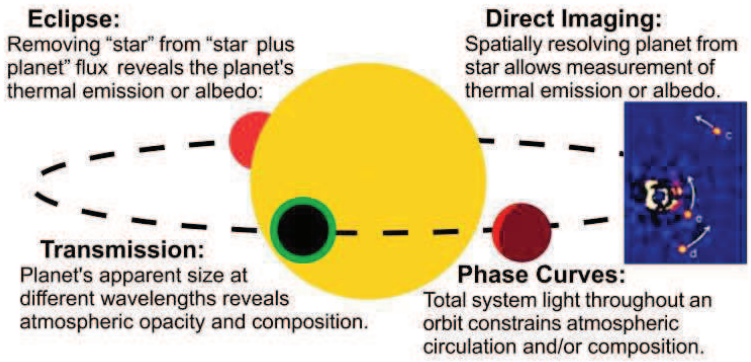

Figure 2.15: Schematic of observation methods used to characterize the atmosphere of Exoplanets. The planet is shown in the different orbital phases related to the different methods. Figure taken from [30].

2.3.3 Exoplanets atmospheres

We are now entering a new era in exoplanetary science; going beyond planet detections, the field is now moving towards detailed characterization of exoplanetary atmospheres. In fact, as written in [30] and therein references, this provides the best hope for distinguishing the makeup of its different layers, and the only hope for understanding the interplay between initial composition, chemistry, dynamics and circulation and disequilibrium processes.

Observations of exoplanetary atmospheres present much more stringent requirements on the instrumental capabilities than planet detection; in particular a combination of significantly higher sensitivity and higher spectral resolution are required for reliable atmospheric detections and characterization ([66]).

The characterization of exoplanet atmospheres through observations has been to date restricted mainly to inflated hot Jupiters, whose large scale-heights and high temperatures make them ideal target for atmospheric observations. In addition atmospheric studies has been also done for some hot Neptunes, a few super-Earths and for a few young and self-luminous gas giant planets.

The main observational techniques for exoplanets atmospheres science, summarized in Fig.2.15, are:

- *Direct Imaging*: Exoplanets detected to date via direct imaging are all young gas giants at large orbital separations. The advantage of direct imaging, as explained in [66], is that the detection of a planet simultaneously results in observation of its atmospheric thermal emission spectrum and albedo, i.e. atmospheric characterization can be pursued simultaneously with detection. The disadvantage of direct imaged exo-atmospheres is that, because of to the their wide orbits, data are available at only one point of the orbital phase which means thermal phase curves (see after) are not observable, thus precluding constraints on atmospheric properties with longitude. As explained before the synergy of this method with spectroscopic analysis can be fundamental to infer the chemistry and abundances in self-luminous planets through the detection

of absorption features.

- *Transit and Eclipse photometry*: exploiting the same principle for transit detection, when the planet has an atmosphere its opacity varies with wavelength and so the radius at which the planet's atmosphere becomes optically thick changes with wavelength ([99]). The measures of the flux decrement at multiple wavelengths gives the planet atmosphere radius as function of wavelength (the so called the "transmission spectrum"). The analysis of the transit signal in specific photometric bands reveals features directly related to the atmosphere chemical composition. The reliable measure of these features requires photometric fractional precision of ppm; for example in the case of an Earth-Sun twin system 1ppm, while a few thousand ppm for a typical hot Jupiter (values taken from [30]). "Secondary Eclipses" allow to reveal and characterize, in the planet day-side, the thermal emission, due to internal atmospheric heating processes or reradiated star-light, in the infra-red wavelength bands and albedo mainly in the optical-UV bands.

- *Phase Curves*: Phase curves track the modulation of planetary thermal emission and/or reflected starlight throughout a planet's orbit; it is therefore required the observation of the system for a substantial fraction of an orbit [55]. This aspect makes these observations to be complementary to secondary eclipses because phase curves provide information about atmospheric conditions across the planet's surface by measuring longitudinal brightness and temperature maps. These maps give relevant clues on the planetary atmospheric dynamics and energetics. Phase curves are also useful in constraining albedo at shorter wavelengths and inferring cloud covering across the whole planet atmosphere [33].

- *Transit, Eclipse and High Resolution Spectroscopy*: this has been the most powerful tool for atmospheres studies since in an exoplanet spectrum is encoded information about the chemical composition, thermal structure and physical processes in its atmosphere (like circulation). Transit spectroscopy is related to the transmission in day-night terminator region of the planet surface, while eclipse spectroscopy to the day-side emission; while transmission spectra have been obtained from UV to mid-infrared wavelengths, thermal emission spectra are mainly obtained in the near to mid infrared (since the planet emission peaks in these bands). The first exoplanet atmospheric transmission spectrum, in 2001, was the one of the hot Jupiter HD 209458 b, observed from space with the Hubble Space Telescope; the spectra were obtained using the medium resolution Space Telescope Imaging Spectrograph (STIS) instrument in the wavelength region $581.3 \leq \lambda \leq 638.2$ nm, where an extra absorption of $\simeq 200$ ppm of the sodium doublet (at $\simeq 589$ nm) was measured [27], see in Fig.2.16 a portion of the spectrum centered on the doublet lines. The HST has been used to study and infer constraints in the atmospheric composition of other hot Jupiters and sub-Jovian planets.

  Fundamental improvements in atmospheric characterization of exoplanets have been possible thanks to the use of ground-based high-resolution spectrographs; in fact large ground-based telescope coupled with high-resolution spectrographs

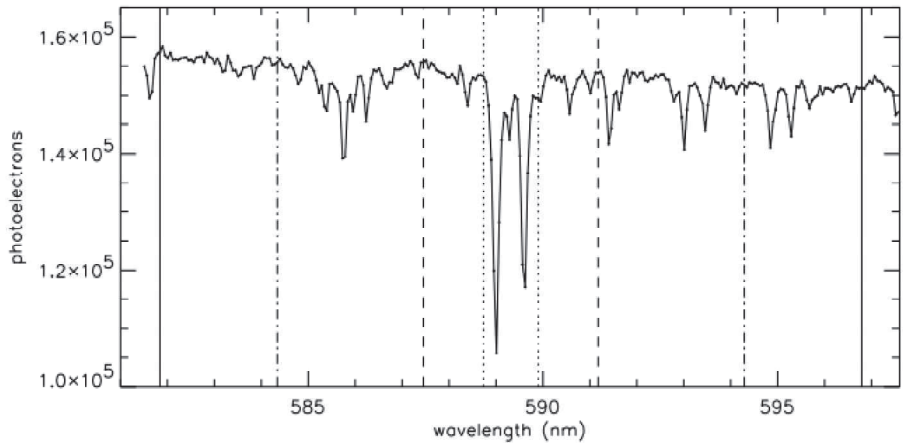

Figure 2.16: Portion of a STIS spectrum of HD 209458, centered on the Na D lines, taken from [27]. As described in the paper, the vertical axis is the number of detected photoelectrons per wavelength pixel after integrating over 17 pixels in cross-dispersion. The vertical lines indicate the band passes over which the spectrum was integrated to produce the photometric time series.

allow to obtain high SNR and well resolved features in the exoplanetary spectra. High dispersion spectroscopic observations can be successfully used for the study of systems with bright hosting star and exploiting large telescopes since the planetary signal diminishes with the increased resolution. The first ground-based detection of an exoplanet atmospheric signature, shown in fig.2.17, was the Na I doublet detected in HD 189733 b with the High Resolution Spectrograph (HRS; $R \simeq 60000$) mounted on the 9 m Hobby-Eberly Telescope [96] and was confirmed in HD 209458 b using the High Dispersion Spectrograph (HDS; $R \simeq 45000$) on the 8 m Subaru telescope [102]. As also reported in [30] high dispersion spectroscopy regularly detects thermal emission from hot Jupiters at the $\simeq 10^{-4}$ level relative to the star (eclipses) and measures molecular abundances as small as $\simeq 10^{-4}$ or $\simeq 10^{-5}$ (transmission). In the infra-red region the high resolving power (R=100000), of the Cryogenic High-Resolution Infrared Echelle Spectrograph (CRIRES) on the Very Large Telescope (VLT) made possible the tracking of the wavelength shift of individual spectral features composing molecular bands of H2O, CO, or CO2 present in the planetary atmosphere. This technique have been also exploited to constraint on the day-night wind velocity in the planetary atmosphere [103]. In addition, near-infrared high resolution spectroscopic observation of direct imaged exoplanets led to the first determination of the spin period of an exoplanet, the young gas giant β Pic b, exploiting the blue-shifted measurement of carbon monoxide in the planet's thermal spectrum [104].

In the following, a brief summary of the observational inferences of atmospheres chemical compositions and physical processes is given, with particular attention to the large amount of properties discovered and/or constrained through transmission spectroscopy and broadband photometry.

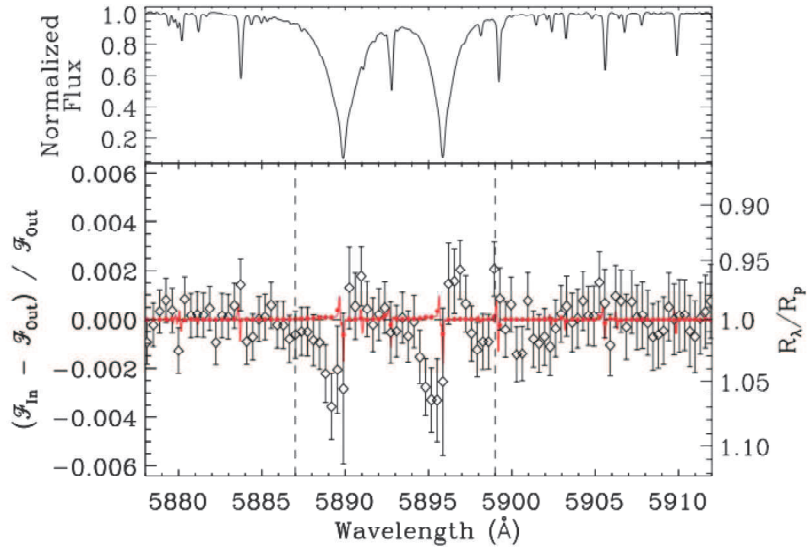

Figure 2.17: *Top left*: Spectrum of HD 189733 near the Na i doublet, from [96]. *Bottom left*: The difference of the relative flux of the in-transit template (F_{in}) and the out-of-transit template (F_{out}). Excess absorption in the in-transit template is clearly detected in both Na i lines. Also shown is the contribution of differential limb darkening (red line and filled circles), which has been removed from the data, but the effect is minimal. The vertical dashed lines indicate the narrow band-pass used to calculate the relative transmission spectrum absorption.

- *Atomic species and Exospheres*: atomic species, like alkali metals (Sodium and Potassium), and ions are expected to exist in highly irradiated planets such as hot Jupiters, where, as described before the dayside temperature can be up to roughly 2000 K. As reported in [30] high-altitude exosphere temperatures can reach up to $\simeq$ 10000 K, hot enough to split molecules and partially ionize the constituent atoms. In the first Na detection (the hot Jupiter HD 209458 b cited before) the spectrum revealed lower Na absorption than predicted by equilibrium models; this can be interpreted as either lower atomic abundances than assumed or non-equilibrium processes such as rainout of condensed species and photoionization of Na/K ([11]). As said before the Na resonance doublet at 589 nm was also detected from ground in the optical transmission spectrum of the hot Jupiter HD 189733 b ([96] and [111]). Na I has been inferred in visible transmission spectra of a few other hot Jupiters (like HAT-P-1 b ([79], and WASP-12 b [23]).

  Similar to Na, several studies have also detected the K resonance double at 770 nm using transmission spectra of hot Jupiters from both space and ground-based instruments, e.g.HAT-P-1b ([110] and WASP-31b [101]).

  Several atomic species and mass losses have also been detected in the exospheres of hot Jupiters using UV transmission spectroscopy; an extended envelope of escaping H in the hot Jupiter HD 209458 b has been observed in the $Ly-\alpha$ of atomic hydrogen [109]. For what concern low mass planet, recently a detection

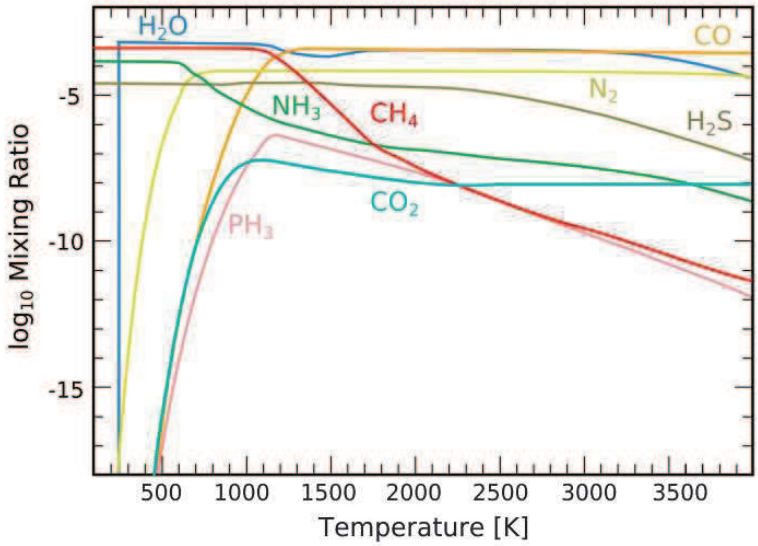

Figure 2.18: Abundances in molecular equilibrium varying with temperature, in Solar-metallicity atmospheres at total pressure of 1 bar. Figure taken from [30].

of escaping atomic hydrogen in the exosphere of the hot Neptune GJ 436 b, seen as about 50% transit depth in $Ly-\alpha$ has been reported by [38]. As explained in [30], the mass loss is qualitatively understood to result from hydrodynamic Roche lobe overflow of the planet exosphere, powered by the extremely high-energy X-ray and FUV flux of the host star .

- *Molecular species*: the detection and relative abundance estimation of molecules is fundamental in the characterization of the complex structure of chemical composition, photochemical processes and atmospheric circulation; nevertheless the complexity of this "puzzle" is due to the fact that some of these processes are strictly related to the different possible exoplanets formation and evolution histories. Molecular detection has been possible mostly in hot close-in Jupiters, since these are easily observed with broadband transit photometry and transit spectroscopy. The theoretical expected abundances of various molecules in equilibrium for most of hot giant exoplanets studied to date is shown in Fig.2.18.

  H_2 is of course the dominant constituent of most envelopes of inflated hot gas giants; it would be above the top of the plot in fig2.18. This feature has been also seen in the $\simeq$ 800 K Neptune-sized GJ 3470 b ([94]).

  H_2O is the most abundant for a wide range of high atmospheric temperatures of hot Jupiters. Infrared water features have been detected in these kind of planets both from ground, using CRIRES at VLT ([21] and [17]), and from space, using the HST Wide Field Camera 3 (WFC3) spectrograph. For example the first WFC3 detection of H_2O was made with the transit spectroscopy of the hot Jupiter HD 209458b ([33]); as reported in [66] the observations led to a

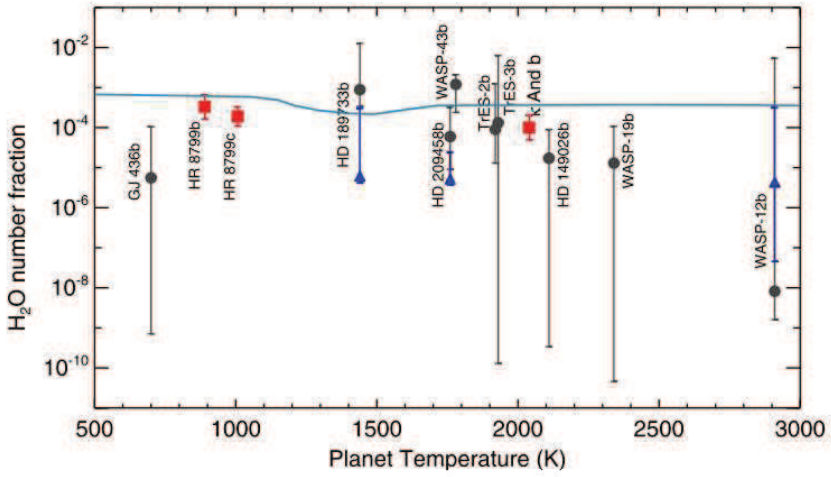

Figure 2.19: H_2O abundances reported in well characterized planet. Red squares indicate directly imaged planets; while the gray circles and blue triangles indicate transiting planet emission and transmission spectra, respectively. No clear and specific trends with temperature can be derived from the present data. As explained in [107], from which the figure is taken, these abundances are roughly consistent with equilibrium condition in a Solar-metallicity atmosphere.

clear $10-\sigma$ detection of H_2O in a single transit thanks to the high brightness of the host star (V $-$ 7.6). For what concern thermal emission spectroscopy using HST WFC3, robust detections of H_2O molecular features in have been reported for the dayside atmospheres of WASP-43 b ([106]), where in addition the first detection of TiO in the dayside atmosphere of the extremely irradiated hot Jupiter is reported. Water has been detected also in a growing number of direct imaged planets thanks to observation of the thermal emission processed by medium and high resolution spectroscopy; for example HR8799 b with OSIRIS in K band ([13]) and in Y, J, and K band with "Project 1640" ([107]). In Fig.2.19 the H_2O derived abundances for all well characterized planets are plotted; they are roughly consistent with equilibrium conditions and a Solar-metallicity atmosphere.

CO is abundant in giant hot exoplanet atmospheres with several proved ground based spectroscopic detections, even if as reported in (see [30] and references therein) in most cases the detection alone is not sufficient to tightly constrain CO atmospheric abundance. CO has also been observed in several directly imaged planets at medium or low dispersion, including HR 8799 b and c ([57] and [13]] and β Pic b ([104]). These studies generally reveal CO abundances consistent with solar metallicity and equilibrium chemistry. While as explained in [30] strong chemical disequilibrium in a high metallicity atmosphere has been suggested to explain the presence of CO and absence of CH4 in the dayside of the relatively low temperature ($\simeq$ 700 K) hot Neptune GJ 436 b.

CH_4 is theoretically more abundant than CO for temperatures lower then $\simeq$ 1000 K, but the measured abundances to date are lower than expected. For example in one of the most convincing spectroscopic detection, the directly im-

aged planet HR 8799b, CH_4 abundance is consistent with Solar-like metallicity and disequilibrium conditions [30]. As in the case of the transiting 700 K hot Neptune GJ 436 b vigorous internal eddy diffusion has been suggested as presumably responsible for quenching the upper-atmosphere abundances of CH_4 (see for example [12], [76] and [66]). Perhaps the first robust detection of CH_4 in any exoplanet atmosphere has been performed using ground-based photometric measurements of the 160 Myr-old GJ 504 b in the 1.6 μm absorption band ([59]); the low effective temperature of this planet (< 600 K) is coherent with what shown in Fig.2.18, where can be seen that at this level strong absorption of CH_4 should be present.

- *Other molecules*: as can be noted in Fig.2.18, molecules like NH_3 and H_2S become increasingly abundant below temperatures of 500 K. As reported in [30] and cited references therein, NH_3 has been detected in sub-equilibrium abundances in cool brown dwarfs and isolated free-floating planetary-mass objects, but has not yet been seen in any exoplanetary atmosphere.

- *Clouds and Hazes*: they form when gaseous species condense out of the atmosphere, producing liquid droplets or solid "dust" particles. As explained in [99] they may contribute significantly to the optical depth in transmission spectra; in fact the amplitude of a spectral feature is directly proportional to the height of the atmospheric annulus through which the star light traverses and the presence of an opaque cloud deck at a given height in the atmosphere means that only the layers above the cloud deck contribute to the transmission spectrum. Thus for a cloud deck located high enough in the atmosphere the amplitude of a spectral feature can be significantly diminished thereby confounding estimates of the corresponding molecular abundances. The featureless transmission spectra in low-mass and low-temperature (T below $\simeq 800$ K) planets have been attributed to the presence of thick high altitude clouds with cloud-top pressures below a mbar. On the other hand, even for hot Jupiters which show unambiguous H_2O features the amplitude of the spectral features are significantly diminished, corresponding to only $\simeq$ 1-2 scale heights ([33]), compared to expectations of 5-8 scale heights ([65]). In hot Jupiters, scattering due to haze particles have also been inferred from visible transmission spectra, which show an inverse power-law dependence on wavelength with parameters different from that due to pure gaseous Rayleigh scattering. Different conclusions have been pointed out concerning the hot Jupiter HD 189733 b; observations with HST revealed a power law slope in the UV and optical indicating, according to some authors ([62] and [100]), the presence of hazes, while, according to others ([73] and [82]), the slope has been instead attributed to a haze-free atmosphere and transit contamination from a non-uniform stellar surface. An additional open point is that the cloud species and size distribution remain unknown.

- *Albedos*: its measurement in different wavelength bands is important to have a relevant indication of the presence of clouds and hazes in exo-atmospheres as well as to infer the chemical composition of these clouds and hazes system. As reported in [30], early broadband photometry of hot Jupiters indicated that they typically have low geometric albedos ($Ag < 0.1$) at optical wavelengths.

On the contrary as described in [66] evidence for high geometric albedos as well as for clouds/hazes in dayside spectra in these planets has been provided in recent observations. For example geometric albedo of 0.35 ± 0.02 for the hot Jupiter Kepler-7b, in the Kepler photometric band ([34]); high geometric albedo ($\simeq$0.5) for the non-transiting planet 51 Peg b has been suggested through high-resolution spectroscopy of its reflected light done with HARPS at ESO 3.6 m telescope ([72]). Since the albedo signal detected so far could be fitted with a wide range of atmospheric and cloud species these are currently unconstrained.

- *Rotations*: planetary rotation rate can be inferred through high resolution spectroscopy; for example this technique has been used to obtain rotation measurement of the directly imaged planet β Pic b, which shows a projected equatorial velocity of 25 km/s ([104]). Other high dispersion spectroscopic observations of the well-studied hot-Jupiters HD 209458 b and HD 189733 b have inferred wind speed measurement at the terminator region ([103] and [111]). High-dispersion spectrographs on the next generation of giant telescopes will measure $v \sin i$ for many additional planets.

- *Thermal Inversions*: a planet thermal structure is said to be inverted when at some altitude temperature increases with increasing altitude. Such inversions can be inferred and derived by looking at the planets thermal spectra, which shows small, narrow emission features in the broader, deeper cores of absorption lines. As explained in [30] different results and conclusions about the presence of this phenomenon in the exo-atmosphers have been suggested; in particular in hot-Jupiters for which it now appears that inversions as initially reported are not present.

Chapter 3

Transmission Spectra Simulator

In this Thesis, as anticipated in the introduction, I focus on tools, simulations and instrumentation for the characterization of the exoplanetary atmospheres. In particular I concentrate on transmission spectroscopy, a technique based on the gathering and combination of different transmission spectra of the targeted system (host star + orbiting exoplanet) for the determination of the so called transmission spectrum. The analysis of the transmission spectrum allows the measurement of different atmospheric components and properties.

Transmission spectra are obtained during different exoplanetary transit epochs, during which the planet occults different parts of the stellar disk. Transmission spectroscopy is a differential technique which require the acquisition of spectra both during and outside the transit. In-transit spectra contain the absorption imprinting of both exoplanet atmosphere and the earth atmosphere, when the observation are ground-based, on the stellar light; Out-Transit spectra contain only the earth telluric features (again, in the case of ground based observation) and not the ones from exo-atmosphere because the planet is no more along the earth-star line of sight.

The transmission spectrum is usually analyzed using the Cross-Correlation Function, described in chapter 2, to detect specific chemical components with the purpose of deriving the atmosphere composition. Moreover, as described before in chapter 2, transmission spectroscopy is a high potential technique not only in the pure detection of atomic and molecular species, but also in exploiting the Doppler spectroscopic information retrieved along with the detection of these species to infer and constraint different physical phenomena in the exo-atmospheres, such as aerosols, exospheric evaporation, temperature gradient and atmospheric circulation (see for example the literature references cited after).

In the following some relevant and interesting results from literature. The presence of clouds and haze has been suggested to explain the weak absorption, (weaker than expected levels for clear atmospheres) of some molecules; for example H2O in HD209458 b and XO-1b observed with HST-WFC3 [33], or the analyses done in [54] and in [101] on a sample of 10 hot Jupiters, with H_2O detection observed with HST-WFC3, which show that terminator-region clouds are common in these type of giants exoplanets.

On the other hand deeper and longer ultraviolet (H Ly-alpha) transit signatures than the ones observed in optical spectra have been interpreted as a large escap-

ing exospheric cloud mainly composed by H, both in hot Jupiters and also for the Neptune-mass planet GJ 436b (see [38] based on transit observed with HST-STIS). In addition it is reported also the attempted and unfortunately not unambiguous detection of absorption signals from the exospheric sodium and singly ionized calcium in the hot super-Earth 55 Cnc-e performed with high resolution optical transmission spectra obtained with three different instruments (UVES at VLT, HARPS at ESO 3.6m telescope and HARPS-N at TNG).

A temperature gradient within the atmosphere has been inferred by means of the associated absorption of Na lines in the transit spectra of HD189733b resolved with the HARPS high resolution spectrograph [111] (see also the theoretical work described in [52] for details).

Atmospheric circulation and winds have been derived and evaluated from Doppler shift measures related to the detection of specific molecular and atomic species. The blue shift of CO has been interpreted as a wind flowing from the irradiated dayside to the non-irradiated nightside of the planet HD209458 b observed in the near-infrared with CRIRES at VLT ([103]). Again high dispersion transmission NIR spectra obtained with CRIRES have been used to measure a small circulation of 1.7 km/s in the other well characterized hot Jupiter HD189733 b [22]. This planet has been also studied in the optical band with transmission spectra from HARPS at ESO 3.6m, where a blue-shift of the Na doublet lines position has been correlated to a strong wind (about 8 km/s [111]) in the upper layer of its atmosphere. A possible explanation of these two different wind speeds is that Na doublet in the optical and CO and water vapor in NIR physically allow to probe different possible circulation regimes present in the exoplanet atmosphere.

As demonstrated with the mentioned results, new frontiers in the exoplanetary science, from the in-depth atmosphere characterization of well-known hot Jupiters to Super-Earth and Earth-like planets probing, will be explored through ground-based high resolution spectroscopy spanning from the visible to the infra-red wavelength range. Since the planetary signal diminishes with the increased resolution the coupling of high dispersion spectrographs with large ground based telescope is required to get the high SNR necessary for this photon starved astrophysical field. In particular it is underlined that challenging SNR performance (> 1000 or even 10000) and control of systematic effects are fundamental to capture signal amplitudes of few ppm for Earth-like planets, which are one of the focal scientific drivers of near and far future instrument like ESPRESSO at VLT and ELT-HIRES. (These instruments will be discussed in detail in chapters 3 and 4).

Large telescope allowing very high contrast could imply the possibility to detect the light emitted from background sources and/or from gravitationally bounded companion of exoplanetary systems, which could act as spectra signal contamination. The investigation of these scenarios has been one of main drivers for the development of a transmission spectra simulator, a tool aimed at generating synthetic spectra combining the star spectrum, exo-atmospheric absorption, earth telluric contribution and also contamination due to gravitationally bounded companions or background objects. In particular the simulator was used to analyze the astrophysical noise level introduced by different background sources, in term of spectral types and apparent magnitude; this analysis has been focused on the signature of the resonant neutral sodium doublet since it is a good proxy to detect and characterize exoplanets atmo-

spheres. For example, recalling the works cited before ([111]; [52]) different regions of the transmission spectrum around the Fraunhofer D lines have been exploited to trace a temperature profile up to high altitudes in the atmosphere of HD 189733b.

In addition to this specific study-case, which is only one of the possible applications, the flexibility and general purpose structure of the simulator allow to use the output spectra as input for the other simulation tool developed within this Ph.D. thesis work, the E2E simulator which will be described in detail in chapter 4.

In the following sections the spectrum simulator is described (in section 2.1), and the results of the performed analyses are shown (in section 2.2).

3.1 The transmission spectra simulator

The transmission spectrum simulator is a general purpose tool developed specifically to generate synthetic spectra for transit spectroscopy analyses. In fact in its full potential it combines the star spectrum, exo-atmospheric absorption, earth telluric contribution and also possible (and faint) contamination due to gravitationally bounded companions or background objects. Moreover, in the Science+Instrum. Simulation mode, it takes into account the telescope collecting area, the exposure time, the whole instrumental chain throughput and the estimated or observed SNR; in this way it produces a DRS-like spectra, i.e. processed in 1D format (wavelength - counts), that can be manipulated to do different kind of data analyses. A top-level schematic is presented in Fig 3.1. Nevertheless its flexibility allows to select which

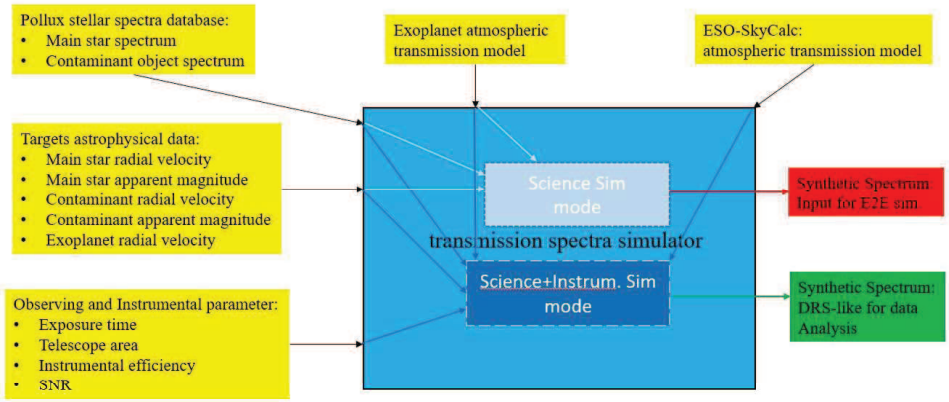

Figure 3.1: Top level schematic of the Transmission Spectra Simulator, presenting the two operative modes. The different input parameters are in the yellow boxes, while the output synthetic spectra are in the red and green boxes; they refers respectively to the spectra used as input for the End-to-End simulator and to the DRS-like spectra, i.e. processed in 1D format (wavelength - counts), which can be used in data analyses.

of these four components are combined to form the full spectrum, according to the specific analysis that the user would like to perform. In addition, in the Science Simulation mode, the simulator can be run skipping the instrumental and noise parameters in order to output synthetic spectra used as input for the End-to-End simulator (see the green path in Fig.3.1), which will be deeply described in chapter 4.

The simulation is based on some modeling and parameter assumptions; the parameters, described in the following, have been divided in different main-categories:

- *Astrophysical target parameters*:
  - Spectral type: real system data, pure random combination of main star and contaminant type, or assumption of particular relation of spectral types;
  - Δ mag: real system data or pure random combination of main star and contaminant apparent magnitude;
  - Radial velocity: real system (main star + contaminant + planet) data, assumed relative orbit (two body Keplerian orbital motion assumed), or real system (main star + planet) and background contaminant;
  - Exoplanet atmosphere: full model template or specific features model.

- *Observation conditions*:
  - Airmass: average value or different values according to the target system position on sky;
  - Seeing: average value or different values based on observation site statistics;
  - Exposure time of the frames.

- *Instrumental parameters*:
  - Telescope primary-mirror size;
  - Resolving power, R: high resolution instrumentation simulated;
  - Instrumental efficiency: targeted on VLT-ESPRESSO and ELT-HIRES, but flexible to be adapted to other instruments.

- *Observable/Reduced data parameter*
  - SNR: derived from Exposure time calculators (ETC) simulations or from real data (e.g. HARPS);

In the following subsections a description of the models used for the four components as well as the way they are combined by the simulator to generate the full spectra is given.

3.1.1 Astrophysical and Telluric spectral models

Here the tools exploited to generate stellar and telluric spectral models, and the assumptions taken into account for exoplanet atmosphere modeling are described. *Stellar spectra (Main target and contaminant)*: to generate them the simulator exploits the already built database POLLUX [1], which is a comprehensive library of theoretical star spectra covering all spectral types and a wide range of atmospheric parameters like effective temperature, gravity and metallicity [Fe/H]. Spectra are acquired through the on-line web page of POLLUX 7^{th} release, available with a query and retrieval interfaces. Example of query interface in Fig3.2. As decribed in [83],

Figure 3.2: Pollux General Query Interface.

the database gathers 8123 high resolution synthetic spectra associated to spectral types O to M and to Wolf-Rayet stars, which are derived from the best available 1–D models of stellar atmospheres: CMFGEN code [53], MARCS code [92], ATLAS12 code [58]. These different codes are associated to different specific line-list database for the spectra computation (see [83] and references therein for details). Moreover, the three models are available for different metallicities, gravity and effective tem-

[1]The POLLUX database is developed at the Laboratoire Univers et Particules de Montpellier (LUPM - Université Montpellier - CNRS) and it has also an on-line graphic display tool. The data can be retrieved in formats compliant to the Virtual Observatory standards (namely FITS and XML VOTable). It is a registered service of the VO $http : //pollux.graal.univ-montp2.fr/ssaserver/tsap$

perature range according to the spectral types they deal with (see again [83] and references therein for details). The synthetic spectra are computed from 3000 Å to 12000 Å at high spectral resolution. As described in [83] the spectra derived from CMFGEN model atmospheres are at R = 150000. Those derived from MARCS or ATLAS model atmospheres are characterized by a constant step in wavelength $\delta\lambda$ = 0.02 Å, leading to R $\geq$ 150000 for these data sets.

Earth atmospheric transmission profile: The telluric transmission profile is calculated using the ESO SkyCalc tool, [2] which is based on the Cerro Paranal Advanced Sky Model (see [80] and [61]). This software is composed by two modules; Module 1 generates synthetic sky spectra exploiting the line-by-line radiative transfer code LBLRTM V12.2 (latest version of this third party code). Module 2 calculates and adds all additional background components to the sky model. As conceptually described in Fig.3.3, the LBLRTM code package takes as input the HITRAN spectrum, based on the HITRAN 2008 database (see [97] and references therein) which gives spectral lines of up to 42 molecules and atoms, and an atmospheric profile that describes temperature, pressure, humidity and abundance of molecular species as a function of altitude, at a specified airmass and for a given observatory site at one particular time. This atmospheric profile is derived by merging three contributions: an

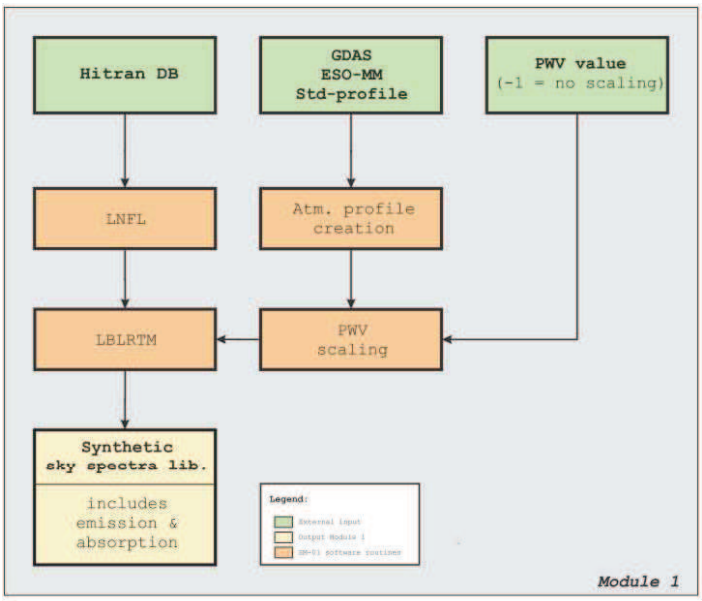

Figure 3.3: SkyCalc tool Module 1.

atmospheric standard profile, the GDAS profiles and ESO Meteo Monitoring (EMM) data. The atmospheric standard profile provides the information on molecular density, for the species of the HITRAN database, as function of height in the range 0-120

[2] It is developed by the Austrian ESO in-kind project with the contribution of Institute for Astro and Particle Physics, University of Innsbruck, and available at the web page *http : //www.eso.org/observing/etc/bin/gen/form?INS.MODE = swspectr + INS.NAME = SKYCALC*

km, for a specific geographical latitude and without any time information. To compensate the lack of time information, the ESO Meteo Monitor (EMM) is used since it gives most frequent updates on the local meteorological conditions at ESO sites of La Silla and Cerro Paranal; because of it is restricted to local on-site measurements, single geoelevation data points are only available. These two data sets are bridged by exploiting the GDAS profiles, provided by the National Oceanic and Atmospheric Administration (NOAA), which contain meteorological vertical data set (pressure, temperature, relative humidity) for 23 pressure levels in the range 0-26 km; these vertical profiles are updated every three hours for specific locations.

As said before in the Module 1 the LBLRTM calculates the synthetic sky emission and transmission spectra and with Module 2 background contributions (see Fig.3.4) to the sky emission are modelled and added.

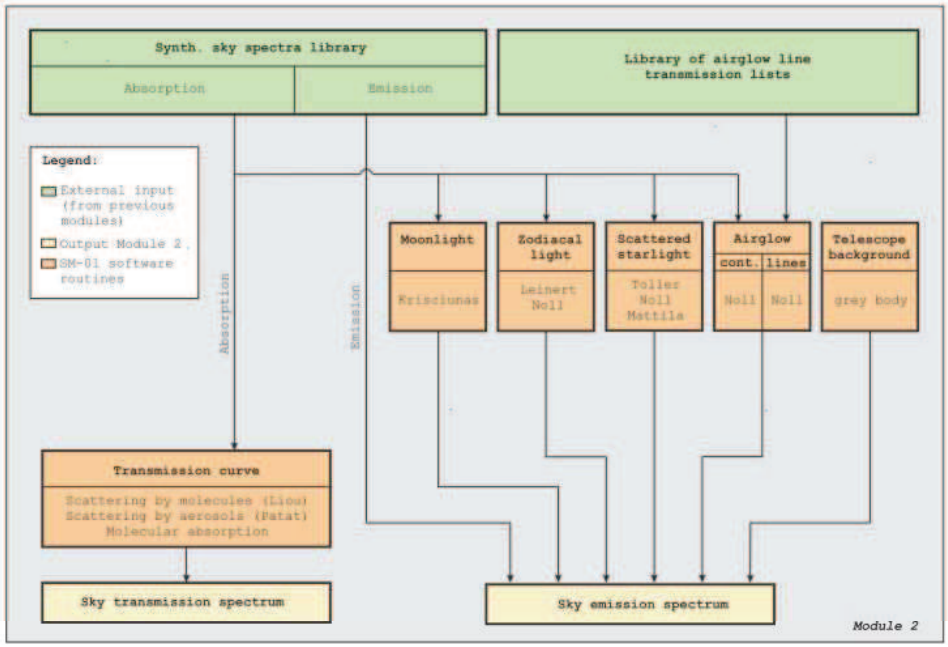

Figure 3.4: SkyCalc tool Module 2.

The SkyCalc is queried using resolution step of 0.006 Angstroms, corresponding to a minimun spectral resolving power of about 500,000 for the minimum wavelength of 3000 Å from the stellar spectra.

Exoplanet atmospheric contribution: The exoplanet atmosphere can be modeled in two different ways. The first one relies on spectra derived from theoretical model (see [37]) while the second one, that is restricted to Na I absorption features, by the adoption of two Gaussian or Lorentian profiles characterized by their proper physical parameters (velocity, full width at half maximum and contrast). The general-purpose architecture allow to exploit both of them by assuming to ingest the transmission profile due to exo-atmosphere as an ASCII file or t-fits table described by wavelength and transmittance.

3.1.2 The transmission spectra simulator modeling details

In this subsection modeling details of the whole simulation chain through which the different input parameters and data are exploited to obtain the full spectrum are presented. For simplicity the different simulation steps are described in the same order with which the code proceeds.
Radial velocity shift: applied on the emitted wavelengths to compute, for each astrophysical objects, the observed wavelengths in the solar system reference frame:

$$\lambda_{obs} = \lambda_{em} \cdot (1 + \frac{RV_{ms}}{C}) \tag{3.1}$$

Band extraction: the observed wavelength range, related to the instrument observation setup or to a specific band analysis, is extracted from the wavelength data expressed in the solar system frame;
Spectra conversion: the Spectral flux density of the main star and contaminant are converted from $erg/(s \cdot cm^2 \cdot$ Å$)$ to $ph/(s \cdot cm^2 \cdot$ Å$)$:

$$F_{\lambda,ph} = \frac{F_{\lambda,erg} \cdot \lambda}{10^7 \cdot h \cdot c} \tag{3.2}$$

Spectral flux density normalization: the normalization is based on the reference Spectral flux density of a star with apparent magnitude m=0 in the V filter at 5500 Å, which is 982.91 $ph/(s \cdot cm^2 \cdot$ Å$)$.The observed Spectral flux density is then scaled by a normalization factor α_{norm}:

$$\mathcal{F}_{\lambda\, ph} = \alpha_{norm} \cdot F_{\lambda\, ph} \tag{3.3}$$

Where α_{norm}:

$$\alpha_{norm} = \frac{F_0 \cdot 10^{(-\frac{m}{2.5})}}{F_{\lambda,ph}(5500)} \tag{3.4}$$

Exoplanet and Earth atmospheric transmission spectra application: the RV shifted exoplanet transmission spectrum and the Earth telluric profile (not RV shifted of course) multiply the normalized spectrum of the main star, while only the Earth telluric profile (not RV shifted of course) multiplies the normalized spectrum of the contaminant.

$$\mathtt{F}_{\lambda,ph,ms} = \mathcal{F}_{\lambda,ph} \cdot \mathcal{T}_{\lambda,exo} \cdot \mathcal{T}_{\lambda,\oplus} \tag{3.5}$$

$$\mathtt{F}_{\lambda,ph,cont} = \mathcal{F}_{\lambda,ph} \cdot \mathcal{T}_{\lambda,\oplus} \tag{3.6}$$

Integration of the normalized Spectral flux density with the required spectral resolution (pitch):

$$\mathbb{F}_{ph,ms}(\lambda) = \int_{\lambda}^{\lambda+\delta\lambda} \mathtt{F}_{\lambda,ph,ms}(\lambda)d\lambda \tag{3.7}$$

$$\mathbb{F}_{ph,cont}(\lambda) = \int_{\lambda}^{\lambda+\delta\lambda} \mathtt{F}_{\lambda,ph,cont}(\lambda)d\lambda \tag{3.8}$$

Multiplication by the exposure time, telescope collecting area and instrumental throughput:

$$\mathfrak{F}_{ph,ms}(\lambda) = \mathbb{F}_{ph,ms}(\lambda) \cdot t_{exp} \cdot A_{Tel} \cdot \eta_{instr} \tag{3.9}$$

$$\mathfrak{F}_{ph,cont}(\lambda) = \mathbb{F}_{ph,cont}(\lambda) \cdot t_{exp} \cdot A_{Tel} \cdot \eta_{instr} \tag{3.10}$$

Sum of all the signals:

$$\boldsymbol{F}_{tot}(\lambda) = \mathfrak{F}_{ph,ms}(\lambda) + \mathfrak{F}_{ph,cont}(\lambda) \tag{3.11}$$

Noises added according to the SNR: the final photon distribution per each integration wavelength is a normal distribution, $N(\mu, \sigma)$, with a mean value equal to the number of integrated photons at that wavelength and a standard deviation related to the noise part of the SNR [3]

$$\mathbf{F}(\lambda) = N(\boldsymbol{F}_{tot}(\lambda), \frac{\boldsymbol{F}_{tot}(\lambda)}{SNR}) \tag{3.12}$$

When the code derived in this section is used for End-to-end simulation as Science module, the noises are not added since they stem directly from the full simulation of 2D echellogram. Instead, when used as a stand alone tool the SNR of each spectrum can be considered in the way reported in Eq. 3.12. In the following image the schematic of the simulator modeling is shown; yellow blocks are the input parameters, while light blue blocks represent the modeling code steps.

[3] Note that here I assumed that the SNR is constant between the continuum and absorption lines. This is of course an over-simplification that it is negligible and valid when absorption lines are not strong or saturated. Otherwise the number of photons decreases significantly and the SNR is largely different between the center of the line and the continuum. Although this situation is fully recovered in the End-to-End simulator (see Chapter 5), in this simulation the limit has been relaxed since only the pure astrophysical noise is considered.

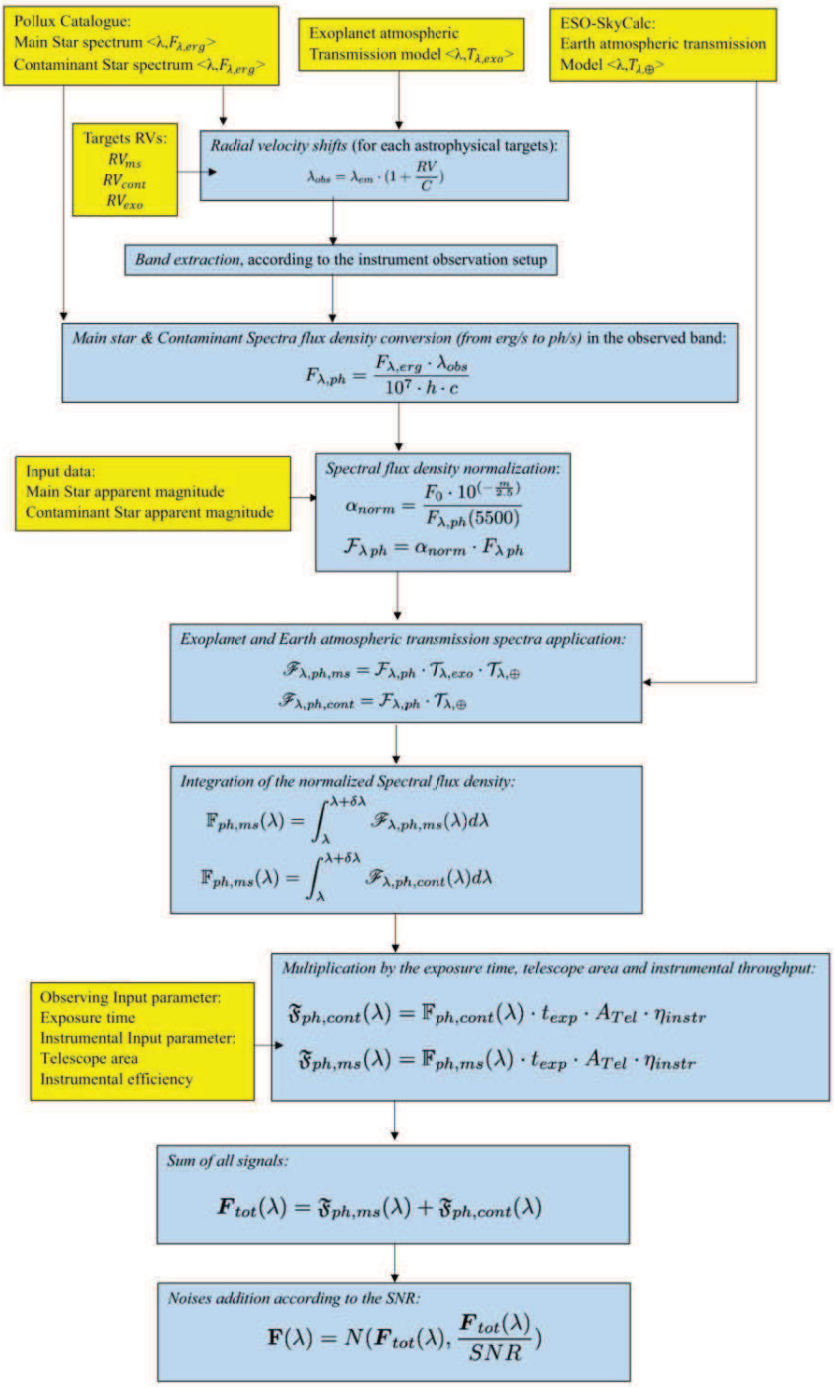

Figure 3.5: Transmission spectra simulator equation flow.

Here below an example of intermediate and output spectra results are shown for a specific simulation scenario. This is the system HD 189733, which is composed by a main star of spectral type K1V with an apparent magnitude m_V=7.68 (see [20]), a companion star of spectral type M4V (see [95]) with a simulated apparent magnitude m_V=12. The simulated radial velocity of both star is 1 km/s with respect to the Solar System rest frame. The exoplanet atmosphere has been modeled, as described before in subsection 3.1.1, taking into account the Na I doublet absorption features characterized by an absorption depth of 0.64% (D2) and 0.40% (D1) respectively and with a FWHM of 0.52 Å (as derived in [111]). The Earth telluric transmission profile has been calculate with the ESO SkyCalc tool, considering Airmass 1 and a seasonal average for the precipitable water vapor (PWV) in La Silla observatory. The observation is simulated with a 8 m class telescope, with instrument resolving power R = 120000 and a total efficiency of 10%. The considered wavelength band is from 5000 Å to 7000 Å, the exposure time is 200 sec and a SNR of 100 per each spectral element is simulated.

The spectral flux density of both the host and contaminant star is shown in Fig. 3.6; it is possible to see the difference due to their relative spectral type. The sodium doublet absorption features are shown in Fig. 3.7, while the Earth telluric profile is in Fig. 3.8 in the considered observation wavelength range.

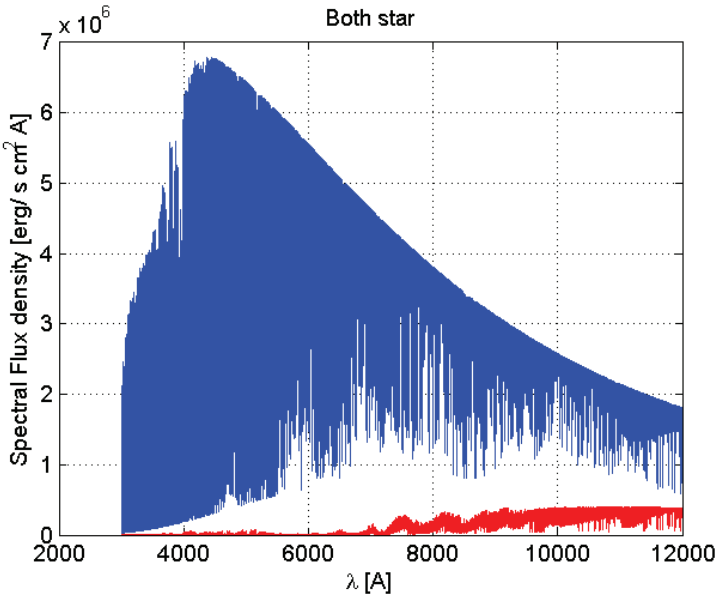

Figure 3.6: Main star (blue) and contaminant (red) spectral model templates.

The main (host) star normalized spectral flux density is plotted in Fig.3.9; for a star with m_V=7.68 and the reference flux F0, the number of photons, checked at 5500 Å, is 0.831. The photon flux density spectrum filtered by the exoplanet and earth atmospheric transmission profiles, in the observation band, integrated in each wavelength bin of 0.01 Å, is shown in Fig. 3.10, where the order of magnitude of the flux level is consistent with Fig. 3.9. The photon flux is plotted in Fig. 3.11, where checked at 5500 Å is $\simeq 8.5{\cdot}10^4$ photons. The same plots for the contaminant star are

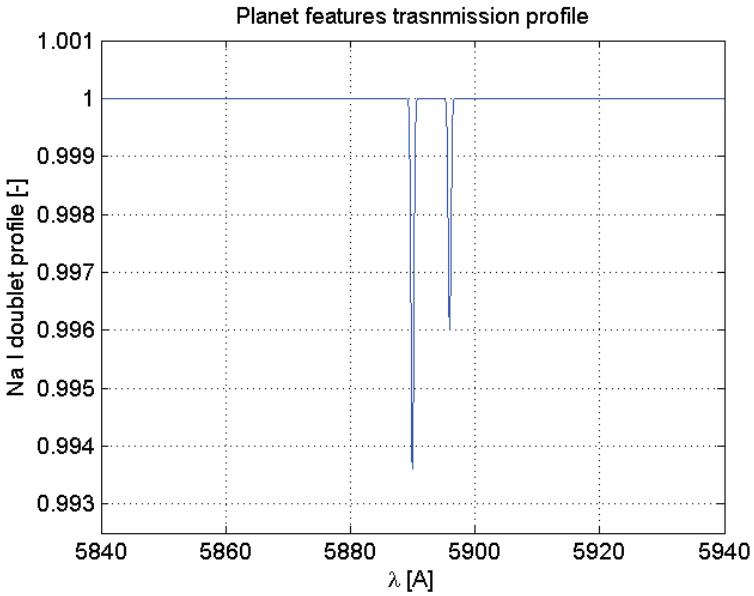

Figure 3.7: Exoplanet atmospheric spectrum features (only Na I doublet modeled).

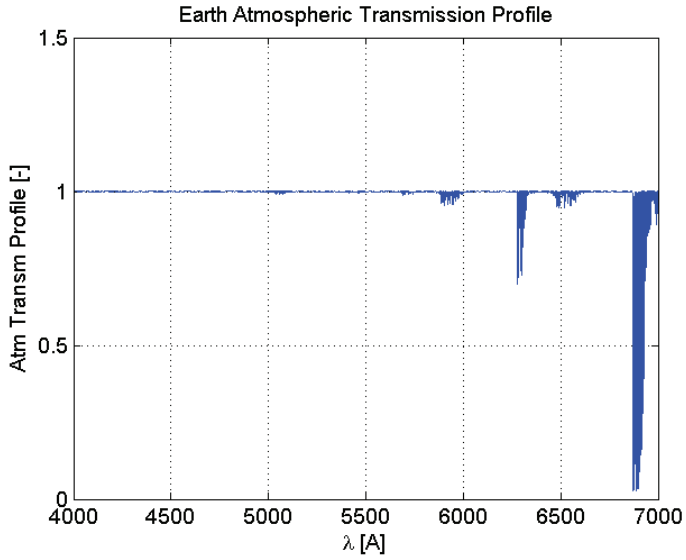

Figure 3.8: Earth atmospheric transmission profile in the selected observation band.

shown in Fig. 3.12, Fig. 3.13 and Fig. 3.14; with the exception that, as described before in the case of gravitationally bounded companion, the contaminant flux is not filtered by the exoplanetary atmospheric profile. The full spectrum, combination of both stars filtered spectra, is shown in Fig. 3.15 and in Fig. 3.16 with noises added on the basis of the simulated SNR.

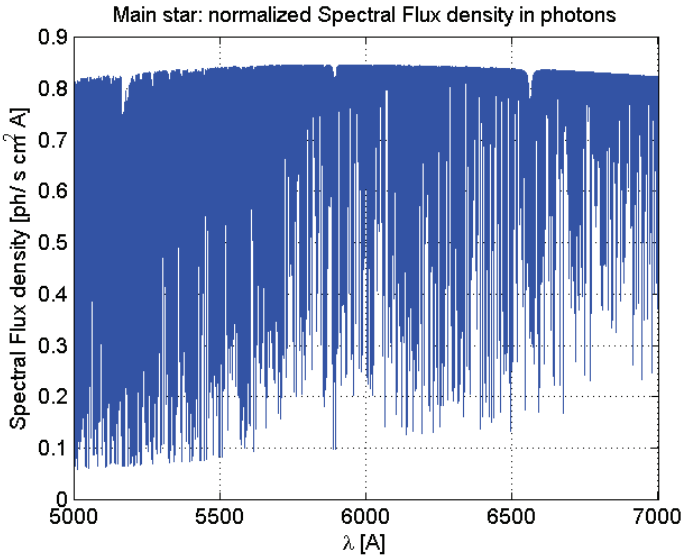

Figure 3.9: Normalized flux of the main star: the number of photons has been checked at 5500 A. For a star with m_V−7.68 and the reference flux F0, the number of photons at 5500 Å, is 0.831.

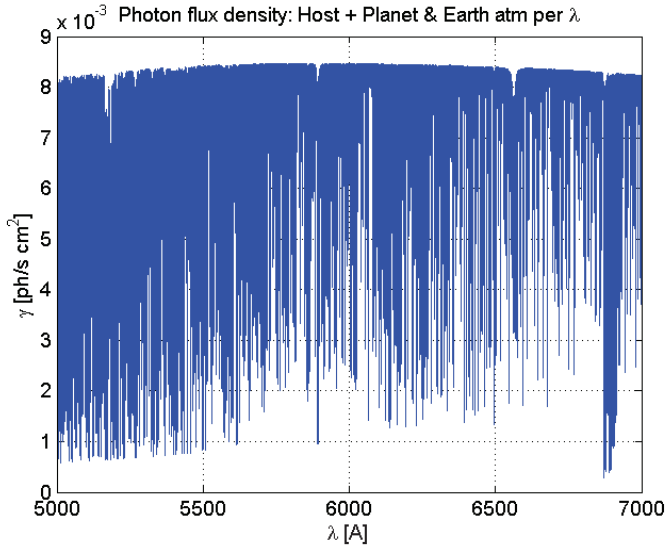

Figure 3.10: The photon flux density of the main star spectrum filtered by the exoplanet and earth atmospheric transmission spectra, in the observation band, integrated in each wavelength bin of 0.01 Å. The order of magnitude is consistent with the previous figure.

3.2 Contaminant Analysis

The problem of stellar companion, both in terms of bounded object or foreground/background stars, has become crucial not only in terms of radial velocity error budgets (see e.g.[31]) but also when careful measurement of transmission spectroscopy is performed. For instance, in the case of RV the work described in [31] used

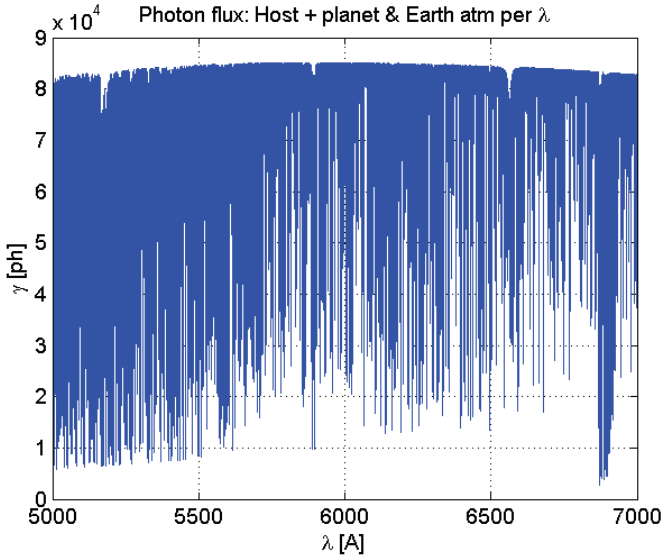

Figure 3.11: Main star photon flux. The photon flux density is recorded in 200 seconds, simulating a 8 m class telescope with instrument-telescope overall efficiency of 10%. The photon flux is checked at 5500 A to be $\simeq 8.5{\cdot}10^4$.

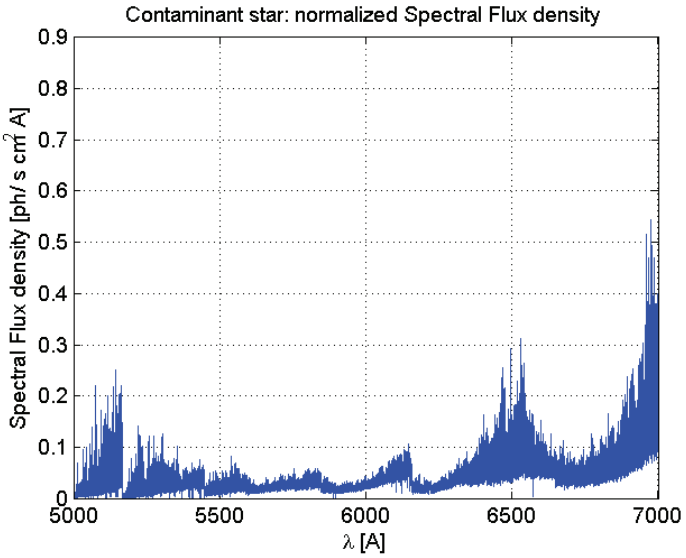

Figure 3.12: Normalized flux of the Contaminant star: the number of photons has been checked at 5500 A. For a star with m_V=12 and the reference flux F0, the number of photons at 5500 Å is 0.0156.

already available HARPS spectra database and found that the impact on the radial velocity calculation is a function of the difference between individual radial velocities, the difference between target magnitude and contaminant magnitude, and also of their spectral types. Although the outcome of the analyses demonstrated that for current spectrographs facilities the contamination is of few cm/sec, for large aperture

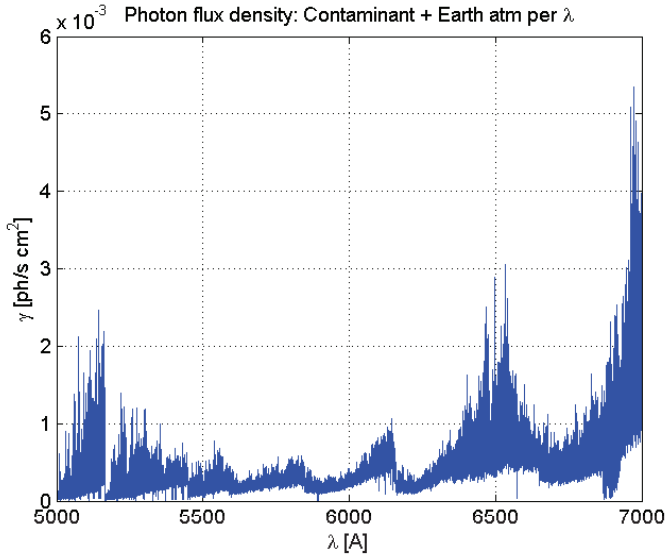

Figure 3.13: The photon flux density of the Contaminant star spectrum filtered by the earth atmospheric transmission profile, in the observation band, integrated in each wavelength bin of 0.01 Å. The order of magnitude is consistent with the previous figure.

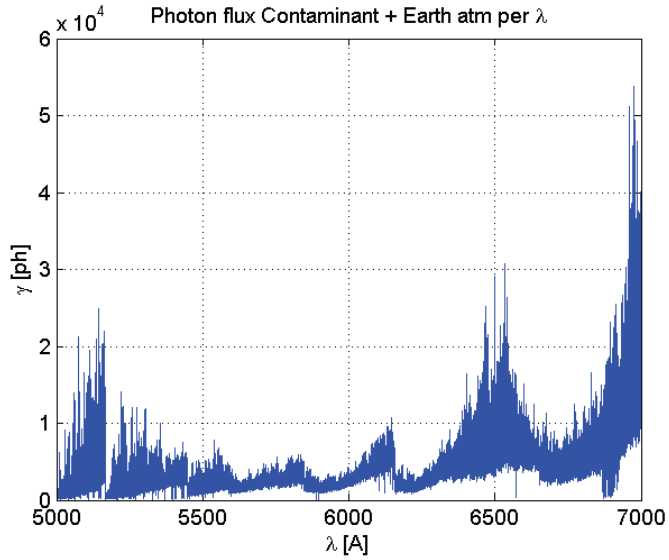

Figure 3.14: Contaminant photon flux. Checked at 5500 A to be $\simeq 1.56{\cdot}10^3$.

telescope this kind of error source cannot be further ignored where more and more accuracy is expected, especially for determination of Earth-like planets.

In this section the aim is to perform similar (and simplified) analyses to investigate the possible contaminations when discussing transmission spectra acquired when the geometry of the system (bounded or unbounded) is not restricted to two bodies. The objective of this work is dual; two different scenarios has been considered in

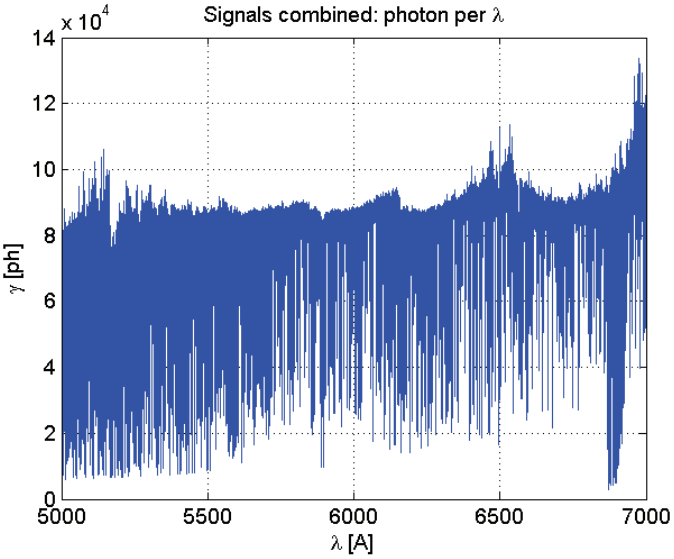

Figure 3.15: Sum of the photon fluxes from both stars.

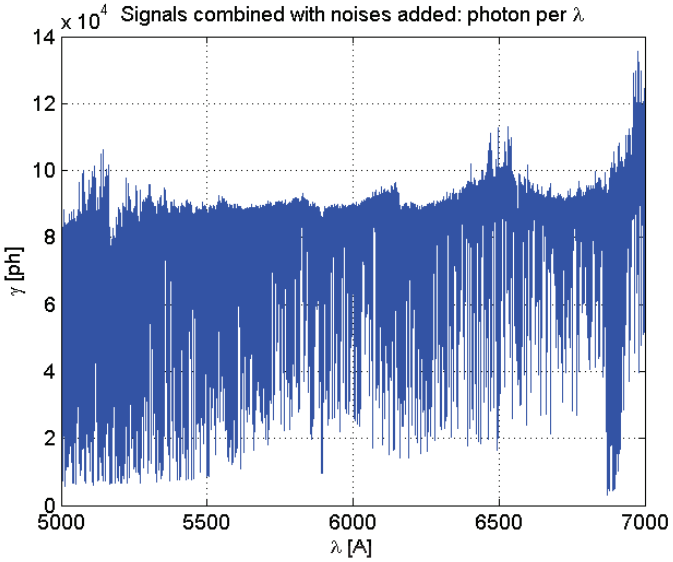

Figure 3.16: Sum of the photon fluxes from both star with noise added.

order to retrieve possible effects of contaminant sources to transmission spectroscopy. In the first case, the astrophysical noise coming from a background (or foreground) source not gravitationally bounded is considered. In this case, in order to assess the contamination, in term of flux in ppm [4], of transmission spectrum the main (host) star and background source contaminant spectra have been simulated. No instrumental noise, SNR or telluric contribution (of Earth and exoplanet) has been considered.

[4]In this case the considered contamination is the flux contamination and not the RV error.

The idea behind this analysis is to understand the impact of the injected contaminant signal in terms of ppm, according to the spectral type of the background/foreground source and its apparent magnitude (with respect to the main host star).

In the second case, a three body problem is addressed. During this PhD activity I started a fruitful collaboration with research group in Geneva (P.I. Christophe Lovis and Francesco Pepe) that is very active in the characterization of exoplanetary atmospheres in transmission (see for example works [111], [2], [52]). Within this collaboration, a new scenario has been investigate where both host star, its orbiting planet and contaminant unbounded object are considered. In this case, also SNR equal to that obtained with observation with HARPS of the system HD189733 has been considered. The aim of this analysis is to understand, not only the full functionality of the simulator (that will feed the Geneva group pipelines), but also to assess possible contamination in observations made by 3 m class telescope where exo-atmospheres have already been detected.

In addition, the analyses were done focusing on the contamination impact on the Na doublet absorption signatures, since it is one of the most exploited features to study and characterize explanetary atmospheres. As anticipated in the introduction of this chapter, the transmission spectrum is derived combining the spectra observed both during (In-transit spectra) and outside the transit (Out-transit spectra) of an exoplanet. Following the method described in [111] and [2], the Out-transit spectra are stacked together to create a master spectrum out-of-transit, the master-out $\mathcal{F}_{out}$. Then each one of the In-transit spectra is divided by the master-out, and then all are summed up. This sum is normalized to the continuum level just outside the region of the sodium doublet lines and the normalized spectrum is subtracted by unity to obtain the final transmission spectrum (which in the full chain, comprising also the explanetary atmospheres imprint, represents the radius of the exoplanet as function of the wavelength [5]. Mathematically, referring to the symbol used for the spectra with no noises added of eq. 3.12 this can be expressed as:

$$R^{'} = \sum_{in} \frac{\boldsymbol{F}_{in}}{\mathcal{F}_{out}} - 1 \tag{3.13}$$

For the first case scenario (assessment of the contaminant signal in ppm from the background source) the parameter space was explored in two main variables: the magnitude of the background source (supposing that it falls fully within the aperture of an HARPS-like spectrograph) and its spectral type. The line-of-sight velocity has been fixed around an average value of 20 km s^{-1} distributed like a Gaussian function with dispersion of few m s^{-1}.

To assess the contribution of a contaminant source in a planetary system (like HD189733) the simulator has been used in order to synthesize observed spectra composed by the starlight from the host and from the contaminant, according to the choose apparent magnitude and relative spectral type.

The obtained 1D data are then processed according to the procedure reported previously to retrieve a possible transmission spectrum coming from absorption features of a transiting planet. Since no other velocity fields (like wind circulation or

[5] As explained in [2] and [99], the spectral features of a transmission spectrum are proportional to the area (and so radius) occulted by the planet over the stellar disk, since the radius of the optically thick atmospheric layers changes according to the atmospheric opacity variation with wavelength.

peculiar motion in the upper layer of the exo-atmosphere) are considered by definition (no planet contribution has been added) the obtained transmission spectra are inspected at wavelengths where the sodium features should be detected.

The apparent magnitude of the contaminant source and its spectral type are explored in a grid in order to build a bubble contamination plot in the plane spectral type - magnitude (see Fig. 3.17). The level of the spurious signal in the transmission spectrum (calculated as rms value in ppm on the transmission spectrum itself) stemming from the contaminant source is expected to be a function not only of the brightness of the source, but also of the spectral type, especially in the region where the sodium resonance features are detected.

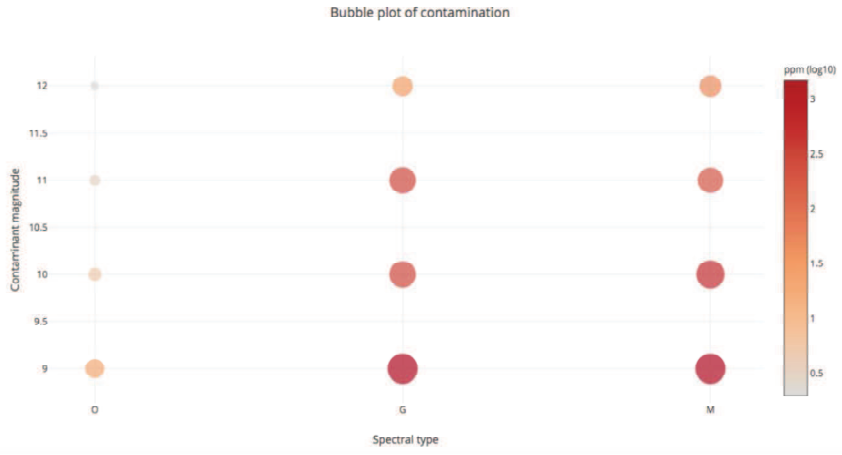

Figure 3.17: Bubble contamination plot. On the X axis, the spectral type of the contaminant source is reported while on the Y axis the apparent magnitude (V band) is spanned. Contamination in ppm in the transmission spectrum is reported as bubble with related size (see colorbar on the right).

The maximum contamination occurs for background object which spectral type matches roughly the one of the host star (G or M type). This results is directly connected to the physical state, abundances and ionization states of the photosphere of these stars where the contribution of absorption lines from sodium is important. For a magnitude of the contaminant between 9 and 11 the contamination in ppm in the region around the sodium lines is assessed to be between 500 and 1000 ppm which is order of magnitude higher than the signal expected from an Earth like planet around a main sequence G star. The effect is instead much lower for hot stars, like O and B types, where the contamination varies between 10 and 4-5 ppm. This is a simplified view since no further components that could add spurious effects in the signal are not considered, for example the stability of the instrumental profile during the experiment. This kind of information, however, could be recovered when a full simulation is performed with the End-to-End model that will be explained in the next chapters.

On the contrary, in the second scenario where the host star, the absorption features from the hot Jupiter atmosphere and the contaminant source are considered, the analysis performed concern the simulation of the observations that Wyttenbach

and collaborator detailed in their paper [111]. Briefly, by analyzing spectra collected by HARPS they recovered the detection of neutral Na I sodium in the upper layer of the hot Jupiter HD198733 b orbiting his main sequence star. This scenario has been used as a test-bed to reproduce what HARPS would be observed if an unbounded companion with apparent magnitude $m_V = 12$ and spectral type M were ingested by the spectrograph since confused in the seeing disk.

For this reason the transmission spectra simulator was used to generate 40 spectra of the system in various phases of the orbit, modeling the contribution of the exoplanetary atmosphere as described in the previous paragraph. The simulated run encompasses 21 spectra during the transit and 19 spectra out transit modeled with proper noises estimated according the SNR reported in the literature. The dataset has been ingested by the same pipeline developed by the Geneva group for the analysis of exoplanetery atmosphere of HD198733 b. The results are reported in Fig.3.18 (no telluric absorption lines have been considered). In the upper panel of the figure

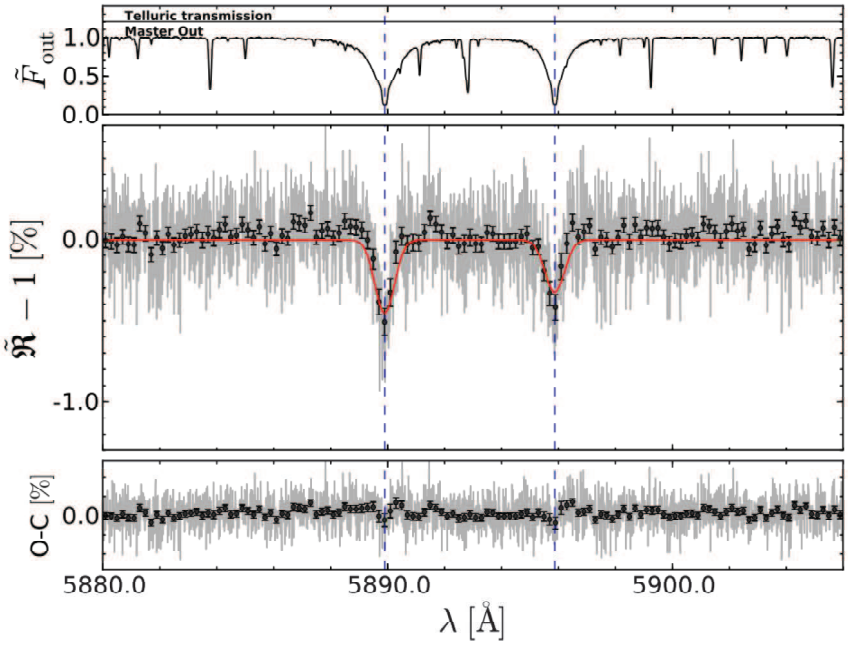

Figure 3.18: Transmission spectrum for the second scenario simulation in the region around the sodium Na I D lines. *Upper Panel*: Master-Out spectrum, the Earth telluric transmission profile is flat since it is not included in the simulations for this scenario (the vertical off-set is only for visibility). *Middle Panel*: Recovered transmission spectrum of the exoplanet atmosphere taking into account all the generated synthetic spectra with the simulator; black circle corresponds to narrow band binning of about 20x resolution elements, while the solid red line is the global fit performed with Gaussian profile for the absorption features. *Bottom Panel*: Residuals between the observed data and the global fit. Courtesy to Aurélien Wyttenbach.

it is reported the Master out spectra, secured by adding all the out-transit spectrum simulated, while in the middle panel the recovered transmission spectrum is shown (black circle corresponds to narrow band binning of about 20x resolution elements). The absorption features of the sodium recovered is clearly visible at the proper wavelength (no wind in the upper layer of the atmosphere or other peculiar motions are

considered) and the global fit performed with two Gaussian profile is reported as a solid red line. Residuals between the observed data and the global fit are reported in the bottom panel (O−C).

The first non-trivial result is that the absorption features coming from the exo-atmosphere has been recovered properly despite the presence of the contaminant star. The empirical Monte Carlo algorithm detailed in [96] was followed to understand (blindly) if the measured Na I absorptions are an artifact of the data. A sub-sample of all the spectra was simulated; the choice of this sub-sample was then fixed (called scenario). Next, this new sample was randomly divided into two parts to create an out-of-transit data-set and an in-out data-set. These two data-sets always contain the same number of spectra. In the first scenario (out-out), the spectra were only selected from out-of-transit spectra expecting to find the distribution of computed relative absorption depth centered at zero for the Na I while in the in-out scenario deviation from the zero (with scattering) should be detect. The out-out and in-out distributions are clearly separated, as recovered for the actual HARPS observation, indicating that the detected spectral lines are not an artifact coming from the data (although, tentatively, some more scattering in the out-out distribution is detected probably due to the contaminant star). Although we know a priori that a planet feature is present in our data, we decided to perform this kind of statistical analysis to check if the contamination could reveal some more information during this bootstrapp re-sampling technique.

The recovered transmission spectrum (see Fig.3.18) has been then fitted with two Gaussian features characterized by two parameters: line center and width. The goodness of fit has been estimated through Bayesian Information Criteria (BIC) that, for our case, is assessed to be 205. The D2 and D1 lines are detect to be 0.49±0.06 % and 0.37±0.06 % at more than 6σ, consistently with the line contrast used for generate synthetic data. The line centroid shift (recovered after taking into account systemic velocity) is -0.004 ± 0.03Å, indicating that no peculiar motion is revealed above the instrumental precision and photon noise level. This is an important outcome of the analysis since this demonstrate that the wind circulation detected in HD198733 b is not reproduced at least with this kind of setup (that represents an average condition) although some line spreading around the centroid (of the order of 0.9Å) is recorded. This line widening is probably due to the signal of Na I absorption lines associated to the contaminant star that introduces, around the spectral region of Na I, counts excess which results in a wider spectral line. As can be expected, the presence of the considered contaminant source ingested in an HARPS like spectrograph does not prevent the detection of exo-atmosphere with transmission spectroscopy nor to infer and speculate on some peculiar motion in the upper layer of the atmosphere. However, as noted in the first analysis, the spurious signal could be up to thousands of ppm for G or M cool dwarf. This kind of situation should be kept in mind when operating with Extremely Large Telescopes; in fact in these conditions signals of few ppm are expected from Earth twins and the signal from more background/foreground objects could be captured and it could emerge, due to larger aperture telescopes, above the noise level of the transmission spectrum. The analysis reported in this Chapter is, however, not satisfactory and aims to be a good starting point for future investigations.

In particular, as outline of the work for next activity is to explore in a more

satisfactory manner the space parameters of the contaminants stars. For example, in terms of velocity fields of the contaminant object and its possible variation during the observation possibly including their peculiar motion due to stellar activity or, even more, the presence of orbiting planet (or stellar companion) in the unbounded sources. A further possible future work is to understand what kind of algorithms or statistical techniques could be exploited or implemented to remove the stemming signal from contaminant sources to improve the measurement up to few ppm.

3.3 Conclusions

In this Chapter the high potential of high resolution transmission spectroscopy in the characterization of different phenomena of exoplanetary atmospheres has been pointed out. In addition the problem of possible contamination in transmission spectra, of stars hosting exoplanets, due to gravitationally bounded object or foreground/background stars which could be captured with large telescope instrumentation has been investigated. This has been one of main drivers for the development of a transmission spectra simulator, a tool aimed at generating synthetic spectra combining the star spectrum, exo-atmospheric absorption, earth telluric contribution and also contamination due to gravitationally bounded companions or background objects.

The architecture of the simulator as well as the way through which it models and combines both the astrophysical spectra and instrumental properties, like telescope aperture and throughput, has been presented and detailed. The simulator has been exploited to generate synthetic transmission spectra in order to perform two kind of analyses.

In the first one the pure astrophysical noise coming from a background (or foreground) source not gravitationally bounded is considered, without taking into account instrumental noise, SNR or telluric contribution (of Earth and exoplanet). The idea behind this analysis is to understand the impact of the injected contaminant signal in terms of ppm, according to the spectral type of the background/foreground source and its apparent magnitude (with respect to the main host star); therefore the parameters space was explored in these two variables. The result is that the maximum contamination (in the order of 1000 ppm) occurs for background object which spectral type matches roughly the one of the host star (G or M type); while a much lower contamination (in the order of 10 ppm) is related to hot stars, like O and B type.

In the second scenario the host star, the absorption features from the hot Jupiter atmosphere and the contaminant source are considered. A data-set of transmission spectra was generated to simulate the observations of HARPS spectra of the system HD189733, through which the detection of neutral Na I sodium in the upper layers of the hot Jupiter orbiting the hosting star was recovered by Wyttenbach and collaborators. This scenario has been used as a test-bed to reproduce what HARPS would be observed if an unbounded companion with apparent magnitude $m_V - 12$ and spectral type M were ingested by the spectrograph since confused in the seeing disk. In the collaboration I started with the Geneva group, a data-set of 40 (21 in-transit and 19 out-transit) spectra, modeled with proper noises estimated according the SNR reported in the literature, were ingested by the pipeline the developed for the study of

atmosphere of HD189733b. The first non-trivial result is that the absorption features coming from the exo-atmosphere have been recovered properly despite the presence of the contaminant star. An empirical Monte Carlo analysis was performed to probe that the detected spectral lines are not an artifact coming from the data. The line centroid shift, recovered after taking into account systemic velocity, indicates that no peculiar motion is revealed above the instrumental precision and photon noise level, demonstrating that the wind circulation detected in HD198733 b is not reproduced at least with this kind of setup. The assessed line widening is probably due to the signal of Na I absorption lines associated to the contaminant star that introduces, around the spectral region of Na I, counts excess which results in a wider spectral line.

As can be expected, the presence of the considered contaminant source ingested in an HARPS like spectrograph does not prevent the detection of exo-atmosphere with transmission spectroscopy. However, as noted in the first analysis, the spurious signal due to G or M cool dwarf could be up to thousands of ppm, which should be taken into account when operating with Extremely Large Telescopes. In fact in these conditions signals of few ppm are expected from Earth twins and the signal from more background/foreground objects could be captured and it could emerge, due to larger aperture telescopes.

Chapter 4

Ground-Based High Resolution Spectrographs

Ground-based high resolution spectroscopes are exceptional instruments to achieve breakthroughs in a wide range of astrophysical areas; the deep characterization of known close-in orbit planets and detection and study of low-mass planets in the habitable zone are science cases that particularly benefits of this kind of instruments. Terrestrial planets in the habitable zone of their parent stars are one of the main scientific topics of the next decades in Astronomy. The instrumental key aspects that link the scientific observational performance and technical requirements for such spectrographs are:

- High resolution
- High efficiency (which in this frame means high instrument throughput)
- High precision and accuracy
- High stability

These are required to overcome the main limitations in radial velocity measurements listed in Chapter 1, which are: photon noise, spectrograph illumination, instrumental drifts and perturbations, photon losses, spectral contamination and stellar noises.

High resolution provides an instrument with the adequate capability of resolve the features in the spectrum of observed target. High resolving power is achieved relying on high dispersion optical elements, like echelle gratings as main dispersive components, and implies large instruments. As explained in Chapter 3, the signal spreading in high dispersion spectrograph could result in a low or reduced SNR; accordingly this affects the required exposure time and the limit magnitude of the observed targets. In order to obtain the required SNR, efficient instruments are needed with designs optimized to avoid vignetting and to reduce throughput losses; for example the number of optical elements, selection of glasses and coatings as well as detector quantum efficiency (QE) are fundamental aspects to be taken into account for minimizing throughput losses. It must be also underlined that adequate spectral

sampling (in any case larger than the Nyquist limit of 2 pixels [1]) plays a relevant role in combination with resolution, total efficiency (from atmosphere to detector QE) and detector noises in the optimization of SNR.

High accuracy RV measurements require very detailed wavelength calibration performance and method (e.g. Iodine cell and/or Simultaneous reference) as well as very stable and well-characterized calibration sources (e.g. Laser Frequency Combs deliver extremely regular pattern of equally-spaced emission lines, which can be controlled with high accuracy and precision by locking the Comb to an atomic clock). Extreme RV precision requires also a very good control of instrumental effects and drifts, so that ultra-stable instruments are fundamental to push the limit towards very tiny signal like the ones for Earth-like planets in the Habitable Zone of quiet solar type stars. Gravity invariance, the decoupling of the instrument with respect to the telescope, and spectrograph illumination stability are critical aspects; fiber-feed design allows to optimize these aspects. In addition, "special tricks" in the implementation of fiber-feed designs like the adoption non-circular fibers with intrinsic better scrambling performance and possible additional fiber-agitator mechanisms enabled relevant increase in scrambling gain [2]. Furthermore, double scrambler designs are used to have both near and far field scrambling; where the far field is the pupil image, while the near field is the target image which can also be affected by guiding errors.

Properly stabilized spectrograph environment is also an extremely important aspect to attain cutting-edge RV precision performance. To do that, typically, spectrographs are housed in so-called coudè-room where the temperature is kept constant and the telescope induced vibrations are dumped by the building foundations. In addition also the instrument bench, vessel and mechanical mountings of optical components are temperature stabilized, with thermal stability down to mK level, in order to avoid thermo-mechanical perturbation of the optical path. Moreover instrument are mounted in depressurized vessel, at order of 10^{-4} mbar, in order to avoid drifts of the spectrum on the detector due to variations in atmospheric pressure.

In the next sections the ESPRESSO spectrograph, which will be installed at the ESO VLT by the end of this year, and the future ELT-HIRES spectrograph, currently at the end of phase-A, are described. The simulation and modeling tools developed for these two instrument are presented, according to their specific project phase.

4.1 ESPRESSO at VLT: a brief description

The Echelle SPectrograph for Rocky Exoplanets Stable Spectroscopic Observations (ESPRESSO) instrument will be installed at the Combined Coudé room of the ESO 8.2 m Very Large Telescope (VLT) observatory, located in Cerro Paranal (Chile)

[1] This is the considered the minimum sampling in spectroscopy domain, coming from the Shannon-Nyquist theorem (also called Whittaker-Shannon-Nyquist theorem), to properly sample a continuous spectral signal with discrete points (pixels). As clearly explained in [41], spectral resolution element features can be reasonably approximated with a Gaussian and interpolation methods for the reconstruction of the spectral signal play a relevant role in combination with the sampling in the resulting SNR.

[2] The scrambling gain (SG) by optical fibers as stated in [5], is defined as the ratio between the displacement of the star in front of the input fiber end and the shift of the point spread function (PSF) on the spectrograph detector.

at an altitude of 2635m (for details on VLT see [39]). It can works in three different operative modes according to the used aperture on sky and the light-feed from the different Unit Telescope (UT) of the VLT observatory (for a detailed description see [39]). Installation and commissioning has been performed in the end of 2017, and at its full potential it will be one of the most powerful spectrographs operating in the optical wavelength range. The top-level requirements derived from the science drivers, described in the following subsection, and main instrumental features are here anticipated and summarized in Tab.4.1.

Table 4.1: The top-level requirements and main instrumental features for the three operative modes of ESPRESSO. Abbreviations: VV stays for Vacuum Vessel.

	UHR (1 UT)	HR (1 UT)	MR (4 UTs)
Wavelengths	Blue arm: 380 – 525 nm, Red arm: 525 – 780 nm		
Spectral coverage	Full		
Resolving Power	$\simeq$ 240000	$\simeq$ 120000	$\simeq$ 55000
Aperture on sky	0.5 arcsec	1 arcsec	4 X 1 arcsec
Spectral Sampling	2.7 pix	5.4 pix	10.8 pix
Spatial Sampling	5.4 pix	10.8 pix	22 pix
Sky-subtraction Sim-Reference	Yes mutually exclusive		
Total efficiency	5%	10%	10%
Instrumental RV precision	10 cm/s	10 cm/s	1 m/s
Temperature stabilization control in VV	$<$ 1 mK	$<$ 1 mK	$<$ 1 mK
Pressure stabilization control in VV	$<$ 5x10^{-3} mbar	$<$ 5x10^{-3} mbar	$<$ 5x10^{-3} mbar

4.1.1 Summary of the scientific drivers

The main scientific drivers were defined by ESO (European Southern Observatory) as follows:

- *Measure high-precision RV for search (and characterization) of rocky planets*: as anticipated at the beginning of this chapter, this will be one of the main scientific topics of the next decades in Astronomy; as reported in [88] high RV precision research programs, like HARPS at ESO 3.6 m La Silla telescope, have identified dozens of extrasolar planet with estimated masses below 10 $M_{\oplus}$. In addition the discovery, also supported by statistics on Kepler satellite detections, that half of the solar-like stars in the sky harbor Neptune-mass planets and super-Earths, trigger to push the limit towards the detection of rocky earth-mass planets in the HZ of G, K and M type stars. This can be done with the 10 cm/s precision of ESPRESSO. A careful selection of the target sample drive to focus the observations on the best-suited candidates ([88]): non-active, non-rotating, quiet G to M dwarfs. In the exoplanetary science, another important

task for ESPRESSO will be the follow-up of transiting planets; while many Kepler transit candidates are too faint to be confirmed by RV instruments, other satellites like GAIA, TESS, CHEOPS and hopefully PLATO will provide many new transit candidates. ESPRESSO will be an ideal instrument for spectroscopic follow-up and with its high stability will also play a relevant role for transit spectroscopy and analysis of the light reflected by the exoplanet.

- *Measure the variation of physical constants*: the fundamental constants, such as the fine-structure constant α and the proton-to-electron mass ratio μ, are of great interest in astrophysics because they can be measured accurately by exploiting the quasar spectroscopic technique. Moreover, as reported in [51], the variation of α, according to some theories, is potentially related to the dynamics of dark energy; this is suggested to drive the acceleration in Universe expansion. If the fundamental constants variation can be traced back in space-time, then it would also be possible to trace the history of Universe expansion. The searched variations are very small (in the order of part per million, ppm, as reported in [25]) and the results of different research groups (see the results reported in [88]), coming from different data and measurements done with different instruments and facilities, show discrepancies that are not understood. As explained in [88] a high resolution spectrograph that combines a large collecting area with extreme wavelength precision can provide clarification. ESPRESSO is then expected to provide an increase in the accuracy of the measurement of these two constants by at least one order of magnitude compared to existing instrumentation like VLT/UVES or Keck/HIRES.

- *Analyze the chemical composition of stars in nearby galaxies*: the detailed information of the chemical composition of stellar environments in local galaxies will give useful hints for the understanding of galaxy formation processes and history. Many efforts and important successes have characterized this field but, for dozens of nearby galaxies chemical abundances are available only for few elements in few stars. The high efficiency spectroscopic capabilities of ESPRESSO coupled with one of the largest telescope in the world will give the opportunity to perform relevant steps ahead in this astronomical field, even if major discoveries will come with the instrumentation of the future ELT class.

As remarked in [86] thanks to its efficiency, the high spectral resolution (in particular the $R \simeq 240000$ mode), the extreme radial velocity precision and stability, and the possibility process the light from the 4 Unit Telescopes of the ESO-VLT, it is expected that ESPRESSO will not only be able to fulfill the main scientific objectives, but also open a new parameter space and frontiers in different areas of observational astronomy, briefly listed here below:

- Investigation of metal-poor stars
- Stellar oscillations, asteroseismology
- Diffuse stellar bands in the interstellar medium
- Chemical enrichment of IGM

- Galactic winds and tomography of the IGM
- Chemical properties of proto-galaxies
- Cosmology [3]

4.1.2 Brief Instrument description

ESPRESSO is a fiber-fed, pupil-sliced, two-arm (blue and red), bench-mounted, cross-dispersed echelle spectrograph placed in vacuum and in a thermally stabilized environment for very high metrological stability. Mechanical (and optical) stability is ensured since no moving parts are foreseen inside the spectrograph. It will be installed in the underground Combined Coudé Laboratory (CCL) of the VLT, and will be linked to the four Unit Telescopes (UT) through four optical paths called Coudé Trains, shown in Fig.4.1. Thanks to these optical links and to its Front-End

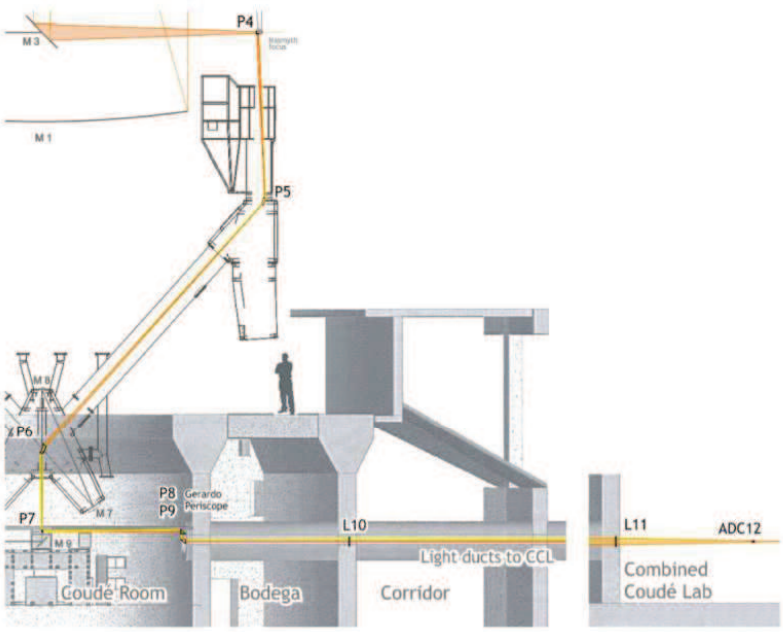

Figure 4.1: Coudé train of ESPRESSO and optical path through the telescope and the tunnels. Figure taken from [74].

(FEU) subsystem, see Fig.4.2, ESPRESSO will be able to collect the light of any UT independently or together, allowing several different configurations among which a 4-UT mode which will make it the first instrument mounted on a 16-m equivalent telescope ([74]). ESPRESSO is designed with a dual fiber system: the first is devoted to transfer the celestial object light, while the second can be used either to record the

[3] as stated in [88] ESPRESSO probably will not be sufficiently sensitive in measuring the extremely tiny signal related to the Sandage test, which aims to observe in the Universe expansion "real-time" by measuring the redshift drift-rate (dz/dt) of cosmologically distant objects; however it will represent an important step forward in setting the scene for the next generation of high resolution spectrographs at the E-ELTs.

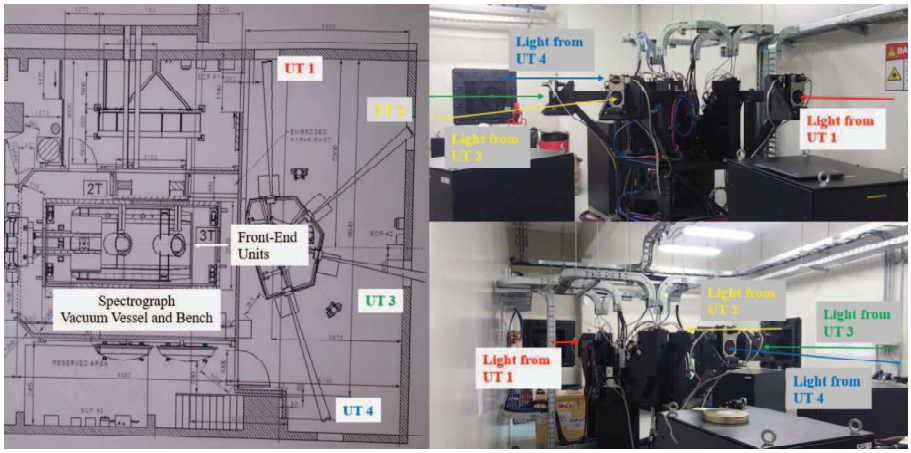

Figure 4.2: ESPRESSO Front-End subsystem in the Combined Coudè Laboratory (CCL) room.

sky or to monitor the spectrograph shifts by recording a simultaneous reference source. Three different pairs of fiber will feed the spectrograph, depending on the observing mode (1UT, 4 UTs) and the related selected resolving power (High Resolution R $\simeq$ 120000, Ultra High Resolution R $\simeq$ 240000 and Medium Resolution R $\simeq$ 55000); a schematic is depicted in Fig.4.3. The full spectral coverage is from 380 to 780 nm,

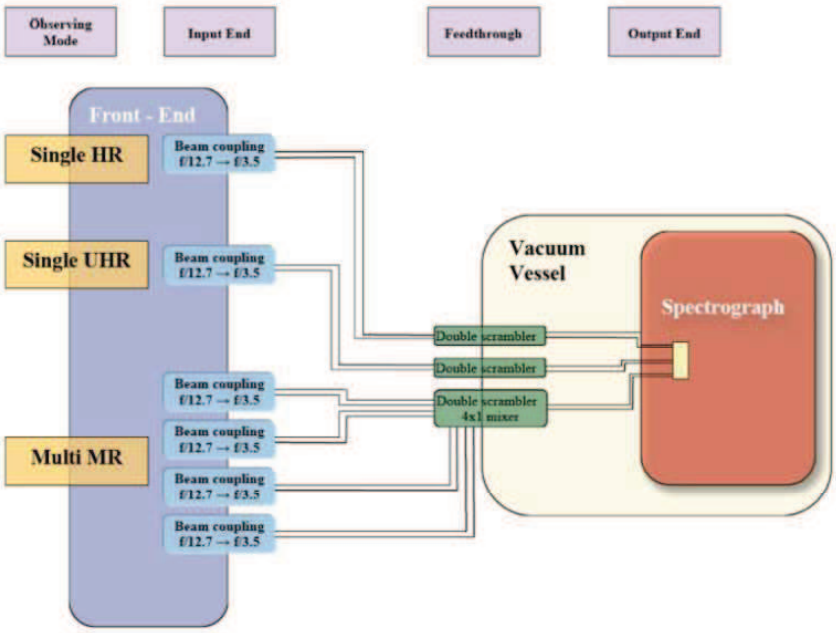

Figure 4.3: Schematic of the different feed-trough for the operative modes. From [88]

with a cut-off between the two arms at about 525 nm. The spectrograph optical layout is shown in Fig.4.4; the optical configuration is the white pupil layout (see [8] for details) with an off-plane echelle grating angle of 1°. The light from the slicer unit

(the APSU described here after) is collimated on the 1.2 x 0.2 m echelle grating mosaic (R4 grating with groove density of 31.6 lines/mm) by the main collimator. This is a large off-axis portion of a parabolic mirror and it is the largest optical element of the instrument with a clear aperture of about 700 x 380 mm. In the double pass the main collimator collects the dispersed light from the grating towards the transfer optics. A dichroic splits the light in the blue and red arm. In the blue arm a field lens compensates for some main collimator field curvature aberrations and in combination with the blue transfer collimator a white pupil is projected onto the anamorphic cross disperser. The beam coming from the transfer collimator has a size of about 150 x 100 mm. In the red arm a similar optical layout has the same function, with the difference that a field mirror is used instead of a field lens. In both arms the diffraction orders are cross-dispersed by a grism based onto a volume-phase holographic (VPH) grating, coupled with an entrance prism to control final anamorphism of the cross-disperser. VPH grating technology is selected for cross dispersion because of its high efficiency in a quite large wavelength band. A 1.5X anamorphic factor has been chosen for the cross-dispersers; in this way, each camera will see a square 150 x 150 mm pupil. The two cameras have a similar optical design composed by a cemented doublet and two lenses, with two aspherical surfaces; different glasses are used in the two arms because of the different wavelength band.

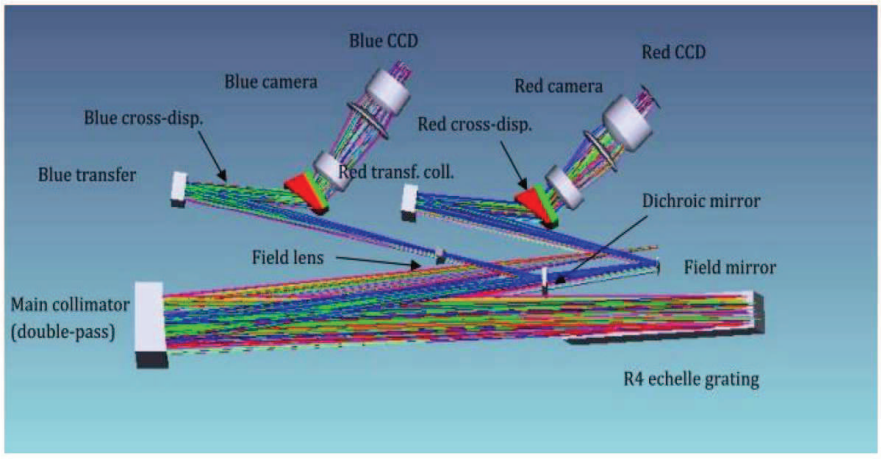

Figure 4.4: ESPRESSO Optical Layout; the different components are labeled and the light beam propagating in the spectrograph is shown.

The high resolving power is achieved thanks to the presence of the Anamorphic Pupil Slicer Unit (APSU, [29] and [44]) at the spectrograph entrance. The pupil slicer increases the resolving power of the spectrograph effectively decreasing slit-width; the slicing of the pupil allow to manage the $A - \Omega$ of the 8 m telescope in order to obtain the required resolving power while keeping the size of optical elements within manufacturing capabilities. At the optical fibers exit a field doublet is glued; this field lens collects the F/3.5 light beam from the fibers and realizes a pupil after its vertex. In this location an annular pick-off mirror is placed to reflect part of the light (the light-rays exiting from the fibers at F/2.5, due to the focal ratio degradation phenomenon) towards the exposure-meter. After the collimator,

two cylindrical objective with different focal length (1:3) introduce anamorphism. An elliptic pupil 30 X 10 mm is realized. Pupil slicing is done with two (almost) achromatic identical couple of prisms likely configured as Risley prisms pair. At the APSU focal plane, which is the effective spectrograph entrance, a multi-mini-prism system (called MMP, composed by 6 pairs for a total of 12 mini-prisms, [29] and [32]) is placed to differently fold each field of the APSU with the final aim of proper illuminating the echelle grating. Each observing modes uses two mini-prism pairs, one for the sky/reference light and one for the scientific object light. The two mini-prisms of each pair are associated to the two pupil slices. The optical layout of the APSU unit is shown in Fig.4.5; while Fig.4.6 gives a detail of the multi-mini-prisms system glued on its silica basement.

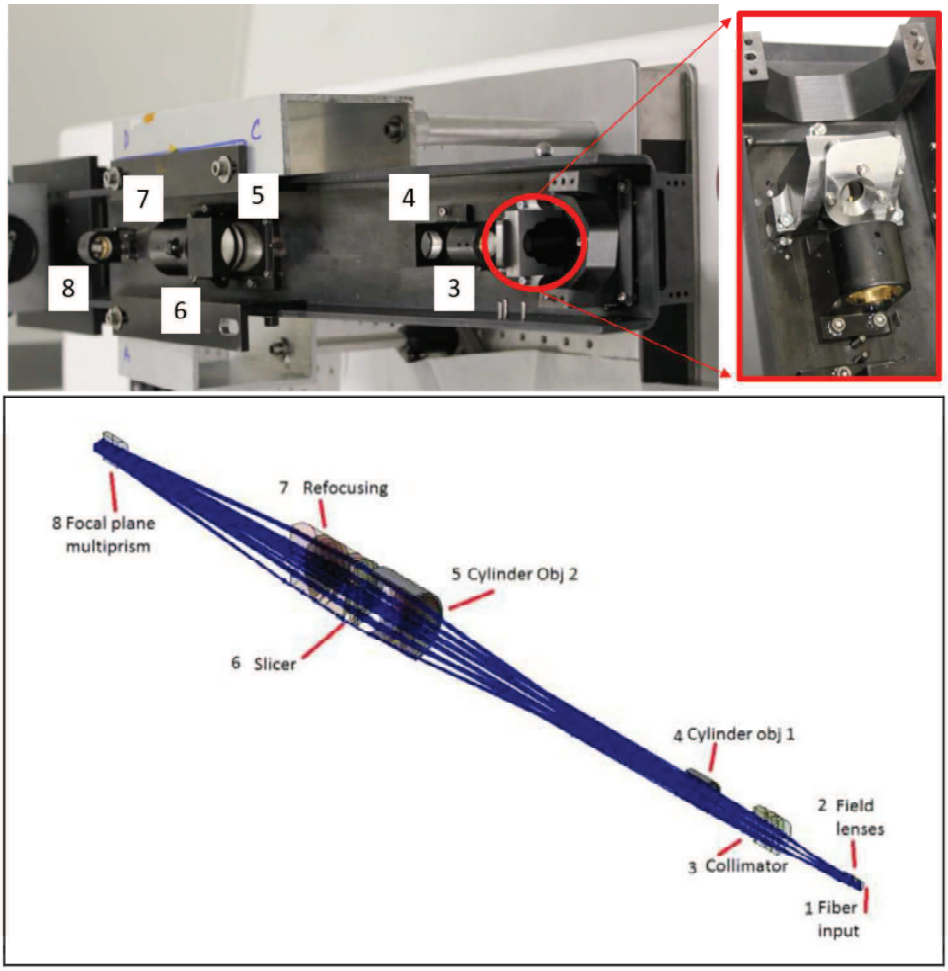

Figure 4.5: Anamorphic Pupil Slicer Unit (APSU). Bottom: Optical Layout. Top left: real optomechanical assembly. Top right. View of the pick-off mirror.

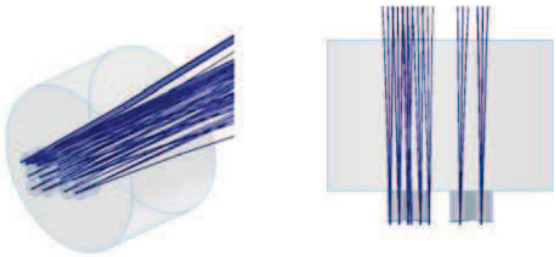

Figure 4.6: Detailed views of the Multi-Mini-Prisms unit at the focal plane of the APSU.

4.2 My contribution to ESPRESSO: analysis and optimization, from modeling to hardware implementation

Instrument modeling through ray-tracing software has been used for component optimization, instrument integration verification with the ultimate goal of achieving the best instrument and scientific performances. For example the multi-mini-prisms (MMP) position definition, described in subsection 4.2.1, was done to maximize the instrument throughput with the purpose of SNR optimization. The same aim drives the half-pupils light intensity balancing, within 10%, achieved with the proper alignment of some optical elements inside the APSU presented in subsection 4.2.2. A sensitivity analysis was exploited for the spectral format centering on the blue ccd, see subsection 4.2.3, which allows the proper behavior of the DRS pipeline in the effectiveness of order tracing and extraction. The image optical quality has been optimize to meet the spectral resolution requirement, both recovering the proper component alignment in the blue arm (see subsection 4.2.4) and re-optimizing the optical prescription of the camera in the red (see subsection 4.2.5)

4.2.1 Fiber-Link analysis and Mini-Prisms position optimization

One of the activities done during the integration and testing of the different parts of the spectrometer was the gluing of the field lens on the fiber link output end at the entrance of the APSU. Images of of the glued group were taken with an optical set-up, shown in Fig.4.7, to verify the gluing process.

Fig.4.8 and Fig.4.9 show the glued group as seen by the test set-up camera and as seen from the spectrograph main collimator.

The images have been analyzed in order to verify, in addition to the gluing process, the positioning errors of the optical fibers within the accuracy tolerance of 5 um. An error in the position of the upper input fiber (called Fiber-A) in the UHR mode was enlighten. The image metrology has been calibrated on the distance between of the two fiber holder in the HR mode which is 940 um by design, through which the estimated Fiber-A center position is shifted of 25 μm up (see Fig.4.10). The same verification has been done for the MR fibers (see Fig.4.11) positioning; they resulted to be within the 5 μm tolerance. The images analysis also shows that this fiber link has a discrepancy with the one of the nominal design: the MR and HR fibers have been

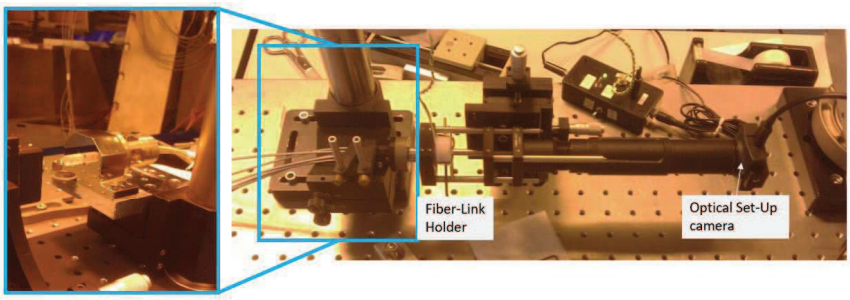

Figure 4.7: Optical set-up built for the verification of the field lens gluing process on the fiber-link output-end. *Left*: zoom view of the field lens and fiber holder group. *Right*: Optical set-up mounted on an optical bench.

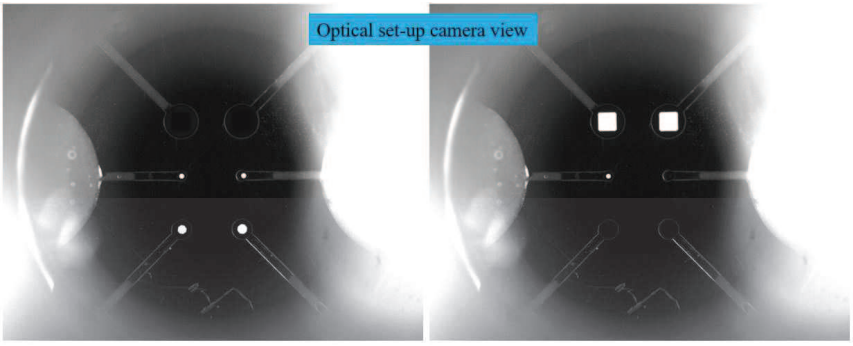

Figure 4.8: Test set-up camera view of the APSU field lens glued on the fiber-holder. *Left*: the HR and UHR fibers are illuminated; *Right*: the MR fibers and Fiber-B of UHR mode are illuminated

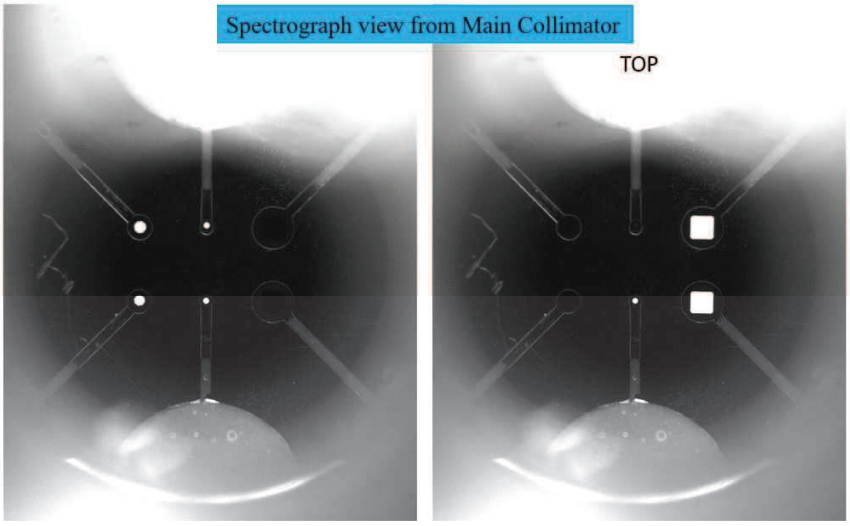

Figure 4.9: Spectrograph main collimator view of the APSU field lens glued on the fiber-holder. *Left*: the HR and UHR fibers are illuminated; *Right*: the MR fibers and Fiber-B of UHR mode are illuminated.

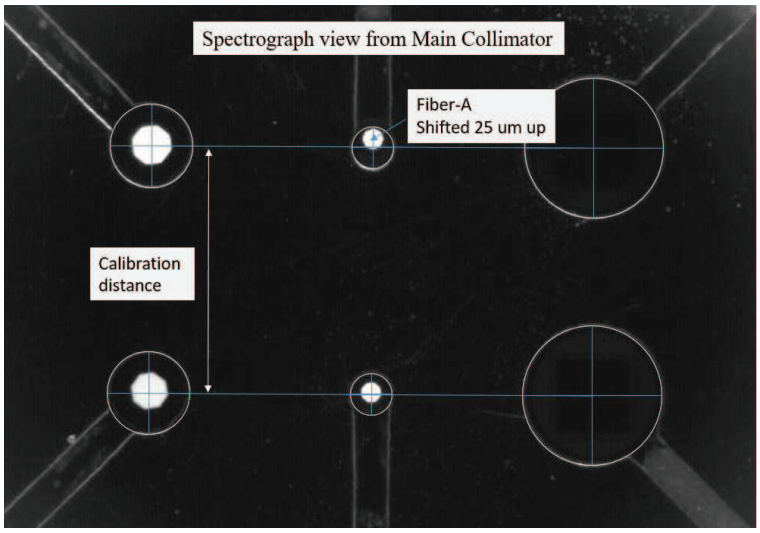

Figure 4.10: Analysis of the spectrograph main collimator view of the APSU field lens glued on the fiber-holder; the HR and UHR fibers are illuminated.

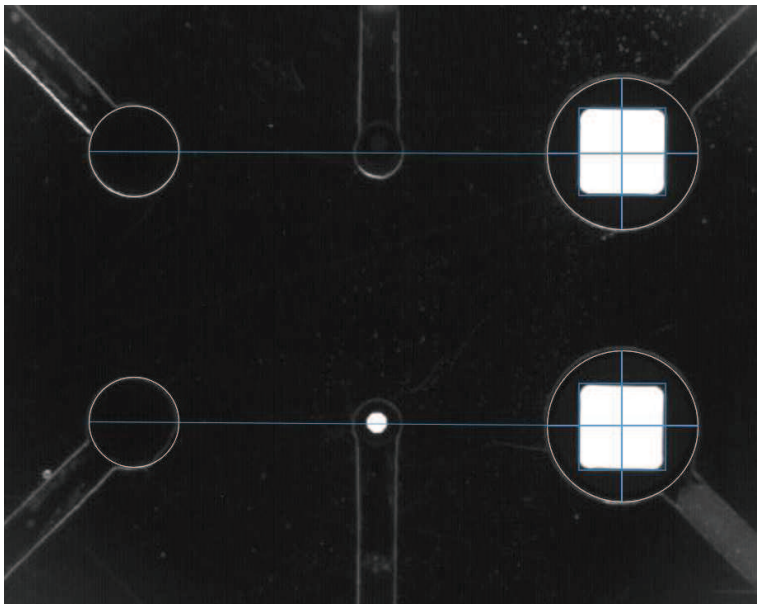

Figure 4.11: Analysis of the spectrograph main collimator view of the APSU field lens glued on the fiber-holder; the MR fibers and the Fibre-B og the UHR mode are illuminated.

inverted each other. In order to compensate this issue was necessary to re-optimize the mini-prisms positions. The Fiber-A shift must be taken into consideration in the new mini-prisms positioning definition in order to avoid vignetting which can result in efficiency loss, and consequent SNR reduction. The degradation of the SNR is crucial, especially for the science case topic which this Thesis refers to. In particular, when SNR is poor not only the determination of the Radial Velocity with proper

accuracy is put in danger, but also the contrast between the detectable signal of the planet and its host star. This kind of consideration is particularly relevant for transmission spectroscopy study where the achievable contrast between the planet's features and host star light is a key parameter to go in deep in the determination of chemical abundances and physical state of the upper layer of the exo-atmosphere. Moreover, it is important to underline that the possible throughput losses should be minimized in the design and optimization of the different components of such a complex instrument. This aspect is relevant since the possible additional losses which can be introduced in the alignment phase could sum up and strongly reduce the total instrument efficiency. The Fiber link is then modeled by the fiber center and the position of edge fields, considering that the min-prisms 3, 9, 4, 10 that before were related to the HR mode fibers, now are related to the MR fibers; on the same way the mini-prisms 5, 11, 6, 12 before related to MR fibers now are related to HR fibers. The positions of the different mini-prisms has been then optimized taking into account three constraints: the light-trough efficiency, the minimum separation between adjacent mini-prisms for the feasibility of positioning-gluing process and the centering of the beam footprint on the UHR and HR mini-prisms to avoid edge scattering phenomena. The optimization result, presented in Fig.4.12, shows the 12 mini-prisms base surface (the one in contact with the silica plate) and the light-rays from five edge-points of the different fibers. As can be noticed in the figure the MR prisms, those in the 3rd column, have some edge-points of their fields at the edges of their base surface and the one at top-right (mini-prism id = P10) has a point that is vignetted; this is due to the constraint on the minimum separation between adjacent mini-prisms.

The verification of the three constraints listed above is reported in the following. The

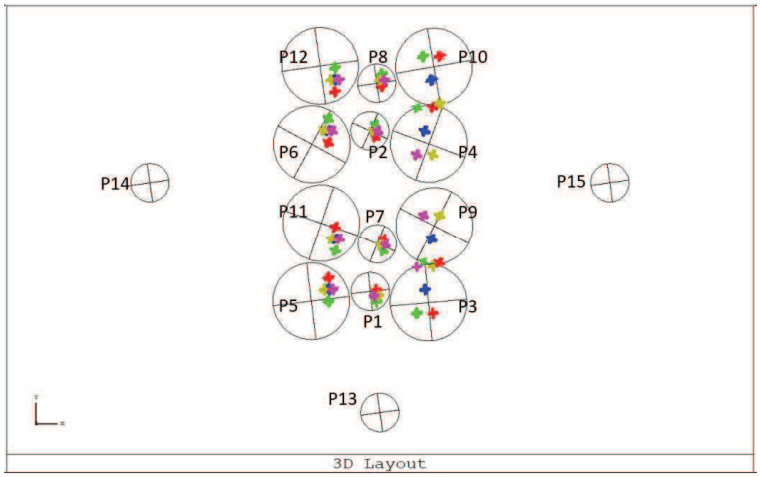

Figure 4.12: Result of the optimization of the mini-prisms position. Other 3 mini-prism are shown; they have been exploited to have reference in the alignment of the MMP unit in its mounting support.

minimum distances between the different mini-prisms have been optimized to take into account the requirement on their relative positions for the gluing process: this

is $> 40\mu m$, except for the MR mini-prisms which is $> 10\mu m$. [4] The verification on the minimum distance can be seen from Fig.4.13, which reports the computation of the adjacent mini-prisms edges distance done with Zemax. In Fig.4.14 the MMP are

P1 – P3	47.4172030
P1 – P5	60.1602482
P3 – P9	15.5892439
P5 – P11	56.5018843
P7 – P11	56.6630978
P7 – P9	62.3699946
P2 – P4	77.0859203
P2 – P6	54.9035340
P4 – P10	14.1995929
P6 – P12	51.2983693
P8 – P12	46.9001261
P8 – P10	50.8062419

Figure 4.13: Adjacent mini-prisms minimum edge distance verification done with Zemax.

shown with a radius respectively of 0.35 mm instead of 0.5 mm and 0.8 mm instead of 1 mm. They are overlapped to the beam footprint, to verify the safety margin from edges and to avoid the possible edges scattering phenomena. As it is clear from the

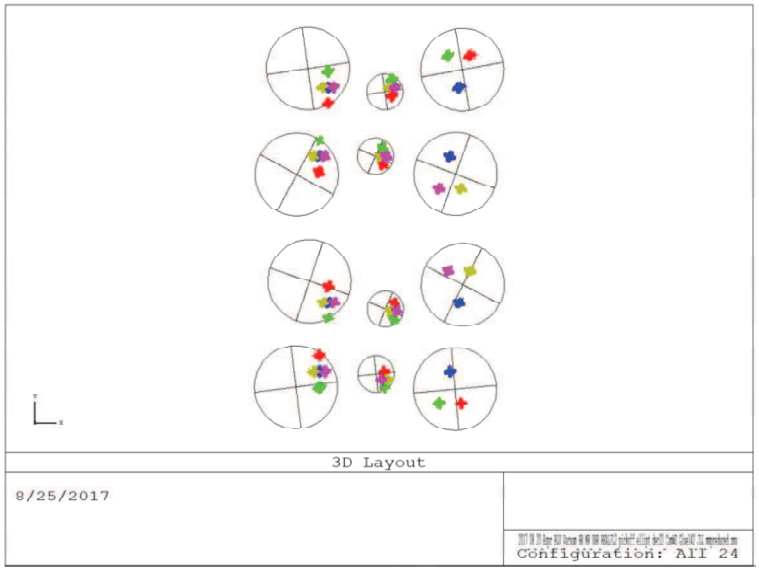

Figure 4.14: Footprint on the MMP base surface, with mini-prisms reduced radius; the UHR with a radius of 0.35 mm instead of 0.5 mm and the others with a radius of 0.8 mm instead of 1 mm. This allows to verify that the beams for the UHR and HR modes are safely distant from the edges.

MMP positioning optimization shown above, the MR prisms suffer from vignetting

[4] These requirements in the mini-prism distances were derived in the analysis and definition of the gluing process.

due to the constraint on the minimum separation between adjacent mini-prisms. The throughput for the MR mini-prisms has been evaluated with a ray tracing modeling tool, built-in in Zemax, which computes the geometric image on the prisms base surface. This allows to estimate the losses at the edges of the MR prisms, which are shown from Fig.4.15 to Fig.4.18. In these figures it is clearly visible the cut that

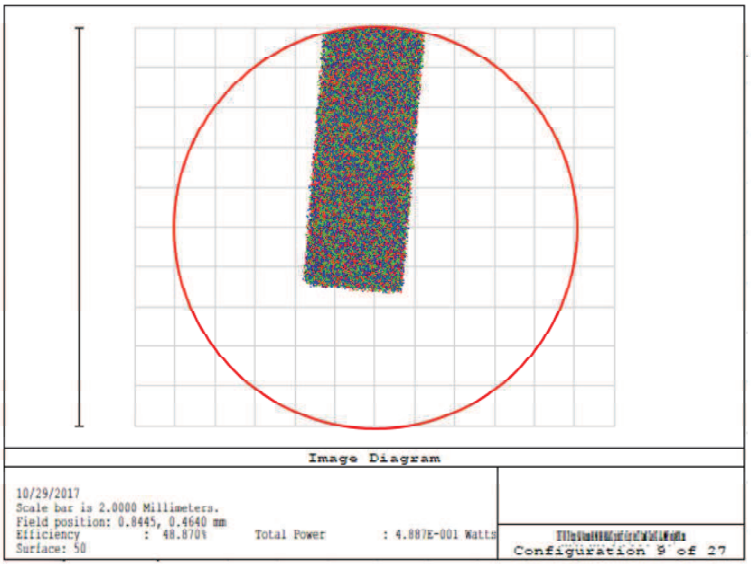

Figure 4.15: Geometric Image Analysis on the base surface of mini-prism P3.

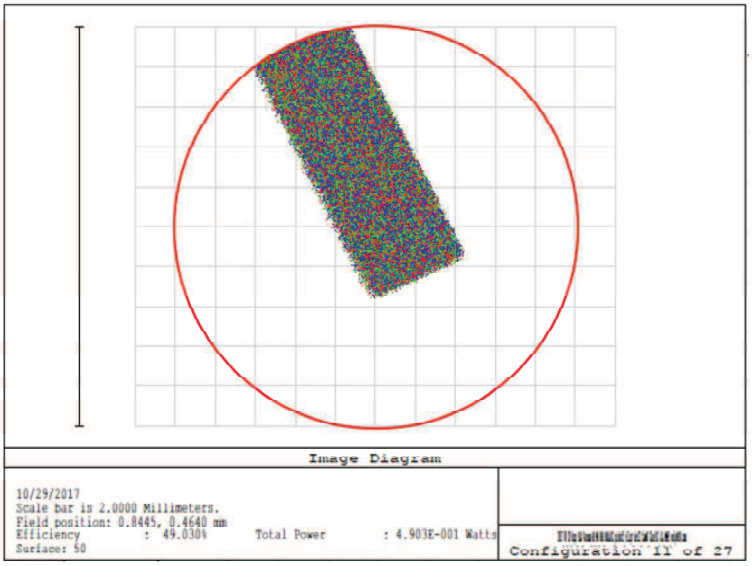

Figure 4.16: Geometric Image Analysis on the base surface of mini-prism P9.

the prisms base induces at the edge of the MR fibers image; the associated losses can be derived from the ray-trough computed with the mentioned analysis tool, and

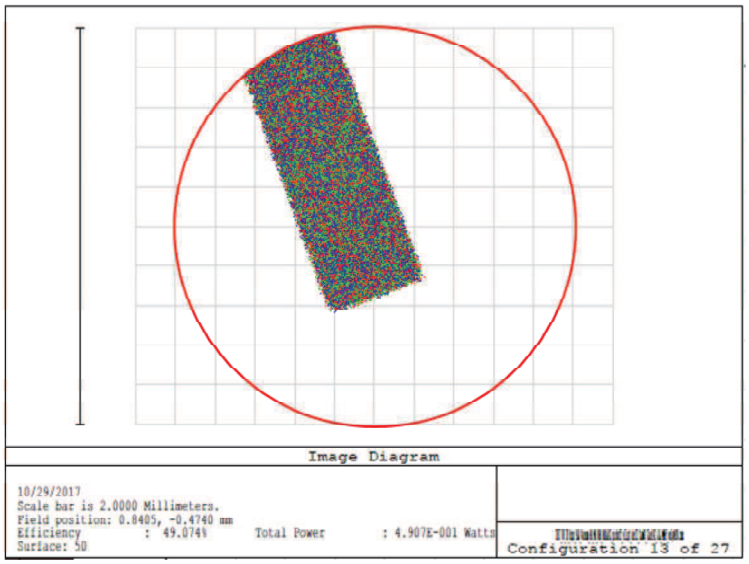

Figure 4.17: Geometric Image Analysis on the base surface of mini-prism P4.

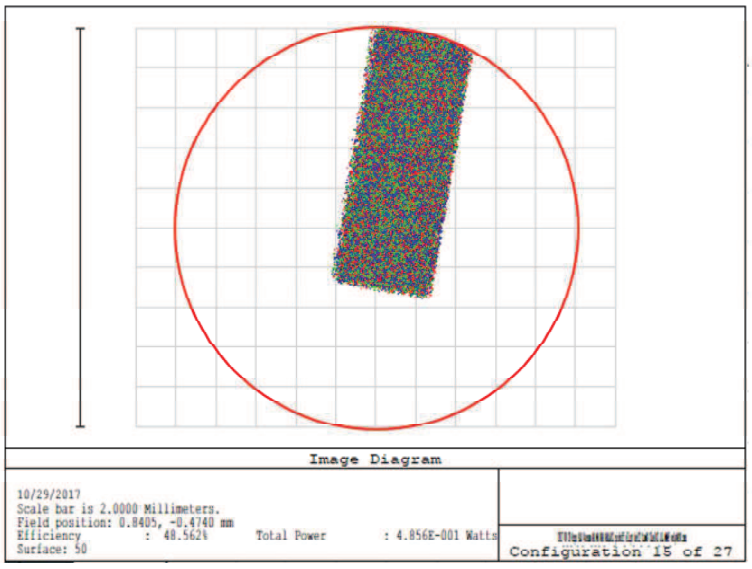

Figure 4.18: Geometric Image Analysis on the base surface of mini-prism P10.

indicated in the figures as "Efficiency", as the complementary to 50%. The reason is because each mini-prism collect the light of half of the pupil. These ray-tracing simulations has been set to take into account the geometrical light propagation from the ASPU input (the field lens which collect the F/3.5 light exiting from the optical fibers) to APSU focal plane at the MMP system; so no losses due to glass coatings and transmission are simulated and computed. During the APSU installation and alignment at VLT the throughput was measured with a power-meter and injecting a

light into the MR fibers; the intensity measures were taken just before and after the MR mini-prisms. The measured losses due to the actual MR mini-prisms alignment is about 3% for P3 and P9 (related to the so-called Fiber-A) and about 4% for P4 and P10 (related to the so-called Fiber-B).

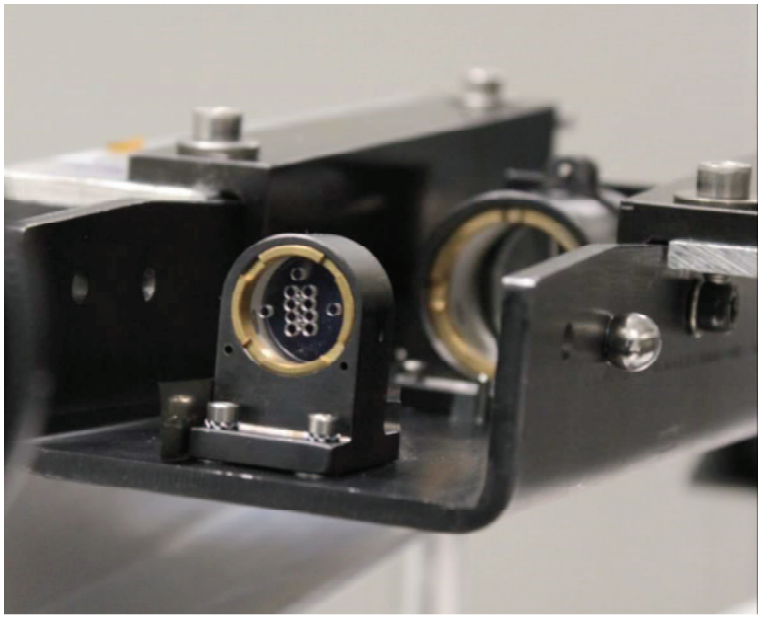

Figure 4.19: MMP re-installation and alignment at Paranal for the final APSU integration in the spectrograph.

4.2.2 Pick-off mirror and pupil-slicer alignment: balancing of the half-slices relative flux

During different alignment and integration phases a problem of different illumination levels of the half slices and problem of relative shift of the half slice images on the detector were noted. The difference in half-slices illumination was more than 20% and the relative images centroid shift was about 2.5 pixels. The first issue would traduce in a different flux read by the detector, for a given exposure time, in the images of the half-slices, which results in a non optimal extraction of the signal from the data reduction pipeline. This in fact could traduce either in a non optimized SNR for one half-fiber when the other one is maximized, or in a saturation of the half-slice with higher flux when the flux of the other one is maximized. The half-slices images shift traduces in a non-optimize data reduction and binning of the signal (for both fibers) which could result in a loss of resolution. As order of magnitude, this images shift would result in a loss of spectral resolution of $\approx 12.5\%$, thus having a relevant negative impact on the instrument performance and scientific capabilities.

Since for the half slices beams there is no differential vignetting in the spectrograph part of the instrument, the first problem is most probably due to the pick-off mirror of the APSU (described in Fig.4.5), which is could be not properly centered on the beam. The second problem could be due to a not correct clock alignment of the slicer

element inside the APSU (see again Fig.4.5), which projects the fiber images on the APSU focal plane and on the spectrograph ccd with a relative shift higher than the one foreseen in the design.

The pick-off mirror has been then shimmed and centered to equalize the slices flux. The slicer has been on the other hand clock-corrected to get the nominal alignment and allow to have the required relative shift of images.

After the re-focuser mount, images were taken placing millimeter paper as a reference to be used for in the evaluation of half-pupils decentering and clock; see Fig.4.20. The image in Fig.4.21 shows the half pupils decentering before the pick-off mirror and

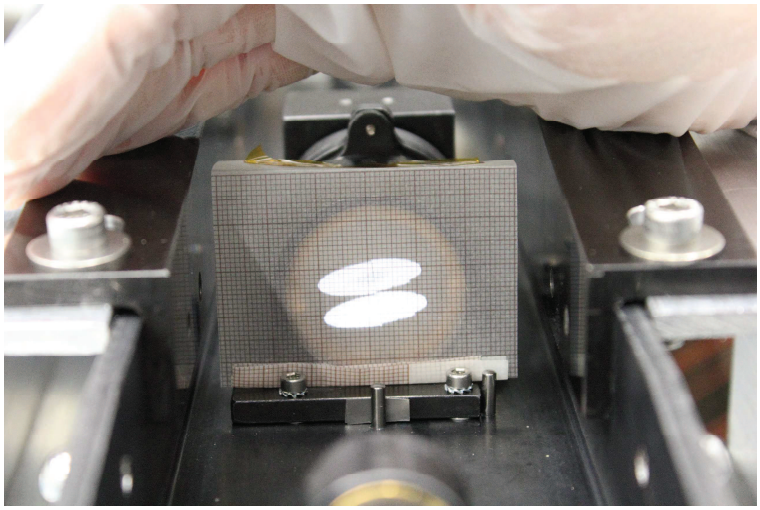

Figure 4.20: Half pupils, for both fibers, beam projection just after the APSU refocuser.

slicer re-alignment. To be properly aligned, the image has to be rotated of 9 deg instead of the nominal 8 deg, proving the slicer clock misalignment; the rotation can be seen looking the rotation of the millimeter-paper lines and the vertical blue line. The yellow ellipses and the blue-square prove pupils decentering of about 1 mm. While Fig.4.22 shows the half pupils re-centering after the pick-off mirror and slicer re-alignment. The image is now rotated of the nominal 8 deg. The yellow ellipses now fit well with both half-slices and the blue-square shows a minimal residual decentering estimated to be lower than 0.2 mm. The vertical relative shift of the half pupils is due to the fact that images have been taken just after the re-focuser mount and its effect of beam deviation for the projection on the APSU focal plane is already visible; a check with Zemax is shown in Fig.4.23. The final alignment of the APSU at Paranal for the integration on the spectrograph at VLT is shown in Fig.4.24. The half pupil balanced illumination was checked both in the alignment tests before the final integration at VLT and after the alignment and integration done at the CCL in the VLT complex at Paranal. In Fig.4.25 an example of the half pupils illumination at the center of the red detector is shown; as can be seen from the values reported the images of the half pupils are properly balanced, with a difference lower than 10%. This check was done also in other detector locations, confirming the results shown in the image. The images relative shift in the main dispersion direction was checked to be within one pixel.

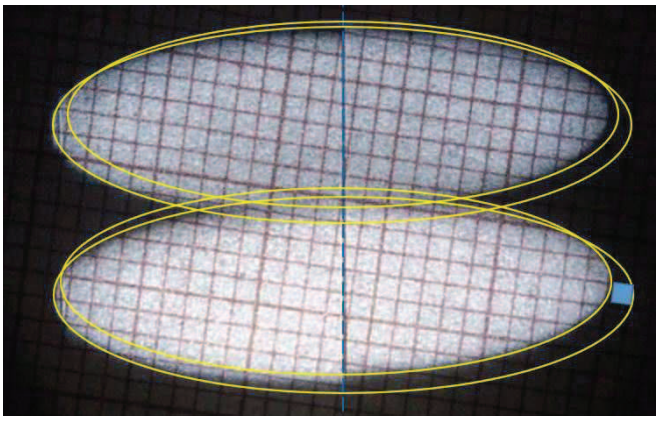

Figure 4.21: Half pupils, for both fibers, beam projection after the APSU refocuser before the correction. This zoom-in image allows to see the pupil decentering, the blue square, evaluated using the millimiter paper.

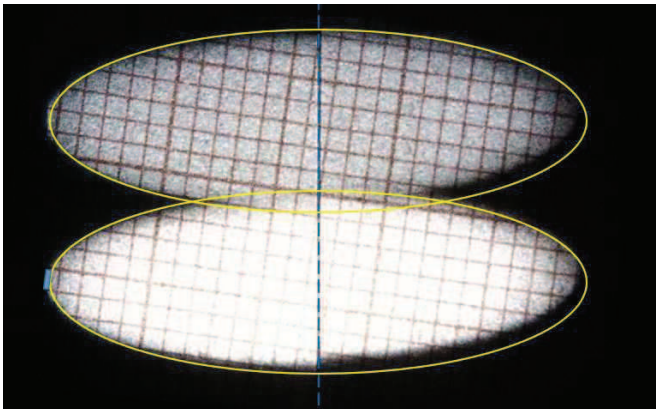

Figure 4.22: Half pupils, for both fibers, beam projection after the APSU refocuser and after the correction. This zoom-in image allows to see the pupil centering.

4.2.3 Transfer collimator tilt: Centering of the echellogram

Due to a misalignment of the camera in the blue arm, the spectral format on the detector was not centered in the main dispersion direction influencing the proper behavior of the DRS pipeline in the effectiveness of order tracing and extraction. Moreover, it should be kept in mind that whenever possible, the image of the echellogram should be arranged as much as possible to the center of the detector where the sensitivity of the detector is maximized and contribution of space-variant noises (like the Dark Current for some family of CCD) is less. This was noted early-on because in the blue arm the field lens was designed to collect only the free spectral range, and thus the wavelength which would fall on the detector edges are vignetted. The echellogram was properly re-centered exploiting the transfer collimator, before the anamorphic cross disperser to have the appropriate condition for the best development of the pipeline, with the goal of having the most effective data reduction for the maximization of the extracted signal quality from scientific on-sky observation.

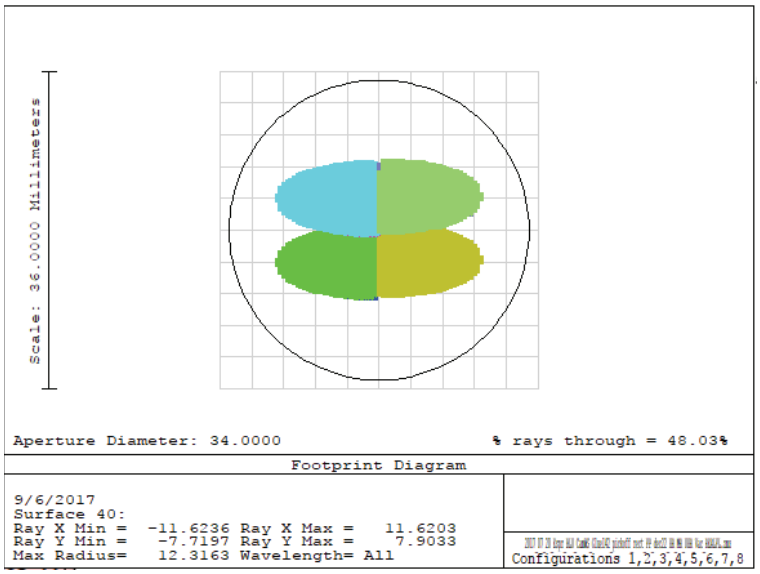

Figure 4.23: Half pupils, for both fibers, beam projection after the APSU refocuser; Zemax simulation.

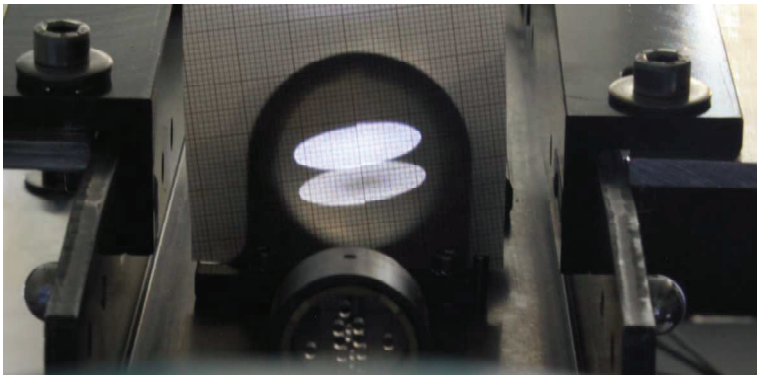

Figure 4.24: Half pupils, for both fibers, beam projection after the APSU refocuser. Image taken after the ASPU alignment for the final integration at VLT.

A sensitivity analysis was performed to set the alignment accuracy of the different optical elements, with respect of the variation of wavelength position on the detector, the image quality and the throughput variation. For this purpose a sensitivity analysis tool (see [44] for a detailed description) was developed combining the flexibility of MATLAB in managing and representation of the large amount of ray-trace data generated by Zemax. This analysis was used for the evaluation of the required transfer collimator tilt of 10 arcmin around its vertical axis. The ray-tracing spectrograph simulations also allowed to confirm the expected correction on the camera mounting alignment of 20 arcmin. This value is expected since the transfer collimator works in reflection and then to recover a general misalignment δ on the camera along the main dispersion direction, where the cross disperser has no effects, a tilt of $\delta/2$ is necessary on the transfer collimator. Here below the ray-tracing simulated spectral format for

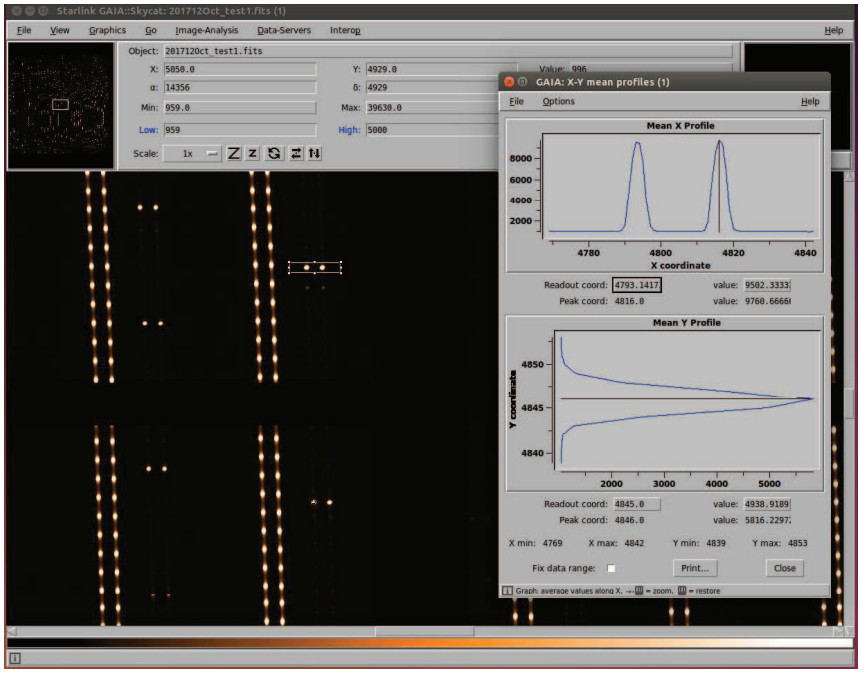

Figure 4.25: Example of the light distribution in the image of the two slices of the Fiber-A in the center of the CCD in the red-arm. The panel for the mean x profile (which actually is the cross dispersion direction) shows that they are properly balanced, with a difference well lower than 10% as can be seen from the values related to the Readout coordinate and the peak coordinate (related to the peak of the left slice and the one on the right respectively)

.

the nominal and actual conditions respectively for the HR mode.

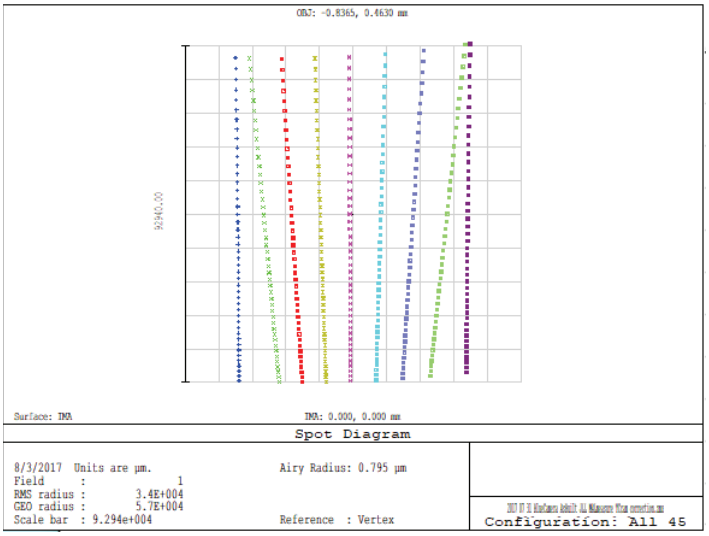

Figure 4.26: ESPRESSO blue arm echellogram in the HR mode. Ray-tracing simulations with camera and transfer collimator in the nominal alignment condition.

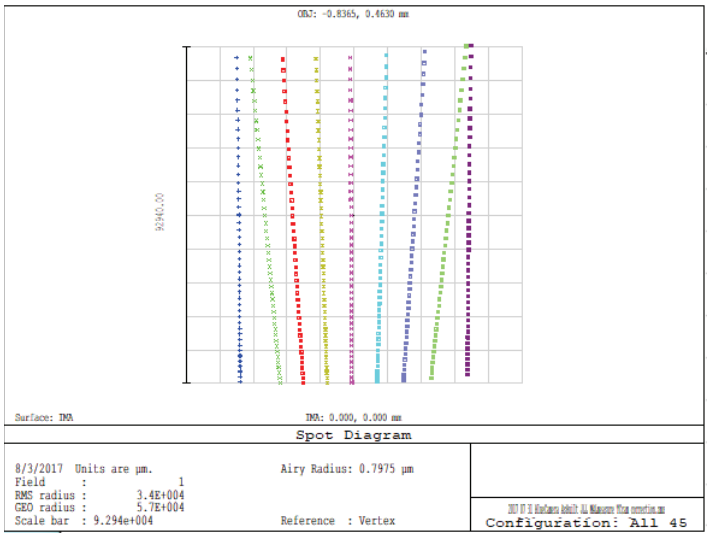

Figure 4.27: ESPRESSO blue arm echellogram in the HR mode. Ray-tracing simulations with camera in the measured alignment condition and transfer collimator tilted around its vertical axis to recenter the spectral format along the main dispersion.

In Fig.4.28, one the blue arm raw frames of the blue echellogram taken after the correction is shown; for both fibers the source is a Thorium-Argon lamp.

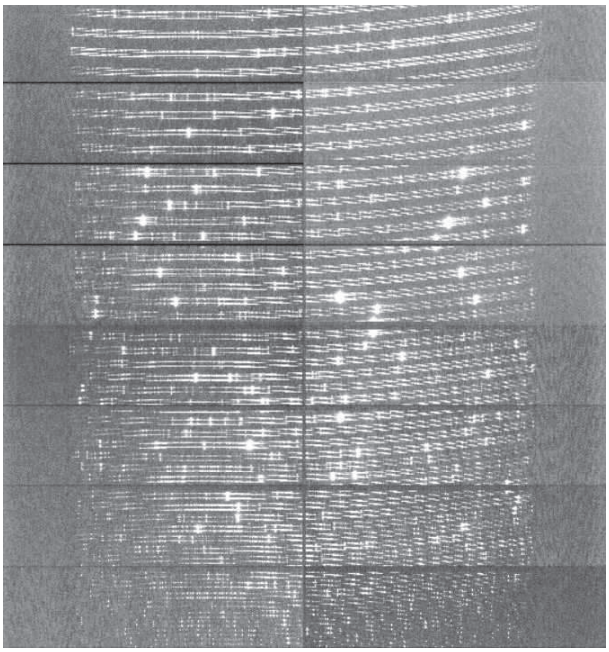

Figure 4.28: ESPRESSO blue arm echellogram in the HR mode. Raw frame taken during the alignment and integration phase. The source for both fibers is the Thorium-Argon lamp.

4.2.4 Dichroic correction for optical quality requirements

Optical quality test on the UHR mode showed a degradation of the RMS spot and Enslitted Energy in the main dispersion direction towards the red wavelengths in each order of the blue chip; this optical quality degradation results in a loss resolving power capability translating in a not acceptable instrument resolution reduction in this Ultra-High-Resolution operative mode. This condition was obtained with through-focus tests moving the APSU along the optical axis with respect the spectrograph bench; according to its position the observed variation in the optical quality suggested a tilt in the focal plane: a good image quality in the blue and central part of the each orders corresponded to a worse quality in the red part, while a good image quality in the red part of the each orders corresponded to a worse quality in the central and blue part. To get a good optical quality in the blue and in the central part of each order the APSU had to be moved 4.9 mm far from the spectrograph, increasing the optical path and thus meaning that some other optical element should be not in its nominal alignment position along the optical axis. Combining detailed inspection inside the spectrometer and ray-tracing simulations we identified the dichroic could be not properly aligned in its nominal position; these simulations have been exploited to evaluate the dichroic misalignment correspondent to the measured APSU position. A dichroic misalignment of 2.2 mm (towards the main collimator) shows a variation of the enslitted energy in the main dispersion direction comparable to what observed in the frames; this is shown in Fig.4.29 to Fig.4.31. This misalignment also gives no variation in the cross-dispersion variation in accordance with observed frames. The

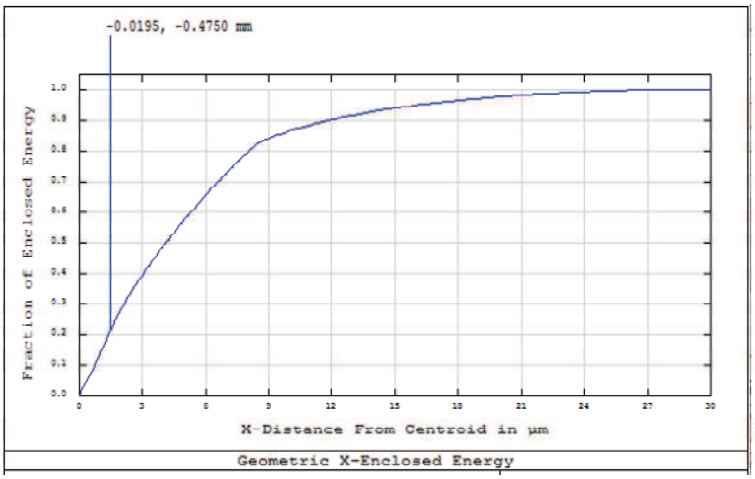

Figure 4.29: Enslitted energy in the main dispersion for a spectral resolution element in the blue part of diffraction orders. As can be seen the 90% of Enslitted energy is related to a radius of about 10 μm.

dichroic position was corrected by a 2.2 mm shift far from the main collimator; the result is a corrected image quality in the whole echellogram.

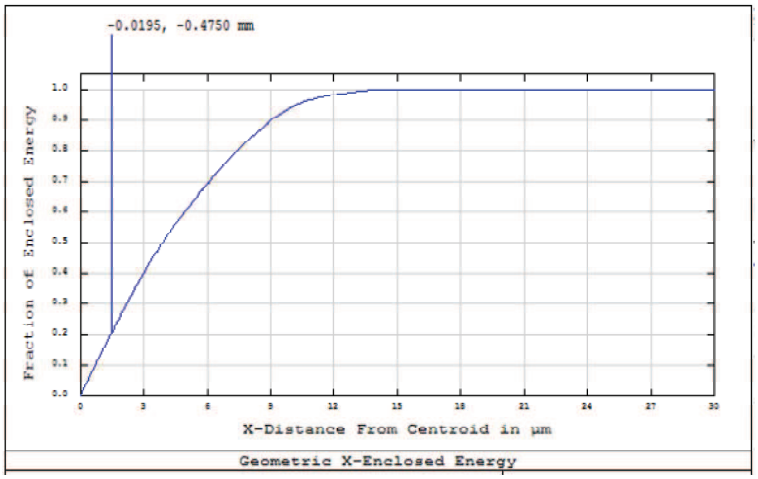

Figure 4.30: Enslitted energy in the main dispersion for a spectral resolution element in the central part of diffraction orders. As can be seen the 90% of Enslitted energy is related to a radius of about 10 μm.

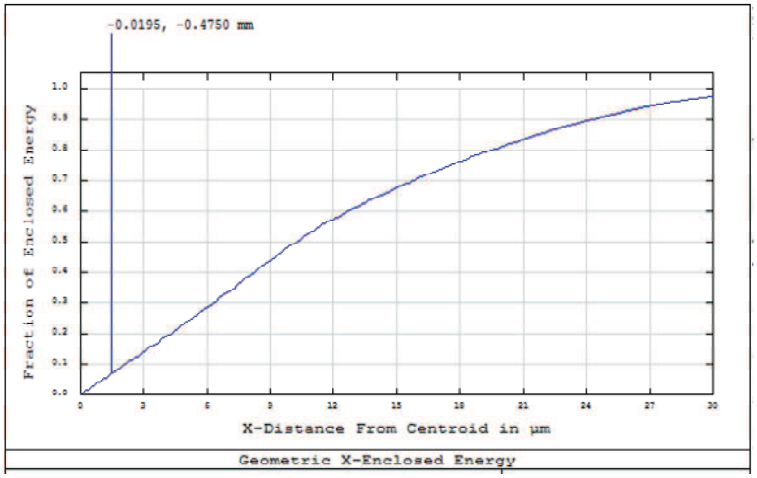

Figure 4.31: Enslitted energy in the main dispersion for a spectral resolution element in the red part of diffraction orders. As can be seen the 90% of Enslitted energy is related to a radius of about 24 μm. This results in a relevant loss of resolving power for the red part of each diffracted order.

4.2.5 Red arm camera optimization

The red camera re-optimization has been performed after the manufacturing of some optical elements of the camera itself; as explained in the brief ESPRESSO instrument description of section 4.1.2, the red camera is composed by a cemented doublet, named L1-L2, and two single lenses, which are L3 and the field lens L4. The L3-lens has been re-optimized once the as-built data concerning the L1-L2 doublet and the camera field-lens L4 were available. This operation is fundamental to guarantee that the final built camera projects the image of the different spectral resolution elements with an optical quality such that their full width half maximum

(FWHM) meets the requirements on the spectral sampling (which is directly related to the requirements on the Resolving power in the different operative modes). The optimization parameters were the radius of curvature of both lens surfaces and the aspheric parameter of the aspheric front surface, while the lens thickness and its position inside the camera are fixed by mechanical mounting constraints. The optimization has been done with the ray-tracing software Zemax by considering the RMS spot radius of the different fields and for 9 different wavelengths in each diffraction order and the L3 position constraint in the merit function. To check the optimization result, the enslitted energy diameter in the main dispersion was computed for all the wavelengths in all the three operative modes of ESPRESSO. Since Zemax gives the possibility to simulated only one order at a time and not all the orders simultaneously a tool has been developed in MATLAB to call and acquire Zemax simulations results. The tools exploits the MZDDE toolbox for MATLAB, through which the data flow between the two software is established. The 50%, 80% and 90% enslitted energy performance is plotted in Fig.4.32 to Fig.4.34.

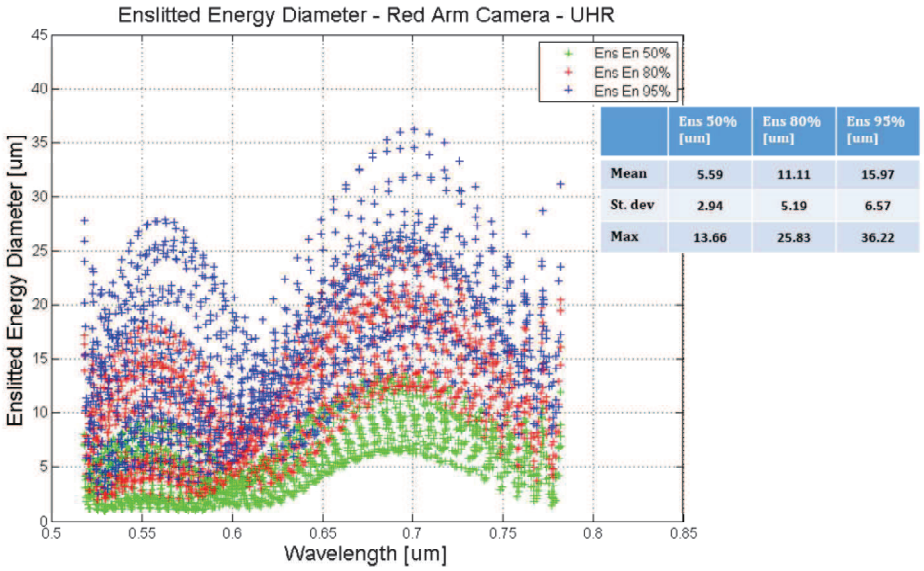

	Ens 50% [um]	Ens 80% [um]	Ens 95% [um]
Mean	5.59	11.11	15.97
St. dev	2.94	5.19	6.57
Max	13.66	25.83	36.22

Figure 4.32: Enslitted energy distribution in main dispersion direction for ESPRESSO red arm in the UHR mode. Attached to the figure there is a tabular summary of the statistics for the mean, standard deviation and maximum of the 50%, 80% and 90% enslitted energy diameter in main dispersion.

The verification of the red-arm optical quality was done after the whole spectrograph integration and alignment in Paranal. An example for the UHR mode is shown in Fig.4.35 and Fig.4.36, where the FWHM of an isolated feature of the Thorium-Argon spectrum injected in the Fiber-A is evaluated with the Graphical Astronomy and Image Analysis Tool (GAIA). The FWHM values in the main dispersion direction properly match the theoretical value of about 2.7 pixels related to a resolving power of 240000.

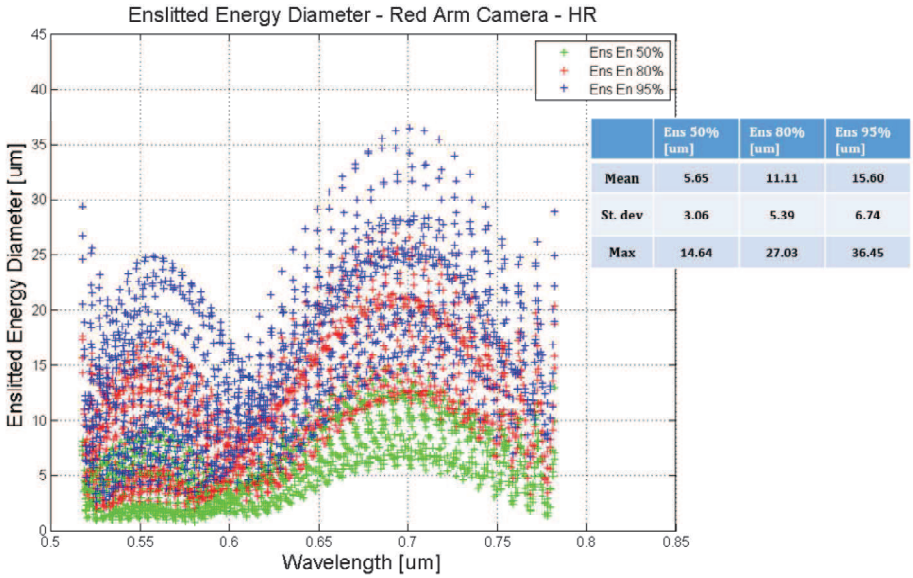

	Ens 50% [um]	Ens 80% [um]	Ens 95% [um]
Mean	5.65	11.11	15.60
St. dev	3.06	5.39	6.74
Max	14.64	27.03	36.45

Figure 4.33: Enslitted energy distribution in main dispersion direction for ESPRESSO red arm in the HR mode. Attached to the figure there is a tabular summary of the statistics for the mean, standard deviation and maximum of the 50%, 80% and 90% enslitted energy diameter in main dispersion.

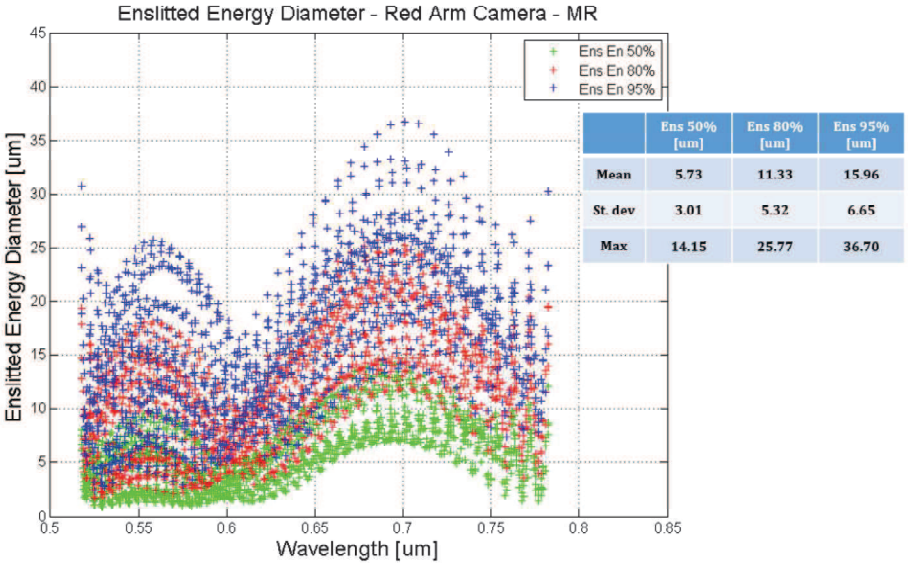

	Ens 50% [um]	Ens 80% [um]	Ens 95% [um]
Mean	5.73	11.33	15.96
St. dev	3.01	5.32	6.65
Max	14.15	25.77	36.70

Figure 4.34: Enslitted energy distribution in main dispersion direction for ESPRESSO red arm in the MR mode. Attached to the figure there is a tabular summary of the statistics for the mean, standard deviation and maximum of the 50%, 80% and 90% enslitted energy diameter in main dispersion.

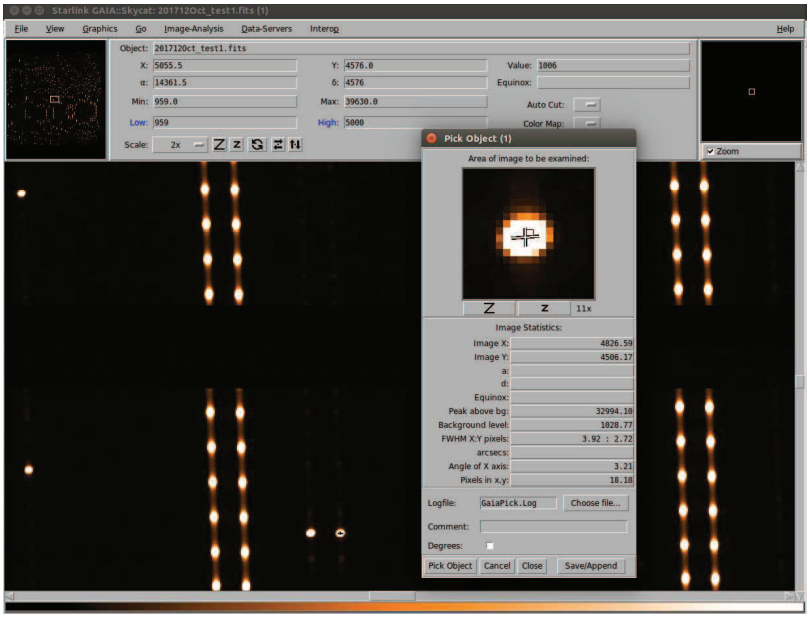

Figure 4.35: FWHM of an isolated feature of the Thorium-Argon spectrum injected in the Fiber-A, slice 1. The evaluation is done exploiting the GAIA software package. The value in the main dispersion direction properly matches the theoretical value of about 2.7 pixels related to a resolving power of 240000.

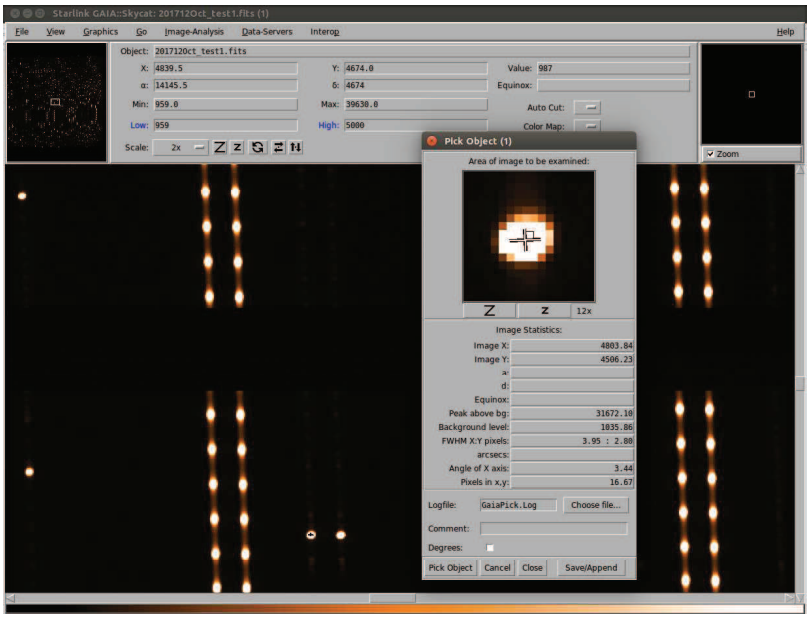

Figure 4.36: FWHM of an isolated feature of the Thorium-Argon spectrum injected in the Fiber-A, slice 2. The evaluation is done exploiting the GAIA software package. The value in the main dispersion direction properly matches the theoretical value of about 2.7 pixels related to a resolving power of 240000.

4.3 Towards the future: ELT-HIRES

The High Resolution Spectrograph for the Extremely Large Telescope, named ELT-HIRES to avoid confusion with the HIRES instrument at Keck-I, is currently in the phase-A of the project. Located in Cerro Armazones (Chile) at an altitude of about 3000 m, the construction of the dome main structure of the ELT started in May 2017 and the first light is currently planned for 2024. The ELT will be the largest telescope to observe in visible and infra-red light, with a primary mirror of 39 m composed by 798 hexagonal mirrors of 1.4 m maximum size (for details on ELT see [40]). The top-level requirements derived from the science drivers, described in the following subsection, and main instrumental features for the proposed architecture and main observing modes are anticipated and summarized in Tab.4.2.

Table 4.2: The top-level requirements and main instrumental features for the proposed main operative modes of ELT-HIRES. These modes were identified and derived from a prioritization of the scientific cases. Abbreviations: VV stays for Vacuum Vessel.

	High Throughput	High RV accuracy	IFU
Wavelengths	330 - 2400 nm		
Spectral coverage	Gaps at: 1350 - 1440 nm; 1800 - 1920 nm		
Resolving Power	$\geq$ 100000	$\geq$ 100000	$\geq$ 100000
N. of apertures on sky	2 (obj + sky)	2 (obj + sky)	1 (obj)
Aperture on sky diameter	0.93 arcsec	0.87 arcsec	0.01 arcsec
N. fibers per aperture	30	26	64
Spectral Sampling	$\geq$ 2 pix	$\geq$ 2 pix	$\geq$ 2 pix
Sky-subtraction	Yes	Yes	No
Simultaneous calib.	No	Yes	No
N. of calib. fibers per aperture	-	4	-
Total efficiency	TBD	TBD	TBD
Instrumental RV precision	$\leq$ 1 m/s	$\leq$ 1 m/s	$\leq$ 1 m/s
Temperature stabilization control in VV	$<$ 20 mK	$<$ 20 mK	$<$ 20 mK
Pressure stabilization control in VV	$<$ 2x10^{-3} mbar	$<$ 2x10^{-3} mbar	$<$ 2x10^{-3} mbar

4.3.1 Summary of the scientific drivers

The huge photon collecting power of the 39 m primary mirror diameter ELT coupled with a High Resolution and very versatile Spectrograph architecture concept will allow the European high resolution community to make fundamental discoveries in wide range of astrophysical areas, outlined by the Science Team of the ELT-HIRES Initiative ([51]). A brief summary is give in the following:

- *Exoplanet - characterization of atmospheres and the detection of life signatures*: the main purpose is the study of exoplanetary atmospheres through the characterization of the chemical composition, stratification and weather in the different atmospheric layers over a wide range of planets, from Neptune-like down to Earth-like including those in the habitable zones [70]. The ultimate goal is the detection of signatures of life; this goal will be possible also thanks to the polarimetric mode which has been foreseen in the proposed architecture concept. All the high performance described at the beginning of this chapter, ensured in the wide wavelength range (0.33-2.4 um) will allow to perform high quality transmission spectroscopy studies (see Chapter 2 for details on this method). ELT-HIRES will also be the key instrument to follow-up the PLATO space mission, recently approved by ESA for launch in 2024. As explained in [70], PLATO will provide thousands of transiting exoplanets, down to Earth-like objects, many of which will urge atmospheric characterization. The science case of Exoplanetary atmosphere in transmission has been ranked as high priority, while the case of Exoplanetary atmosphere in reflection as medium priority.

- *Star and planet formation*: the deep comprehension of the chemistry, dynamics and physical condition of the inner-most regions of stellar accretion and protoplanetary disks will be a key step in understanding the physics of star formation as well as other phenomena like jet-ejection which can affect the planets formation mechanism. As explained in [70] the high spectral resolution coupled with IFU capability (IFU mode) in the near IR will be complementary to the observation that will be performed at other wavelength bands from other facilities like ALMA. This science case has been ranked as medium priority.

- *Stellar physics, chemistry, asteroseismology and astro-archaeology*: exploiting the combination of wide spectral coverage, high resolution, and large photon collecting power different aspects of stellar physics will be better investigated. In fact the extremely high quality data of ELT-HIRES will allow to trace in detail the chemical enrichment pattern of solar-type and cooler dwarf stars out to distances of several kpc, therefore sampling most of the Galactic disk and bulge [70]. Moreover the detailed chemical mapping of numerous elements and isotopes will reveal the origin and the formation history of ancient stars. High precision spectroscopic analyses of stars seismic data allows to calibrate theoretical stellar models and infer properties of stellar interiors and their link with oscillation modes. The additional polarimetric capabilities are very useful to give hints in the magnetic field of a star and its role for stellar evolution and cosmic-ray shielding for its planets. This science case has been ranked as medium priority.

- *Galaxy formation*: one of the key prospects in this context is the detection of elements synthesized by the first stars in the Universe. These observations will reveal the nature and physical properties of the first stars that populated the Universe. As claimed in [70], ELT-HIRES will probably be the first facility that could unambiguously detect the fingerprint of Pop-III stars by measuring the chemical enrichment patterns typical of this population in the Inter-Galactic Medium (IGM) and Inter-Stellar Medium (ISM) exploiting the foreground of

Quasars. Thanks to the high resolution and wide spectral coverage this instrument will allow astronomers to trace the history of the Universe reionization process and the subsequent thermal history of the IGM, providing crucial information on the classes of sources responsible for the reionization. As explained in [70], if equipped with an IFU sampling the telescope diffraction limited PSF, the high resolution of ELT-HIRES will also allow to measure the low mass end of supermassive black hole in galactic nuclei, enabling a more comprehensive study and test between different galaxy-black hole co-evolutionary theories.

- *Fundamental Physics and Cosmology*: as explained for ESPRESSO in subsection 4.1.1, also ELT-HIRES will be an instrument capable of addressing issues related to the domain of fundamental physics. In particular, as claimed in [70], HIRES will provide the most accurate tests for the assessment of stability of the fundamental constants (like the fine structure constant and the proton-to-electron mass ratio). Moreover, Since ESPRESSO at VLT will achieve many of the design requirements (in terms of resolving power, efficiency in the blue part of the spectral range processed and wavelength calibration accuracy) before the ELT will be built, the definition of an optimal fundamental constants observational program for ELT-HIRES will take into account ESPRESSO results. Furthermore, as explained in [70], many of the spectra gathered by ELT-HIRES could be exploited for the investigation of the first measurement of the redshift drift-rate dz/dt deep in the matter dominated era of the Universe. This is a unique, direct, non-geometric and completely model-independent measurement of the Universe's expansion history (the Sandage test). This specific science case requires excellent wavelength calibration with an accuracy in the order of 2 cm/s over the whole lifetime of the instrument. The Variation of the Fundamental Constants is ranked with medium-high priority, while the Sandage test as medium-low priority mainly because of the extreme demanding requirement of calibration accuracy.

4.3.2 Brief Instrument description

The ELT-HIRES instrument preliminary functional architecture concept, shown in Fig.4.37, is highly modular. It foresees different independent fiber-fed echelle cross-dispersed spectrographs optimized for different wavelength bands of the whole spectral coverage, which goes from 330 nm to 2400 nm. The split in wavelengths over the spectrograph is influenced, among all other parameters, by the optical transparency of the different types of fibers available on the market. Therefore, the different modules can be positioned at different distances from the telescope focal plane. As conceptually summarized in Fig.4.37, the light from the telescope is split, via dichroics, into the different spectral channels. Each one is equipped with several fibers bundles that feed the related spectrograph module. Each fibers bundle corresponds to an observing mode. All spectrometer modules have a fixed configuration, i.e. no moving parts. They include a series of parallel entrance slits, each consisting of an array of micro-lenses glued to a specific fibers bundle.

The proposed architecture also allows different main observing modes, each one with several sub-modes which can be implemented relying on the modularity of the

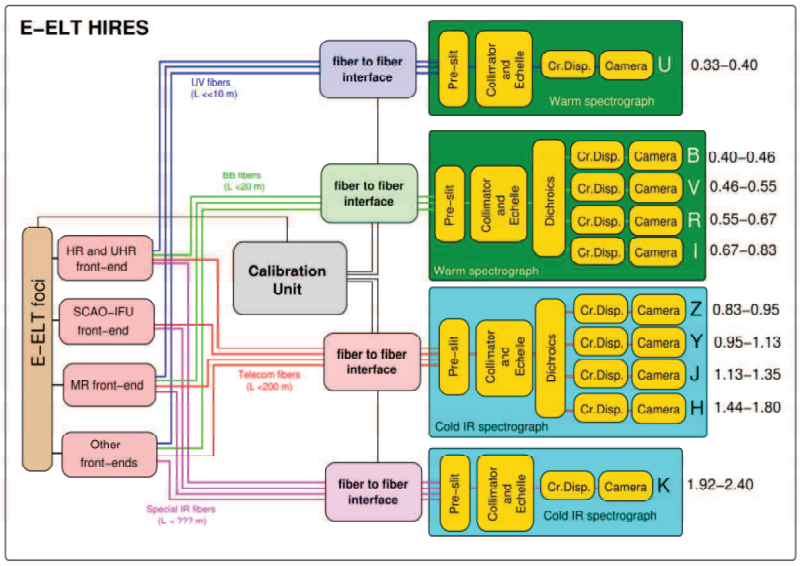

Figure 4.37: Schematic of the proposed ELT-HIRES functional architecture concept. The different sub-systems of the instrument (front-end, fiber link, calibration unit, spectrometers) are indicated, as well as the possible length of the fiber bundles, according to the specific wave-band. The wavelength splitting in the different spectrograph modules are also reported (in μm).

fiber-slits array. The main observing modes are:

- Throughput maximization
- Spectral (Radial Velocity) accuracy maximization
- Spatially resolved information (IFU)
- Possible add-on modes: Spectropolarimetry and Multi-objects medium resolution spectroscopy

The Front-End (FE) sub-system located at the ELT-Nasmyth Focus B2, devoted to redirect the light coming from the telescope to the different fiber bundles of the Fiber-Link (FL) sub-system, is composed by 4 different arms. Two are used for the simultaneous object and sky acquisition, one for the SCAO-IFU mode and the other for the Polarimeter. A schematic of the optical components of one of the two arms for single object observing mode is shown in Fig.4.39; it is composed by 4 spectral modules separated by dichroics to feed the 4 spectrograph modules.

In order to better accomplish the specific scientific goals, for the different main observing modes two possible resolution capabilities ($R = 100000$ and $R = 150000$) are foreseen, which can be implemented by feeding the spectrograph modules with different fibers bundles. The technique used by the FL sub-system to feed the huge $A\Omega$-product at the spectrograph entrance in the selected architecture is the field dicing (see for details reference [84]), in which each fiber of the bundle is looking at a slightly different part of the object. A conceptual example of this method is in Fig.4.40. Moreover in this way the spectrometers entrance slit width is reduced

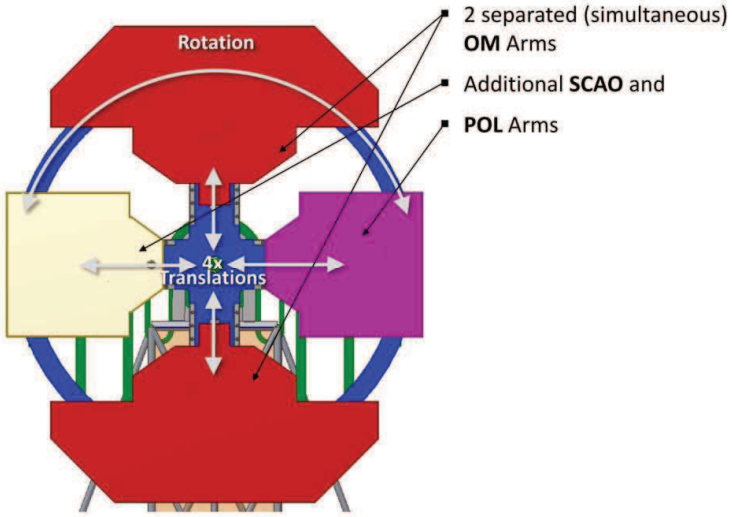

Figure 4.38: Schematic of the Front-End sub-system arms.

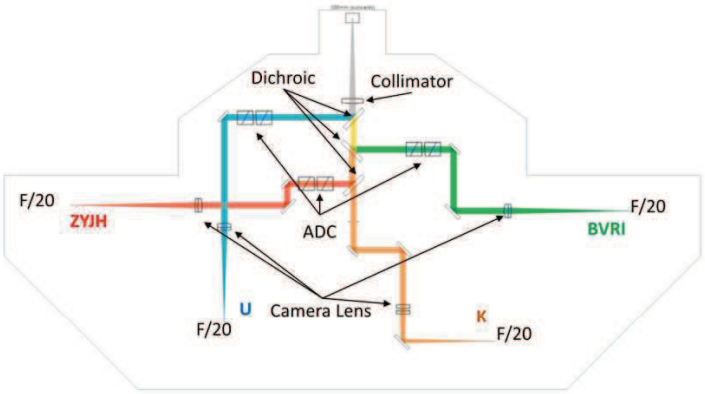

Figure 4.39: Schematic of the Front-End sub-system optical components. four different spectral channels feed the four different spectrograph modules. The splitting is done by dichroics; Atmospheric Dispersion Correction (ADC) is foreseen in all channels with exception of the K band.

allowing high resolving power performance keeping the components size within manufacturing capabilities.

Two additional aspect which characterized the proposed general architecture of the instrument and of the Fiber-Link sub-system must be underlined. First, The fibre bundles are split into two segments and have two different routings. The first segment connects the FE to the Fiber-to-Fiber interface box, while the second segment connects the Fiber-to-Fiber interface box to the spectrographs. The two segments can be directly connected, to maximize throughput, or coupled via a double scrambler optical system, to enhance the scrambling of both the near and far field, thus optimizing the spectrograph illumination and then radial velocity accuracy. Second the fiber bundles related to the different observing modes, which are interchangeable, are

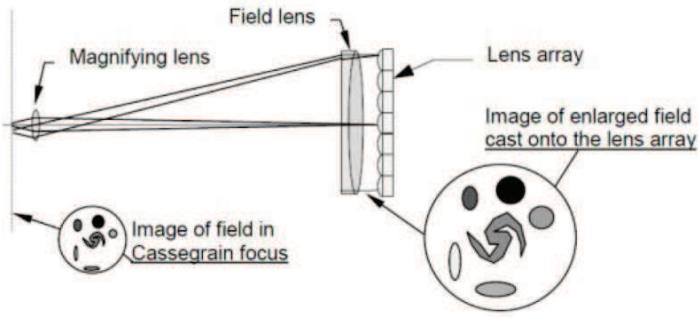

Figure 4.40: Schematic of the field dicing concept exploited in the propesed architecture of the ELT-HIRES.

the ones of the first segment; the second segment bundles, connected to the spectrograph modules entrance, are kept fixed. As anticipated before, on this side the fibers are connected to a linear array of micro-lenses which act as input slit; a schematic is depicted in the Fig.4.41.

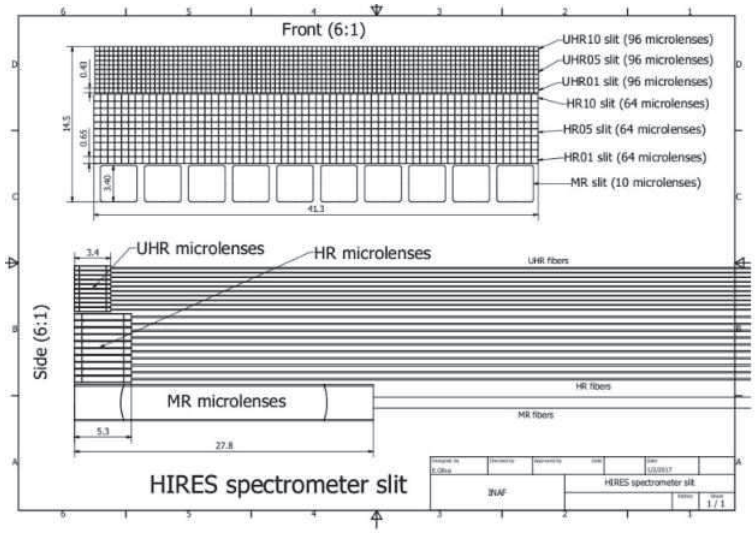

Figure 4.41: Schematic of the different entrance fiber-slit arrays related to the different observing modes and sub-modes.

The different spectrometers can be ideally divided according to their specific function into two units: the pre-slit unit, a re-imaging system which collects the light from the fiber optics and feeds the spectrometer unit, which has the usual purpose of separate the light into its constitutive wavelengths and then refocus them onto the detector surface. The spectrometer units optical configuration is the white pupil layout (see [8] for details) with an off-plane echelle grating angle of 1 deg. The layout is very similar to that of ESPRESSO (see subsection 4.1.2). The main collimator works in double pass, the echelle grating mosaic is composed by four tiles (see the analysis in subsection 4.4.4). A field lens is designed to work in the whole wavelength band

of a single spectrometer unit, see the example of the infra-red spectrometer shown in Fig.4.42. Anamorphic prisms and cross dispersers are in this case separated, due to the presence of dichroics which split the different arms, although they have the same function as in ESPRESSO. The camera optical configuration is the Schmidt camera.

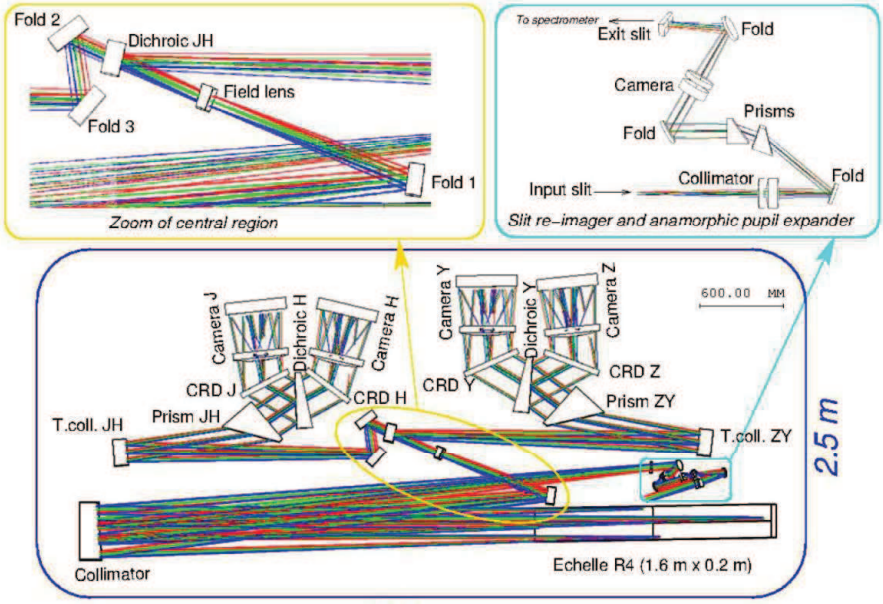

Figure 4.42: Optical design layout of the ZYJH spectrograph.

4.4 My contribution to ELT-HIRES: the Paraxial Model

In this sub-section a flexible paraxial parametric model of the high resolution spectrograph is described. The flexibility and reliability of this optical model can be very useful for different purposes. From the design side to evaluate the impact that the different optical components parameters can have with respect to defined performance requirements and technical constraints. At system engineering level to preliminary explore and compare different possible instrument architectures; in this respect this parametric model can be flexibly run by of the End-to-End simulator as the spectrograph unit of the instrument module (see chapter 4 for details concerning the End-to-End simulator and its modules and units).

The model is detailed starting from the assumptions taken into consideration (see subsection 4.4.1, then describing all the equations for all the optical components and the related relevant (paraxial) effects (in subsection 4.4.2. The application of this modeling tool for a design analysis for the ZYJH spectrometer module of the ELT-HIRES is presented in subsection 4.4.4; while in chapter 4 its use within the E2E simulator is shown.

4.4.1 Model Assumptions

According to the paraxial nature of the derived model the aberrations that may be induced by the collimating, focusing optics and other optical elements are not specifically modelled; the other general assumptions are:

- The optic systems that can be exploited to dice the field and to feed the spectrograph entrance are not modelled; only the relevant parameters directly related to the spectrograph design (number of fibres and fibre core diameter) are taken into consideration.
- The anamorphic effects are modelled simply by using different x and y beam resizing coefficients; these coefficient are always formally defined as the ratio of the beam size (both for x and y directions) after the effect over the beam size before.
- The echelle grating works in quasi-Littrow condition according to the white pupil optical configuration of the proposed spectrometer units' design.
- The transfer collimator aspect taken into consideration is the beam resizing effect expressed with a coefficient, as done for the anamorphic effects.
- The cross-dispersion element is assumed to be a Volume Phase Holographic grating (VPH grating [5]) having the plane of fringes parallel to the plane of the VPH grating and working in the so called Bragg condition for the central wavelength of the cross-dispersed band [6];
- The VPH diffraction efficiency is modeled with Kogelnik theoretical model (see for details [56]). As explained in [16], the main hypothesis of this model is that the VPH grating works in the Bragg regime, which means that the light is sent only to the first diffraction order other then the zero order.

4.4.2 Model equations flow

Starting from the fixed data of the telescope diameter D_T and the angular aperture diameter χ of the object image on the telescope focal plane (due to the seeing condition, in the case of seeing-limited observation), the number of fibers N_{fib} used to dice the field and the physical constraint on their working input focal ratio F_{fib} set the fibers core diameter as:

$$D_{fib} = \frac{D_T F_{fib}}{\sqrt{N_{fib}}} \frac{\chi}{206265} \tag{4.1}$$

The size of the micro-lenses, $D_{\mu L2}$, at the input of the pre-slit unit (then at the exit of the optical fiber bundles) is derived from the Etendue conservation (the law of

[5] AS explained in the instrument description of ESPRESSO, VPH gratings a selected as cross-dispersing elements in echelle spectrograph because of the high efficiency they are able to guarantee over a large wavelength range.

[6] This condition between the fringes and the VPH plane is usually termed as "unslanted fringes", for which the grating period (equivalent to the groove spacing on a ruled grating) coincides with the separation between fringes. For unslanted VPH the Bragg condition corresponds to the Littrow diffraction since the diffraction angle is equal to the incidence angle. See [7] for details.

energy conservation for an optical system) between the Dicing unit input focal plane (which is the FE focal plane) and the input focal plane of the pre-slit unit; specifically $D_{\mu L2}$ is expressed as:

$$D_{\mu L2} = \frac{F_{coll,Y}}{F_{fib}} D_{fib} \tag{4.2}$$

The angular slit length at the input of the pre-slit unit can be written in term of the portion of the entrance aperture angular diameter sampled by each fiber ($\frac{\chi}{\sqrt{N_{fib}}}$) and the total number of fibers, and then micro-lenses, which compose the entrance slit. The total number of fibers (micro-lenses) of the entrance slit takes into consideration possible dark fibers (micro-lenses) in between of the fiber-bundles of the two apertures, $N_{fib,dark}$ and also the number of calibration fibers per each aperture, $N_{fib,cal}$.

$$sL_1 = \frac{\chi}{\sqrt{N_{fib}}}[2N_{fib} + N_{fib,dark} + 2N_{fib,cal}] \tag{4.3}$$

The linear slit length is simply the size of the micro-lens multiplied by the total number of fibers:

$$sL_2 = D_{\mu L2}[2N_{fib} + N_{fib,dark} + 2N_{fib,cal}] \tag{4.4}$$

Setting the main collimator x and y F-ratio ($F_{coll,X}$ and $F_{coll,Y}$), directly related to its design and manufacturing complexity, the pre-slit anamorphic factor and the x and y dimensions of the effective equivalent entrance slit of the spectrometer unit (related to a single fiber core, thus a single micro-lens of the "fiber-slit") are:

$$PS_{AF} = \frac{F_{coll,Y}}{F_{coll,X}} \tag{4.5}$$

$$D_{eqslit,X} = \frac{F_{coll,X}}{F_{fib}} D_{fib} \tag{4.6}$$

$$D_{eqslit,Y} = \frac{F_{coll,Y}}{F_{fib}} D_{fib} \tag{4.7}$$

The total illuminated length of the echelle grating mosaic, W, required to diffract the whole collimated beam after the main collimator is derived form the imposed resolving power R (which is a top level requirement) and from the grating blaze angle value δ (known from the echelle gratings available on the market):

$$W = \frac{D_{eqslit,X} R}{2sin(\delta) F_{coll,X}} \tag{4.8}$$

The collimated beam x and y size (after the main collimator) can be expressed then as:

$$d_{coll,X} = W cos(\delta) \tag{4.9}$$

$$d_{coll,Y} = d_{coll,Y}/PS_{AF} \tag{4.10}$$

It is possible to derive the required number of echelle gratings ($N_{grat,X}$ and $N_{grat,Y}$)

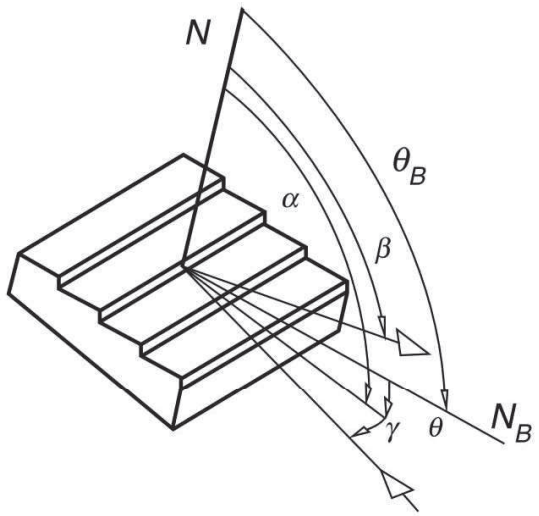

Figure 4.43: Example of general angles for the Echelle grating working in quasi-littrow configuration; N is the grating normal, N_B is the grating facette normal. θ_B is the blaze angle, γ is the off-axis angle (called γ_{EG} in the text), α and β are the incidence and diffraction angle respectively. Figure taken from [41].

to form the mosaic from the data on the ruled width (Rul_W) and groove length (G_l) of the echelle gratings available on the market:

$$N_{grat,X} = W/Rul_W \tag{4.11}$$

$$N_{grat,Y} = d_{coll,Y}/G_l \tag{4.12}$$

The main collimator focal length is then:

$$f_{coll} = F_{coll,X} d_{coll,X} = F_{coll,Y} d_{coll,Y} \tag{4.13}$$

As explained before, the white pupil optical configuration foresees the echelle grating working in the so called quasi-littrow condition for which the grating has an off axis angle (γ_{EG}) to separate the incoming and diffracted beams along the spatial direction. This angle is the angle that the plane containing the angle of incidence and angle of diffraction has against the grating normal. An example with general incidence and diffraction angles (α and β) is shown in Fig.4.43. Each field of the equivalent slit at the input of the spectrometer unit has its specific off-axis angle, different with respect to that of the echelle grating γ_{EG}. This is dependent on the specific y-coordinate of the field along the input slit ($Y_{f,i}$) as:

$$\gamma_{f,i} = \gamma_{EG} + Y_{f,i}/f_{coll} \tag{4.14}$$

From a given wavelength band and setting the echelle grating parameters through the grating equation (referred to the central field of the input slit) it is possible to derive, per each diffraction order, the following parameters related to the grating dispersion effects:

- the diffraction order number m
- the blaze wavelength λ_b
- the maximum and minimum wavelength in the free spectral range (FSR), λ_+ and λ_-
- the diffraction angles related to the maximum and minimum FSR wavelengths, respectively β_+ and β_-
- the spectral resolution $\delta\lambda$

In particular, working at high resolution and high diffraction orders, the maximum and minimum FSR wavelengths for each order can be generally expressed as:

$$\lambda_+ = \lambda_b(1 + c_+/m) \tag{4.15}$$

$$\lambda_- = \lambda_b(1 - c_-/m) \tag{4.16}$$

where c_- and c_- are two coefficients used to set overlapping (typically 10%) between consecutive diffraction orders, which is required for the reconstruction of the entire 1-D spectrum in each band.

The diffraction intensity distribution of the different echelle orders is the product of the blaze function (BF) and the normalized interference function (G_{norm}). They are dependent on their phases in the following analytic form:

$$BF(\delta) = (\frac{sin\delta}{\delta})^2 \tag{4.17}$$

$$G_{norm}(\psi) = \{\frac{sin(N\psi)}{Nsin\psi}\}^2 \tag{4.18}$$

It can be derived that the phase ψ is such that $\psi = m \cdot \pi$; since both the order number m and the N number of illuminated grating grooves are integers, then the arguments of the two sines function composing the normalized interference function (G_{norm}) are both integer which multiplies π. This results in a 0/0 form which can be demonstrated to be 1. As a conclusion the diffraction intensity distribution of the different echelle orders is simply the blaze function (BF).

Through the transfer collimator coefficient (see model assumption listed before) the x and y size of the beam, after the transfer collimator, are:

$$d_{TC,X} = d_{coll,X} TC_{coeff} \tag{4.19}$$

$$d_{TC,Y} = d_{coll,Y} TC_{coeff} \tag{4.20}$$

Note that these are the sizes of the beam related to the blaze wavelength of each diffraction order. The effect of the cross disperser (for both ESPRESSO and ELT-HIRES) can be modeled as the one from a grism based onto an entrance prism coupled with a volume phase holographic (VPH) grating; a schematic is shown in Fig.4.44. The anamorphic effect in the main dispersion (x) and cross dispersion direction (y) is expressed with two coefficients, $Pr_{AF,x}$ and $Pr_{AF,y}$ respectively. This two coefficients

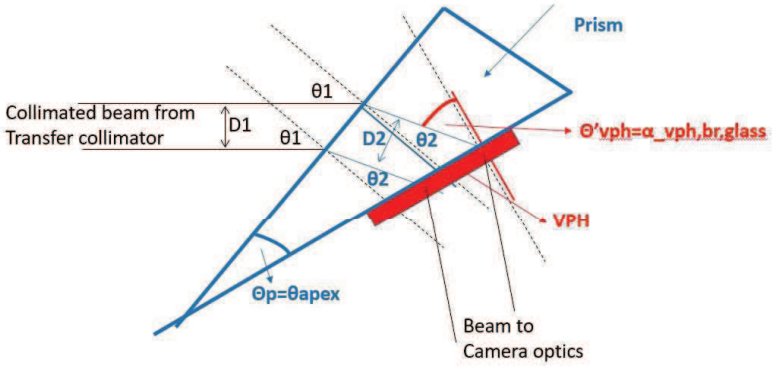

Figure 4.44: Grism schematic. The beam coming from the Transfer collimator has a size D1 and incident angle θ_1; the size and refraction angle of the beam inside the prism are D2 and θ_2 respectively. The incident angle on the VPH is $\theta^{'}$.

can be related according to the ratio of spectral and spatial sampling and the pre-slit anamorphism as in the following equation:

$$\frac{Pr_{AF,y}}{Pr_{AF,x}} = \frac{S_x}{S_y} PS_{AF} \tag{4.21}$$

In this way setting the beam re-sizing effect of the prism in one direction it is possible to derive the value in the other one. Referring to Fig.4.44 the prism anamorphism in cross dispersion direction is expressed as:

$$Pr_{AF,Y} = \frac{cos\theta_2}{cos\theta_1} \tag{4.22}$$

where θ_1 is the angle of the incident beam on the first surface of the prism, while θ_2 the refraction angle. These two angle are also related according to the Snell law through the prism refractive index (the refractive index of the medium before the prism is the environment of the spectrograph where the refractive index can be assumed to be 1). The angles inside the prism can be related as:

$$\theta^{'}_{VPH} = \theta_2 + \theta_{apex} \tag{4.23}$$

The angles θ_1 and θ_2 can be derived starting from the Eq.4.22 and using the Snell law to express the refraction angle θ_2 as function of the incidence angle $\theta^{'}_{VPH}$:

$$(Pr_{AF,Y} \cdot cos\theta_1)^2 = 1 - (\frac{sin\theta_1}{n_{prism}})^2 \tag{4.24}$$

After a bit of algebra the two angles are:

$$\theta_1 = \arcsin(\sqrt{\xi}) \tag{4.25}$$

$$\theta_2 = \arcsin(\frac{\sqrt{\xi}}{n_{prism}}) \tag{4.26}$$

$$\xi = \frac{(Pr_{AF,Y}^2 - 1)n_{prism}^2}{Pr_{AF,Y}^2 \cdot n_{prism}^2 - 1} \tag{4.27}$$

Recalling the two prism anamorphic coefficients , the central blaze wavelength beam sizes after the prism are:

$$d_{XD,X} = d_{TC,X} Pr_{AF,X} \tag{4.28}$$

$$d_{XD,Y} = d_{TC,Y} Pr_{AF,Y} \tag{4.29}$$

To derive the parameters related to the VPH grating the total linear separation between two consecutive orders on the detector surface, Δy must be set; this is expressed in terms of the number of fibers, pixel size, required spatial sampling, required separation between object and sky fibers (dark fibers) and separation between consecutive orders (inter order separation):

$$\Delta y = [(2N_{fib} + N_{fib,dark} + 2N_{fib,cal}) \cdot S_y + IO_{sep}] \cdot \frac{d_{pix}}{1000} \tag{4.30}$$

From the angular dispersion equation the VPH cross disperser working angle for the Bragg condition in air is:

$$\theta_{VPH} = atan(\frac{\lambda_b}{2} \frac{\Delta y}{f_2 \Delta \lambda_b}) \tag{4.31}$$

where in this case λ_b is the central blaze wave of the specific wavelength band (the one for which the Bragg efficiency condition is set) and $\Delta\lambda_b$ is the difference in wavelengths between the central blaze wave and the consecutive one; f_2 is the camera focal length that is evaluated with Eq.4.37. From the classical diffraction equation (with the VPH cross disperser working spectral order $m_{cd} = 1$) the VPH groove density is:

$$\rho_{VPH} = \frac{2 \sin \theta_{VPH}}{m_{cd} \lambda_b} \tag{4.32}$$

Using the grating equation for the VPH disperser the diffraction angle related to the blaze wavelength of all the diffraction orders is calculated.

The VPH diffraction efficiency in the whole wavelength band is evaluated and optimized with Kogelnik theoretical model ([56]) acting on the two parameters: gelatin thickness t and gelatin index modulation Δn. The Kogelnik model express the diffraction intensity distribution, for a VPH in Bragg condition, as function of:

- Gelatin thickness, t
- Gelatin index modulation Δn
- Mean refractive index of the gelatin, n_g
- The line density of the VPH, ρ_{VPH}
- The VPH Bragg angle, θ_{VPH}

The Kogelnik model is valid and comparable with the rigorous coupled-wave analysis (RCWA; see for a detailed description e.g. [67] and [43]) when the loss power parameter LP is low. The loss power can be estimated, with good approximation, as the inverse of the square of the ρ_{LP} parameter:

$$\rho_{LP} = \frac{\lambda^2}{n_g \Delta n t^2} \longrightarrow LP \approx \frac{1}{\rho_{LP}^2} \tag{4.33}$$

The optimization is performed on the $t - \Delta n$ parameter space; the VPH grove density and Bragg angle are determined by Eqs. 4.31 and 4.32, while the mean refractive index of the gelatin is set to about 1.455. [7] The optimal $t - \Delta n$ pair is searched only among the range of their combinations which give an efficiency, at the Bragg wavelength, in the Kogelnik model $\geq$ a threshold, set to 0.85. For all the combinations which satisfy the threshold the diffraction efficiency in the whole spectral band, $\eta_{VPH}(\lambda)$, is evaluated with the Kogelnik model. Also the loss power parameter is evaluated for each wavelength and the efficiency distribution is modified to take losses into account as:

$$\eta_{VPH,\rho}(\lambda) = \eta_{VPH}(\lambda) \cdot (1 - LP(\lambda)) \tag{4.34}$$

The figure of merit considered for the optimization is the RMS deviation of this modified efficiency distribution from the theoretical maximum, 1; thus the combination of $t - \Delta n$ which minimizes the RMS deviation over the whole wavelength range is selected.
The camera optics F-ratios are derived by the spectral and spatial sampling value (S_X and S_Y) and by the pixel size for the available detectors on the market according to the specific wavelength band (optical CCD or IR detectors) as:

$$F_{cam,X} = \frac{d_{pix} S_X}{D_{eqslit,X}} F_{coll,X} \tag{4.35}$$

$$F_{cam,Y} = \frac{d_{pix} S_Y}{D_{eqslit,Y}} F_{coll,Y} \tag{4.36}$$

So the camera focal length is:

$$f_2 = F_{cam,X} d_{XD,X} = F_{cam,Y} d_{XD,Y} \tag{4.37}$$

where, as explained in Eqs. 4.28 and 4.29, $d_{XD,X}$ and $d_{XD,Y}$ are the sizes of the Bragg wavelength beam. The variation of the beam size on the camera and the relative change of the camera F-ratio is evaluated both in main dispersion and in cross dispersion direction. In main dispersion direction:

$$d_{CAM,X,\lambda} = d_{XD,X} \cdot \frac{cos\beta(\lambda)}{cos\theta_B} \tag{4.38}$$

$$F_{cam,X,\lambda} = \frac{f_2}{d_{CAM,X,\lambda}} \longrightarrow S_{X,\lambda} = S_X \cdot \frac{F_{cam,X,\lambda}}{F_{cam,X}} \tag{4.39}$$

In cross dispersion direction:

$$d_{CAM,Y,\lambda} = d_{XD,Y} \cdot \frac{cos\beta_{VPH}(\lambda)}{cos\theta_{VPH}} \tag{4.40}$$

$$F_{cam,Y,\lambda} = \frac{f_2}{d_{CAM,Y,\lambda}} \longrightarrow S_{Y,\lambda} = S_Y \cdot \frac{F_{cam,Y,\lambda}}{F_{cam,Y}} \tag{4.41}$$

With all the spectrograph optical parameters evaluated it is possible to produce the echellogram format at the detector plane. This can be done simulating either a

[7] average value taken from measurements of processed gelatin (see for example [18] and [36]).

single field or a number of different fields at the entrance slit of the pre-slit unit. For each echelle order m, each selected wavelength λ and each field $Y_{f,i}$ the echelle grating equation is exploited to evaluate the difference between the diffraction angles $\beta(\lambda, Y_{f,i})$ and the blaze angle θ_B:

$$\Delta\beta(\lambda, Y_{f,i}) = \beta(\lambda, Y_{f,i}) - \theta_B = \arcsin(\frac{m\rho\lambda}{cos\gamma_{f,i}} - sin\theta_B) - \theta_B \tag{4.42}$$

Then the effect of the Transfer collimator in the beam apertures along the main dispersion is taken into account:

$$\Delta\beta(\lambda, Y_{f,i}) = \Delta\beta(\lambda, Y_{f,i}) \cdot \left(\frac{1}{TC_{coeff}}\right) \tag{4.43}$$

The transfer collimator does not affect the beam angles in cross dispersion since in the optical layout it is before the grism in the light propagation path. For each echelle order m, each selected wavelength λ and each field $Y_{f,i}$ the VPH grating equation is exploited to evaluate the difference between the diffraction angles along the cross dispersion direction $\beta_{VPH}(\lambda, Y_{f,i})$ and the Bragg angle θ_{VPH}; in the grating equation for the VPH it must be considered that the delta diffraction angles in the main dispersion with repsect to the blaze angle, $\Delta\beta(\lambda, Y_{f,i})$ are seen from the VPH as off-axis angles:

$$\begin{aligned}\Delta\beta_{VPH}(\lambda, Y_{f,i}) &= \beta_{VPH}(\lambda, Y_{f,i}) - \theta_{VPH} = \\ &= \arcsin(\frac{m_{cd}\rho_{VPH}\lambda}{cos\Delta\beta(\lambda, Y_{f,i})} - sin\theta_{VPH}) - \theta_{VPH}\end{aligned} \tag{4.44}$$

The x and y projection of different fields of the different spectral resolution element (SRE) through the camera optics on the focal plane (detector plane) are simply computed as:

$$X_{SRE}(m, \lambda, Y_{f,i}) = f_2 \cdot \Delta\beta(\lambda, Y_{f,i}) \tag{4.45}$$

$$Y_{SRE}(m, \lambda, Y_{f,i}) = f_2 \cdot \Delta\beta_{VPH}(\lambda, Y_{f,i}) \tag{4.46}$$

According to the described equation for the echellogram format it can be understood the known effect of order curvature and the equivalent-slit tilt which characterize the spectral format. They are both dependent and determined by the variation of the off-axis angles. The order curvature is due to the fact that the VPH off-axis angle change with the wavelengths in the same order and in the different echelle orders. According to Eq.4.42 the wavelengths approaching the FSR have a larger difference diffraction angle $\Delta\beta(\lambda, Y_{f,i})$ than wavelengths near the blaze; at a larger $\Delta\beta(\lambda, Y_{f,i})$ corresponds an increased $\Delta\beta_{VPH}(\lambda, Y_{f,i})$ which means a wider dispersion along the spatial direction. The equivalent-slit image tilt is due to the fact that wider fields at the equivalent entrance slit have a larger off-axis angle, $\gamma_{f,i}$, at the echelle and so the related echelle diffraction angles are larger; thus also the VPH off-axis angle are different for the wavelength beam related to each SRE field. This translates in a rotated image of each SRE in the detector plane.

4.4.3 Model verification example

Here the verification of the paraxial model is presented by means of a comparison with physical and simulated data (from ray-tracing calculations) of the ESPRESSO spectrograph. Specifically first some of the main optical component parameters are summarized in Tab. 4.3, then the red-arms cross disperser VPHG efficiency optimized with the model is analyzed in comparison to the theoretical curve computed by by Kaiser Optical System, Inc (KOSI); finally the red-arm echellogram generated with the parametric model is compared with the one from ray-tracing calculations.

Table 4.3: Parametric Paraxial Model results comparison with ESPRESSO physical data. The model output parameters considered, are labeled a in the text; Ψ_X and Ψ_Y are the fraction of detector surface width and height covered by the echellogram.

Results	Paraxial Model	ESPRESSO
f_{coll} $[mm]$	3056	3000
δ $[deg]$	76	76
ρ $[l/mm]$	31.6	31.6
$N_{grat,X}$ $[-]$	3.033	3
$N_{grat,Y}$ $[-]$	0.978	1
$F_{cam,X}$ $[-]$	2.7	2.7
$F_{cam,Y}$ $[-]$	2.7	2.7
θ_{apex} $[deg]$	25.3	25.25
θ_{VPHG} $[deg]$	14.26	15.08
ρ_{VPHG} $[l/mm]$	786	800
Ψ_X $[-]$	0.91	0.92
Ψ_Y $[-]$	0.95	0.97

From the derived values of VPH Bragg angle and line density, assuming a mean refractive index of the DCG resin of 1.455, the VPH diffraction efficiency is optimized acting on its thickness and index modulation according to the procedure explained before. The result is thickness 7.55 μm and index modulation 0.04; the efficiency curve in the ESPRESSO red band in Fig.4.45 shows both the result of Kogelnik model and the RCWA. As can be expected the RCWA is lower than Kogelnik since it takes into account losses due to the light propagation in orders different then the first diffraction order.
The light lost in other orders, computed with the RCWA model are plotted in Fig.4.46. Most of the light not propagating in the first diffraction order is in the zero order (this is what is common to both theoretical models), in addition the difference between the Kogelnik and RCWA models is larger at short wavelengths where some light is diffracted also in orders m – -1 and m – 2.
The efficiency losses are compared in Fig.4.47, where the losses estimation from the Kogelnik model, the light lost in orders $m = -1$ and $m = 2$ computed with RCWA, and the difference between the diffraction distribution from Kogelnik and RCWA are shown. The three curves present an increase in losses towards small wavelengths.

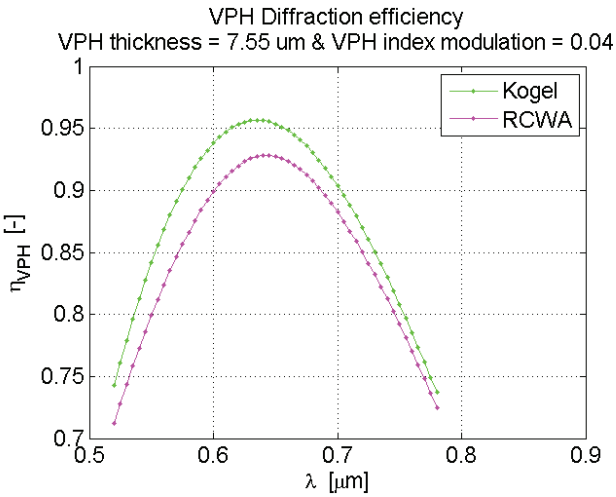

Figure 4.45: VPH diffraction efficiency computed from the optimization of thickness ans index modulation described in the text. Both the efficiency computed with the Kogelnik model and the one computed using the rigorous coupled wave analysis (RCWA) is shown.

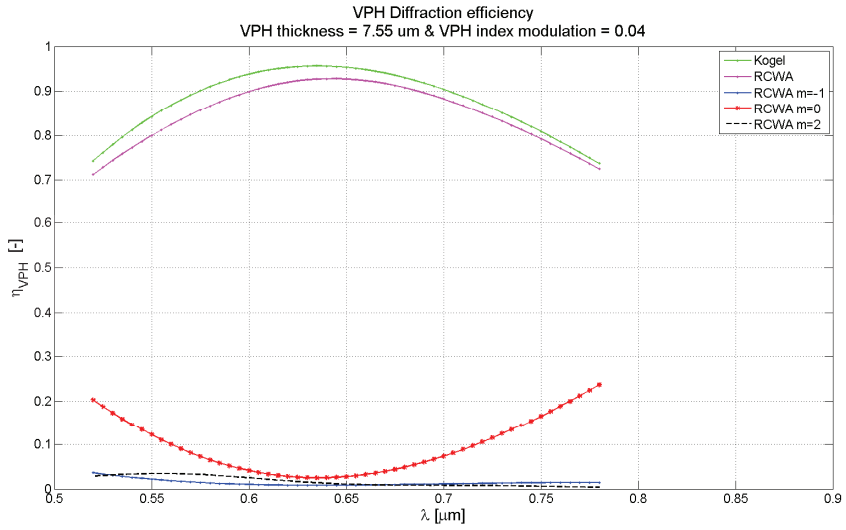

Figure 4.46: VPH diffraction efficiency curves as in Fig.4.45 with the addition of the light propagating in other orders. Red line-dot refers to zero-order, blue line-dot refers to order -1, while the black dashed line refers to order 2.

This is in accordance with the LP estimation from Kogelnik (see Eq.4.33) and also with the plot of orders -1 and 2 in Fig.4.46. It can be also noted that the difference between Kogelnik and RCWA models is close to the lost power from other orders computed with RCWA, while the lost power estimated with the LP parameter is overestimated.
The efficiency curve, plotted in Fig.4.46, computed with the RCWA is compared with the theoretical evaluation done by Kaiser Optical System, Inc (KOSI), shown in blue

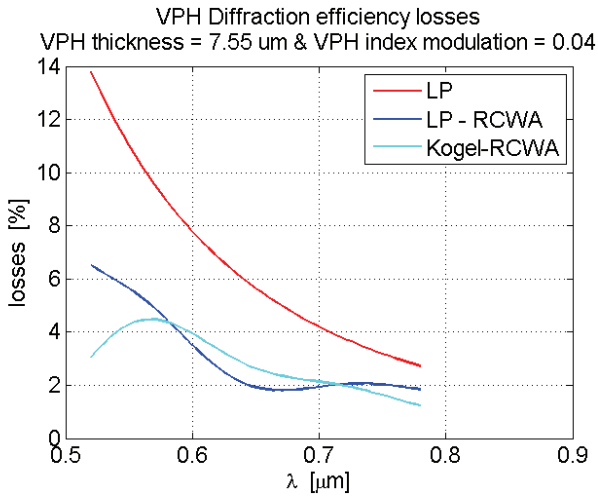

Figure 4.47: VPH diffraction efficiency losses. The computation is done for the efficiency related to the optimized values of thickness ans index modulation described in the text. The light blue line (Kogel−RCWA) represents the difference between the efficiency estimated from the Kogelnik model and the one with RCWA; the blue line (LP - RCWA) represents the light lost in diffraction order different from m = 1 computed with the RCWA. The red line (LP) represents the estimated lost power expressed with Eq.4.33.

line in Fig.4.48. The peak from the computed RCWA model and the RCWA theoretical performance estimated by KOSI are very similar: 93% compared with 91%. Also the shape of the diffraction efficiency curve is similar, while a discrepancy between the efficiency values at the wavelength band edges, in the order of 2% at $\lambda \simeq 530$ nm and of about 6% at $\lambda \simeq 780$ nm, can be noted. This discrepancy is ascribed to the fact that in our computation average values of prism and grating anti-reflection coatings reflectivity as well as the gelatin refractive index are considered, while in the theoretical performance estimation of KOSI these parameters are taken into account from detailed models and measurements.
The last verification is done comparing the echellogram computed with the described paraxial model and the one evaluated with ray-tracing of the complete optical model of ESPRESSO red arm in Zemax. The comparison, presented in Fig.4.49, shows a good matching between the two spectral formats.

4.4.4 Application of the Paraxial Parametric Model to design analysis

The following analysis has the purpose to illustrate how the parametric paraxial model can be used to help and drive the optical design and to explain/justify the selection of the optical component parameters. The optical design selection criteria are:

- Instrument efficiency optimization
- Design consistency with some technological constraints on the instrument size (echelle grating mosaic and camera input footprint) and complexity (camera F-ratios)

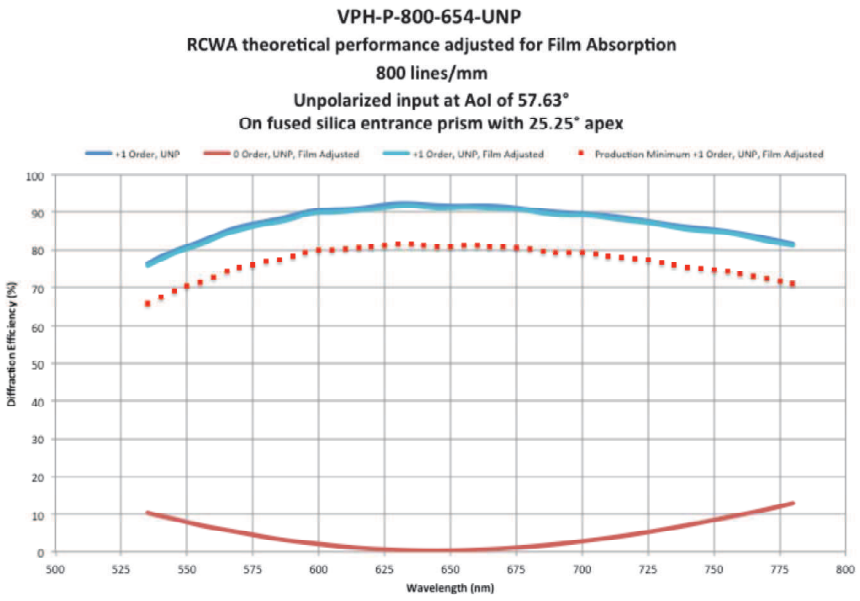

Figure 4.48: RCWA theoretical performance computed by Kaiser Optical System, Inc (KOSI). The light blue curve takes into account the gelatin film absorption. The red solid line curve represents the zero order transmission, while the red dotted curve shows the minimum production acceptance. Figure taken from [4].

The analysis is performed in the H band, of the HJYZ spectrometer module, since it is the one with the largest echellogram free spectral range (with respect to the other bands like J, Y, z) and thus the one that guides the echelle grating selection.
The top level requirements that are considered in this design analysis are:

- Resolving power: Single object High Resolution mode (the main observing mode), R–100000
- Wavelength band: the wavelength splitting and in particular the gap between J and H bands derives from the atmospheric transmission profile regions with good telluric transmission (see Fig. 4.50).
- Inter-order separation: minimum inter-order separation of 20 pixels
- Spectral sampling: target spectral sampling of at least 2 pixel per resolution element. (Goal of 3 pixel sampling is desirable).

In the following analysis the input variable parameters are:

- Fiber-Slit length, sL_1,at the spectrograph pre-slit unit entrance: this is related to the total number of fibers and fiber size that can be used to populate the "fiber-slit".
- Echelle grating dispersing features: blaze angle and relative groove density.

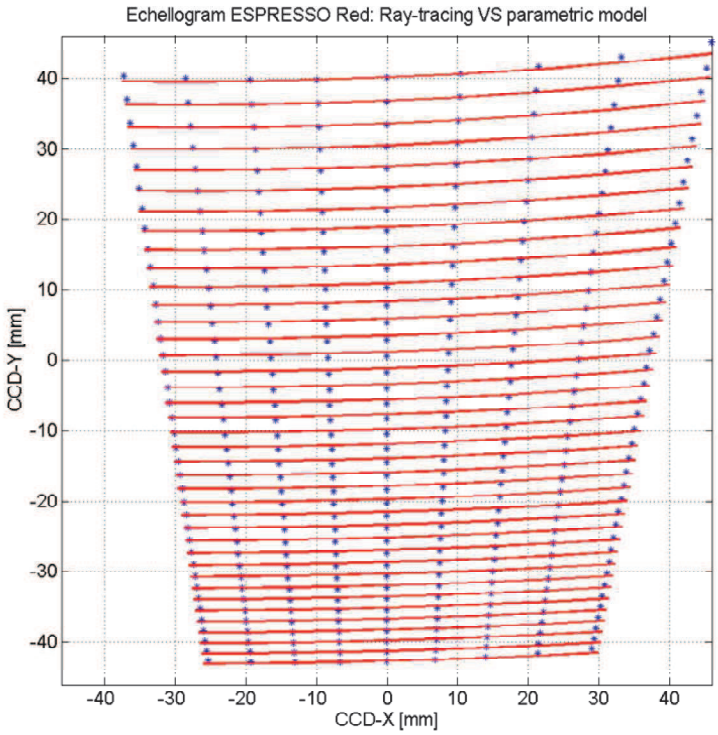

Figure 4.49: ESPRESSO red arm spectral format. The red lines are the diffraction orders computed with the described paraxial parametric model, while the blue dots represent wavelengths propagated with ray-tracing of the complete optical model built with Zemax

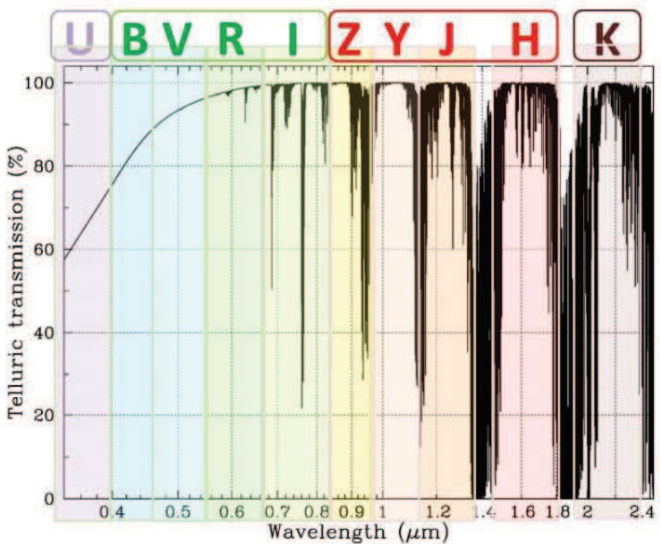

Figure 4.50: Atmospheric transmission profile

Other fixed parameters:

- The telescope diameter of the ELT is D_T is 39 m.
- The angular size of each entrance aperture, χ, is $0.87 arcsec$.
- The optical fiber working F-number, F_{fib}, is 3.5.
- The main collimator F-ratios are: $F_{coll,X} = 10$ (main dispersion) and $F_{coll,Y} = 20$ (cross dispersion dispersion); thus anamorphic factor of 2 in the pre-slit unit.
- The transfer collimator coefficient, TC_{coeff} is set to 0.65.
- In addition to the top level requirements, the sampling values at the blaze wavelengths of the different diffraction orders are: $S_X = 2.7 pix$ and $S_Y = 2.5 pix$.
- The detector pixel size, d_{pix}, is $15 \mu m$

The plots in the following analysis show the different spectrograph output parameters trend as function of the entrance fiber-slit angular length and parametrized for different possible echelle grating blaze angle. Note that that the echelle grating line density is change according to the blaze angle in order to fit the larger diffraction order to the detector width (it has been checked that the minimum diffraction order m_{min} is always larger than 65, so that no problem of shadowing will occur for the diffracted beams).

In Fig.4.51 and Fig.4.52 the fiber core diameter and the number of fibers per each entrance aperture are shown; these are function only of the fiber-slit angular length. The larger the number of fibers, the larger the angular length of the input slit; in addition the fiber core diameter required to sample the same entrance aperture reduces if these two parameters increase.
The collimated beam size, both in main dispersion (Fig.4.53) and cross dispersion direction (Fig.4.54), reduces for a longer fiber-slit since for the same aperture on sky size the longer the slit length the smaller the fiber diameter and thus the equivalent slit width at the entrance of the spectrometer unit. In addition it can be seen that the R4 grating (the one for $\theta_B = 76°$) is the one which allows the smallest beam.
The trend for the total echelle grating mosaic length, shown in Fig.4.55, is the same as for the collimated beam size both for what concern the dependence on the slit length and for what concern the impact of the echelle blaze angle. This is in accordance with Eq.4.8, as the trend of the collimated beam sizes was in accordance with Eq.4.9 and Eq.4.10.
To evaluate the required number of gratings to form the mosaic, the size of the single echelle grating tile considered is the largest one form Richardson Grating Laboratory (RGL), which is $410x205mm$. In Fig4.56 and Fig4.57 the required number of gratings in main and spatial direction are shown. These graphs are very important since it can be seen that the R4 grating is the only one that, in the considered range of slit length, allows to avoid exceeding a mosaic composed by $4X1$ echelle. This is a constraint which comes both from technological reasons, since the alignment of more than 4 grating with common accuracy is very difficult, and from cost budget due to the price of echelle gratings (to give an examplethe R4 echelle gratings installed for

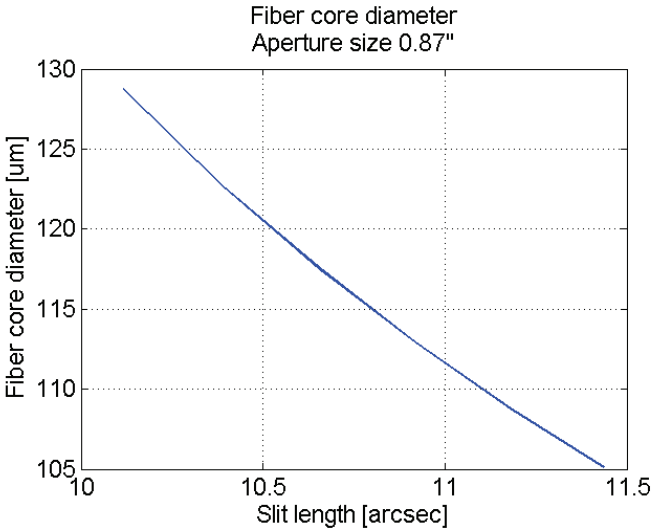

Figure 4.51: Fiber core diameter trend function of the fiber-slit angular length. The slit length is for a single entrance aperture of size 0.87 arcsec. The fibers core diameter reduces because with the increase of the slit length also the number of fibers required increases (see Fig.4.52).

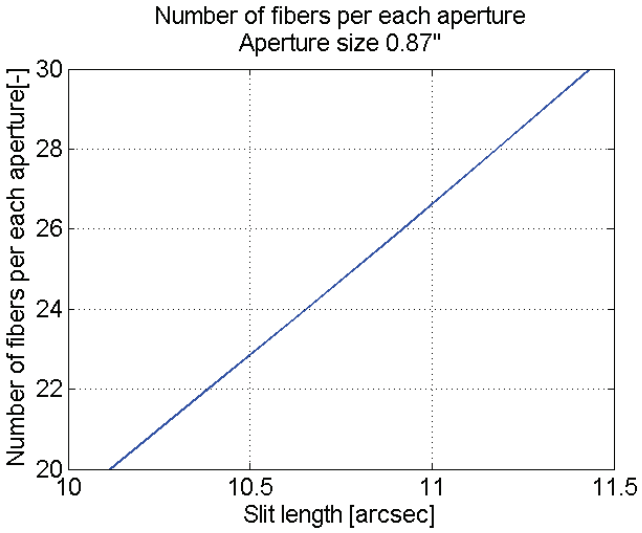

Figure 4.52: Number of fibers trend function of the fiber-slit angular length.

ESPRESSO have a cost of 200 k€ per tile).
The anamorphism that the prism must introduce before the VPH cross disperser is related, as in Eq.4.21, to the sampling values (2.7 in spectral direction and 2.5 in cross dispersion) and to the pre-slit anamorphism (set by the collimator F-numbers); as can be seen in Fig.4.58 this is not depend on the echelle grating type. The graph on the apex angle, in Fig.4.59, shows that if one prism is considered the apex angle reduces when a larger angular dispersion is required, i.e. for a longer slit, and for higher number of cross dispersed orders (higher blaze angle).

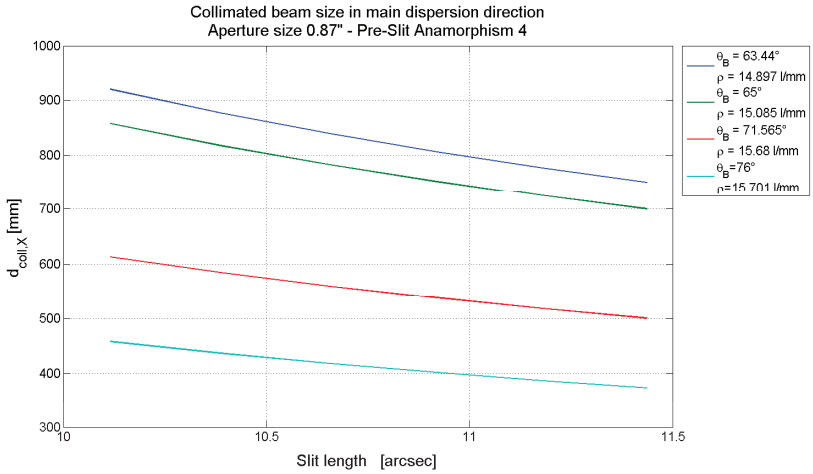

Figure 4.53: Size of the collimated beam in main dispersion direction function of the fiber-slit angular length. This is the beam collimated by the main collimator and incident on the echelle graitng. This reduces as the fiber-slit length increases. The R4 grating allows the smallest beam.

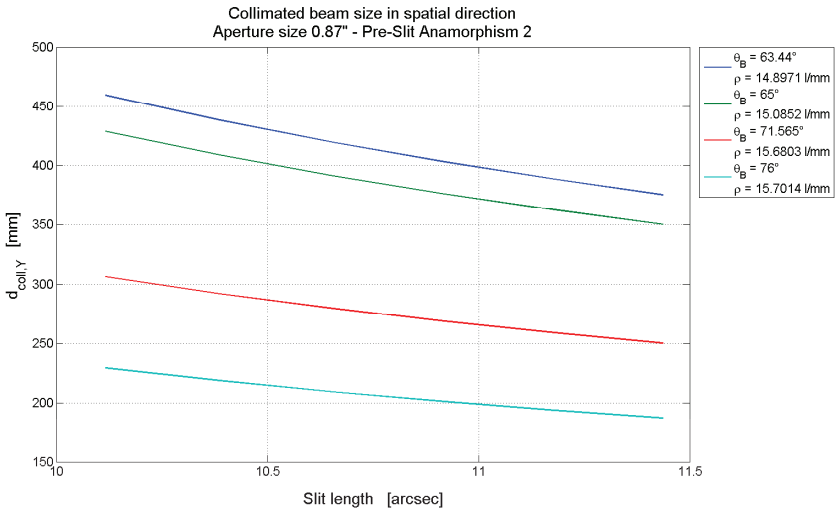

Figure 4.54: Size of the collimated beam in cross dispersion direction function of the fiber-slit angular length. The same comment for Fig.4.53 is still valid also in cross dispersion direction.

The Bragg angle (calculated in air) and line density of the VPH cross disperser are presented in Fig.4.60 and Fig.4.61 respectively. Both of them increase as the slit length increases. The reason is that also the slit length projected on the detector increases and consequently the same happens for the total linear separation between two consecutive orders (called Δy in Eq.4.30). Therefore a larger angular dispersion is required to the VPH and according to Eq.4.31 and Eq.4.32 θ_{VPH} and ρ_{VPH} increase. They also increase with the echelle grating blaze angle because the larger the blaze angle, the lower is the difference between consecutive blaze wavelengths (this is related

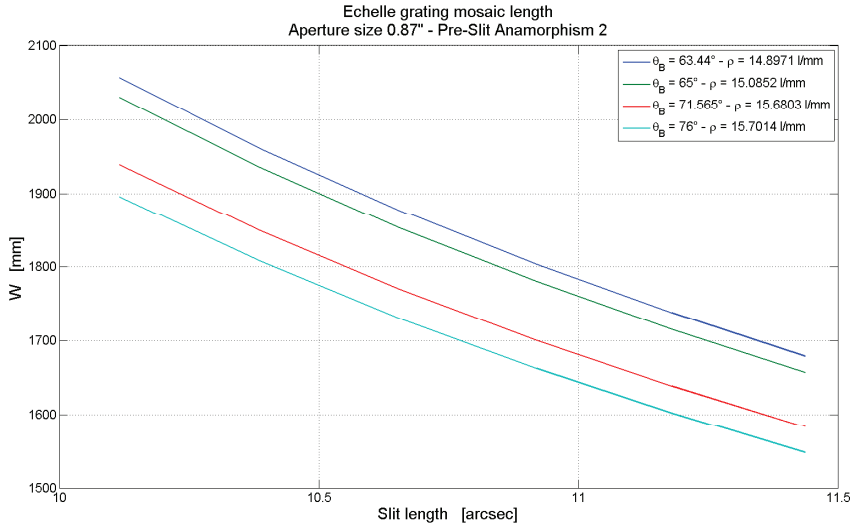

Figure 4.55: Total echelle grating mosaic length function of the fiber-slit angular length. The same comment for Fig.4.53 is still valid as explained in the text.

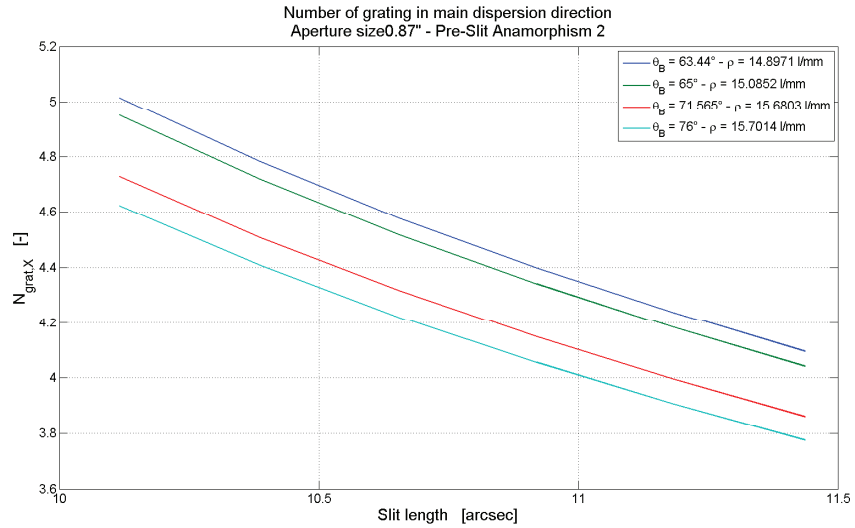

Figure 4.56: Required number of gratings in main dispersion direction, to form the mosaic, function of the fiber-slit angular length. As can be noted, in the considered range of slit length only the R3 and R4 gratings allow to require no more than 4 tile in main dispersion. It must be also noted that increasing shortly the slit length, also with the other two types of grating it would be possible to have less than 4 gratins to collect all the light along the main dispersion direction.

to the fact that the FSR reduces). Therefore the term $\Delta\lambda_b$ appearing in Eq.4.31 reduces, thus θ_{VPH} and ρ_{VPH} increase.

As for the other parameters related to the beam size (and thus instrument size) also the maximum beam footprint at the camera first lens, plotted in Fig.4.64, reduces for a taller and thinner fiber-slit as well as for larger grating blaze angle. Also for this

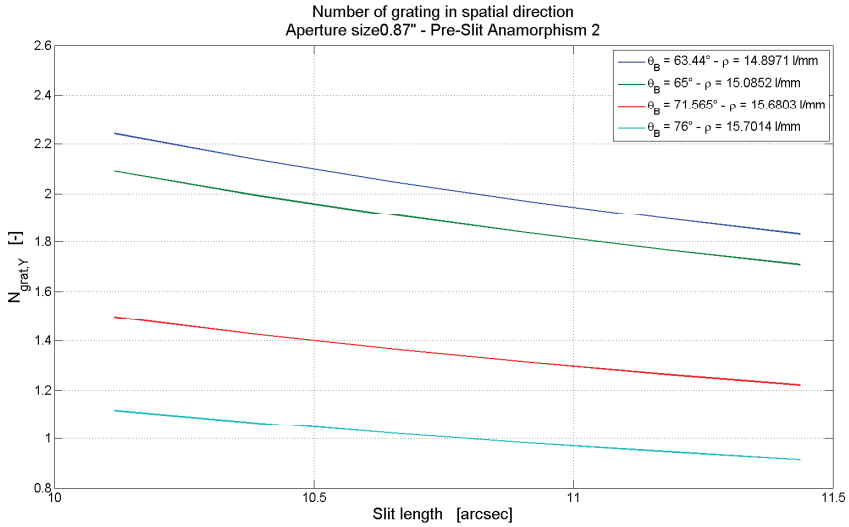

Figure 4.57: Required number of gratings in cross dispersion direction, to form the mosaic, function of the fiber-slit angular length. As can be noted, in the considered range of slit length only the R4 grating allows to require no more than 1 tile in cross dispersion. Contrary of what can be stated for the main dispersion (see previous figure), here a relevant increase of the slit length is necessary to have no more than one tile required also for the other types of grating.

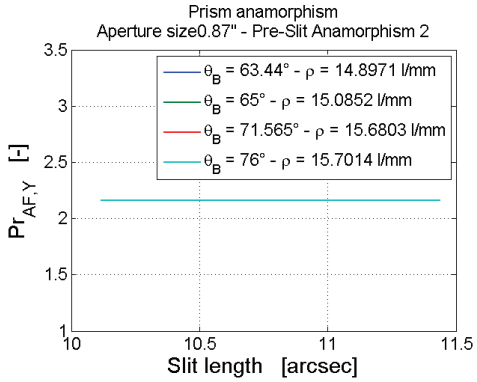

Figure 4.58: Prism anamorphism trend function of the fiber-slit angular length. This is not dependent on the slit length and grating blaze angle as stated in Eq.4.21.

feature it is important to underline that the R4 grating, in the considered range for the slit-length, is the only one that allows to have cameras with a not-extreme size (Maximum size of the first camera optical element).

The camera F-ratios increase with the angular slit length because the taller the slit the thinner it is. Therefore for a defined collimator and fixed sampling values a thinner slit means a smaller effective equivalent entrance slit for the spectrometer unit, then larger F-ratios according to Eq.4.35 and Eq.4.35.
As explained before, the echelle grating line density is set according to the blaze angle in order to fit the larger order of the echellogram on the detector width (main dispersion direction). This is the reason why in Fig.4.65 the detector coverage is close

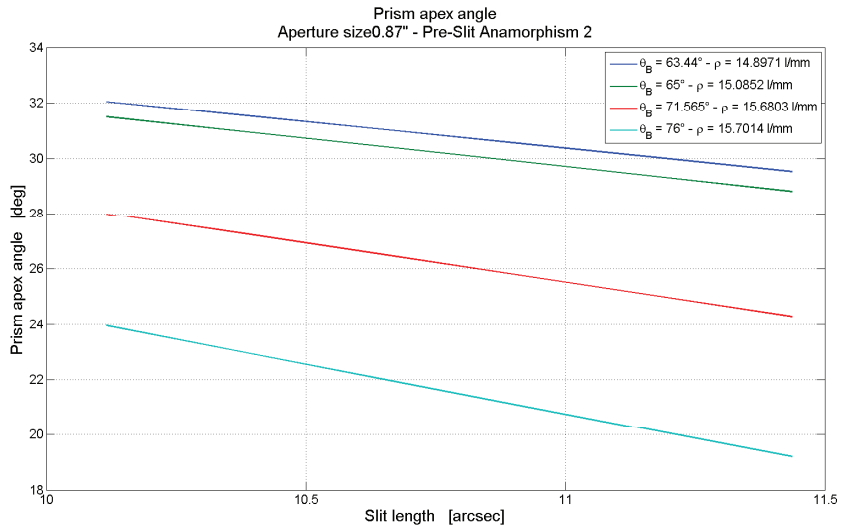

Figure 4.59: Prism apex angle trend function of the fiber-slit angular length. See the text for comments, no prohibitive values result from the simulated slit length range and echelle blaze angles.

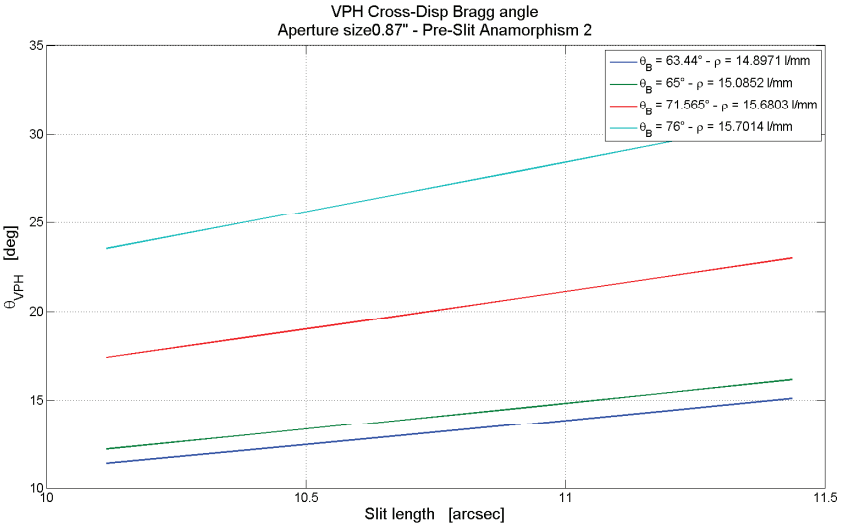

Figure 4.60: VPH Bragg angle trend function of the fiber-slit angular length. As explained in the text it increases with the slit length because this requires a larger angular dispersion as expressed in Eq.4.31. The Bragg angle also increases with the echelle grating blaze angle, because the larger the blaze angle the shorter the FSR and then a larger angular dispersion is required to the cross disperser to separate orders.

to 1 for all the blaze angles, and not dependent on the slit length. The projected echellogram height on the detector (the coverage along the cross dispersion, displayed in Fig.4.66) increases with the blaze angle and also with the slit length. In the first case, the reason is the increased number of order to be cross dispersed and in the second because of the taller slit image to be projected on the detector. The derived

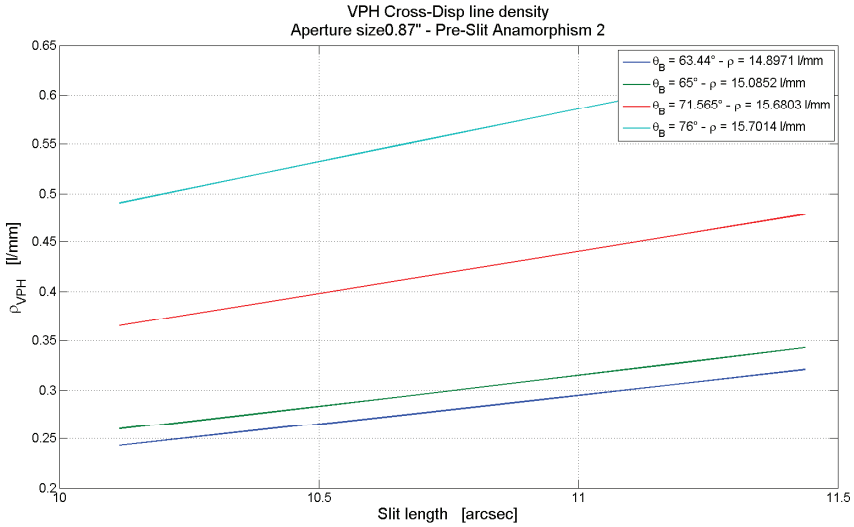

Figure 4.61: VPH groove density trend function of the fiber-slit angular length. The same comments done for the Bragg angle trend (Fig.4.60) are still valid for the VPH groove density.

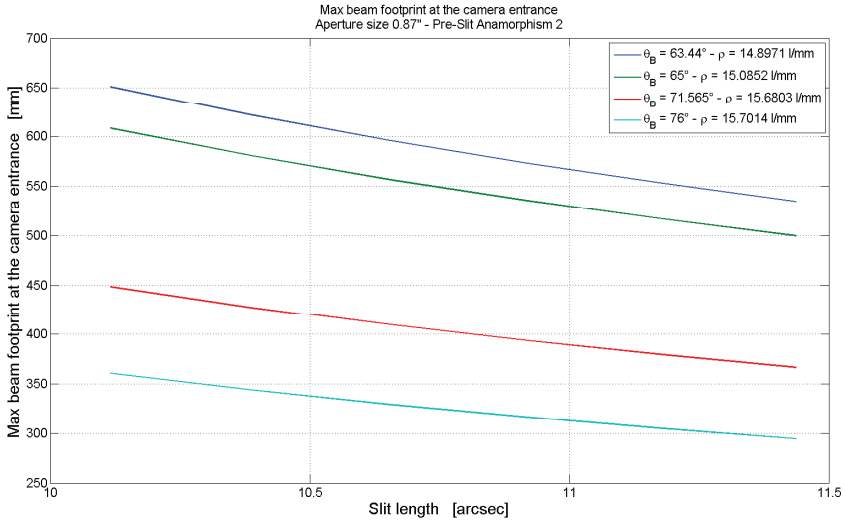

Figure 4.62: Maximum beam footprint at the camera first lens function of the fiber-slit angular length. This refers to the maximum size of the first camera optical element and not to the size of the other optical elements which comes from the detailed design of the camera. As explained in the text only the R4 grating allows to have cameras with a not-extreme size.

message of Fig.4.66 is also that the number of detectors required to collect the light of the whole echellogram is a constraint which limits the slit length.
In this comparative design analysis the efficiency of the spectrograph is evaluated considering the effects of: the theoretical diffraction blaze function of the ehelle grating as explain in Eq.4.17, the Echelle grating coating (the simulated one is aluminum) as well as real practical value of the peaks at the blaze function and VPH cross

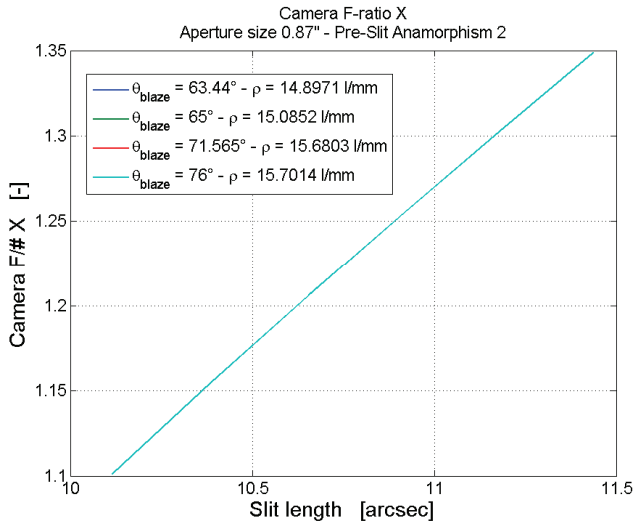

Figure 4.63: Camera F-ratio in main dispersion direction function of the fiber-slit angular length. This is not dependent on the grating blaze angle; in addition it increases with the slit length because the reduced fiber core diameter which means a smaller effective equivalent entrance slit for the spectrometer unit.

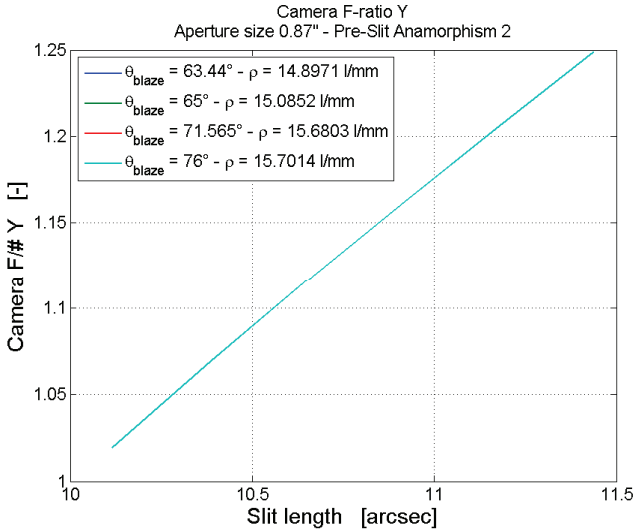

Figure 4.64: Camera F-ratio in cross dispersion direction function of the fiber-slit angular length. This is not dependent on the grating blaze angle. The same comment done for the main dispersion direction holds for the cross dispersion.

disperser diffraction intensity distribution as described in the optimization of the gelatin thickness and refractive index modulation. The reflective and transmission properties of the other optical components could be added to retrieve more accurate and representative efficiency spectral trend, but does not impact on this comparative analysis because all the added terms would be multiplicative factors equal for all the simulated gratings and slits. The figure of merit evaluated is the RMS efficiency

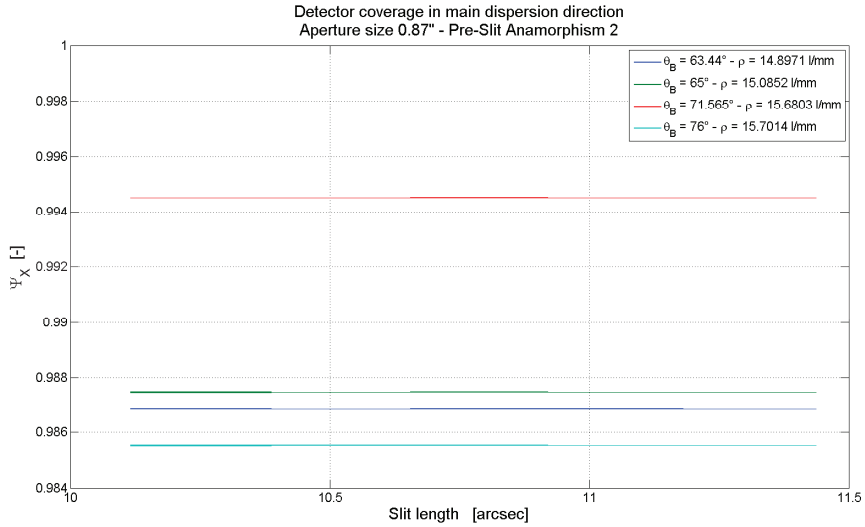

Figure 4.65: Detector coverage in main dispersion direction function of the fiber-slit angular length. This refers to the coverage of the FSR. As explained in the text, this parameter is close to 1 for each value of slit length and echelle grating blaze angle because the echelle grating line density is set to fit the larger order of the echellogram on the detector width.

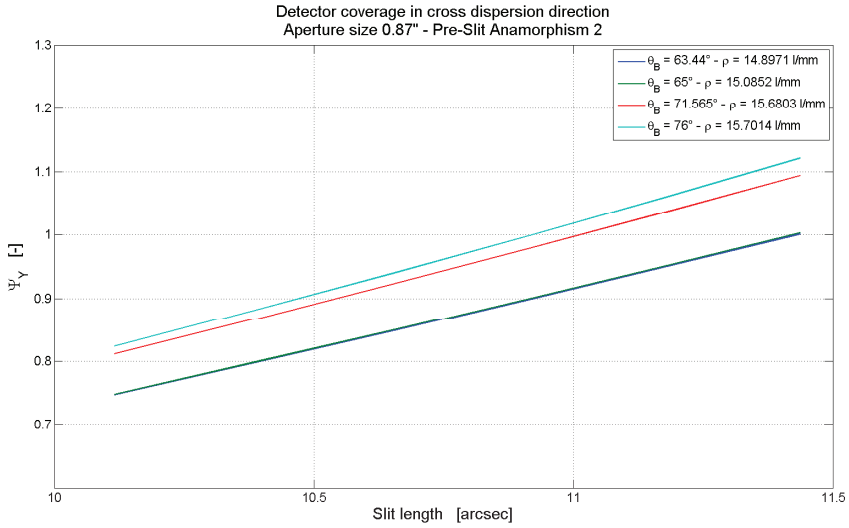

Figure 4.66: Detector coverage along cross dispersion direction function of the fiber-slit angular length. This increases with the slit length and is larger for larger blaze angle since the number of order to be cross dispersed increases. As remarked in the text, the important message from this figure is that the number of detectors required to collect the whole echellogram is a constraint which limits the slit length.

deviation, which is is defined as the rms of the deviation of the computed efficiency η_{diffr} with respect to the grating coating reflectivity $\eta_{eg,coat}$ for all wavelengths in

the band; analytically the RMS efficiency deviation is expressed as:

$$\eta_{RMS} = \sqrt{\frac{1}{N}\sum_{i=1}^{N}([\eta_{diffr}(\lambda_i) - \eta_{eg,coat}(\lambda_i)]^2)} \tag{4.47}$$

From Fig.4.67, it can be noted that the R2 echelle gratings below 11 arcsec slit length are characterized by a larger efficiency loss with respect to gratings with higher blaze angle. This can be explained by the VPH resin thickness optimization value which, for the R2 gratings in the region of slit length lower than 11 arcsec, should be set larger than 30 μm to reduce the losses This is not feasible because a thickness of 30 μm is a practical limit in the VPH fabrication ([10] and [7]). Above 11 arcsec, in the considered slit length range, the differences are of order of 1%. What can be conclude is that in the case of reduced slit length the R4 grating is the favorable one (even if the R3 would be even slightly better) and in the region around 11 arcsec the "efficiency performance" of the different echelles are basically equivalent.

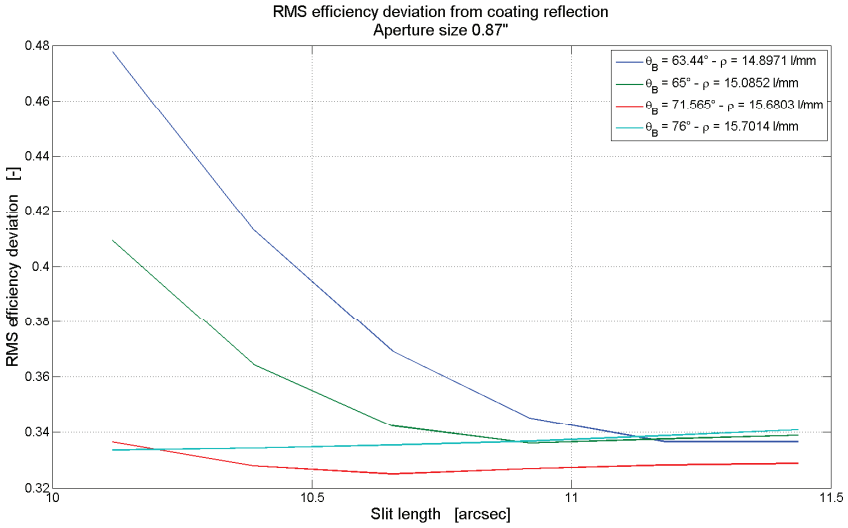

Figure 4.67: RMS efficiency deviation trend function of the fiber-slit angular length. The R2 gratings trend below 11 arcsec is due to the limit on the VPH resin thickness optimization value which is 20 μm.The performance related to the R4 and R3 gratings is very similar in the considered range of slit length.

4.5 Conclusions

Ground-based high resolution spectrometers are exceptional instruments for achieving breakthroughs in a wide range of astrophysical areas. In this Chapter the instrumental key aspects that link the scientific observational performance and technical requirements for such spectrographs have been pointed out. In my Ph.D. work I have been involved in two projects related to Ground-based high resolution spectroscopes: ESPRESSO and ELT-HIRES.

For what concern ESPRESSO in section 4.2 the instrument modeling through ray-tracing software and ad-hoc developed sensitivity analysis tool has been fruitfully used for component optimization, instrument integration and alignment verification with the ultimate goal of achieving the best performance, like optical quality and throughput essential for the maximum scientific return. This was demonstrated with the successful installation and commissioning at the VLT complex in Paranal.

In the framework of the ELT-HIRES project, a parametric paraxial model of the spectrograph has been developed with the purpose to evaluate the impact that the different optical components parameters can have with respect to defined performance requirements and technical constraints. This tool has been detailed described, verified and then fruitfully exploited in the optical design analysis of the ELT-HIRES instrument, for the definition of the main parameters of the optical components of the spectrometer. Specifically the case of the infra-red (H, J ,Y and z bands) spectrograph module has been presented.

Chapter 5

The End-to-End simulator for the ELT-HIRES spectrograph

End-to-End instrument models (E2E) are simulators which allow physical modeling of the whole system: from the light source to the raw-frame data. Synthetic raw-frames are the output which are ingested by the Data Reduction Softwares (DRS) to be analyzed in order to assess if the scientific requirements (in terms of spectral resolution, SNR, Radial Velocity accuracy and precision, etc.), related to the specific science drivers, are satisfied with the specific instrument design and architecture.

These simulators are necessary to evaluate the different effects which can influence the final performance of the more and more complex astronomical instrumentation, like the high resolution spectrograph for the future Extremely Large Telescope (so called ELT-HIRES), required to perform front-line researches in astrophysics. In particular, the science case related to transmission spectroscopy for exoplanet atmospheres requires a careful analysis and design of the experiment in order to succeed. Moreover, the End to End simulator for HIRES, an instrument that aims to reach about 5 ppm in exo Earth atmosphere, will allow Data Reduction, Data Analysis and scientist to overcome possible problem related to instrument well before the first light. In fact for example (not exhaustive) with this tool it could be possible to understand the full chain (from scientific light) to 1D data characterizing the whole error budget, systematic effects and analysis technique well before the on sky emission.

The detection of exo-Earths atmosphere is a challenging (as anticipated in Chapter 3) measure. In this context, the full characterization of Instrumental Profile (IP, or Line Spread Function LSF) from top to the bottom in an End-to-End simulation fashion is crucial to assess not only the detectability of the signal, but also to proper manage possible spurious effects stemming from a non perfect characterization of the IP.

The aim of this work is to design and develop the physical model of the different modules, which compose the entire End-to-End simulator, directly during the project design phase of the High Resolution Spectrograph for the Extremely Large Telescope, so called ELT-HIRES described in Chapter 4. The purpose is to develop a tool as much precise as possible that could be exploited in the next phases of the instrument design to characterise properly this science case. The extreme modularity of the tool will also allow to cover the full scientific topics that HIRES will try to cover in the

next 30 years.

The chapter is organized as follows: the motivations and design philosophy are presented in section 5.1 and section 5.2 respectively. In section 5.3 the global architecture of the system is described while the split down of each module (with appropriate description) is reported in section5.4. The computational architecture is explained (both Cloud oriented and local) in section 5.5 while in section 5.6 the E2E outputs (results) are presented to demonstrate the feasibility of this tool and the proper functionality by adopting (for obivious time constraint) a stellar spectrum simulated from top (theoretical model) to the bottom (extraction with CRIRES+ data reduction pipeline).

5.1 Motivation and main goals

In the last decades, astronomical observation projects have become more and more complex both in term of technologies, instrumentation, operative modes and procedures. This arises both from the infrastructure needed by large aperture telescopes and even more heterogeneous and complex instrumentation, required to perform front-line researches in a wide range of fields in astrophysics. In order to overcome and mitigate this situation, it became necessary to develop End-to-End instrument models (see for example [49] and [60]), i.e. simulators which allow physical modeling of the whole system from the light source to the reduced data.

The aim of this work is to design and develop the physical model of the different modules, which compose the entire End-to-End system, directly during the project design phase of the ELT-HIRES. This approach will benefit the entire project of such a complex instrument since it allows:

- keeping the whole system and its different modules efficiently under control during every phase of the project (both design and assembly-integration phases);
- exploiting reliable tools (the different operative modes of the simulator) at a system engineering level to evaluate the effects of the main instrument parameters on the final performance (given a defined architecture);
- evaluating the effects on the final performance of the different instrument architectures and technologies;
- a deep understanding of the design as well as design optimization and improvements exploiting the capability of early identification of system level problems;
- early performance verification purposes ensuring design requirements are met;
- generation of synthetic detector images for the development of the data reduction software in parallel to the instrument design, or alternatively synthetic images used for testing and verification of existing data reduction pipelines, exploring the possibility of reusing existing pipeline code;
- giving reliable inputs for calibration procedures;

- generation of synthetic detector images closely representing the expected one from the commissioned instrumentation will serve for detailed scientific verifications of the proposed observations;
- improvement in the effectively achievable scientific goals, through the observation performance optimization during simulation, long before it is carried out in practice;
- efficient planning of observation proposals and programs.

What clearly comes out from the main goals here listed is that the End-to-End simulator plays a key role in allowing a successful cooperation of a wide range of users: from project manager and engineers to instrument scientist and astronomers. It is also underlined that the development of such a complex simulator requires the interface and interaction with the work-package managers and expertise of other work-packages in the whole framework of the ELT-HIRES project.

5.2 End-to-End simulator design philosophy

The design philosophy of the E2E simulator is characterized by three fundamental aspects:

- Modularity: the system is organized in Modules and Units, each in charge of its own responsibility, with specified interfaces and possibly with the maximum degree of independence. Since the instrument is itself complex (telescope, fiber link, spectrograph, detectors) one of the key step is to identify and define the different Modules (and Units) and their interfaces. This allows to well characterize the behavior and the functionalities of each of them;
- Flexibility: Since Units and Modules are, at first level of approximation, independent the system should allow to choose what to simulate or not, or to by-pass some units (e.g. simulate only emission from the object without atmospheric contamination or, instead, simulate the echellogram without taking into account PSF diffraction);
- Speed: It is straightforward to expect that a certain amount of simulations will be performed during the whole design phase of the instrument. For this reason, it is crucial to design a solution that could achieve a fast computational time by adopting the proper state-of-the-art technologies. For this reason, the system has been design by the adoption of Cloud-Computing that allow to speed up by various orders of magnitude the computational time.

5.3 End-to-End simulator global architecture

The End-to-End simulator architecture is highly modular, composed by different modules each one with specific tasks, units-functionalities and interfaces. Modularity and flexibility are key points in the definition of interfaces among different modules and among different units or elements. In details, a Unit is a piece of software,

function or interface of a part of the HIRES spectrograph and could be considered as a black-box that exchange data both with other units of the same module, or even with other modules (as represented in Fig.5.1 and 5.2. Modules are piece of software that model either an external component such as Telescope, or the Spectral Energy distribution of the object to simulate, or a piece of software that has not a counterpart on the actual hardware (e.g. the Image Simulator module). In Fig.5.1 the general schematic diagram of the End-to-End simulator architecture is reported. The light path and data-logic path through the different units are shown. Instrument related units of the End-to-End simulator are colored in orange, while in blue are shown the module independent from ELT-HIRES Spectrograph. The units, which compose the Instrument Module, are grouped by the grey box. The data-logic path exploded view with comments is also reported in Fig.5.2.

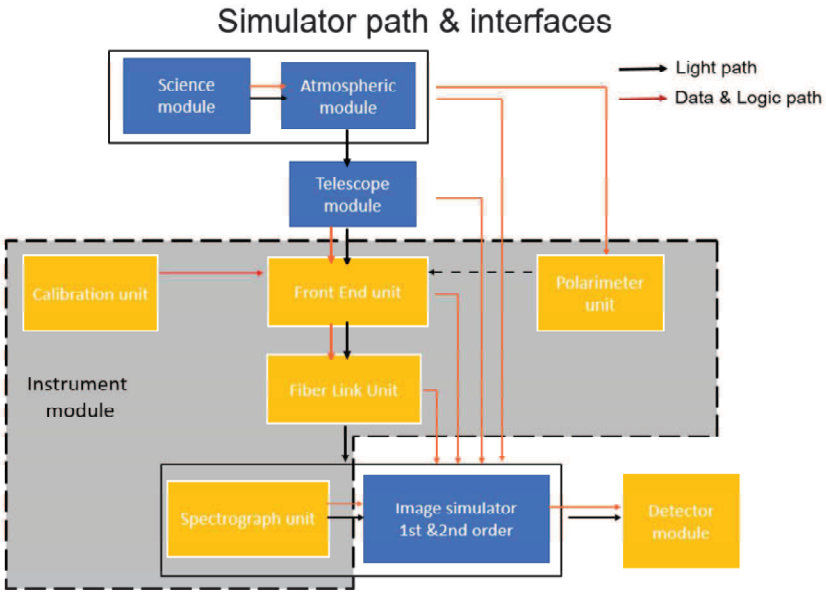

Figure 5.1: General schematic diagram of the End-to-End simulator modules, with the related interfaces. The light path and data-&-logic path through the different units are shown. Instrument related units of the End-to-End simulator are colored in orange, while in blue other units simulated by the End-to-End model but independent from ELT-HIRES Spectrograph. The units which compose the Instrument Module are grouped by the grey box.

Each module or unit are identified and characterized by these main points:

- the main tasks
- the inputs required
- the expected outputs in the expected format (like tfits table, image, etc.)

As one might expect, there are a lot of interface with external work-packages that are needed in order to carry out the simulation. For instance, the detector module which is in charge to simulate the behavior of the detectors should know the characteristic

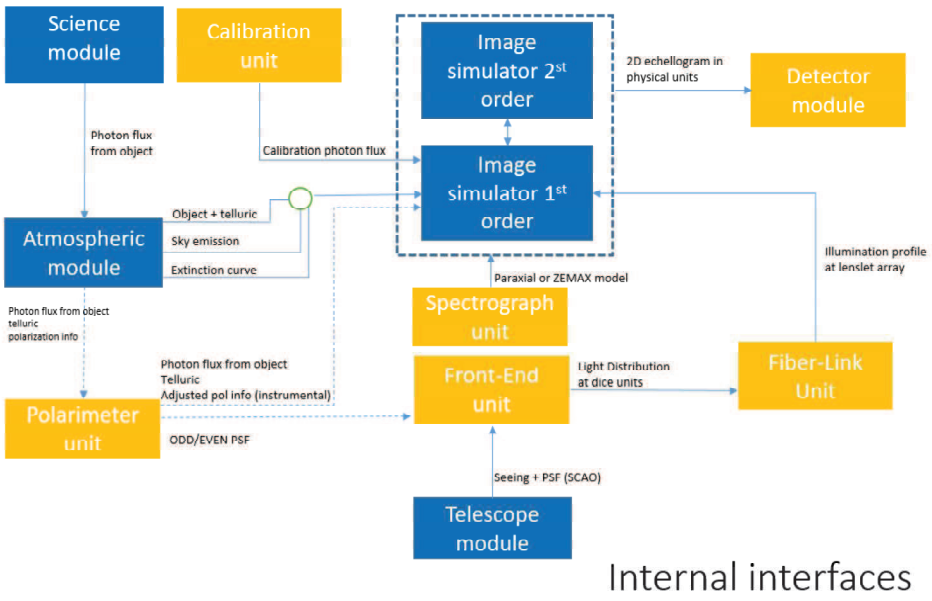

Figure 5.2: Exploded view of the data-logic path between internal modules or units. The color code of the different blocks, representing the different modules and units, is the one described in Fig.5.1.

of the actual hardware (e.g. the Read Out Noise or the Quantum Efficiency) that could be recovered by the Work Package Manager (WPM) in charge that, in this example, is the detector architect. A schematic view of this situation is depicted in Fig. 5.3. The semantic of the data-flow is indicated by the direction of the arrow. For example, the WP32600A (Detectors) feeds both the detector module (e.g. to know the RON, Dark current, etc) and the spectrograph (e. g. number of detector for each band). The whole inputs, outputs and interface link are reported in Tab.8 in the Appendix.

5.4 End-to-End simulator breakdown and description of units and modules

In this section, the description of each block reported in the schematic view of Fig.5.1 is given.

5.4.1 Science Module

In the science module, a synthetic spectrum is created from a set of input parameters related to a specific science case, or source. Currently the module is set for stellar science cases, for which the input parameters are: the spectral type (with specified effective temperature and surface gravity), magnitude, radial velocity and exposure time. For each stellar source, when the magnitude is provided in a given photometric band, the observed energy density is converted, in the same way described for the transmission spectra simulator (see chapter 2, subsection 3.1.2), to photon-flux and

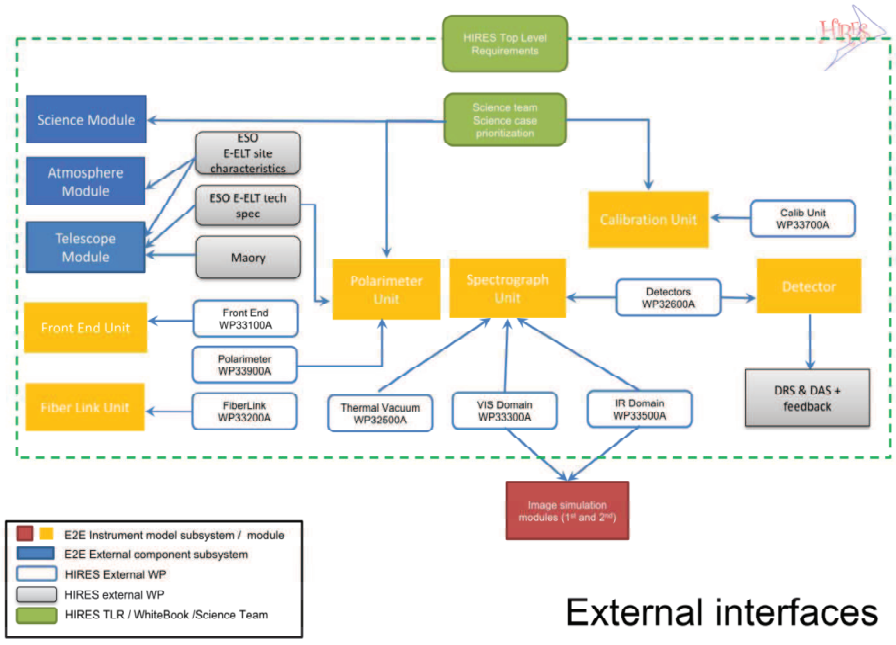

Figure 5.3: E2E simulator external interfaces. These are the interfaces of the different modules and units with other work-packages, external with respect to the E2E WP, in the ELT-HIRES project.

the spectrum is normalized at the reference wavelength of the provided magnitude pass-band and then re-scaled accordingly. This module provides an output file, a FITS table, composed by two columns: the first one is the wavelength, in Angstroms, and the second one is the flux, in CGS units, or photon flux. An example of a synthetic 1D spectrum is reported in Fig.5.4, while a zoom around the H-delta absorption line from Balmer series in a typical main sequence star of effective temperature 5000 K, surface gravity log(g)—4.5 and solar metallicity is reported in Fig.5.5.

The module will also be set for both to stellar populations and extragalactic science (QSO, etc). In fact, adopting the same strategy, it can be extended for the whole science cases of HIRES whenever the theoretical spectrum is known (e.g. for QSO and Ly-α forest for the Sandage Tests simulations). The module for stellar population simulations will consist of a grid of stellar spectra in the Effective Temperature-surface gravity-metallicity space; it will derive the science spectrum from an interpolation of the spectra from those closest to the input stellar parameters within the grid. The grid spectra will be built from extensive libraries of stellar atmospheres and synthetic spectra covering the entire HIRES wavelength range (4000-25000 Angstrom) at very high resolution ($R \simeq 500000$). For the specific cases of transmission spectroscopy the operative mode of the module is the same described in Chapter 2, for the addition of the planetary atmosphere to the star synthetic spectrum.

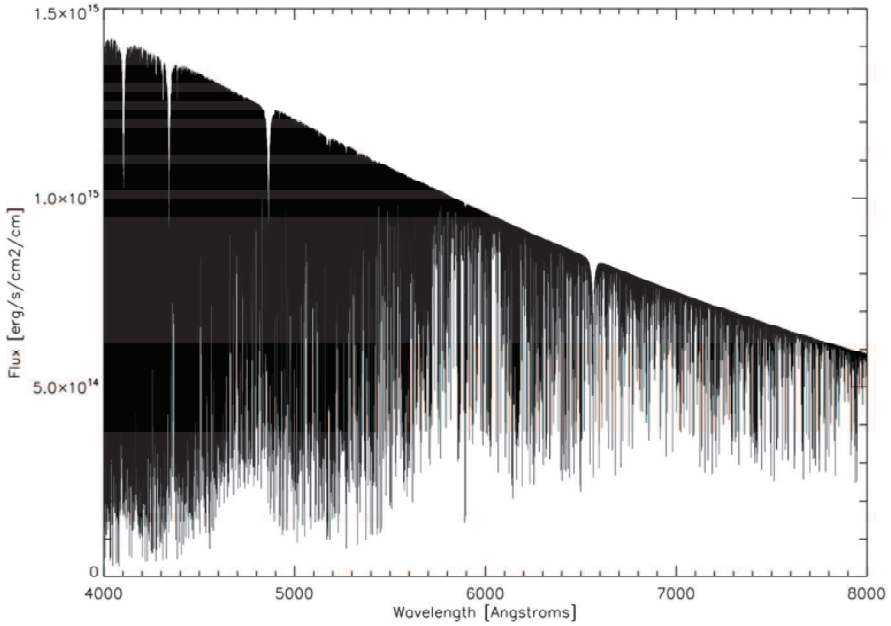

Figure 5.4: Syntethic emission spectrum from a G2V star obtained by the science module.

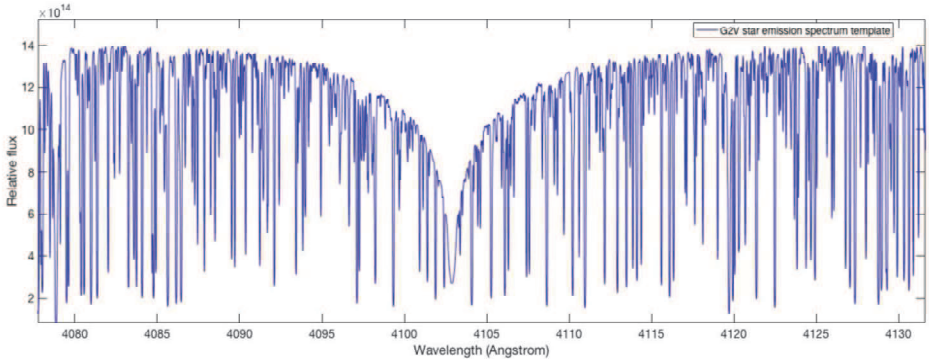

Figure 5.5: Zoom around H-delta absorption line. Typical main sequence star of effective temperature 5000 K, surface gravity log(g)=4.5 and solar metallicity.

5.4.2 Atmospheric Module

The main aim of this module is to model the scattering, absorption and emission occurring in the Earth's atmosphere, and to introduce it to the simulated science observations. This is done by using the ESO SkyCalc tool, described in subsection 3.1.1 of chapter 2.

For the current version of the E2E simply the yearly average meteorological conditions at Paranal are used, a seasonal average of precipitable water vapor is considered and the model is only calculated at the zenith. For the full End-to-end simulator different sky conditions and zenith distances will be probed. The SkyCalc is queried

using resolution step of 0.006 Angstroms, corresponding to at least spectral resolving power of about 550000 with the wavelengths range of ELT-HIRES. The sky spectrum obtained from SkyCalc is rebinned to the same wavelength scale as is used in the synthetic science spectrum.

SkyCalc gives two different outputs: sky radiance (in $\frac{ph}{s \cdot m2 \cdot \mu m \cdot arcsec^2}$) and sky transmission (in transmission fraction) at Paranal. For the End-to-end simulation purposes the sky transmission is divided into two components: general extinction curve, and telluric absorption lines (see Fig.5.6). Extinction curve, shown in the example of Fig. 5.7, is obtained by a spline fit to the data from which the saturated absorption lines are excluded. The absorption lines component, on the other hand, is given by removing the extinction from the total sky transmission spectrum.

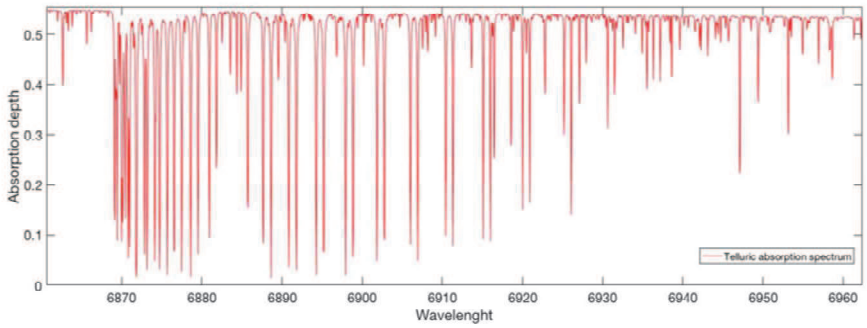

Figure 5.6: Example of telluric spectrum recovered adopting the procedure reported in the text (y axis is in relative units).

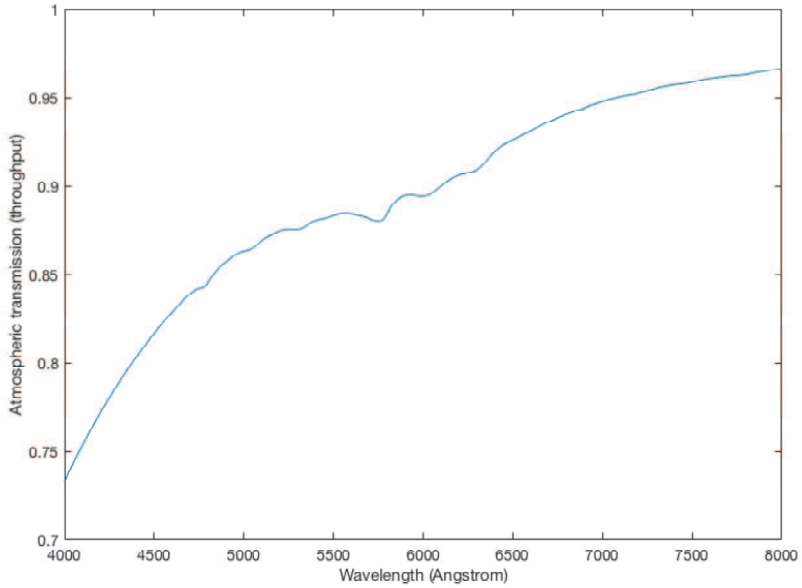

Figure 5.7: Atmospheric extinction curve adopted.

The sky radiance is calculated at the area of one individual HIRES fiber (0.17 arcsec diameter of sky projection) and then the units are converted in $\frac{ph}{s \cdot m2 \cdot \mu m}$. An example of sky emission spectrum is plotted in Fig.5.9.

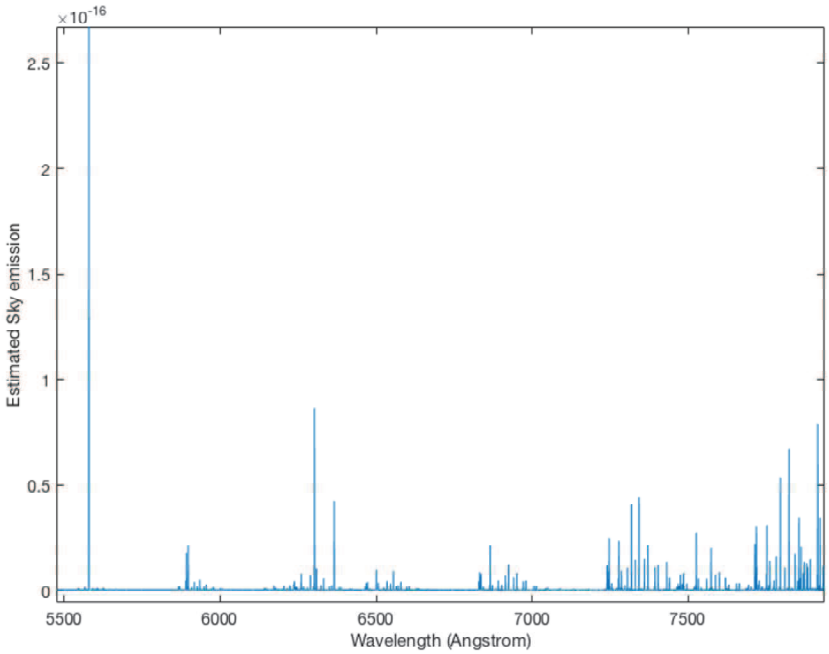

Figure 5.8: Sky emission spectrum in the region of ELT-HIRES R-I bands.

5.4.3 Telescope Module

The aim of this module is to predict the telescope point spread function (PSF) with and without adaptive optics (AO) system corrections, the image at the telescope focal plane and the telescope throughput. This module relies on the PASSATA software ([1]), developed by the Adaptive Optics group of the Arcetri observatory for Monte-Carlo end-to-end adaptive optics simulations and managed by the Telescope Simulation and AO group in the framework of the ELT-HIRES project. The interaction with this work-package has been set for the definition of the interfaces between the simulations of this independent software and the E2E simulator.

The input parameters are: zenith angle, seeing, the estimated average wind speed (from wind profiles of different atmospheric layers), telescope wave-front error matrices (WFEM), the AO system parameters and telescope coatings reflectivity profile. The WFEM and telescope transmission profiles are gathered from ESO, while the set AO system parameters (like actuators number and frequency, number of wave-front modes to be controlled and system acquisition frequency) are internal parameters used by the PASSATA software. The output interfaces are with Instrument Module, for what concern the telescope PSF (both with and without the AO correction), and Image Simulation Module for what concern transmission. The output telescope PSF is given with a sampling of 0.008 arcsec/pixel.

An example of the PSF profile (non-normalized) simulated by the Telescope Module, both in seeing limited and SCAO (Single Conjugate Adaptive Optic) operative mode for ELT-HIRES. The SCAO correction performance is simulated in different conditions of seeing (best seeing = 0.47 arcsec; median seeing = 0.8 arcsec) and source magnitude, for zenith distance = 0 at λ = 1000 nm.

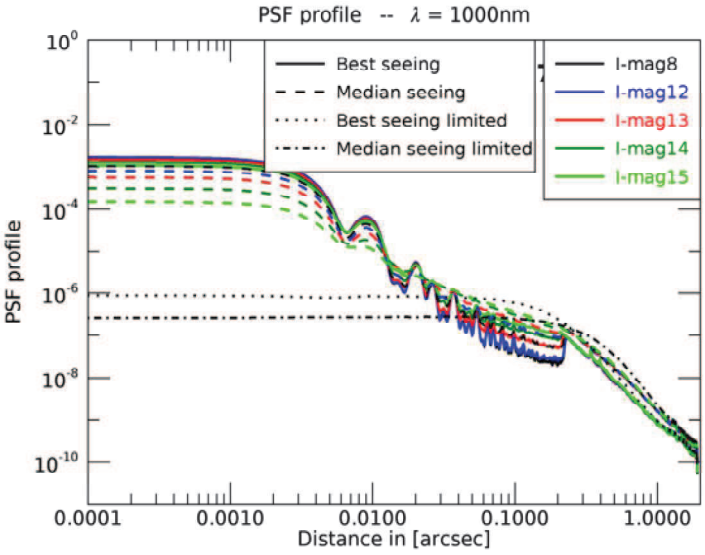

Figure 5.9: Mean profiles of the non-normalized PSFs under different seeing conditions and source magnitude, for zenith distance = 0 at λ = 1000 nm. The comparison bewteen the AO correction and seeing limited case shows that the PSF profiles, at a certain distance from central core, drop to the seeing limited case because not corrected.

5.4.4 Instrument Module

This module is in charge to generate data for rendering the geometrical images of the instrument focal plane, to evaluate the instrument PSF and instrument throughput. In addition it models also the link between telescope and instrument (optical train and optical fibers in the specific case of ELT-HIRES) and it produces the spectral energy distribution of the selected calibration sources at a given resolution for flat-field and/or wavelength calibration. The module is organized in units:

- The Front End Unit and Fiber Link Unit models the link between the telescope and instrument;
- Calibration Unit produces the SED of the selected calibration sources;
- The Spectrograph Unit models the optical path along the optical train taking into account distortion, the effects of dispersive elements and the optical quality in different conditions are evaluated in order to compute the whole point spread function for different wavelengths and positions on the instrument image plane. The transmissivity and reflectivity of the different optical components as well

as the echelle grating blaze function and cross disperser diffraction efficiency are modeled for the instrument throughput calculation;

- The Polarimeter Unit is aimed at simulating the telescope polarization effects and the final odd and even flux at the polarimetry arm output.

The Front-End Unit

The task of this unit is to predict the light distribution at the FE focal plane and to predict the FE throughput. The required inputs are: telescope focal plane image (internal interface in the E2E simulator), the Front-End optical design and optical parameters like the proposed glasses and coatings (input from external WP) in order to estimate the FE point spread function (and the FE throughput). The FE focal plane is the plane where the dicing-unit samples the field (in case of field-dicing technique selected) with a micro-lens array and separates the different parts of the field feeding the corresponding fibers in the fiber bundle (part of the Fiber-Link unit).

In order to predict the light distribution at the FE focal plane (see Fig.5.10) the telescope focal plane image is projected on this plane and then convolved with the estimated PSF of the Front-End. The telescope image in input is sampled with a defined resolution of 0.008 arcsec/pixel; the FE estimated PSF size is 0.025 arcsec.

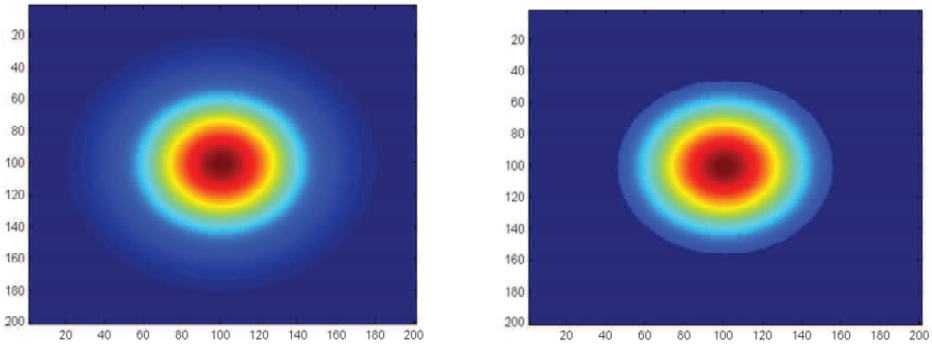

Figure 5.10: Front-End focal plane. *Left panel*: the telescope focal plane image is convolved with the estimated FE PSF of 0.025 arcsec. *Right panel*: Portion of the FE unit focal plane light distribution that feeds the dicing unit aperture.

The dicing-unit micro-lens array has been modeled by simulating the different micro-lenses as sub-circles placed in the FE focal plane according to an hexagonal packing. An example with 30 fibers is reported in Fig.5.11

The amount of flux taken by each micro-lens is computed by evaluating how much of light with respect to the total is captured by each fiber, so that it is possible to estimate the amount of light processed by each of them. Finally the FE throughput is calculated by the modeling of the different glasses and coatings transmissivity and reflectivity. A general order of magnitude is considered starting from the design of other similar projects like ESPRESSO. The output tables with amount of light and related fibers, and FE throughput as function of wavelength are transmitted to the Image Simulator Module.

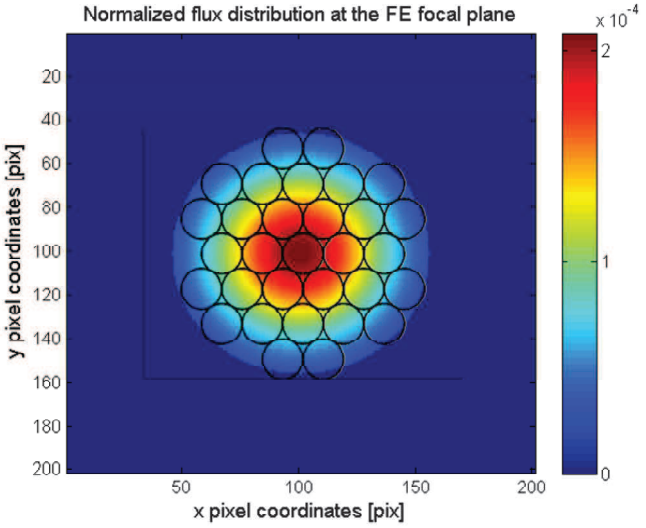

Figure 5.11: Dicing unit array example. 30 micro-lenses modeled as circles and packed in hexagonal layout.

Fiber-Link Unit

This unit has the purpose to predict the light distribution at the end of the fibers by taking into account all the possible effects that could occurs while light passes through the fiber (like modal noise and non uniform illumination).

In the current version of the simulator, a perfect scrambling system is assumed so that at the output end of each fiber it is expected to see a top-hat function. Nevertheless, the whole set of physical parameters foreseen to be considered for a more detailed simulation (which will be part of the next E2E simulator versions) are: fibers-bundles layout, fibers type and geometry and the operative conditions in term of temperature and mechanical stresses.

According to physical optics, diffraction should be taken into account so this profile could be safely approximated by a top-hat function plus the Airy diffraction disk. The most straightforward equation that is able to capture these effects is the so-called Super-Lorentian function (see the eq. 5.1, eq. 5.2 and Fig.5.12).

$$I_{SL}(r) = \frac{I_0(R_{SL}, M)}{1 + (\frac{r}{R_{SL}})^M} \tag{5.1}$$

$$I_0(R_{SL}) = \frac{M \cdot sin(2\pi/M)}{2\pi^2 \cdot R_{SL}^2} \tag{5.2}$$

The free shape parameter M was tuned to M=30 in order to recover to proper dimension and the amount of diffraction effect coming from the finite aperture of the system. In the next versions of the simulator, this module should be able to reproduce physical effects observed in optical fibers, like the modal noise, taking into account the set of input parameters mentioned before.

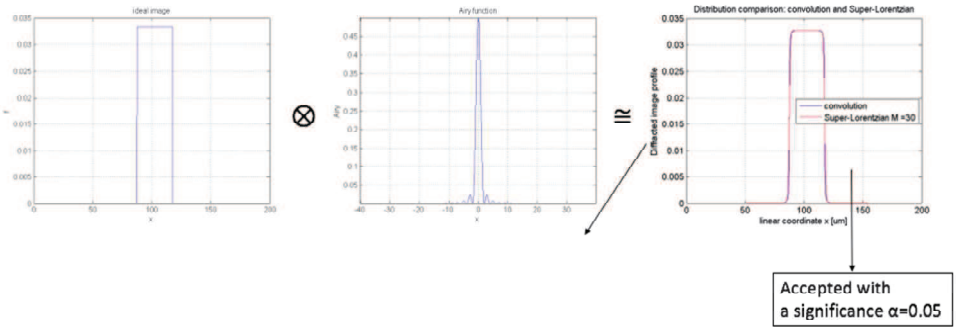

Figure 5.12: *Left panel*: top hat function that model the output of a perfect optical fiber. *Center panel*: diffraction pattern from the output fiber. *Right panel*: comparison between the top-hat function convolved with the Airy disk and the Superlorentian function.

Calibration Unit

The calibration unit is in charge to simulate the Spectral Energy distribution of the calibration sources acting in the same way of the Science module. Both arc lamp and flat field are simulated. This unit requires to know which kind of lamps ones would simulate (flat field, ThAr, Fabry Perot, etc.), the instrument maximum resolution and returns a tfits table that contains the spectral energy distribution of the required lamp in the proper units. An example of this is reported in Fig.5.13, where it is shown a portion of a Fabry-Perot etalon used as a wavelength calibration source.

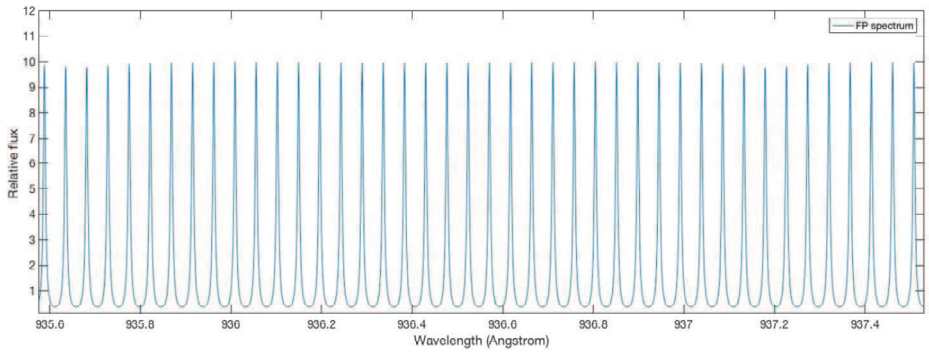

Figure 5.13: Example of SED produced by the calibration unit (Fabry Perot etalon).

Polarimeter Unit

The polarimeter has the aim to give the obtained odd/even PSFs at the level of the proper front end arm, the relative flux in the two modes and the overall efficiency. In the current version of the simulator no modeling is implemented for this Unit.

Spectrograph Unit

The purpose of this Unit is to simulate the physical effects of the different optical components of the spectrometer with the final aim of predict the echellogram (spectral format) at instrument focal plane, the throughput and the light distribution of the camera entrance pupil (this is exploited to simulate/estimate the second order effects on the object spectrum due to pupil obstruction and non-uniform illumination).

Aberrations, distortion and diffraction effects have already been taken into account at this current simulator version, while the physical operative conditions of the instrument in term of ambient, mechanical and thermal effects will be introduced in the future versions.

The spectrograph can be modeled using two different alternative approches: the Parametric Version and Ray-Tracing Version. The former is based on a physical parametric model, deeply described in section 4.4, built with the physical equations and relations which characterize the optical elements, while the latter is a ray-tracing version built with commercial optical design software (e.g. Zemax).

The Parametric Version is a useful tool which can be exploited to have a complete run of the simulator, even if the optical design of the instrument is only at a preliminary phase and the detailed optical ray-tracing files and documentation are not already complete and available, with the purpose of doing considerations regarding the orders curvature, lines tilt, fibers alignment which are relevant aspects for the data reduction software. In addition this approach allows for quick parametric evaluations and analyses concerning different possible spectrograph design choices and architectures.

While the Ray-Tracing Version takes as input directly the ray-tracing optical design files, built in the commercial software package Zemax, and uses some specific software tools to extract the required outputs (spectral format at instrument focal plane, the throughput and the light distribution of the camera entrance pupil), the Parametric Version needs some input parameters to model the spectrograph; these parameters are the same parameters which the optical designer takes into account in the design and optimization of the spectrograph with the ray-tracing software. In the frame of the End-to-End simulator architecture the inputs have been divided in the following types:

- Top level requirements and input performance data:
  - Resolving power
  - wavelength coverage and band division
  - Inter-order separation (separation of the different diffracted orders projected onto the detector surface)
  - Spectral and spatial sampling values
- Inputs Parameters form other modules:
  - Telescope primary mirror diameter
  - Angular aperture diameter of the object image on the telescope focal plane (which is actually related to the seeing condition, the observing mode and should be maximized during the instrument design)

  - Detector pixel size

- Input variable parameters:
  - Number of optical fibers and their working F-ratio (in alternative the entrance slit length can be considered)
  - Main collimator F-ratios (which could be different in the x, spectral, and y, spatial, directions)
  - Echelle grating blaze angle, groove density and tile size (normally high resolution performances require a mosaic made by more than one echelle grating)
  - Cross disperser working angle and groove density
  - Various different possible anamorphic effects generated by the spectrograph optical components
  - Glasses transmission properties (related to the operative conditions)
  - Coatings reflection properties (related to the operative conditions)
  - Optical component emissivity (related to the operative conditions)
  - Operative conditions: temperature and pressure

The echellogram in output from this Unit is composed by the coordinates of the projected resolution elements per each fiber/lens-let on the detector surface; these are passed as input to the Image Simulation Module for the generation of synthetic diffracted spectra (which will be commented in details in the Image Simulator Module). An example of the echellogram format retrieved by the Instrument Module is shown in Fig.5.14.

Examples of the simulation of the projected beam on the first camera lens are shown from Fig.5.15 to Fig.5.15. These figures gives the beam footprint of the smallest wavelength (Fig.5.15), central wavelength (Fig.5.16) and largest wavelength (Fig.5.17) per each diffraction order; all are computed both with the Paraxial approach and Ray-Tacing approach described before.

5.4.5 Detector Module

The task of this module is to simulate, on the rendered data, the effects produced by the detector. Besides the nominal Quantum Efficiency response and the usual noises (like photon noise, Read-Out-Noise, Dark Current, pixel non uniformity, etc.) that are well characterized and, in most cases, straightforward to simulate, this module will be also in charge to add other effects that could be relevant for high precision RV measurement. In particular, three blurring types of the Spectral Resolution Elements (SRE) caused by the detector itself are taken into account:

- The defocusing due to the not ideal planarity of the detector surface: Detector surface could have a typical peak-to-valley un-planarity of the order of 10-20 μm. This means that, with a typical pixel size of 10-15 μm and a camera F-ratio of the order of unity (or generally fast camera like the ones foresee in the current ELT-HIRES design), local defocuses as large as one pixel will be

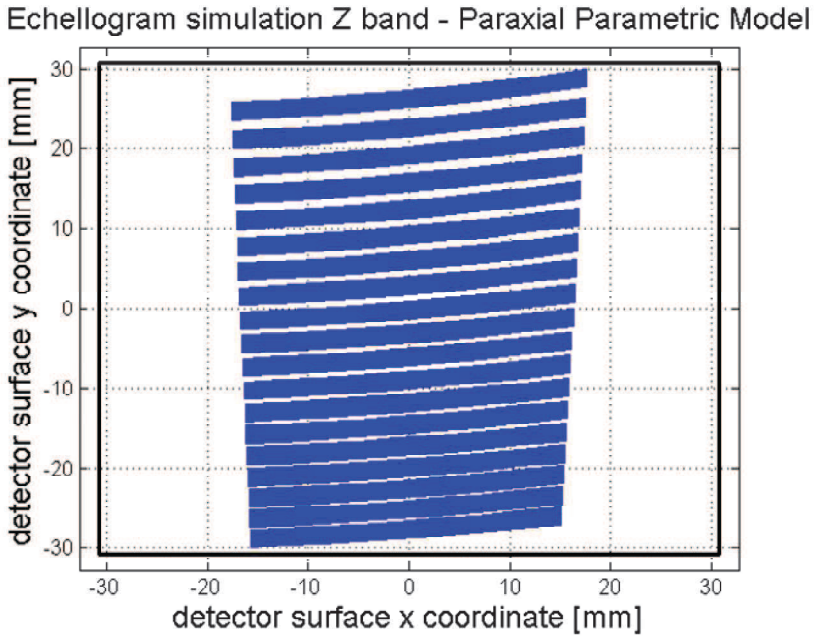

Figure 5.14: Echellogram format example from the Instrument Module Paraxial Parametric Model computation. Note that all the fibers per each order are plotted, including the dark fibers which are exploited to separate the fibers dedicated to the sky and object in the High RV accuracy mode, so that the plot is representative of the IFU mode.

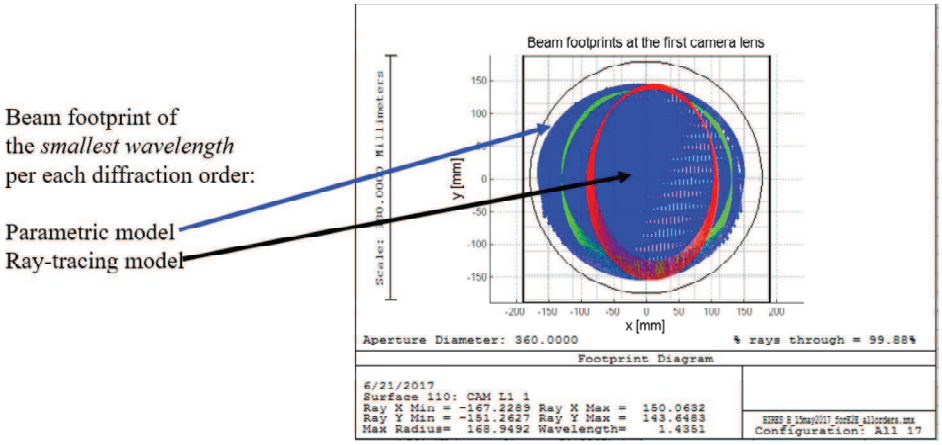

Figure 5.15: Beam footprint on the first camera lens, of the smallest wavelength per each diffraction order. As indicated by the arrows the blue circle represents the boundary of the footprint coming from the paraxial calculation, while the blue area is the footprint computed with ray-tracing simulations. The two results are consistent one to each other.

produced, as depicted in Fig.5.18. To simulate this effect, this module will convolve the SRE image with an uniform circle (to first order) whose radius varies with the (x,y) position on the array. The input of this stage are: a 2D

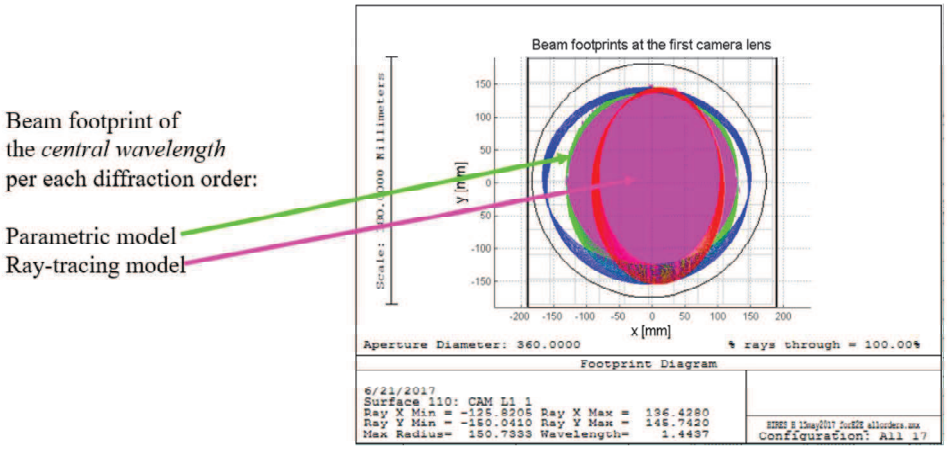

Figure 5.16: Beam footprint on the first camera lens, of the central wavelength per each diffraction order. As indicated by the arrows the green circle represents the boundary of the footprint coming from the paraxial calculation, while the purple area is the footprint computed with ray-tracing simulations. The two results are consistent one to each other.

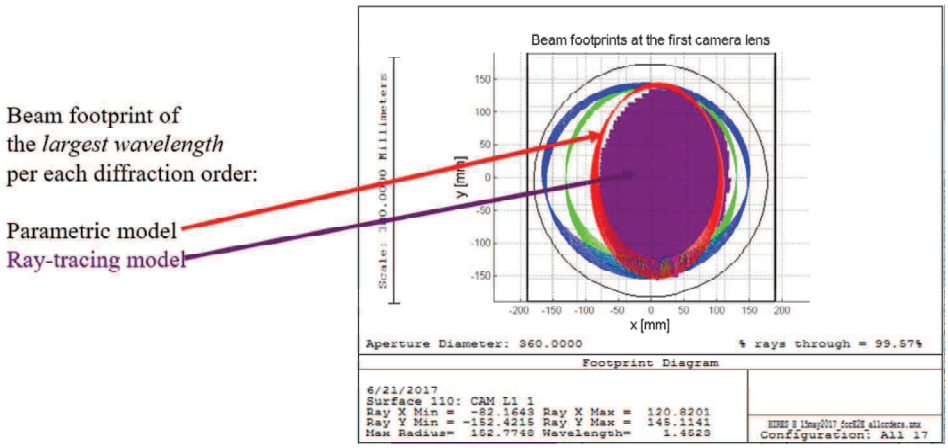

Figure 5.17: Beam footprint on the first camera lens, of the largest wavelength per each diffraction order. As indicated by the arrows the red circle represents the boundary of the footprint coming from the paraxial calculation, while the dark-purple area is the footprint computed with ray-tracing simulations. The two results are consistent one to each other.

map of the planarity deviation in μm, and the 2D image of the SREs produced by the Image Simulator 1st order Diffraction. The output is a 2D array with the locally defocused PSF, at same sampling of the input one.

- The optical defocusing of the diverging beam after focal point, while it penetrates in the detector substrate and is absorbed: This effect depends on the thickness of the detector sensitive layer, which can be very thin, as few μm in Near Infrared detectors, or very thick, as 50 to 300 μm in the fully depleted CCDs, used in the visible bands. We describe hereafter the latter case. At

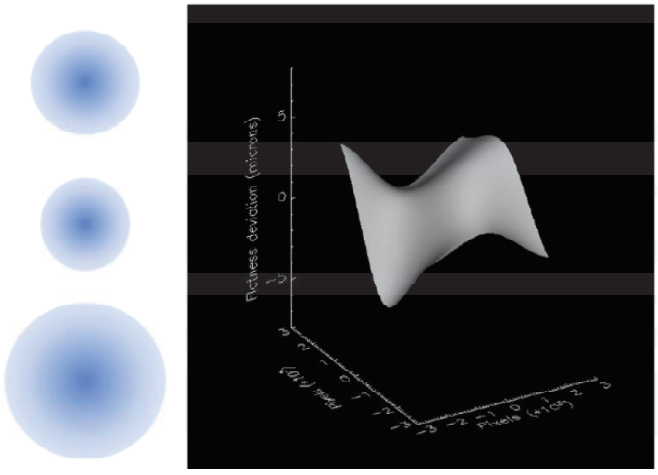

Figure 5.18: Simulation of a non-planar detector surface used to reproduce the local defocusing effect, for which a general PSF is defocused in a different way through the focal plane.

wavelengths greater than approximately 900 nm, the quantum efficiency of silicon CCDs is known to rapidly fall, due to the increase in absorption depth of the silicon substrate. The use of a thick CCD, with substrate thickness greater than 100 μm, is therefore required for the visible channel in order to maintain high efficiency. However, as the optical beam passes through the thick CCD it gradually diverges, as shown in Fig.5.19, resulting in an extra blurring of the final PSF. This effect is simulated by using both ray-tracing simulations to model the beam divergence at the level of the detector and mathematical modeling software package (like MATLAB). On the right side of the figure it is possible to see that, as the depth in the silicon increases, the blurring also increases. Moreover, this blurring is asymmetric for any off-axis ray, for which the centroid of the resulting photons distribution moves laterally depending on the entering angle of the beam. Inputs parameters are: the entering angle of current beam, and optical properties and thickness of the sensitive material. The output is a 2D "Detector PSF" to be convolved with the photon distribution provided in the Image Simulator module 1st effect (see proper section) for each spectral resolution element.

- Gaussian blurring due to the dispersion of electrons across the sensitive material: When a photon is absorbed within a CCD silicon substrate it generates an electron, which then moves towards the collection region of the CCD pixel under an applied voltage. As the electron moves through the silicon, it can drift into a neighboring pixel if the applied voltage is not sufficient to move it quickly to the collection region. This effect, known as Lateral Charge Diffusion, causes the measured FWHM of the SREs to broaden and, for a fixed voltage, increases with sensor thickness.[1] According to [81] a typical broadening of 4 μm RMS at

[1] A full description of the diffusion process, and the way to calculate the corresponding blurring, is given in [81].

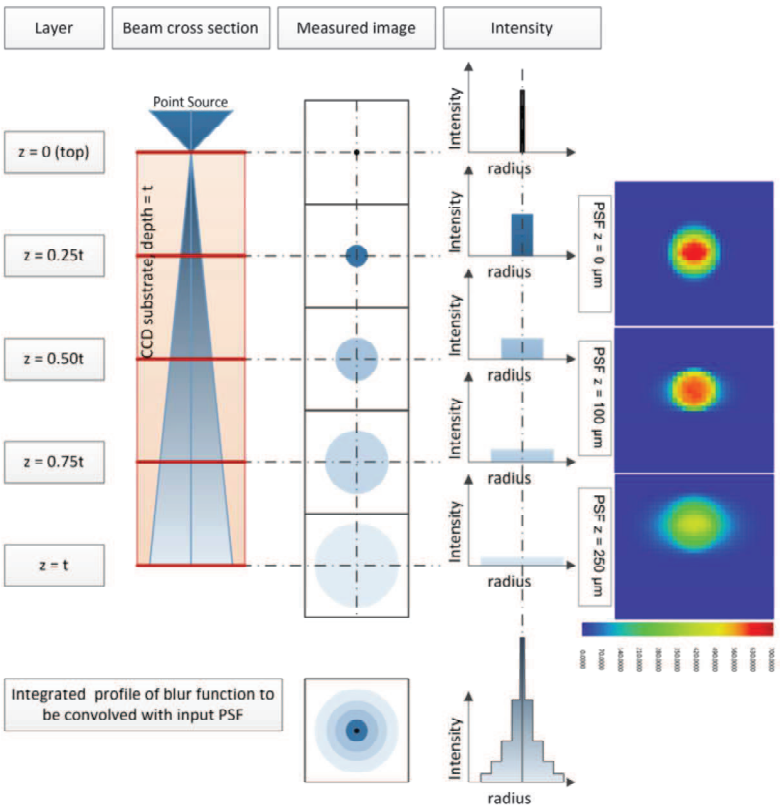

Figure 5.19: Schematic of the process of beam divergence in a thick CCD (courtesy from David Lee).

a wavelength of 650 nm is expected for a 250 μm thick CCD operated at 100 V. A similar effect, due to both charge diffusion and inter-pixel capacitance, is also present in the thin CMOS used for Near Infrared channels, and cause a cross talk to the first neighbor pixels with a typical value of about 2%. Inputs are voltages, thickness of the sensitive material and the size of the charge collection region, while the output is the FWHM of the Gaussian kernel to be convolved with all previous optical broadening effects.

The net result of these three effect is a kernel function (possibily modeled as a 2D image) to be added by means of convolution to the diffraction photon distribution computed by the Image Simulator Module.

5.4.6 Image Simulator Module

This portion of the simulator is the kernel of the whole system. This piece of software, which runs heavily in parallel in a cloud distributed environment (see next section), is responsible for rendering the photons distribution of each resolution element for each fiber, for each order for each wavelength as should be detected at the level of the detector. A portion of this module, written in MATLAB, is also in charge to glue the various Units and Modules to produce the actual echellogram.

In particular, each Spectral Resolution Element (SRE) is computed as the surface integral for each pixel in a reasonable region around it, to estimate the light distribution. Since the SREs are independent and can be summed up at the end of the computation, each SRE is computed independently of the others and this procedure could be parallelized easily by adopting a certain number of computing nodes (see next Section for further details).

The perfect image of the fibers as seen at the level of the focal plane is estimated as explained in the Fiber-Link Unit subsection. Then, this distribution must be convolved with the PSF of the instrument that includes both aberration, diffraction and effects from the optics of the spectrograph. This is referred as *1st order PSF effect*. This estimated could be carried out in two ways:

- Analytically, using only the spectrograph paraxial model. In this scenario, the net effect is a Gaussian function which FWHM represent the quality of the system as the familiar rms spot radius used by Zemax to assess the image quality.
- Using ray tracing, by polling Zemax to recover the map of the PSF that could be used as a kernel that could be convolved with the light distribution coming from the fiber.

For the current version of the E2E simulator the first mode (analytically) has been adopted, although the whole architecture of the system is able to handle also the second one.

The actual PSFs, however, contain also other effects coming from the detector, as explained in the proper section, and from diffraction coming from the obstruction due to the design of the spectrograph camera, especially in the case of Schmidt optical configuration.

Diffraction spikes in the PSF are generated by the presence of sharp edges in the beam shape at pupil position. Each spike extends towards orthogonal direction with respect to the edge that produced it, and has higher intensity for thicker structures and for sharper borders, with a flux asymptotically decreasing as r^2, i.e. much higher than the asymptotic decrease proportional to r^3 of the Airy diffraction halo (as explained in [63]).

The importance of simulating diffraction spikes for a spectrograph like ELT-HIRES is that, if a spike happens to extend along the spectral direction in the final image, it will spread the flux of any bright spectral line onto the adjacent spectral intervals, thus increasing the local stray light contamination, an effect especially important around the sky emission lines, which are narrow and intense.

Fig.5.20 shows an example of this problem, where a pupil obstruction, formed by a vertical fiber slit, a square detector box and a three-arm spider, (top left) produces various diffraction spikes in the PSF at focal plane (top right). The horizontal spikes coming out from the bright sky emission lines (OH line in this near infrared example) are due to the vertical edges in the obstruction, and they overlap to the spectral direction producing a bright false continuum (bottom).

A correct spikes simulation allows to quantify this contamination and to provide possible solutions, as done e.g. in the E2E simulator for the spectrograph MOONS at VLT ([63]), for which a re shaping of the pupil obstruction has been designed to

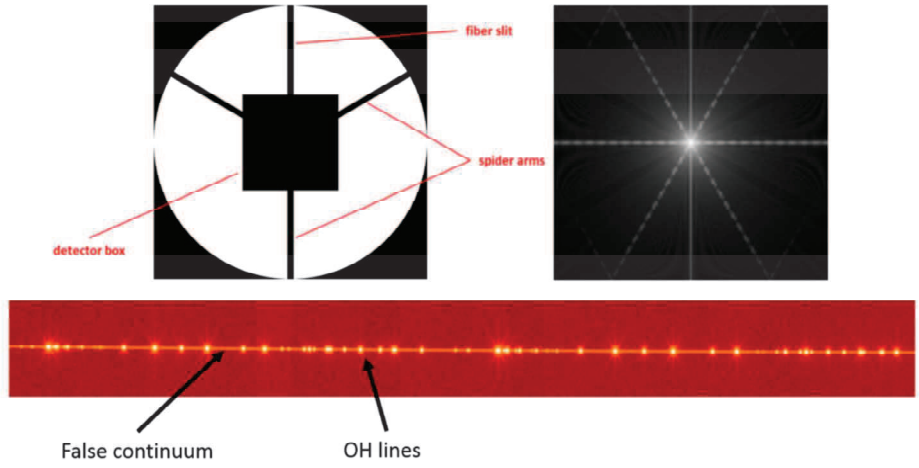

Figure 5.20: Example of diffraction spikes: see text for details. Figure taken from [63].

deviate the diffraction spikes and avoid their overlapping on the spectral direction (see Fig.5.21 and Fig.5.22). In this context, the Image Simulator Module (2^{nd}

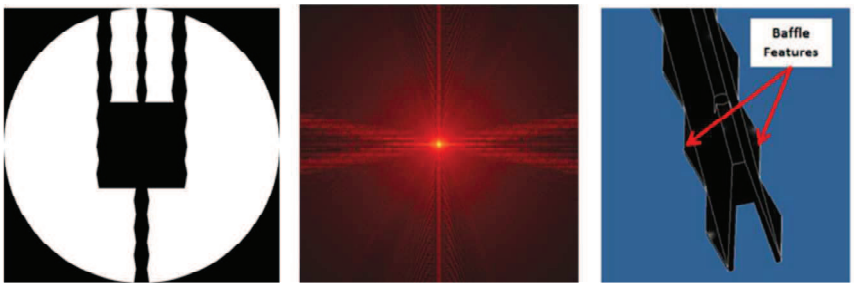

Figure 5.21: Optimized obstruction shape for MOONS-VLT: both the fiber slit, the two-rib fork spider which holds the square detector box, and the lateral side of the detector box itself, are masked with a 10 deg triangular wave profile (left), in order to split the horizontal diffraction spikes in two branches and avoiding its overlapping to the spectral trace (middle). The mechanical design of the spider mask is shown in right panel. Figures taken from [63]

order PSF effect) first computes an high resolution model of the beam obstruction, which depends on the beam shape, angle and position when the beam intersects the obstructing elements (different for each field and wavelength, and passed as inputs to this module, coming from the Spectrograph Unit of the Instrument Module). Then, it computes the diffraction component of the PSF shape by means of a Fast Fourier Transform of the obstruction model, adopting suitable routines already developed and tested for MOONS spectrograph to guarantee the accuracy of the result.

The diffraction effect that influences the shape of the PSF is the possible non-homogeneity of the beam at pupil position, which causes the Airy image to be distorted, depending on the way the different regions of the pupil are illuminated. Such non-homogeneity could be caused, in fiber-fed spectrographs, by angular non-homogeneity of the beam at fiber output, possibly due to fiber modal noise and/or

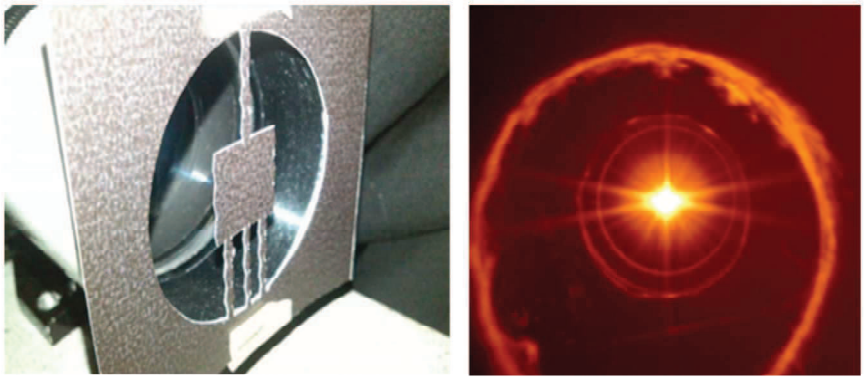

Figure 5.22: Lab test to confirm the diffraction shape shown in central panel of Fig.5.21. *Left panel*: hand cut obstruction mask at the entrance of the test camera; *right panel*: resulting diffraction spikes. Courtesy of G. Li Causi.

focal ratio degradation. When, in future versions of the E2E simulator, the distribution of such angular non-homogeneity of the fiber output is available and passed as input, it is combined with the obstruction module and propagated through the FFT.

The output of this module is a 2D image of the diffraction component computed on a sub-pixel sampling, to be combined with the 1st order optical aberration PSF (explained before) and with PSF map estimated in the Detector module. Finally, the photon distribution coming from fiber output end (see eq.5.1) is convolved with the whole whole PSF model estimated, as explained.

It is now worth to spend few words about the computation of the image of each SRE. In particular, for the case of high resolution spectrograph where HIRES aims to reach 10 cm/s of radial velocity precision and wavelength accuracy, the wavelength image barycenter reconstruction accuracy will be the primary performance of this module; to give an order of magnitude the spectral resolution element barycenter reconstruction accuracy should be better than $\sim$ 1 nm. This requires, as expected, that the computation of the surface integral should be performed with high precision.

For this reason, we have developed our own integral computation procedure using an innovative approach based on heavy parallel computing CUDA by NVIDIA for the evaluation of single point convolution value. The procedure is based on standard integration algorithm and, among others, foresees two different variable parameters exploited to directly control the computation accuracy and cost. These parameters are the single pixel partition for the integral calculation and the pitch scanning of the Fiber illumination equation and PSF for the point convolution evaluation.

The adoption of parallel computing is crucial, since the simulations of synthetic spectra gathered by HIRES involve a huge amount of computational power. In particular, each resolution element (SRE) must be simulated with an accuracy of few nm on the detector and the number of SRE (including sampling anti-aliasing) is in the order of 7 x 10^9. It is thus clear that the complexity in time is a key factor in the design of our simulator. The image of single resolution element is obtained computing the convolution of the illumination profile that can be safely modeled as a Super-Lorentzian function with parameter M = 30 (see Fiber-Link Unit description

for details), with a Gaussian Point Spread Function that represent the PSF of the spectrograph itself (as explained before).

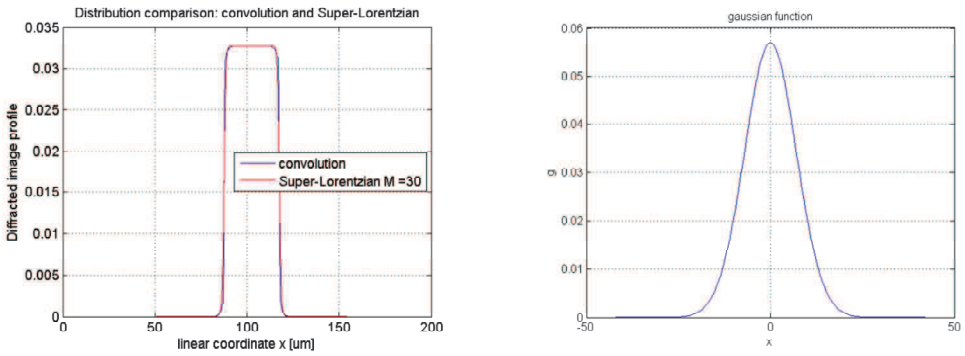

Figure 5.23: Left panel: fiber exit illumination profile assuming a Super-Lorentzian function. Right panel: Gaussian Point Spread Function that represent the PSF due to optical aberrations of the spectrograph itself (paraxial and analytical). The two functions are convolved to evalaute the photon distribution for each single SRE.

The computation of each SRE image is performed on a grid of 10x10 pixels sampled in step of 0.1 pixels as depicted in the schematic of Fig.5.24. In particular, for each pixel a Computation CUDA Block is assigned and, for each one of the 100 sub-pixels, a worker thread compute the value of surface integral in that point. This kind of approach, allows to run in parallel 10.000 worker thread on a single GPU kernel allowing to decrease the time of computation up to 0.001 μs for each SRE. Since the problem is, as explained, parallelizable and SREs are independent of each

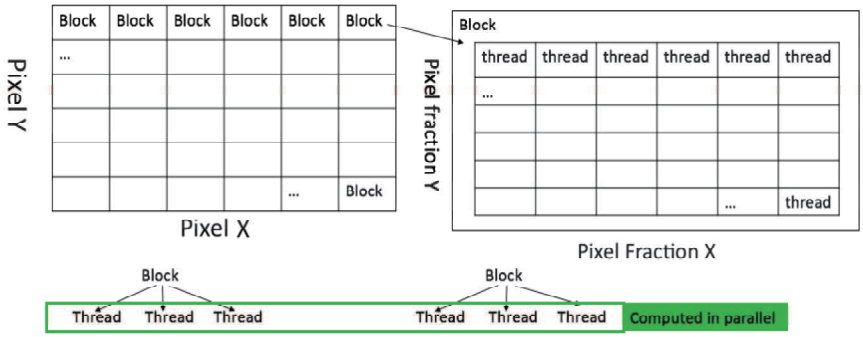

Figure 5.24: Schematic of CUDA Block and Worker Thread architecture for the computation of convolution and surface integral on each detector pixel.

other, we exploited the capability of cloud computing using the Elastic Computing 2 of Amazon Web Services (AWS) to increase the number of computer available to perform the whole simulation (details in the next section).

5.5 Computational Architecture

In this section, we briefly illustrate the architecture of the computation of the echellogram that take places in E2E simulator. The whole chain is carried out both locally and in Cloud Computing paradigm. For this reason, the logical flow is first described and then the details on the Cloud Architecture designed that will be suitable for the present and future versions of the E2E simulator are given.

In order to better illustrates how the various modules and units work togheter, we assume to simulate the observation of a $m_V = 10$ star with exposure time of 50 sec in polarimetric mode (SNR = 50 combining both slices), which means that Object A and Object B fiber-bundles contain the same object but with different polarimetric states (odd or even flux). We further assume to perform a hot calibration (simultaneous reference) and to include only the 1^{st} order PSF effects in this demonstration because of computational cost reasons.

5.5.1 Logical steps

For simulating a synthetic echellogram (for each band) these steps are followed:

1. The spectrograph Unit is queried (through MATLAB) for the band to simulate and for the relative observing mode (e.g. Z band that is the one this example refers to) in order to retrieve a database that contains the following information for each resolution element:

   - Number of the order;
   - SRE ID (used only for debugging purposes);
   - Fiber ID;
   - SRE central wavelength (in μm);
   - X and Y coordinate of the position of the SRE on the detector (pixels);
   - Dimension in the X and Y direction of the image of the fiber (Super-Lorentian profile parameters);
   - Boundaries in X and Y that models the region (and its size) on the detector where to perform the computation of the surface integral to obtain the light distribution coming from this SRE;
   - PSF X and PSF Y FWHM (in μm).

   This database is stored as binary file table. Fig.5.25 reports a small sample of it.

m	SRE ID	Fib ID	wave	xcoord	ycoord	Sampl X	Sampl Y	xcoord in	ycoord in	Npix box		PSFx	PSFy
50	1	1	0.6517766	1287.640388	1539.644534	2.73826	3.12924	1282.00	1534.00	10.00	8.00000	8.00000	10.000
50	2	1	0.6517832	1290.379171	1539.448912	2.73847	3.12924	1285.00	1534.00	10.00	8.00000	8.00000	10.000
50	3	1	0.6517898	1293.118160	1539.253144	2.73867	3.12924	1288.00	1534.00	10.00	8.00000	8.00000	10.000
50	4	1	0.6517964	1295.857354	1539.057232	2.73888	3.12924	1290.00	1534.00	10.00	8.00000	8.00000	10.000

Figure 5.25: Portion of the database computed by the Spectrograph Unit.

2. For each row, a CUDA routine compute the surface integral needed to estimate, with an accuracy of few cm/sec, the light distribution (normalized to 1) for the related SRE. At this stage, when the diffraction spikes effects are added in the simulation, the Image Simulator Module 2^{nd} *order PSF effect*, is polled to obtain the PSF map to be convolved in order to add the simulation of all the diffraction spike effects that contribute to the whole point spread function of the instrument. The 100 pixels and region boundaries computed are stored in a binary file that represent the *illumination solution file* of the echellogram. This step is carried out on Amazon Web Services premises and it is divided in more than one computer node (see next subsection).

3. When the illumination solution is known, it could be used independently on the scientific object to simulate, sky condition, seeing, etc. As long as the design is frozen and no other effects are assumed (e.g. thermal expansion, etc.) this solution could be used to produce calibration frames, scientific frames (and so on) as explained before, allowing to save a huge amount of computational time.

4. The illumination solution file is then parsed by a simple Matlab routine that follows these steps:

   - An empty matrix that models the detector pixels is instantiated (dimensions are obtained by the spectrograph unit)
   - The science spectrum, compute by the Science Module, is multiplied by the telluric absorption at the selected air mass, computed by the Atmospheric Module;

   Then, for each record in the illumination solution file these steps are carried out:

   - Reading the record on the current SRE;
   - Polling the Spectrograph Unit with the fiber ID to know what kind of signal that fiber carries (science, sky, calibration, blank);
   - If the fiber carries science signal, the Science Module/Atmospheric Module are polled (with proper inputs, such as magnitude, exposure time. ecc.) to obtain the theoretical number of photons inside the wavelength range spanned by the SRE (telluric absorption are considered). Then, the same operation is done on the Atmospheric module to know the amount of photons (on the same range) coming from the sky emission. If the fiber carries calibration light, the Calibration Unit is polled to know the number of photons;
   - The Telescope module is polled to obtain the PSF (seeing or SCAO) and the results is passed to the Front End Unit and Polarimetric Unit to assess how much of the seeing disk is processed by the considered fiber;
   - Each unit is polled (including the Atmospheric Module) to obtain the efficiencies at the central wavelength that are multiplied together to obtain the whole throughput;

- The illumination profile of the SRE, since normalized to 1, is multiplied by $(N_{obj} + N_{sky}) \cdot \eta$; where ($N_{obj}$ is the number of estimated photons from the object, (N_{sky} is the number of estimated photons from the sky and η is the whole throughput;
- The position on the detector of the SRE is reconstructed from the boundaries of computation and pixels are added to the matrix instantiated (see first bullet). In this way, signal from overlapping SRE is recovered for each pixel.

5. The echellogram is now ready to be passed to the Detector Unit where QE response, photon noise, dark current, RON, ADU conversion and blurring types are considered;

6. The image is ready to be processed by the DRS.

5.5.2 The Cloud Architecture

In Fig.5.26 it is reported the cloud architecture (based on Amazon Web Services) that has been implemented for the E2E simulator. In details, as soon as the spectro-

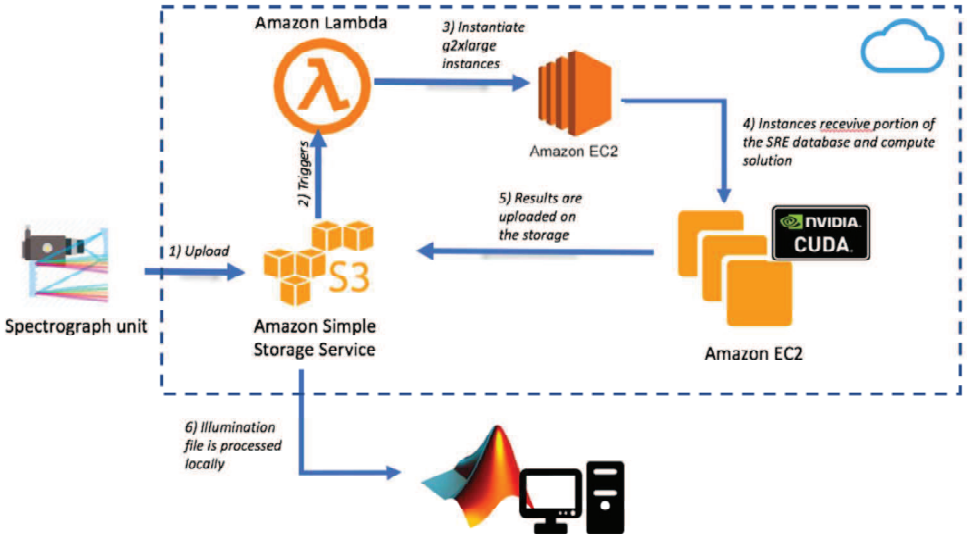

Figure 5.26: Cloud architecture for the E2E CUDA base simulator.

graph units produces his database (see point 1 in Logical Steps section) this file is uploaded to the Amazon Simple Storage Service (S3), which is a cloud based storage system (like Dropobox). When the file is upload at (1), a Lambda function (which is a piece of software that runs in the cloud somewhere) is triggered. This function is in charge to split the SRE database in pieces (user definable) and to instantiate some amount of Amazon EC2 instances (that are basically a dedicated computer) of type g2.xlarge that provides NVIDIA Tesla graphic cards (to exploit the CUDA parallel programming) and a decent amount of RAM (64 GB). These instances, when the computation of their portion of software is completed, upload the result again

on the same S3 bucket. From this point, the illumination profile database can be downloaded and processed locally in MATLAB.

It is worth noting that if also 2^{nd} *order PSF effects* are considered, PSF maps should be uploaded to S3 prior the computation to be available to the instance to estimate the actual image (fiber profile + PSF). Another option is to equip the instances with the software contained in the 2^{nd} *order PSF effect* of the Image Simulation Module. In both cases, the simulator architecture is ready to handle them.

5.6 Results

5.6.1 Performances

As stated in the previous sections, one of the most important issue that should be investigated is the computational cost, especially in terms of complexity in time. This is the most critical point that could results in a showstopper. In particular, with the adoption of the Cloud Architecture explained previously, the E2E is able to recover the illumination solution file in approximately 0.5 days using 5 g2x.large instances on AWS. This kind of computational time, which consider most of the effect needed to be simulated, allow to confirm that the current architecture is suitable for intensive simulation scenarios with large margin that could be used in the case of increased computational time required to add other effect (such as modal noise or the contribution of 2^{nd} order PSF effects) which should be roughly of the same order. Moreover, it should be considered that since the illumination solution file is independent on the spectral energy distribution of which is simulated (far all the scientific cases that can be considered), the number of required iterations on the cloud are order of magnitude less than the ones locally required to apply the SED as explained in the previous section.

5.6.2 Raw frames rendering and Data Reduction Software

One final activity required in the design of the E2E simulator is aimed at demonstrating the capability to close the loop with DRS, since the delivered frames of the simulator will act as input for this pipeline.

The strong link between the E2E and DRS is crucial especially in the next E2E simulator versions since this will allow to characterize the performances of the instrument by translating directly a optical/mechanical/electrical architecture in scientific terms, by simulating all the main ELT-HIRES science cases.

As explained before for others modules and units of the simulator, also in this case an interaction with the groups in charge for the data reduction and data analysis software development was set to define the interface required to close the loop of the complete end-to-end simulation.

To demonstrate that this synergy is settled with proper interface and to see if the simulated echellograms can be handled by a DRS pipeline, the DRS group applied the beta recipes of the CRIRES+ DRS [2] that is currently under development. In spite of HIRES being fiber-fed and CRIRES+ a true slit spectrograph, they share

[2]Details on CRIRESE+ Instrument and its DRS can be found at the following website link: *https* : *//www.eso.org/sci/facilities/develop/instruments/crires*$_{u}$*p.html*

enough similarities in the echellograms being high-resolution, cross dispersed, tilted and inclined (pseudo-)slits, that the recipes could be applied without relevant modifications.

Two different raw frames (with exception of the BIAS trivial ones, not reported here) have been produced with the E2E simulator. The first one is a flat field frame in the Z Band as seen by HIRES (left panel of Fig.5.27) and the second one is a scientific frame of a G2V star with $m_V = 10$ and exposure time = 50 s observed and seeing = 0.85 arcsec (that produces different illuminated slits) in the HIRES Z Band (see Fig.5.28) in polarimetric mode (both slices illuminated by the same object) with simultaneous Fabry-Perot reference. Then, these frames are passed to the DRS of CRIRES+. The order tracing, i.e. finding the spectral orders and fitting them

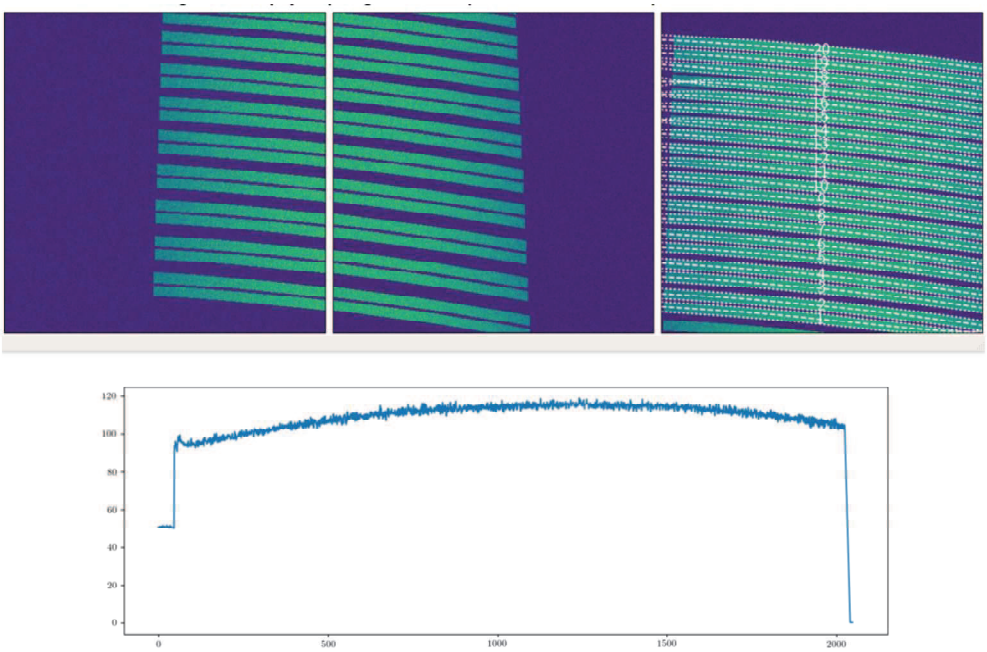

Figure 5.27: ELT-HIRES Z Band flat field frame produced with the E2E simulator. *Left*: RAW data. *Right*: order tracing from CRIRES2 pipeline. *Bottom*: recovered flat field 1D which shows the characteristic blaze function shape.

with polynomials, was successful. The occurrence of sub-optimal edge-detection in some orders is due to badly chosen recipe parameters. A well-detected order was chosen for extraction. Perfectly vertical alignment of the fiber-slit to pixel columns was assumed, since this is how the simulations were made. An example of this, is reported on the right and bottom panel of Fig.5.27.

For the scientific frame, the optimal extraction was done by slit-decomposition (see for details [91]), a robust algorithm that is independent of the slit-illumination function, meaning that differently illuminated fibers (due to the seeing) along the pseudo-slit can be extracted together (see panels of Fig.5.29). The same flat-field frame that was used for order tracing was first extracted and recovered the blaze-function along a single order.

We then extracted an order from the first available E2E science frame with simul-

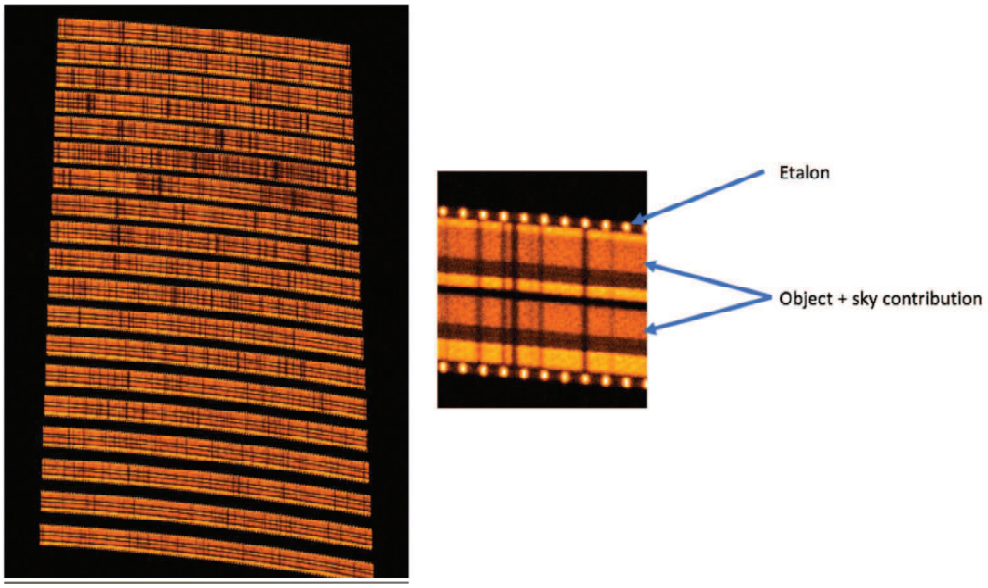

Figure 5.28: ELT-HIRES G2V star simulated raw frame (see text for details).

taneous etalon-calibration on either side of the slit. The etalon was extracted separately from the science, keeping identical pixel scales so that wavelength-calibration is possible after measuring the etalon lines in 1D and by adopting a proper recipe for wavelength solution.

The one dimensional spectra has been wavelength calibrated (using the extracted FP spectra) with a simple fit computed in MATLAB and then the theoretical spectrum has been cross correlated using a CCF function with the recovered one (spectrum) by DRS. The overall dispersion and uncertainty (excluding obvious systematic effect stemming from a simplified wavelength solution) is roughly few m/s that is the expected accuracy for a SNR of about 40 in a single RV measurement.

5.7 Conclusions

In this Chapter the motivations for the development and use of End-to-End simulators in astronomical observation projects have been highlighted, especially for spectroscopic instrumentation which has among the science drivers the study and characterization of Exo-Earths atmospheres in Habitable zones of Sun-like stars. In fact, high resolution spectroscopy, exploited to probe exo-atmospheres, requires high fidelity spectra which can be produced only through a careful analysis and design of the instrument and the data reduction pipeline. This is the case of ELT-HIRES spectrograph, for which in my Ph.D. activity I worked on the design and development of an End-to-End simulator. The simulator architecture has been set up with the purpose (and ultimate goal for future developments) of modeling the full observation chain as much realistic as possible. This allows to perform reliable evaluations of the different effects which can affect the final instrumental performances, like resolving power, stability and throughput, which directly influence the scientific data observational

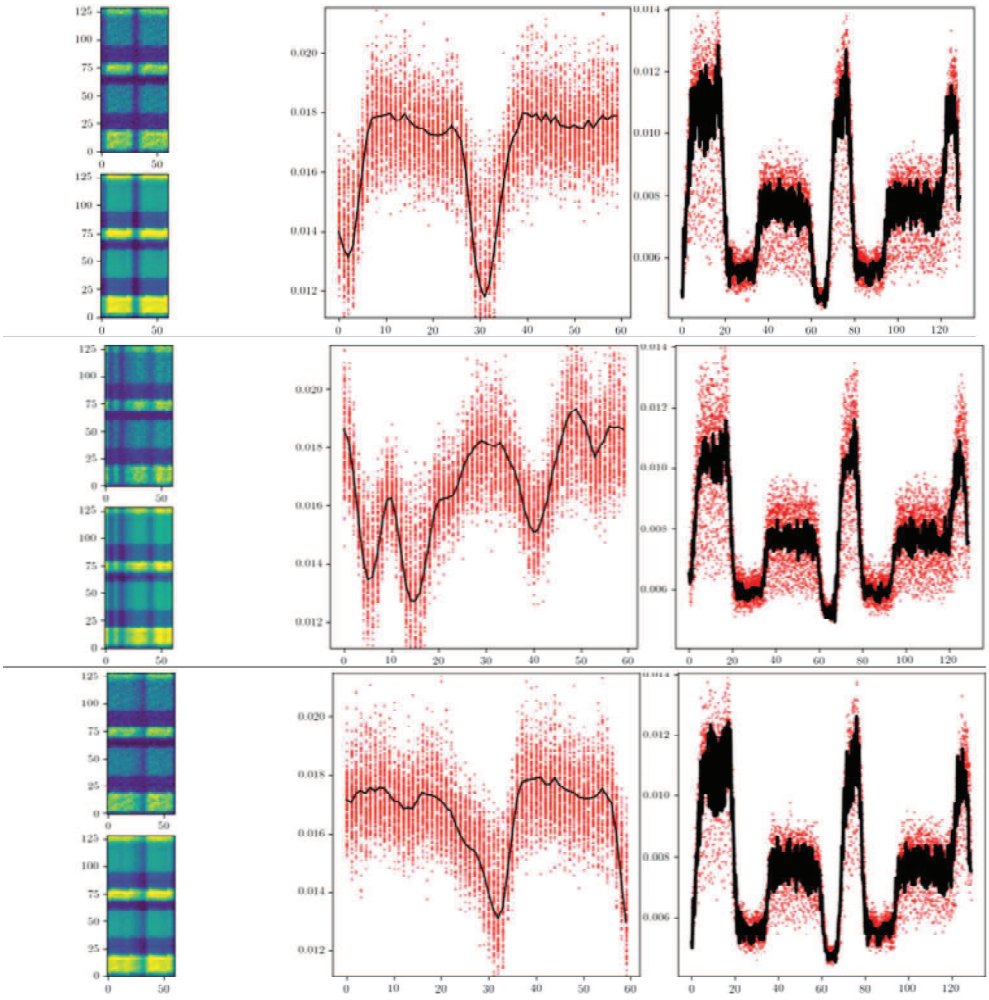

Figure 5.29: Order tracing along spectral direction of the order 146 of HIRES Z band. *Left upper panel*: RAW data. *Left bottom panel*: reconstructed surface. *Right panels*: Extracted scientific spectrum and illumination profile of the fiber-slit.

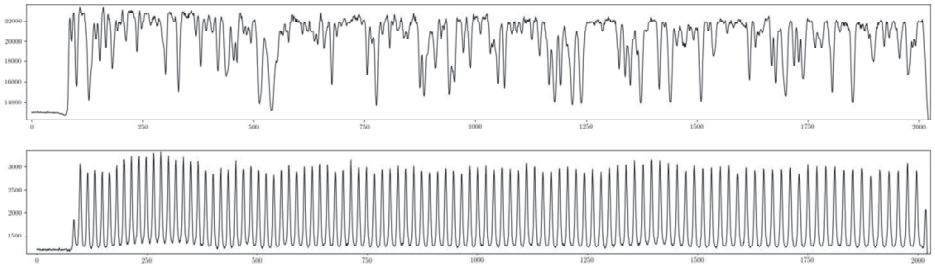

Figure 5.30: Extraction of the 146^{th} order of the ELT-HIRES Z Band. *Upper panel*: scientific spectrum. *Lower panel*: simultaneous reference etalon.

performances (e.g. in terms of stability, instrumental profile, SNR). The modular and flexible design philosophy as well as the physical modeling of the different Modules (and Units), which compose the entire tool have been described. Furthermore the computational architecture of the simulator has been detailed, highlighting its speed performance. The results concerning the synthetic echellogram (raw frame) produced and successfully processed by the beta recipes of the CRIRES+ instrument DRS have been presented, thus probing the full chain feasibility and consistency of the system. This is a key step for the future developments of both the E2E simulator and the DRS pipeline (the specific one for ELT-HIRES) which will help the future design and architecture development of the spectrograph and will enable astronomers and engineers to perform science verification as well as instrument optimization (or to overcome possible problems) well before the first light.

Chapter 6

Conclusions

The spectroscopic characterization of exoplanets atmospheres is a very challenging task, not only for current state of the art instruments like HARPS and ESPRESSO, but especially for future facilities like the ELT-HIRES instrument, where the ambitious aim is to detect and characterize atmospheric signatures of Earth-like planet in the habitable zone.

In this Ph.D. work I learned what kind of physical phenomena of exo-atmospheres, like thermal gradients and circulation, can be inferred and constrained through the transmission spectroscopy technique. This method requires high resolution, precision and SNR spectra to capture with high fidelity not only the hot gas giant features, but especially the few ppm signatures that Exo-Earths imprints in the spectra of their host star. In this frame high dispersion, ultra stable and efficient spectrographs coupled with 10 m telescopes class and the future ELTs promise breakthrough discoveries in this photon starved field of astronomy. Large telescopes allowing very high contrast could imply the possibility to detect the light emitted from background sources and/or from gravitationally bounded companion of exoplanetary systems, which could act as spectra signal contamination. The investigation of these scenarios has been one of main drivers for the development of a transmission spectra simulator, a tool aimed at generating synthetic spectra combining the star spectrum, exo-atmospheric absorption, earth telluric contribution and also contamination due to gravitationally bounded companions or background objects. In particular, the simulator was used to analyze the astrophysical noise level introduced by different background sources, in term of spectral types and apparent magnitude; this analysis has been focused on the signature of the resonant neutral sodium doublet since it is a good proxy to detect and characterize exoplanets atmospheres. The result is that the maximum contamination (in the order of 1000 ppm) occurs for background object which spectral type matches roughly the one of the host star (G or M type); while a much lower contamination (in the order of 10 ppm) is related to hot stars, like O and B type. In the simulated scenario of a HARPS-like spectrograph observation of the system HD189733 with the presence of a m_V =12 M-type contaminant star, the detection of the exo-atmosphere is not prevented; however, the spurious signal due to G or M cool dwarf could be up to thousands of ppm, which should be taken into account when performing this kind of research with Extremely Large Telescopes where signal of few ppm are expected

from Earth twins and more background/foreground objects could be ingested above the noise level due to the larger aperture. It is important to emphasize that this tool has been developed keeping in mind flexibility and a general purpose structure such that the outputted spectra can be used as input for the other simulation tools developed within this Ph.D. thesis work, i.e. the E2E simulator.

In these three years of work I have also been involved in the ESPRESSO project for the final design, installation and commissioning phases. Thanks to its ultra high resolving power and to its capability of collecting the light of any of the four telescopes of the VLT complex independently or together (the 4-UT mode will make it to be the first instrument mounted on a 16 m equivalent telescope) this spectrograph will be one of the most powerful instrument for rocky and earth-size exoplanets detection and study as well as the assessment of possible variations of fundamental constants of Physics. Concerning this project the instrument modeling through ray-tracing software and ad-hoc developed sensitivity analysis tool have been successfully used for component optimization, instrument integration verification with the ultimate goal of achieving the best performance, like optical quality and throughput essential for the maximum scientific return. Being part of such a heterogeneous project gave me the opportunity to improve my knowledge of several different aspects which are essential for the real and practical realization of a complex spectrograph, which culminated in the experience of the successful installation and commissioning at the VLT in Paranal.

Toward the future, I have had also the possibility to be part of the project for the High Resolution Spectrograph for the future 39 m Extremely Large Telescope, the ELT-HIRES project. The unprecedented photon collecting power of the ELT coupled with a high dispersion and high stability spectrograph will allow to do relevant discoveries in many astrophysical fields like ESPRESSO. The peculiarity of this instrument is that the study and characterization of exoplanets atmospheres (both in transmission and reflection) is the highest priority science case. In this context I developed a parametric paraxial model of the spectrograph to evaluate the impact that the different optical components parameters can have with respect to defined performance requirements and technical constraints. This tool has been detailed described, verified and then fruitfully exploited for the design analysis of the ELT-HIRES instrument. Specifically the case of the infra-red (H, J ,Y and z bands) spectrograph module has been presented. At system engineering level this parametric model can be used to preliminary explore and compare different possible instrument architectures; in this respect this parametric model can be flexibly run by of the End-to-End simulator as the spectrograph unit of the Instrument Module.

One of the main reasons for the development of an End-to-End simulator for ELT-HIRES is that the science case related to transmission spectroscopy for exoplanet atmospheres (in particular for the study and characterization and Exo-Earths atmospheres in the Habitable zones of Sun-like stars) requires a careful analysis and design of the experiment in order to succeed. Therefore this kind of simulator is necessary to evaluate the different effects which can affect the final instrument performances, like resolving power, stability and throughput, since they directly influence the scientific data observational performances, like the SNR. In addition the design and continu-

ous development and update of End-to-End simulator(s) directly during the different design phases of a complex instrument like ELT-HIRES, will allow Data Reduction, astronomers and engineers to perform science verification as well as to overcome possible problems related to the instrument well before the first light. The End-to-End simulator design philosophy, global architecture have been described underlining the modularity and flexibility aspects. The development of the physical model of the different Modules (and Units), which compose the entire tool, was an interesting and fruitful experience of collaboration with different kinds research groups and of expertise involved in the ELT-HIRES project. Furthermore the computational architecture of the simulator has been detailed, highlighting its speed performance. The results concerning the synthetic echellogram (raw frame) produced and successfully processed by the beta recipes of the CRIRES+ instrument DRS have been presented, thus probing the full chain feasibility and consistency of the system.

As future perspective of the simulation tools presented in this Thesis, I personally express my interest in continuing the development of both the E2E simulator and the transmission spectra simulations. In the former case, for example the implementation of different spectral templates related to different science drivers (e.g. the QSO for extragalactic science) or the development of fibers physical modeling including the modal noise effects. In the latter case, a more deep exploration of the parameters space (spectral type-apparent magnitude-radial velocity) for the analysis of the transmission spectrum contamination in different instrumentation scenarios (i.e. from 10 m telescope spectrograph like VLT-ESPRESSO to the future 39 m ELT-HIRES).

Appendix A - List of publications

Title: MMP: multi mini prism device for ESPRESSO APSU, prototyping, and integration.
Authors: S. Dell' Agostino, M. Riva, M. Genoni, M. Landoni, M. Moschetti, M. Aliverti, F. Pepe, D. Megèvand, F.M. Zerbi, S. Cristiani, A. Cabral, P. Conconi.
Publication: Proc. SPIE 9147, Ground-based and Airborne Instrumentation for Astronomy V, 91475W.
Publication date: 24 July 2014.
DOI: 10.1117/12.2056528.
Abstract: The multiprism device is a crucial component of the Espresso Anamorphic pupil Slicer (APSU). At the end of the slicer, is necessary to differently fold each field to correctly illuminate the echelle. The solution is made by gluing cylindrical prisms with proper bending low angle onto a support double plate silica window. We present here the integrated robotic system conceived to reach the required tolerances in term of alignment and Integration. It consist in a tip tilt stage to select the folding angle, coupled to an x-y stage to position the elements and a z axis to perform the gluing.
Keywords: Extra-solar Planet Atmospheres, High Resolution Spectroscopy, Espresso, front End.

Title: APSU at ESPRESSO: final design towards the integration.
Authors: M. Riva, P. Conconi, Manuele Moschetti, S. Dell'Agostino, M. Genoni, et al.
Publication: Proc. SPIE 9147, Ground-based and Airborne Instrumentation for Astronomy V, 91477D.
Publication date: 28 July 2014.
DOI: 10.1117/12.2056428.
Abstract: This paper presents the Espresso Anamorphic pupil Slicer (APSU) implementation. For ESPRESSO that will be installed on ESO's Very Large Telescope (VLT). In this work we will present the design and trade off for the pupil slicing system introduced in order to increase the resolving power, effectively decreasing slit width. It's based onto simplified optical component that introduce large anamorphism while keeping low aberrations by means of cylindrical optics. We describe here the trade off between slicing through two adjacent squared doublets and two achromatic prisms. Preliminary integration and procurement is also discussed here.

Title: Optical parametric evaluation model for a broadband HIRES at E-ELT.
Authors: M. Genoni, M. Riva.
Publication: Memoria della Società Astronomica Italiana (MemSAIt), Vol. 86-N.3, 494, 2015.
Publication date: July 2015.
DOI: .
Abstract: We present the details of a paraxial parametric model of high resolution spectrograph which can be used as a tool, characterized by good approximation and reliability, at a system engineering level. This model can be exploited to perform a preliminary evaluation of the different parameters as long as different possible architectures of high resolution spectrograph like the E-ELT HIRES. The detailed equations flow concerning the first order effects of all the spectrograph components is described; in addition a comparison with the data of a complete physical ESPRESSO spectrograph model is presented as a model proof.
Keywords: Spectrograph: high resolution – Spectrograph: paraxial model – Spectrograph: E-ELT HIRES – Spectrograph: field dicing – Spectrograph: echelle cross dispersed.

Title: Spectrograph sensitivity analysis: an efficient tool for different design phases.
Authors: M. Genoni, M. Riva, G. Pariani, M. Aliverti, M. Moschetti.
Publication: Proc. SPIE 9908, Ground-based and Airborne Instrumentation for Astronomy VI, 99086Z.
Publication date: 9 August 2016.
DOI: 10.1117/12.2233294.
Abstract: In this paper we present an efficient tool developed to perform opto-mechanical tolerance and sensitivity analysis both for the preliminary and final design phases of a spectrograph. With this tool it will be possible to evaluate the effect of mechanical perturbation of each single spectrograph optical element in terms of image stability, i.e. the motion of the echellogram on the spectrograph focal plane, and of image quality, i.e. the spot size of the different echellogram wavelengths. We present the MATLAB-Zemax script architecture of the tool. In addition we present the detailed results concerning its application to the sensitivity analysis of the ESPRESSO spectrograph (the Echelle Spectrograph for Rocky Exoplanets and Stable Spectroscopic Observations which will be soon installed on ESO's Very Large Telescope) in the framework of the incoming assembly, alignment and integration phases.
Keywords: Spectrograph sensitivity analysis – Spectrograph image stability – Spectrograph image quality – ESPRESSO spectrograph.

Title: End-to-end modeling: a new modular and flexible approach.
Authors: M. Genoni, M. Riva, M. Landoni, G. Pariani.

Publication: Proc. SPIE 9911, Modeling, Systems Engineering, and Project Management for Astronomy VI, 99112G.
Publication date: 8 August 2016.
DOI: 10.1117/12.2233531.
Abstract: In this paper we present an innovative philosophy to develop the End-to-End model for astronomical observation projects, i.e. the architecture which allows physical modeling of the whole system from the light source to the reduced data. This alternative philosophy foresees the development of the physical model of the different modules, which compose the entire End-to-End system, directly during the project design phase. This approach is strongly characterized by modularity and flexibility; these aspects will be of relevant importance in the next generation astronomical observation projects like E-ELT (European Extremely Large Telescope) because of the high complexity and long-time design and development. With this approach it will be possible to keep the whole system and its different modules efficiently under control during every project phase and to exploit a reliable tool at a system engineering level to evaluate the effects on the final performance both of the main parameters and of different instrument architectures and technologies. This philosophy will be important to allow scientific community to perform in advance simulations and tests on the scientific drivers. This will translate in a continuous feedback to the (system) design process with a resulting improvement in the effectively achievable scientific goals and consistent tool for efficiently planning observation proposals and programs. We present the application case for this End-to-End modeling technique, which is the high resolution spectrograph at the E-ELT (E-ELT HIRES). In particular we present the definition of the system modular architecture, describing the interface parameters of the modules.
Keywords: End-to-End model – End-to-End modular modeling – End-to-End flexible modeling – Spectrograph parametric model – High resolution spectrograph – E-ELT telescope.

Title: Optical parametric evaluation model for a broadband high resolution spectrograph at E-ELT (E-ELT HIRES).
Authors: M. Genoni, M. Riva, G. Pariani, M. Aliverti, M. Moschetti.
Publication: Proc. SPIE 9911, Modeling, Systems Engineering, and Project Management for Astronomy VI, 99112L.
Publication date: 8 August 2016.
DOI: 10.1117/12.2233978.
Abstract: We present the details of a paraxial parametric model of a high resolution spectrograph which can be used as a tool, characterized by good approximation and reliability, at a system engineering level. This model can be exploited to perform a preliminary evaluation of the different parameters as long as different possible architectures of high resolution spectrograph like the one under design for the E-ELT (for the moment called E-ELT HIRES in order to avoid wrong association with the HIRES spectrograph at Keck telescope). The detailed equations flow concerning the first order effects of all the spectrograph components is described; in addition a comparison with the data of a complete physical ESPRESSO spectrograph model is presented as

a model proof.
Keywords: E-ELT High resolution spectrograph, Spectrograph paraxial model, Field dicing, Echelle cross dispersed spectrograph.

Title: MMP, the Multi Mini Prism device for ESPRESSO APSU: prototyping and integration.
Authors: L. Oggioni, G. Pariani, M. Moschetti, M. Riva, M. Genoni, M. Aliverti, M. Landoni, .
Publication: Proc. SPIE 9908, Ground-based and Airborne Instrumentation for Astronomy VI, 990872.
Publication date: 9 August 2016.
DOI: 10.1117/12.2233477.
Abstract: The multi mini prism device is a crucial component of the Espresso Anamorphic Pupil Slicer (APSU). At the end of the slicer, is necessary to differently fold each field to correctly illuminate the echelle and this is made by cylindrical prisms glued onto a silica window. We present the integrated robotic system conceived to reach the required tolerances in term of alignment and integration. It consists in a tip/tilt stage to select the wedge angle, a rotational stage to select the right clock angle, coupled to an x-y stage to position the elements on the window and a z axis to perform the gluing.
Keywords: Extra-solar Planet Atmospheres, High Resolution Spectroscopy, Espresso, front End.

Title: The end-to-end simulator for the E-ELT HIRES high resolution spectrograph.
Authors: M. Genoni, M. Landoni, M. Riva, G. Pariani, E. Mason, P. Di Marcantonio, K. Disseau, I. Di Varano, O. Gonzalez, P. Huke, H. Korhonen, Gianluca Li Causi.
Publication: Proc. SPIE 10329, Optical Measurement Systems for Industrial Inspection X, 103290Z.
Publication date: 26 June 2017.
DOI: 10.1117/12.2271953.
Abstract: We present the design, architecture and results of the End-to-End simulator model of the high resolution spectrograph HIRES for the European Extremely Large Telescope (E-ELT). This system can be used as a tool to characterize the spectrograph both by engineers and scientists. The model allows to simulate the behavior of photons starting from the scientific object (modeled bearing in mind the main science drivers) to the detector, considering also calibration light sources, and allowing to perform evaluation of the different parameters of the spectrograph design. In this paper, we will detail the architecture of the simulator and the computational model which are strongly characterized by modularity and flexibility that will be crucial in the next generation astronomical observation projects like E-ELT due to of the high complexity and long-time design and development. Finally, we present synthetic

images obtained with the current version of the End-to-End simulator based on the E-ELT HIRES requirements (especially high radial velocity accuracy). Once ingested in the Data reduction Software (DRS), they will allow to verify that the instrument design can achieve the radial velocity accuracy needed by the HIRES science cases.
Keywords: End-to-End model – End-to-End modular modeling – End-to-End flexible modeling – Spectrograph parametric model – High resolution spectrograph – E-ELT telescope.

Title: Optical and mechanical architecture for the E-ELT HIRES polarimeter.
Authors: Di Varano, K. G. Strassmeier, M. Woche, M. Weber, U. Laux, S. Yuan, S. Covino, M. Riva, P. Di Marcantonio, M. Genoni, M. Landoni, G Li Causi, E. Mason.
Publication: Proc. SPIE 10330, Modeling Aspects in Optical Metrology VI, 103300C.
Publication date: 26 June 2017.
DOI: 10.1117/12.2272051.
Abstract: We introduce the opto-mechanical architecture of a high precision, full Stokes vector, dual-channel polarimeter for the European Extremely Large Telescope's High Resolution spectrograph (E-ELT HIRES). It is foreseen to feed two spectrograph modules simultaneously through the standard Front End sub-unit located on the Nasmyth platform via two fiber bundles; one optimized for the optical (BVRI), the other optimized for the infrared (zYJH) bands. The polarimeter is located below M4 in the f/4.4 intermediate focus, representing the only rotationally symmetric focus available, and is retractable. We illustrate the strategy of repositioning and aligning the instrument, provided that it has to withstand wind and earthquake loads and that the PSF is varying in width and position due to the active compensation by the co-phasing corrections. Preliminary results of its expected polarimetric sensitivity and accuracy are also analyzed for several configurations of M1 segments and suggest a stunning performance in the intermediate focus with cross talks of the order of 10 -7 but 10 -2 if it were located in the Nasmyth focus.
Keywords: spectroscopy, polarimetry, Mueller matrices.

Acknowledgments

After many years of passionate study, sacrifices and satisfactions, this thesis formally closes my long student career. I believe it's time to thank all the people who have been part, more or less in depth, of my journey. I state, first of all, that these acknowledgments will be sincere and "done my way". Then, those who do not want to go through some (perhaps) boring pages can avoid reading; while for those who want to proceed, I would suggest to sit back, relax and do not interrupt (just on this occasion... even though they can stop reading whenever they want).
First of all, I want to thank the gOlem research group, located in the Merate astronomical observatory (which is part of the astronomical observatory of Brera, Milan), where I mainly worked in these three years of Ph. D. Thanks to this research group I have had the opportunity to do different, rich, training and fascinating working experiences. It has been a stimulating and funny working environment. I also must remember some moments where we had misunderstandings and where a bit of tuning and personal knowledge have been necessary to achieve good and proper equilibrium, as well as trust, in the working activities.
A big thank, then, goes to the current members: Matteo (your peace of mind in dealing with different situations always fascinated me, and your «a bit elastic concept of 10 minutes» is something I think I will never forget), Luca (under the irreplaceable supervision of Giorgio, we succeeded in making the Multi-mini-prisms system of ESPRESSO properly working; I also thank you for your great cooking capacities), Alessio (for his frankness and clear opinions, even different of mine, about many topics), Andrea (your wise advices and suggestions in the VPHG efficiency modeling were fundamental; I also would like to thank you for one of the most welcome congratulations, after my second Ph.D. year seminar), Lorenzo, Paola and Edoardo. I really want to express my gratitude to my mentors: Marco (Landoni) and Giorgio. Giorgio, who was the first to understand my (maybe few) working capabilities, and with whom, in the last two years, I have had a continuously growing respect and synergy in all working activities. Moreover I would also like to thank him for the support he gave me in dealing with all the other experience life is challenging me with. Marco (Landoni), my supervisor, who has always been like an "older brother", showing really a great confidence towards me and my skills (in many moments much more than my self-confidence). Thank you for sharing with me your great enthusiasm and passion, your sensitivity and brotherly advice. Another special thank goes to Marco (Riva), the boss who believed in me since the very beginning and still believed in me also when, at the end of my master thesis, many people (including myself) would not have bet a cent. I thank Filippo (Zerbi) with whom I always found fascinating to talk with, although the occasions in which we met were rare.

I would also like to remember those who were part of the gOlem group in the past: Martino, Stefano e Manuele. Especially Manuele with whom I also shared the joyful experience of "Foresteria studenti", and who made me taste his famous and delicious "pasta with sausages" (now one of my favorite dishes).
Mentioning the "Foresteria studenti", it is my pleasure to remember all the guys who shared with me the experience of Master Thesis and those who lived there during my first Ph.D. year. I really want to thank all who helped me in one of the saddest period of my student life, during the final steps of the Master Thesis. Furthermore, a sincere thank goes to Chiara, with whom I always have a really emphatic relationship in discussing about many different life aspects (some times also cruel life experiences). In all sincerity I must also admit, with regret, the fact that, besides the nice foresteria environment, with all of them I have been not able to go on with relationships. Probably, this is mostly due to my "hypersensitivity" towards some facts and behaviors, but for sure this is a completely different topic which does not find here the proper context for discussion.
I would like to thank all university mates, with whom I experienced the life, challenges, opportunities and "pains" which Politecnico di Milano offers to all engineering students. A big thank goes to Pierluigi and Lorenzo, close mates during the Bachelor degree in Aerospace Engineering. Samuele, Alessandro, Lorenzo (Obi), Michele (Mike), Mattia, Nicolò (Catta) e Siddarth: awesome and heterogeneous group of mates with whom it has been a pleasure to do the Master degree in Space Engineering. I would also like to acknowledge all the professors I met, for their wide knowledge and first quality expertise; I do not forget also the two or three professors, who in many circumstances taught me what a good professor should avoid in order to convey his teaching.
Talking about professors, I want to express a heartfelt thank to professor Emanuela Lavorato, "my" mathematics and physics professor of scientific high school. The best professor I have ever had, in term of competence, teaching and human level. For some years now, a very good friend, more then a professor, with whom I also shared some happy moments of our football passion.
During the valuable working experience in ESPRESSO and in developing the TSS , I have had the opportunity to collaborate with the Exolplanets research group of Geneva astronomical observatory. I would like to thank Aurelien e Romain for their enthusiasm and willingness. A special mention goes to Ian, for his extraordinary kindness, and Francesco, a really special person who have always taught me something in every single meeting or video-conference, from both technical and human point of view.
I would like also to thank the whole ELT-HIRES team, and in particular the Visible-spectrograph, IR-spectrograph and E2E simulator work-packages. All these people helped me in a in-depth examination of many aspects and details investigated in this work. In particular I am grateful to Phil Rees, who always showed a great appreciation in the spectrograph paraxial modeling analysis. Another serious thank is for Ernesto (Tino) Oliva, for his considerable willingness towards my copious questions about spectrograph optical design.
It is impossible not to direct a sincere thank to Paolo Conconi, another amazing teacher for me; I wish I could have learnt more than I actually have been able to do.
I am deeply grateful to the reviewers of this Ph.D. Thesis, Stefano Cristiani (OATs)

and Debra Fischer (Yale University), for their precise corrections and fundamental suggestions which significantly improved the quality of the work. I really would like to remark my gratitude to professor Fischer, for her enthusiastic appreciation of the whole work produced.
It is also a pleasure for me to remember all the others Ph.D. students in Physics and Astrophysics I met at Insubria University. In particular Riccardo, for his kindness and wide interest in my activity, Michele, with whom I really had a funny and productive collaboration in preparing our seminar concerning the modeling of crowd dynamics. I also want to express a hearty thank to professor Massimo Caccia, who has always made me feel his esteem and consideration (despite my background and being an engineer), and with whom I really would have had the pleasure and fun to work and collaborate with (maybe never say never in the future...).
It is now time to thank all the friends with whom in these years I shared, more or less deeply and affectionately, moments of high satisfaction, even though they were patient in "crashing" against some side of my strange character: Bruno, Federica (thank you for the precious review of this section), Jacopo, Elisa e Marco. Another big thank goes to Cristian, who always makes me feel a very special person, introducing me to all the people as a "really important scientist-engineer". Thanks to Cinzia, an "impossible to find a proper english translation" with whom, despite the distance, I always feel a sincere empathy and affinity (also at the musical level, something really important to me!). Thanks to all "Friends" and to my personal "Don Camillo" (... they will recognize them-self), who always make me feel like an "old friend" and for being always so curious and interested in my "strange-work".
I would like to thank all my family; they believe I can bring them into space. I am greatful to my dear relatives who, from a "special position", have observed and guided my long and strange journey.; I hope that, also in this moment where our paths appear to me so distant, they could be a bit happy.
An immense thanks goes to my mother, who has always respected and supported all my choices with love, sometimes with constructive criticism and always trying to hide her worries about my future.
An infinite thank is for Cecilia, the wonderful girl and woman with whom I have grown up and I have shared, in the most genuine and intimate way, every single moment. I thank her for having lovely encouraged me in each step and for have balanced with a wise equilibrium the different skepticism moments. I am fully grateful to her for continuously stimulating me in pursuing one of my dreams, although in this moment of our lives this means for her a professional career sacrifice and (even in the past) a bit of "healthy jealousy". I will fight so that everything I have learned professionally and not, can benefit the future family we are going to build together.
To conclude I would like to state another last thanks... Well, I would like to thank myself because, despite my many flaws and being often able to make my life more complicated than it could have been, I have always faced every single challenge with the greatest enthusiasm, passion, dedication, coherence and honesty towards other people. I am grateful to myself because I have seen my dignity trampled and even in the moments when it seemed to me that I could not even breathe even more, I managed (perhaps by chance or luckily) to find in myself a necessary and sufficient glimmer of strength. It is not my intention to praise myself, and I recognize that I still have to face many challenges and situations in life, but I think it is fair to write

this thought here, black and white, even and especially to my future memory.

Dopo tanti anni di studio appassionato, sacrifici e soddisfazioni, con questa tesi si chiude formalmente il mio lungo periodo da studente e credo che sia giunto ora il momento di ringraziare le persone che hanno, in modo più o meno profondo, fatto parte di questo mio cammino. Premetto che saranno dei ringrazimenti sinceri e fatti a mio modo. Quindi per chi non ha voglia di andare incontro a pagine (forse) un po' logorroiche può anche evitare di procedere nella lettura; mentre a coloro che hanno voglia di proseguire mi permetto di suggerire di mettersi comodi e non interrompermi (almeno in questa occasione... a meno che non abbiano voglia di concludere la lettura a loro piacimento).
Naturalmente ci tengo a ringraziare il groppo di ricerca del gOlem dell' osservatorio di Merate dove ho svolto il lavoro di questi tre anni di dottorato e attraverso cui ho potuto fare delle esperienze lavorative estremamente ricche, formanti e affascinanti. Ringrazio perchè è stato un ambiente di lavoro molto stimolante e divertente, dove devo ricordare anche i momenti dove ci sono state delle incomprensioni e dove si è reso necessario un certo "tuning" ed una certa conoscenza personale per raggiungere un buon equilibrio di organizzazione e fiducia lavorativa.
Un grande grazie va quindi ai componenti attuali: Matteo (la cui serenità nell' affrontare tutte le cose mi ha sempre affascinato, e il cui «concetto un po' elastico di 10 minuti» sarà qualcosa che non scorderò mai credo), Luca (con cui abbiamo fatto funzionare i "prismini" di ESPRESSO e per le ottime capacità in cucina), Alessio (per la sua franchezza e nitidezza di opinioni, anche contrarie alle mie, su molte tematiche di cui abbiamo discusso) e Andrea (per i suoi saggi e fondamentali consigli sulla modellazione di efficienza dei VPHG e per avermi fatto uno dei più graditi complimenti dopo il seminario di fine secondo anno di dottorato), Lorenzo, Paola ed Edoardo. Ringrazio di cuore i miei mentori: Marco (Landoni) e Giorgio. Giorgio per essere stato uno dei primi a capire i miei (forse pochi) pregi lavorativi e con cui negli ultimi due anni ho avuto un crescente rapporto di stima ed intesa lavorativa e soprattuto con il quale ho potuto condividere molte delle altre grandi esperienze che la vita mi ha chiesto di affrontare. Marco (Landoni), mio supervisor, per essere stato sempre il mio "fratello maggiore", mostrando verso di me una fiducia molto più grande in alcuni momenti di quella che io stesso nutrivo personalmente; lo ringrazio per l' entusiasmo e la passione che ha sempre trasmesso, per la sensibilità e i consigli fraterni. Altro speciale ringraziamento va a Marco (Riva), il capo che sin dall' inizio ha creduto in me e che ha continuato a credere in me anche quando, alla fine della tesi di Laurea Magistrale, molti (compreso io stesso) non avrebbero scommesso un centesimo su di me. Ringrazio Filippo (Zerbi) con il quale, sebbene le occasioni in cui ci siamo incontrati siano state rare, è sempre stato stimolante e affascinante parlare. Ringrazio coloro che hanno fatto parte in passato del gOlem: Martino, Stefano e Manuele. In particolare quest' ultimo con cui ho condiviso anche l' esperienza della Foresteria studenti e per avermi fatto assaggiare una delle pietanze più buone che abbia mai mangiato, e cioè la famosissima pasta con la salsiccia che ai tempi che furono portò più di venti persone a mangiare in foresteria.

Citando la foresteria studenti è mio grande piacere ricordare tutti i "forestali" che hanno condiviso con me il periodo della tesi magistrale e quelli che hanno vissuto la foresteria durante il mio primo anno di dottorato. Ci tengo particolarmente a ringraziare tutti coloro che mi sono stati vicino durante uno dei periodi più brutti della mia vita durante le fasi finali della tesi di laurea. In aggiunta un sentito ringraziamento va a Chiara, con la quale ho sempre avuto un intesa particolarmente bella e quasi fraterna nel parlar di tante tematiche e delle esperienze, a volte molto crude, della vita. In tutta sincerità devo anche ammettere, con rammarico, il fatto che oltre al caloroso ambiente della foresteria non si sia riusciti a continuare il rapporto; probabilmente ciò è in gran parte dovuto alla mia eccessiva sensibilità in merito a certi comportamenti, ma questa è tutt' altra tematica che non trova qui la sua opportuna sede di discussione.
Ringrazio tutti i compagni di università con cui ho vissuto la vita, le sfide, le opportunità e le "sofferenze" che il Politecnico di Milano offre agli studenti di Ingegneria. Un grosso grazie va a Pierluigi e Lorenzo, stretti compagni della triennale, a Samuele, Alessandro, Lorenzo (Obi), Michele (Mike), Mattia, Catta, Siddarth: fantastico ed eterogeneo gruppo di ragazzi con i quali è stato un piacere trascorrere i due anni della laurea specialistica in ingegneria spaziale. Ringrazio anche tutti i professori che ho avuto nei vari corsi del Politecnico, per la loro vasta cultura e competenza di prima qualità; ringrazio anche i due o tre professori con cui non ho mai legato e che in alcuni casi mi hanno comunque insegnato cosa un professore non deve fare per veicolare il suo insegnamento.
Parlando di professori, è sentitissimo il ringraziamento che va alla Prof. Emanuela Lavorato, la "mia" professoressa di matematica e fisica del triennio di liceo scientifico. La migliore professoressa che ho avuto, sia sotto l' aspetto della preparazione, professionalità e insegnamento, sia sotto il profilo umano. Ormai da un po' di anni un' amica, oltre che professoressa, con la quale ho condiviso anche le gioie della passione calcistica.
Durante la grande esperienza di ESPRESSO e nell' attività di sviluppo del TSS, ho avuto modo di collaborare con parte del gruppo di ricerca su Esopianeti dell' osservatorio astronomico di Ginevra. Volevo quindi ringraziare Aurelien e Romain per il loro entusiasmo e la loro disponibilità. Ringrazio anche tutto il gruppo che ha lavorato e collaborato con me in ESPRESSO; in particolare Ian, per la sua straordinaria gentilezza, e Francesco, per avermi sempre insegnato qualcosa in ogni singolo incontro o teleconf, sia dal punto di vista tecnico che umano.
Ringrazio tutto il team di ELT-HIRES, ed in particolar modo i gruppi di lavoro dello spettrografo Visibile ed InfraRosso, e del Simulatore End-to-End. Tutte persone senza le quali non sarei riuscito ad approfondire molti degli aspetti trattati in questo lavoro. Ringrazio in particolar modo Phil Rees per avermi sempre fatto sentire una grande fiducia ed apprezzamento nel lavoro di modellazione parassiale dello spettrografo. Altro sentito ringraziamento va ad Ernesto (Tino) Oliva per la grande disponibilità che ha sempre mostrato nei confronti delle mie numerose domande sulla progettazione ottica degli spettrografi.
Impossibile per me non esprimere un fervido ringraziamento a Paolo Conconi, altro eccezionale maestro per me dal quale avrei voluto imparare molto di più di quanto non sia riuscito a fare.
Ringrazio profondamente i revisori di questo scritto, Stefano Cristiani (OATs) e De-

bra Fischer (Yale University), per le loro mirate correzioni e fondamentali consigli che hanno permesso di migliorare significativamente il lavoro in fase correzione. Ringrazio Debra Fischer, inoltre, per l' apprezzamento entusiasta di tutto il lavoro prodotto.
Ci tengo a ricordare anche tutti gli altri studenti di dottorato in Fisica ed Astrofisica che ho conosciuto in università, in particolare Riccardo, per la sua bontà ed interesse nella mia attività, e Michele, con il quale è stato davvero proficuo e divertente collaborare per il nostro "seminario ortogonale". Rivolgo un caloroso ringraziamento al prof. Massimo Caccia per avermi sempre fatto sentire la propria stima (nonostante la mia formazione e natura di Ingegnere), e con il quale mi sarei veramente divertito a lavorare (mai dire mai in futuro...).
Giunge quindi il momento di ricordare tutti gli amici con i quali in questi anni ho, più o meno direttamente ed intensamente, condiviso i momenti di soddisfazione, ma che hanno anche avuto la pazienza di scontrarsi con i tormenti originati dal mio carattere: Bruno, Federica (grazie per la preziosissima revisione di questo capitolo), Jacopo, Elisa e Marco. Grazie a Cristian che ha il dono di farmi sempre sentire importante e per presentarmi a tutte le persone come un "grande scienziato-ingegnere". Grazie a Cinzia, una "zia" con la quale, nonostanze la lontananza e le rare occasioni di passare del tempo insieme, sento sempre grande vicinanza, sintonia ed intesa musicale (l' unica che mi capisce da questo assai rilevante punto di vista!). Grazie ai "Friends" e al mio personale "Don Camillo" (...loro capiranno), per avermi sempre trattato come un "amico di vecchia data" e per aver mostrato sempre una vivissima curiosità al lavoro da me svolto.
Ringrazio tutti i miei parenti presenti, i quali mi hanno sempre visto come qualcuno che avrebbe potuto portarli nello spazio. Rinnovo il ringraziamento che più volte ho indirizzato ai miei cari che hanno osservato, e credo anche guidato, il mio lungo e strano percorso da una "posizione particolare"; spero anche che in questo periodo, in cui mi pare proprio che le nostre strade si siano divise, siano minimamente contenti.
Un immenso ringraziamento va a mia Mamma per avere sempre rispettato e sostenuto le mie scelte con amore, a volte con sguardo constrtuttivamente critico, e cercando sempre di nascondere le sue paure per il mio futuro.
Un infinito ringraziamento a Cecilia, la straordinaria ragazza e donna con cui sono cresciuto e con la quale ho condiviso nella maniera più genuina e profonda ogni singolo momento. La ringrazio per avere incoraggiato con amore ogni mio passo e per avere bilanciato con saggio equilibrio i vari momenti sfiducia. Le sono grato per continuare ad incentivarmi nel perseguire uno dei miei sogni, sebbene in questo nostro momento di vita le costa un sacrificio dal punto di vista professionale ed (anche in passato) un pizzico di "sana gelosia". Lotterò affinchè tutto ciò che ho imparato professionalmente e non, possa giovare alla futura famiglia che andremo a costruire insieme.
Per concludere ci tengo a fare un altro ringraziamento... Ebbene ringrazio me stesso perchè anche se ho reso in primis a me, moltissime volte, la vita difficile, ho affrontato sempre ogni sfida con il massimo entusiasmo, passione, dedizione, coerenza e correttezza verso gli altri. Ringrazio me stesso perchè in questi anni ho spesso visto la mia dignità calpestata, e anche nei momenti in cui mi è sembrato di non riuscire neanche più a respirare sono riuscito (forse per caso o per fortuna) a sentire in me un necessario e sufficiente barlume di forza. Non è mia intenzione lodarmi, e riconosco che devo affrontare ancora moltissime sfide e situazioni nella vita, ma credo sia giusto scrivere qui, nero su bianco, questo pensiero, anche e soprattutto a mia futura memoria.

Bibliography

[1] G. Agapito, A. Puglisi, S. Esposito, *FASSATA - Object oriented numerical simulation software for adaptive optics.* Proc. SPIE 9909, Adaptive Optics Systems V, 99097E, 2016.

[2] R. Allart, C. Lovis, L. Pino, et al. *Search for water vapor in the high-resolution transmission spectrum of HD 189733b in the visible.* A&A, 2017.

[3] G. Anglada-Escudé, A.P. Boss, et al. *Astrometry and radial velocities of the planet host M DWARF GJ 317: new thrigonometric distance, metallicity, and upper limit to the mass of GJ 317.* ApJ, 746, 37, 2012.

[4] J. A. Arns, *Performance characteristics of two volume phase holographic grisms produced for the ESPRESSO spectrograph.* Proc. of SPIE Vol. 9908, 990861, 2016.

[5] G. Avila, P. Singh, B. Chazelas. *Results on fibre scrambling for high accuracy radial velocity measurements.* Proc. of SPIE Vol. 7735, 773588, 2010.

[6] G. A. Bakos, R. W. Noyes, et al. *HAT P-1B: a large radius low density exoplanet transiting one memeber of a stellar binary.* ApJ, 656, 552, 2007.

[7] I. K. Baldry, J. Bland-Hawthorn, J.G. Robertson, *Volume Phase Holographic Gratings: Polarization Properties and Diffraction Efficiency.* PASP, 116, 403–414, 2004.

[8] A. Baranne, *White pupil story or evolution of a spectrographic mounting.* ESO Conference on Very Large Telescopes and their Instrumentation, Vol. 2, 1195, 1988.

[9] A. Baranne, D. Queloz, et al. *ELODIE: a spectrgraph for an accurate radal velocity measurements.* A&A suppl. ser, 119, 373, 1996.

[10] S. C. Barden. *Volume phase holographic gratings and the efficiency of the three simple vph gratings.* Astronomical Society of the Pacific, 112, 809, 2000.

[11] T. S. Barman. *Identification of Absorption Features in an Extrasolar Planet Atmosphere.* Astrophys. J. Lett 661, 191, 2007.

[12] T. S. Barman, B. Macintosh, et al. *CLOUDS AND CHEMISTRY IN THE ATMOSPHERE OF EXTRASOLAR PLANET HR8799b.* Apj 733, 65, 2011.

[13] T. S. Barman. *Simultaneous Detection Of Water, Methane And Carbon Monoxide In The Atmosphere Of Exoplanet HR 8799b.* 2015.

[14] J.P. Beaulieu1, D.P. Bennett, P. Fouqué, et al. *Discovery of a cool planet of 5.5 Earth masses through gravitational microlensing.* Nature 439, 437, 2006. Beaulieu1

[15] J. L. Beuzit, M. Feldt, K. Dohlen, et al. *SPHERE: a 'Planet Finder' instrument for the VLT.* Proc. of SPIE Vol. 7014, 701418, 2008.

[16] A. Bianco, G. Pariani, A. Zanutta, et al. *Materials for VPHGs: practical considerations in the case of astronomical instrumentation.* Proc. of SPIE Vol. 8450, 84502W, 2012.

[17] J.L. Birkby, R.J. de Kok, et al. *Detection of water absorption in the day side atmosphere of HD 189733 b using ground-based high-resolution spectroscopy at 3.2 μm.* MNRASL 436, L35–L39, 2013.

[18] L.T. Blair, L. Solymar and J. Takacs *Nonlinear recording in dichromated gelatin.* Proc. of SPIE, 1136, 1989.

[19] L.T. Blair, L. Solymar and J. Takacs *Grating profiles in dichromated gelatin.* Optics Communications, 1989.

[20] F. Bouchy, S. Udry, M. Mayor, et al. *ELODIE metallicity-biased search for transiting Hot Jupiters. II. A very hot Jupiter transiting the bright K star HD 189733.* A&A, 444, L15, 2005.

[21] M. Brogi, R.J. de Kok, et al. *Carbon Monoxide And Water Vapor In The Atmosphere Of The Non-Transiting Exoplanet Hd 179949 B.* A&A, 2014.

[22] M. Brogi, R.J. de Kok, S. Albrecht, et al. *Rotation and winds of exoplanet HD 189733 b measured with high-dispersion transmission spectroscopy.* ApJ, 817, 2016.

[23] J.R. Burton, C.A. Watson, P. Rodriguez-Gil, et al. *Defocussed Transmission Spectroscopy: A potential detection of sodium in the atmosphere of WASP-12b.* MNRAS, 446, 1071, 2015.

[24] A. Cassan. *New Worlds Ahead: The Discovery of Exoplanets.* L'Univers, Seminaire Poincare XX, 2015.

[25] Centro de Astrofisica da Universidade do Porto. *ESPRESSO main scientific driver.*
http://espresso.astro.up.pt/science.php.

[26] D. Charbonneau, T.M. Brown, et al. *Detection of Planetary Transit across a sun-like star.* The Astrophysical Journal, 529:L45–L48, 2000.

[27] D.Charbonneau,T.M. Brown, et al. *Detection of an Extrasolar Planet Atmosphere.* The Astrophysical Journal, 2001.

[28] G.Chauvin, A.M. Lagrange, et al. *A giant planet candidate near a young brown dwarf: direct VLT/NACO observations using IR wavefront sensing.* A&A,425, L29, 2004.

[29] P. Conconi, M. Riva, F. Pepe, et al. *ESPRESSO APSU: Simplify the life of pupil slicing.* Proc. of SPIE Vol. 8842, 88420P, 2013.

[30] I.J.M. CROSSFIELD. *Observations of Exoplanet Atmospheres.* The Astronomical Society Of The Pacific, 127:941–960, 2015.

[31] D. Cunha, P. Figueira, N.C. Santos, et al. *Impact of stellar companions on precise radial velocities.* A&A, 550, A75, 2013.

[32] S. Dell' Agostino, M. Riva, M. Genoni, et al. *Mmp: multi mini prism device for espresso apsu, prototyping and integration.* Proc. of SPIE, 9147, 2014.

[33] D. Deming, A. Wilkins, et al. *Infrared Transmission Spectroscopy Of The Exoplanets Hd209458b And Xo-1b Using The Wide Field Camera-3 On The Hubble Space Telescope.* The Astrophysical Journal, 2013.

[34] B. O. Demory, J. de Wit, et al. *Inference Of Inhomogeneous Clouds In An Exoplanet Atmosphere.* ApJL, 2013.

[35] X. Dumusque, F. Pepe, et al. *An Earth mass planet orbiting Alpha Centauri B.* 2012.

[36] J. L. Salter and M. F. Loeffler *Comparison of dichromated gelatin and Du Pont HRF.700 photopolymer as media for holographic notch filters.* SPIE Vol. 1555, Computer and Optically Generated Holographic Optics (Fourth in a Series), 1991.

[37] D. Ehrenreich, A. Vidal-Madjar, T. Widemann, et al. *Transmission spectrum of Venus as a transiting exoplanet.* A&A, 537, L2, 2012.

[38] D. Ehrenreich, V. Burrier, P.J. Wheatley, et al. *A giant comet-like cloud of hydrogen escaping the warm Neptune-mass exoplanet GJ 436b.* Nature 522, 459, 2015.

[39] European Soutern Observatory. *The VLT white book.* 1998.

[40] European Soutern Observatory. *The E-ELT construction proposal.*

[41] T. Eversberg and K. Vollmann, *Spectroscopic Instrumentation: Fundamentals and Guidelines for Astronomers.* Springer, 2015.

[42] D. Fischer, A. W. Howard, et al. *Exoplanet Detection Techniques.* Protostars and Planets VI proceedings, 2015.

[43] T.K. Gaylord, and M. G. Moharam, *Analysis and applications of optical diffraction by gratings.* Proc. IEEE, 73, 894, 1985.

[44] M. Genoni, M. Riva, G. Pariani, et al. *Spectrograph sensitivity analysis: an efficient tool for different design phases.* Proc. SPIE 9908, Ground-based and Airborne Instrumentation for Astronomy VI, 99086Z, 2016.

[45] M. Genoni, M. Riva, G. Pariani, et al. *Optical parametric evaluation model for a broadband high resolution spectrograph at E-ELT (E-ELT HIRES).* Proc. SPIE 9911, Modeling, Systems Engineering, and Project Management for Astronomy VI, 99112L, 2016.

[46] M. Genoni, M. Riva, M. Landoni, G. Pariani, *End-to-end modeling: a new modular and flexible approach.* Proc. SPIE 9911, Modeling, Systems Engineering, and Project Management for Astronomy VI, 99112G, 2016.

[47] M. Genoni, M. Landoni, et al. *The end-to-end simulator for the E-ELT HIRES high resolution spectrograph.* Proc. SPIE 10329, Optical Measurement Systems for Industrial Inspection X, 103290Z, 2017.

[48] M. Gillon, A.H.M.J. Triaud, B.O. Demory, et al. *Seven temperate terrestrial planets around the nearby ultracool dwarf star TRAPPIST-1.* Nature, 542, 456, 2017.

[49] M. Goodwin, S. Smedley, S. Barnes, et al. *Data simulator for the HERMES instrument.* Proc. of SPIE Vol. 7735, 77357U, 2010.

[50] W. Hayek, D. Sing, et al. *Limb darkening laws for two exoplanet host stars derived from 3D stellar model atmospheres.* A&A 539, A102, 2012.

[51] R. Maiolino, Haehnelt, M. Murphy, D. Queloz, L. Origlia, J. Alcala, Y. Alibert, P.J. Amado, C. Allende Prieto, M. Asplund, M. Barstow, and et al. A community science case for e-elt hires. 2013.

[52] K. Heng, A. Wyttenbach, B. Lavie, et al. *A NON-ISOTHERMAL THEORY FOR INTERPRETING SODIUM LINES IN TRANSMISSION SPECTRA OF EXOPLANETS.* ApJ, 817, 2016.

[53] D.J. Hillier, D. L. Miller. *The Treatment of Non-LTE Line Blanketing in Spherically Expanding Outflows.* ApJ, 803, L9, 2015.

[54] A.R. Iyer, M. R. Swain, R.T. Zellem, et al. *A CHARACTERISTIC TRANSMISSION SPECTRUM DOMINATED BY H_2O APPLIES TO THE MAJORITY OF HST/WFC3 EXOPLANET OBSERVATIONS.* ApJ, 823, 109, 2016.

[55] H. A. Knutson, N. Madhusudhan, et al. *A Spitzer Transmission Spectrum For The Exoplanet Gj 436b, Evidence For Stellar Variability, And Constraints On Day-side Flux Variations.* The Astrophysical Journal, 735:27 (23pp), 2011.

[56] H. Kogelnik, *Couple Wave Theory for Thick Hologram Gratings.* The Bell System Tech Journal, 48, 9, 1969.

[57] Q. Konopacky, T.S. Barman, et al. *Carbon and Oxygen in the spectrum of HR8799c.* American Astronomical Society,AAS meeting 221, 2013.

[58] R.L. Kurucz. *ATLAS12, SYNTHE, ATLAS9, WIDTH9, et cetera.* MemSAIT v8, 14, 2005.

[59] Kuzuhara, M., Tamura, M., Kudo, T., et al. *Direct Imaging of a Cold Jovian Exoplanet in Orbit around the Sun-like Star GJ 504.* ApJ, 774, 11, 2013.

[60] A. Jarno, R. Bacon, et al. *Confronting the numerical simulations of the VLT/MUSE instrument with the first real data.* Proc. of SPIE Vol. 8451, 84512E, 2012.

[61] A. Jones, S. Noll, et al. *An advanced scattered moonlight model for Cerro Paranal.* A&A 560, A91, 2013.

[62] A. Lecavelier Des Etangs, A. Vidal-Madjar, et al. *Rayleigh scattering by H_2 in the extrasolar planet HD 209458b..* A&A 485, 83, 2008.

[63] G. Li Causi, A. Cabral, et al. *"Virtual MOONS", a focal plane simulator for the MOONS thousand-fiber NIR spectrograph .* Proc. of SPIE Vol. 9147, 914764, 2014.

[64] B. Macintosh, J.R. Graham, P. Ingraham, et al. *First light of the Gemini Planet Imager.* PNAS, 111, 12661, 2014.

[65] N. Madhusudhan, S. Redfield *Optimal measures for characterizing water-rich super-Earths.* International Journal of Astrobiology 14, 177, 2015.

[66] Madhusudhan, N., Agúndez, M., Moses, J.I. et al. *Exoplanetary Atmospheres—Chemistry, Formation Conditions, and Habitability.* Space Sci Rev (2016), 205, 285, 2016.

[67] R. Magnusson and T. K. Gaylord *Equivalence of multiwave coupled-wave theory and modal theory for periodic-media diffraction.* Journal of the Optical Society of America Vol. 68, 12, 1777, 1978.

[68] M. Mayor, D. Queloz *A Jupiter-mass companion to a solar-type star.* Nature 378, 355, 1995.

[69] G. Marcy, P. Butler, D. Fischer, et al. *A Planet at 5 AU Around 55 Cancri.* ApJ, 581, 1375, 2002.

[70] A. Marconi, P. Di Marcantonio, V. D'Odorico, et al. *EELT-HIRES the high-resolution spectrograph for the E-ELT.* Proc. SPIE 9908, Ground-based and Airborne Instrumentation for Astronomy VI, 990823, 2016.

[71] C. Marois, B. Zuckerman, et al. *Images of a fourth planet orbiting HR 8799.* Nature, 2010.

[72] J. H. C. Martins, N. C. Santos, et al. *Evidence for a spectroscopic direct detection of reflected light from 51 Peg b.* A&A, 576, A134, 2015.

[73] P.R. McCullough, N. Crouzet, et al. *WATER VAPOR IN THE SPECTRUM OF THE EXTRASOLAR PLANET HD 189733b. I. THE TRANSIT.* ApJ, 791, 55, 2014.

[74] D. Mégevand, F.M. Zerbi, P. Di Marcantonio, et al. *ESPRESSO, the radial velocity machine for the VLT.* Proc. of SPIE Vol. 9147, 91471H, 2014.

[75] A. Morbidelli, J. Chambers, et al. *Source regions and timescale for the delivery of water on Earth.* Meteoritics and Planetary Science, 35, 1309, 2000.

[76] J.I. Moses, M.R. Line, C. Visscher et al. *COMPOSITIONAL DIVERSITY IN THE ATMOSPHERES OF HOT NEPTUNES, WITH APPLICATION TO GJ 436b.* ApJ, 777, 34, 2013.

[77] P. Mroz, A. Udalski, et al. *No large population of Jupiter mass free floating planet.* Nature 548, 183, 2017.

[78] NASA, *NASA Exoplanetary Archive.* https://exoplanetarchive.ipac.caltech.edu/.

[79] N. Nikolov, D.K. Sing, F. Pont, et al. *Hubble Space Telescope hot Jupiter transmission spectral survey: a detection of Na and strong optical absorption in HAT-P-1b.* MNRAS 437, A46, 2014.

[80] S. Noll, W. Kaush, et al. *An atmospheric radiation model for Cerro Paranal.* A&A 543, A92, 2012.

[81] P. OConnor, V. Radeka, D. Figer, et al. *Study of Silicon Thickness Optimization for LSST.* d Proc. of SPIE Vol. 627662761W, 2006.

[82] S. Oshagh, W. Kaush, et al. *Impact of occultations of stellar active regions on transmission spectra: Can occultation of a plage mimic the signature of a blue sky?.* A&A 568, A99, 2014.

[83] A. Palacios, M. Lebre, M. Sanguillon *POLLUX DATABASE – USER GUIDE.* Version 7 - March 2015.

[84] I. Parry, M. A. Kenworthy, and K. Taylor. Spiral phase a: A prototype integral field spectrograph for the aat. *Proc. of SPIE 2871, Optical Telescopes of Today and Tomorrow*, 1997.

[85] F. Pepe, M. Mayr, et al. *The CORALIE survey for southern extra-solar-planets VII: Two short period saturnian companions to HD108147 and HD168746.* A&A, 388, 632, 2002.

[86] F. Pepe, S. Cristiani, R.F. Lopez, et al. *ESPRESSO: the Echelle spectrograph for rocky exoplanets and stable spectroscopic observations.* Proc. of SPIE Vol. 7735, 77350F, 2010.

[87] F. Pepe, C. Lovis, D. Ségransan et al. *The HARPS search for Earth-like planets in the habitable zone I. Very low-mass planets around HD 20794, HD 85512, and HD 192310..* 2015.

[88] F. Pepe, P. Molaro, S. Cristiani, et al. *ESPRESSO: The next European exoplanet hunter.* Astron. Nachr. / AN 335, 1, 10, 2014.

[89] F. Pepe, D. Ehrenreich, et al. *Instrumentation for the detection and characterization of exoplanets.* 2015.

[90] M. Perryman. *The Exoplanet Handbook.* Cambridge University Press, 2011.

[91] N. E. Piskunov and J. A. Valenti, *New algorithms for reducing cross-dispersed echelle spectra.* A&A, 385, 1095, 2002.

[92] B. Plez, J. Brett, A. Nordlund. *Spherical opacity sampling model atmospheres for M-giants. I - Techniques, data and discussion.* A&A 256, 551, 1992.

[93] D.L. Pollaco, I. Skillen, A. Collier Cameron, et al. *The WASP Project and the SuperWASP Cameras.* Publications of the Astronomical Society of the Pacific 118, 1407, 2006.

[94] K. Pont, D.K. Sing, N.P. Gibson, et al. *The prevalence of dust on the exoplanet HD 189733b from Hubble and Spitzer observations.* MNRAS 432, 2917, 2013.

[95] K. Poppenhaeger, S.J. Wolk. *Indications for an influence of hot Jupiters on the rotation and activity of their host stars.* A&A 565, 2014.

[96] S. Redfield, M. Endl, et al. *Sodium Absorption From The Exoplanetary Atmosphere Cf Hd 189733b Detected In The Optical Transmission Spectrum.* The Astrophysical Journal, 673:L87–L90, 2008.

[97] L.S. Rothman, I.E. Gordon, A. Barbe, et al. *The HITRAN 2008 molecular spectroscopic database.* Journal of Quantitative Spectroscopy & Radiative Transfer 110, 533, 2009.

[98] N.C. Santos, F. Bouchy, et al. *The Harps Survey For Southern Extra-Solar Planets.* A&A 426, L19, 2004.

[99] S.Seager and D.D. Sasselov. *Theoretical Transmission Spectra During Extrasolar Giant Planet Transits.* The Astrophysical Journal, 537:916E921, 2000.

[100] D.K. Sing, F. Pont, S. Aigrain, et al. *Hubble Space Telescope transmission spectroscopy of the exoplanet HD 189733b: high-altitude atmospheric haze in the optical and near-ultraviolet with STIS.* MNRAS 416, 1443, 2011 (b).

[101] D.K. Sing, J.J. Fortney, et al. *A Continuum From Clear To Cloudy Hot-Jupiter Exoplanets Without Primordial Water Depletion.* 2015.

[102] I.A.G. Snellen , S. Albrecht, et al. *Heoretical Transmission Spectra During Extrasolar Giant Planet Transits.* A&A, 2008.

[103] I.A.G. Snellen , R.J. de Kok, et al. *The orbital motion, absolute mass, and high-altitude winds of exoplanet HD209458b.* 2010.

[104] I.A.G. Snellen ,B.R. Brandl, et al. *The fast spin-rotation of a young extra-solar planet.* 2014.

[105] R.A. Street ,A. Udalski, et al. *Spitzer Parallax of OGLE-2015-BLG-0966: A Cold Neptune in the Galactic Disk.* ArXiv e-prints, (2015).

[106] K.B. Stevenson , J.M. Desert, et al. *Thermal structure of an exoplanet atmosphere from phase-resolved emission spectroscopy.* Science, 346, 838, 2014.

[107] K.O. Todorov, M.R. Line, et al. *The Water Abundance Of The Directly Imaged Substellar Companion κ And b Retrieved From A Near Infrared Spectrum.* 2016.

[108] S. Udry, X. Bonfils, X. Delfosse, et al. *The HARPS search for southern extra-solar planets.* A&A 469, L43, 2007.

[109] A. Vidal-Madjar, A. Lecavelier des Etangs, et al. *An extended upper atmosphere around the extrasolar planet HD209458b.* Nature, 442, 143, 2003.

[110] P.A. Wilson, D.K. Sing, N. Nikolov, et al. *GTC OSIRIS transiting exoplanet atmospheric survey: detection of potassium in HAT-P-1b from narrow-band spectrophotometry.* MNRAS, 450, 192, 2015.

[111] A. Wyttenbach, D. Ehrenreich, C. Lovis, et al. *Spectrally resolved detection of sodium in the atmosphere of HD 189733b with the HARPS spectrograph.* A&A, 577, A62, 2015.

[112] A. Wolszczan, D.A. Frail. *A planetary System around the millisecond pulsar psr1257 + 12.* Nature, 355, 145, 1992.